Écoulements viscoélastiques et compressibles avec application à la simulation 3D de l'injection de polymères

Luisa Alexandra Rocha da Silva

HAL Id: pastel-00001274
https://pastel.hal.science/pastel-00001274

Submitted on 6 Jun 2005

THÈSE

pour obtenir le grade de

DOCTEUR de L'École Nationale Supérieure des Mines de Paris

Spécialité: **MÉCANIQUE NUMÉRIQUE**

présentée et soutenue publiquement par

Luísa Alexandra ROCHA DA SILVA

LE 20 DÉCEMBRE 2004

VISCOELASTIC COMPRESSIBLE FLOW
AND
APPLICATIONS IN 3D INJECTION MOLDING SIMULATION

Directeur de Thèse: **Thierry COUPEZ**
Co-Directeur de Thèse: **Jean-François AGASSANT**

Jury

Professeur	Gerrit M. W. PETERS	Rapporteur
Professeur	Robert GUENETTE	Rapporteur
Professeur	José M. CESAR SA	Examinateur
Professeur	Gilles REGNIER	Examinateur
Docteur	Jocelyn MAUFFREY	Invité
Docteur	Andrès RODRIGUEZ-VILLA	Invité

abraço especial ao pessoal : à Bárbara e à Paula, aos Sérgios, aos Nunos, ao Miguel, ao Carlos... a todo o gang do Porto. Obrigado sobretudo pelos mails que me fazem sentir uma saudade...

Je remercie enfin et surtout Hugues, qui a un peu vécu ce travail, pour son soutien au quotidien. Un grand merci aussi à toute "la" belle-famille, les Sarda-Digonnet. Leur intêret par mon travail tout au long de ma thèse m'a beaucoup touché.

E sobretudo obrigado ao meus pais e à minha irmã (com um P e um I enormes), ao resto da minha familia. É com o vosso apoio que eu consegui começar e acabar esta tese !

Ser poeta é ser mais alto, é ser maior
Do que os homens!
Morder como quem beija!
É ser mendigo e dar como quem seja
Rei do Reino de Áquem e de Além Dor!
É ter de mil desejos o esplendor
E não saber sequer que se deseja!
É ter cá dentro um astro que flameja,
É ter garras e asas de condor!
É ter fome, é ter sede de Infinito!
Por elmo, as manhãs de oiro e de cetim...
É condensar o mundo num só grito!
E é amar-te, assim, perdidamente...
É seres alma, e sangue, e vida em mim
E dizê-lo cantando a toda a gente!

Florbela Espanca

Aos meus pais
A minha irmã
Ao Charco, que eu gostaria de ter visto viver mais tempo

Contents

Chapter 1

Introduction

The widespread application of polymers in almost every area of modern industry results in an increasing need for injection molds that must often satisfy the specifications concerning high quality parts. Injection molds are usually complex pieces with high dimensional requirements. Furthermore, to guarantee the quality of the final parts a precise characterization and monitoring of the injection molding process is required.

However, polymer processing is complex: polymers present high and temperature dependent viscosity, non linear viscoelastic behavior, low thermal diffusivity, crystallization and solidification kinetics, etc... To manufacture products with specifications in terms of dimensional stability or mechanical behavior, knowledge is required in how the processing variables, the rheology of the material, the geometry of the mould will influence the final properties of the product. The influence of these parameters on the final properties is far from obvious. It often results in a large amount of trials and errors when new products are developed. Numerical tools can speed up product innovation, reduce the associated costs, and help us to understand the material behavior all along the process.

This chapter will focus on the main features that must be addressed for polymer injection molding simulation and especially with the extension of the filling to the post-filling stage of the process. A brief description of the process shows its specificities, and an overview of the bibliography allows the identification of the main computational needs.

1.1   Injection molding

Plastic parts are extensively used for both professional and consumer products. Injection molding is the leading process in plastic transformation allowing, in a single operation, the production of complex parts at high production rates and with a large degree of automation. Basic equipment in injection moulding consists of an injection molding machine and a mold. Other auxiliary equipment may increase the efficiency and quality of the production.

1.1.1   Injection molding cycle

The injection molding cycle of a plastic part is composed of the following steps (figure 1.1):

- plastification
  The material, usually in the granule form, enters in the barrel through the hopper. The granules are melted inside the barrel which is heated by electric heaters. A screw is used to convey and pressurize, and plastification results not only from electrical heating but also from heat generation caused by friction between the granules and the screw barrel system. The screw moves backward against the adjustable hydraulic pressure until the amount of material (shot volume) required for the next cycle is plastified.

- filling
  Once the required amount of material is plasticized and the preceding injection cycle is achieved, the screw moves forward and pushes the melt through the machine nozzle and runner/gate system into the cavity of the mold. The melt is prevented from flow back into the barrel through a no-flow valve at the tip of the screw.

- packing/holding
  Once the mold has been volumetrically filled, the packing/holding phase starts. More melt is forced to enter the mold cavity in order to compensate for the densification of the material resulting from thermal shrinkage and phase changes in the material.

- cooling and ejection
  The so-called "cooling" phase starts when the polymer is solidified in the gate, even though material cooling begins as soon as the polymer enters in the cavity. The temperature of the material falls down to the mold temperature, by conduction. The mold is open and the solidified part is removed (ejection). It closes again and a new cycle starts.

This study intends to unify all the stages of the process through a general model of the material behavior.

1.1.2   Injection molding pressure

A significant feature in injection molding is the pressure curve. If the thermomechanical history variables (pressure, temperature, filling rate, stress, cooling rate, shrinkage rate...) can be accurately measured or predicted, one can expect that the molded product properties (density and shrinkage, elastic modulus,...) would be accurately predicted. Figure 1.2 shows a typical pressure profile inside the mold cavity and its main features.
The pressure in the cavity is today the most important measurable parameter to establish a correlation between process conditions and dimension and weight of the final part. Any changes in the process (melt or mold temperature, flow rate, packing pressure,...) modify this profile.
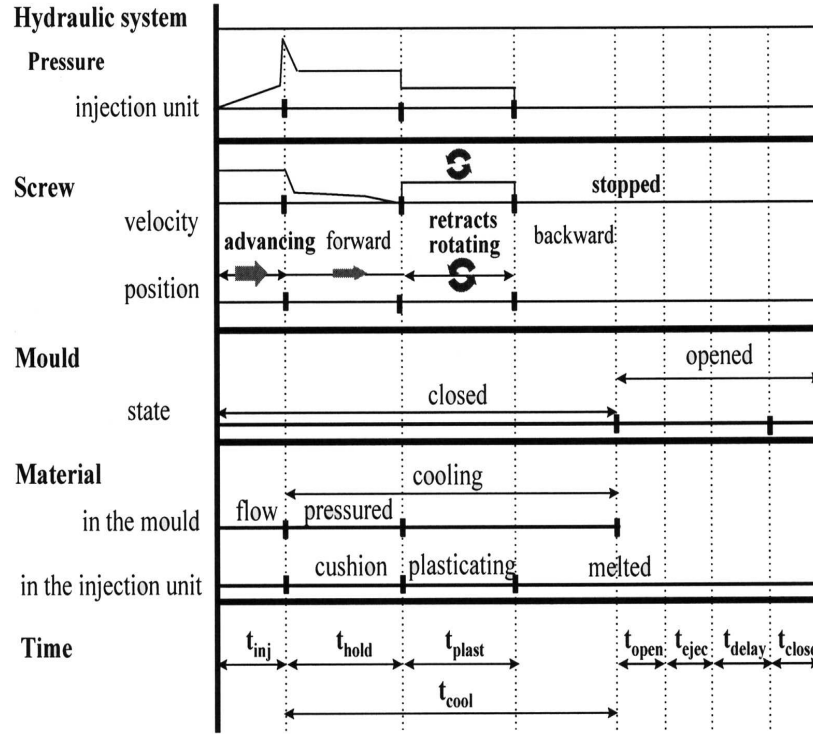
Figure 1.1: *Injection molding cycle (t_{inj} - filling time, t_{hold} - holding time, t_{plast} - plasticating time, t_{cool} - cooling time, $t_{open/close}$ - mold opening/closing time, t_{ejec} - ejection time) [Pontes, 2002].*
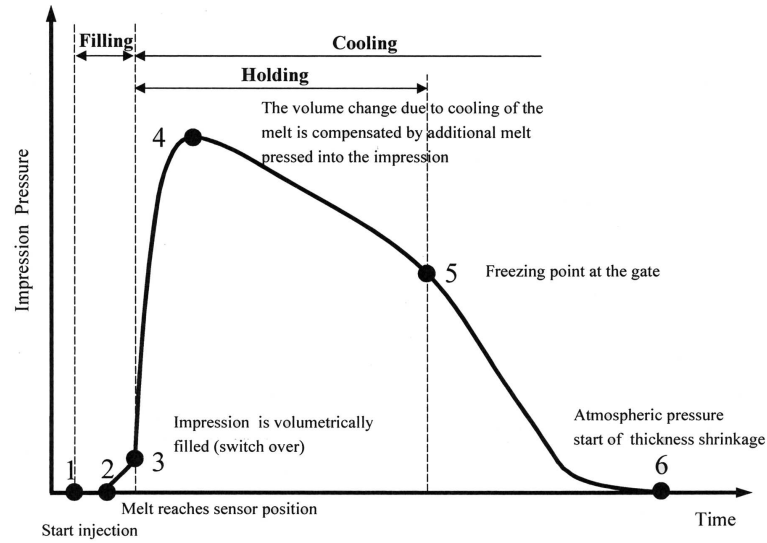
Figure 1.2: *Typical pressure evolution inside the mold cavity [Pontes, 2002].*

The pressure trace is important to establish a comparison between the results obtained by simulation and the experimental measures.

1.2 An unified model

1.2.1 Specificities of the process

The flow of polymer melts into a cold cavity is a typical example of an unsteady, non-isothermal three dimensional flow of compressible, viscoelastic fluids. One of the characteristics of the process is the coupling between the flow and the cooling process. Every particle in the material experiences a different thermo-mechanical history. During the process the material is object of mechanical and thermal phenomena in the fluid, rubbery and glassy states.

During <u>filling</u>, when the melt flows through the gate into the cavity, polymer macromolecules orient, inducing both shear and normal stresses - <u>viscoelastic</u> nature stresses. The cooling rates are high (especially near the walls), and highly oriented layers directly solidify, without being able to relax.

At the <u>end of filling</u>, there is an increase in pressure and the <u>compressibility</u> of the melt enables an extra material flow into the cavity. Stresses induced during filling can relax and new stresses are built up during packing. The amount of stress relaxation depends on the cooling rate, which depends strongly on the distance to the wall. Consequently, some of the flow induced stresses built-up will remain as frozen-in stress. In the meantime, thermal stresses are created in these layers because of the inhomogeneous cooling and the prohibited shrinkage. Thus, there are two types of stresses, which both contribute to the final frozen-in residual stresses [Flaman, 1990].

During the <u>holding</u> stage, two phenomena become competitive. First the high packing pressure, which forces more material into the mold to compensate shrinkage, tries to maintain an uniform pressure level. Secondly, the continuous cooling increases the viscosity and the density. The pressure decays, starting at the end of the cavity. Although shear rates are low, the stresses can be high due to the continuously increasing viscosity. When the gate freezes off, no more material can enter the mold and the pressure in the cavity falls down. While the temperature decreases, the relaxation times increase. When the part is assumed to be rigid enough, it is <u>ejected</u>. Then it is no longer constrained by the mould and the stresses relax, causing shrinkage and warpage. Relaxation continues until an equilibrium is reached, which can take several months.

A general model of the material includes a general constitutive law, where the stress is obtained by considering both viscoelastic and compressible material behavior.

1.2.2 A short literature review

The main aim of the numerical simulation of the injection molding process is not only to analyze the processing stage, but also to predict the end-use properties, starting from the material properties and the processing conditions.

After the work of Harry and Parrot [Harry and Parrot, 1970], a large number of studies were devoted to the simulation of the injection molding process. Initially, it was restricted to the simulation of the filling. Pioneer studies are attributed to M. Kamal and co-workers [Kamal and Kenig, 1972], and other authors [Williams and Lord, 1975], who used the finite difference method to predict temperature, velocity and pressure in simple geometries. The flow was considered uni-dimensional and Newtonian, and lubrication theory was applied. Subsequently, H. Lord [Lord, 1979] introduced a constitutive equation for viscosity, showing its dependence on the shear rate.

Bi-dimensional analysis of filling are firstly attributed to E. Broyer [Broyer et al., 1974], through the Flow-Analysis Network method (FAN). Later, M. Ryan [Ryan and Chung, 1980] studied the effects of gate dimensions on pressure distribution inside the cavity and on flow front advancement. Extension to a non-isothermal non-Newtonian fluid was done by M. Kamal's research group [Kuo and Kamal, 1976].

An important improvement was given by C. Hieber and S. Shen [Hieber and Shen, 1980] when they introduced a finite element/finite difference scheme to model the filling step for a generalized Hele-Shaw

flow of a non-Newtonian fluid under non-isothermal conditions. Based on this work, [Wang et al., 1986] developed a commercial software.

At the same time, [Isayev and Hieber, 1980] performed the first attempt to incorporate the effects of viscoelasticity in mold filling. The prediction of residual stresses, orientation and birefringence was made by considering the uni-dimensional non-isothermal flow of a viscoelastic melt with constitutive law described by the Leonov model [Leonov, 1976].

[Kamal et al., 1986] dealt with the simulation of the fountain flow phenomena to better understand the relationship between fluid element deformation, flow induced stresses and microstructure development at the surface of the part. Simulation was done using a marker-and-cell (MAC) computational scheme, incorporating a viscoelastic rheological equation and taking into account non-isothermal crystallization kinetics.

First attempts to model the post-filling stage were done by [Kuo and Kamal, 1977]. Their analysis included inertia effects of impinging flows and compressibility of the melts. Simultaneously, [Titomanlio et al., 1980] extended the [Lord, 1979] model to the holding phase. The cristallisation effect was considered using an equivalent specific heat that takes into account heat generated by cristallisation. Effect of viscoelasticity in post-filling was neglected until the work of [Flaman, 1990].

The work towards an unified model was firstly done by [Chiang et al., 1991], who developed an unified model for the filling and post-filling stages based on early works of [Wang et al., 1986]. A generalised Hele-Shaw model of a compressible viscous fluid is assumed in the analysis. Numerical solution is based on the finite element/finite difference method to determine pressure, temperature and velocity fields, and a finite volume method for flow front computation.

Recent developments concern the 3D modelling of the injection molding process [Pichelin and Coupez, 1998], [Illinca and Hetu, 2001], incorporation of cristallisation kinetics [Smirnova et al., 2004], prediction of microstructure development [Ammar, 2001] and simulation of non-conventional injection molding techniques. 3D simulation is an important improvement to accurately predict some features of injection molding which are difficult to capture through an Hele-Shaw model: complex geometries, complex flow, fibre and molecular orientation,...

Very few authors propose 3D models, and the ones proposed treat independently each stage of the process. In this study, we use a single material model, compressible and viscoelastic, allowing a continuous computation all along the process.

1.3   Context, objectives and outline

This work was done within the **REM3D** project context, which includes the following members:

- **Arkema** (www.arkema.com) : petro-chemical, polymer furnisher

- **DOW Chemicals** (www.dow.com) : polymer producer

- **Essilor International** (www.essilor.com) : polymer glasses producer

- **FCI** (www.fciconnect.com) : connector and connecting systems producer;

- **Plastic Omnium** (www.plasticomnium.com) : automotive equipment

- **Schneider Electric** (www.schneider.fr) : electrical parts distribution, plastic equipment

- **Snecma Propulsion Solide** (www.snecma.fr) : aeronautic equipment

- **Transvalor** (www.transvalor.fr) : industrialization and commercialization of material forming software (FORGE2, FORGE3, TFORM3, THERCAST, **REM3D**)

Before this work, **REM3D** performed the filling stage of the process through:

- a mechanical solver, determining velocity and pressure during the filling stage;

- a transport solver to determine the flow front position;

- a temperature solver to compute temperature in the fluid.

The material was considered incompressible and viscous during the whole filling stage. Validation of the models implemented was mainly done through comparison between experimental and numerical short-shots (figure 1.3), not sufficient to predict part quality or influence of the injection molding parameters.
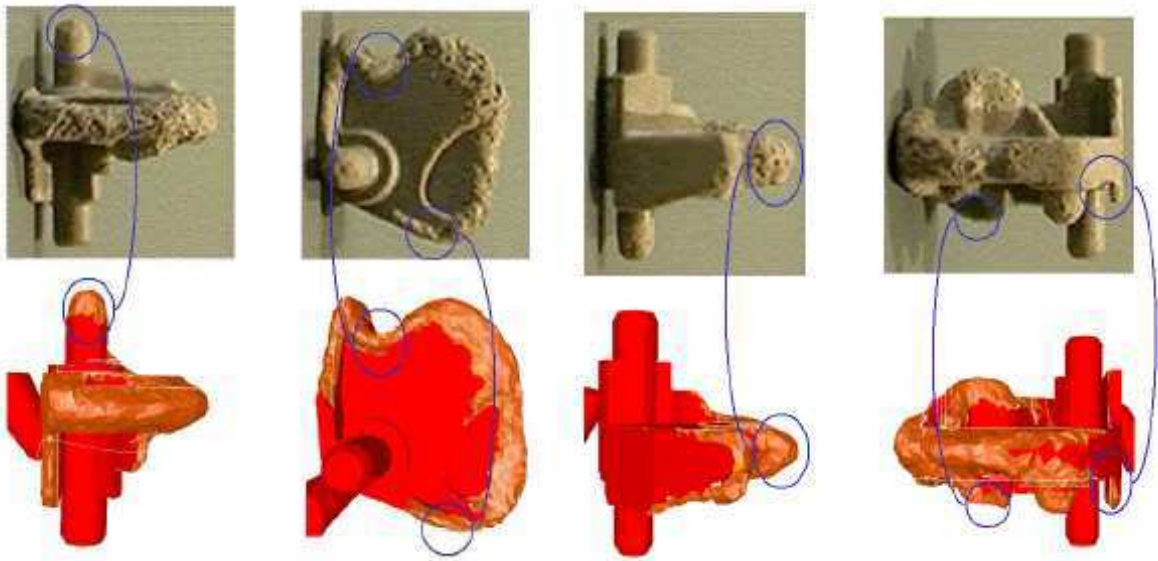
Figure 1.3: *Comparison between experimental and numerical results with REM3D through the short-shots [Batkam et al., 2003].*

Thus, the purpose of our work is, knowing the part geometry and injection parameters, to predict:

- position of the flow front at each instant of the filling stage;

- thermodynamical state of the material at each instant of the injection molding cycle, given by its pressure, temperature, and conformation tensor, (molecular orientation and chain stretch) or stress;

- the shrinkage rate eventually from the part, when it is ejected.

To extend the **REM3D** software from the filling to the post-filling stage, with an unique material behavior model, several objectives need to be accomplished.

Firstly, material's compressibility must be taken into account. On one hand, it allows an extra amount of polymer to enter the mold, and on the other hand it induces important thermal stresses. At this stage, an important result is the pressure trace on the whole injection molding cycle, giving quantitative information about what happens inside the cavity. Furthermore, the computed shrinkage rate provides qualitative data on regions of the molded part more susceptible to shrink.

Secondly, because of the viscoelastic nature of polymers, it is necessary to follow the development and relaxation of stresses throughout the various stages of the molding cycle. The source of this viscoelastic behavior is based on the orientation and stretch of the polymer's macromolecular chains. Quantitative results of both these features are of prime importance for the prediction of the parts' final properties.

However the integration of the model is done by a viscosity dependence with temperature, which remains a simplification beyond solidification. Crystallization or solidification mechanisms are still not taken into account in this work.

> *By introducing a unique material model, our main objective is to describe the thermodynamical state of the material at each instant of the injection molding cycle, given through pressure, temperature, and conformation tensor, (molecular orientation and chain stretch) or stress.*

This work is divided in five main chapters. After this short introduction, we will explain how compressibility has been modeled. Therefore, we consider conservation equations given by continuum mechanics in fluid domain, with a simple viscous and compressible behavior. The numerical methods developed to solve viscous compressible flows and benchmarks are detailed, as well as their extension to free surface flows.

Polymers' viscoelasticity is introduced and its numerical determination described in Chapter 3. Validation is shown and extension to the compressible viscoelastic case is taken into account.

Chapter 4 gives a more realistic approach of injection moulding. In this chapter, we study the non-isothermal compressible viscoelastic flows with free surfaces, with application to injection molding problems. Validations are done with the literature and by comparison with experimental work.

Finally, conclusion opens the discussion to the perspectives.

Chapter 2

Compressibility

Contents

The objective of this chapter is to define the main features of a compressible flow in injection molding, and to describe the numerical methods of resolution. The molten polymer can be considered as a slightly-compressible fluid to which a high pressure will induce a compressible flow.

The first part of this chapter presents the equations derived from continuum mechanics to the compressible case, without considering temperature influence. The conservation of mass and the conservation of momentum lead to a system of equations where velocity and pressure are still the unknowns. Neglecting inertia effects (as usual with polymers), we get a compressible-like Stokes system, the pressure time derivative term giving it a non steady character. The Mixed Finite Element framework can still be applied to such equations.

The second part of the chapter describes the thermomechanical coupling and its influence on material's compressibility. The energy balance equation is introduced and a splitting technique is adopted between mechanics and temperature balance equations, even if there exists a strong coupling between these two equations. The heat equation, that is basically a convection-diffusion equation, presents in the compressible case an additional term related to the dilatation/contraction of the material. It is solved through a space-time finite element method, in a mixed temperature/heat flux form.

A restriction of the equations to the molten polymer case is presented. We observe that significant changes are introduced since the material behavior becomes now strongly non-linear, considering both viscosity and density. We will see in the next chapter that the rheological behavior may even be more complex (viscoelastic).

Finally, the last part is devoted to the extension of the equations to free surface compressible flows. Introduction of a moving free surface is considered, with its appropriate method of resolution. Applications to free surface compressible flows show the feasibility of the methods developed in other situations than injection molding flows.

2.1 Isothermal compressibility

Let us start by considering a compressible viscous (Newtonian) fluid. In this section we establish the equations that allow the computation of the velocity and pressure distributions in this fluid, when it flows through a channel without temperature regulation. In this case $\Omega \subset \mathbb{R}^d = \Omega_f$ is our material domain, closed and bounded, that evolves throughout time, so that our true computational domain is $\mathcal{D} = \Omega \times [0, \Theta]$. The spatial boundaries $\partial \Omega_i$ move with the velocity of the fluid particles at each boundary, giving $\partial \Omega(t)$ (figure 2.1).

The mechanical boundary conditions that we have to face may be:

- in velocity

$$\mathbf{v}(\mathbf{x}, t) = \mathbf{v}_{imp} \quad \forall (\mathbf{x}, t) \in \partial \Omega_m \times [0, \Theta] \tag{2.1}$$

- in stress

$$\sigma \mathbf{n} = -\mathbf{F}_{imp} \in \partial \Omega_m \times [0, \Theta] \tag{2.2}$$

where $\mathbf{n}$ is the outward unit normal, in a local referential, and $\mathbf{v}_{imp}$ and $\mathbf{F}_{imp}$ are imposed values of velocity and force.

We also need to define the initial state of our domain, through the initial conditions (at the instant t_0) in velocity and stress:

$$\begin{aligned} \mathbf{v}(\mathbf{x}) &= \mathbf{v}_0 \qquad \forall \mathbf{x} \in \Omega(t_0) \\ \sigma &= \sigma_0 \end{aligned} \tag{2.3}$$

In the viscous case, the condition in stress can be seen as a pressure at the beginning of the computation. It is evident that if we start from rest, velocity will be zero and pressure will be the atmospheric one.

The whole system must satisfy the conservation equations given by continuum mechanics and is described in the following subsections.
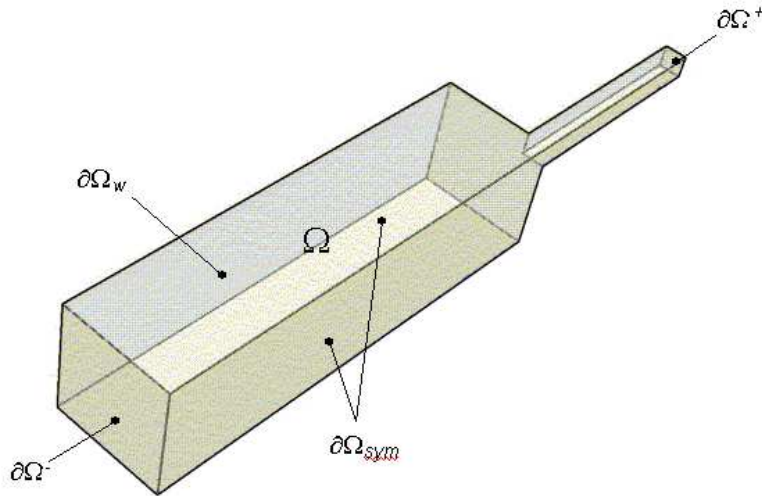
Figure 2.1: *Computational domain when studying the flow through a channel: $\partial \Omega^-$ is the inlet gate, $\partial \Omega^+$ is the outlet gate, $\partial \Omega_{sym}$ is a symmetry plane and $\partial \Omega_w$ is the wall.*

2.1.1 Flow equations and considerations

Conservation of mass and state law

The differential form of the mass conservation equation (also called the continuity equation) is

$$\frac{\partial \rho}{\partial t} + \nabla \cdot (\rho \mathbf{v}) = 0 \quad \forall (\mathbf{x}, t) \in \Omega(t) \times [0, \Theta] \tag{2.4}$$

We have also (preferred form):

$$\frac{1}{\rho} \frac{d\rho}{dt} + \nabla \cdot \mathbf{v} = 0 \quad \forall (\mathbf{x}, t) \in \Omega(t) \times [0, \Theta] \tag{2.5}$$

In an <u>incompressible</u> flow the rate of density change of a fluid particle, $\frac{d\rho}{dt}$, is negligible compared with the component terms of $\rho \nabla \cdot \mathbf{v}$. This means that:

$$\nabla \cdot \mathbf{v} = 0 \quad \forall (\mathbf{x}, t) \in \Omega(t) \times [0, \Theta] \tag{2.6}$$

or

$$\frac{d\rho}{dt} = 0 \quad \forall (\mathbf{x}, t) \in \Omega(t) \times [0, \Theta] \tag{2.7}$$

This form expresses the incompressibility of the flow by stating that the density of a fluid particle does not change as it moves through the flow field. It is important to emphasize that an incompressible flow does not require that the density have the same constant value throughout the flow field but only that the density be unchanging along a particle path. We call such a flow a <u>constant-density</u> flow. However, not all incompressible flows are constant-density flows. To classify a flow as compressible, one of three different situations must occur:

- the density of the fluid is changed by a significant amount;

- the flow velocity is not small compared to the speed of sound;

- in the case of unsteady flow, the time for the velocity to change appreciably is not long compared to the time for a sound wave to go through the flow field.

In the context of this work, we consider a slightly-compressible fluid, on which a high pressure applied will induce a compressible flow. Thus, density varies and its evolution is taken into account through a <u>state law</u>. For example, for barotropic flows, the state equation of the fluid gives $\rho = \rho(p)$; for nonbarotropic flows, it is of the form $\rho = \rho(p, e)$, where e is the internal energy of the fluid (and we consider an equation for e, the energy equation). Each state variable contribution to the variation of the density may be considered independently:

$$\chi_\alpha = -\frac{1}{v} \left(\frac{\partial v}{\partial \alpha} \right) = \frac{1}{\rho} \left(\frac{\partial \rho}{\partial \alpha} \right) \tag{2.8}$$

and added

$$\frac{1}{\rho} \frac{d\rho}{dt} = \sum_i \chi_{\alpha_i} \frac{d\alpha_i}{dt} \tag{2.9}$$

Let us consider the generic form $\rho = \rho(p, e)$. This means that the mass conservation equation form for our problem resolution is generically

$$\nabla \cdot \mathbf{v} + \chi_p \frac{dp}{dt} = \chi_e \frac{de}{dt} \tag{2.10}$$

In these equations, χ_p has a physical sense and represents the <u>isothermal compressibility</u>, typical of each material (the inverse of the Bulk modulus). This last expression is the form of the conservation of mass that we are going to consider in the following.

Conservation of momentum and mechanical behavior

Momentum's conservation equation can be written as:

$$\nabla \cdot \sigma = \rho(\mathbf{g} - \frac{d\mathbf{v}}{dt}) \quad \forall (\mathbf{x}, t) \in \Omega(t) \times [0, \Theta] \tag{2.11}$$

where σ is the Cauchy stress tensor, $\rho \mathbf{g}$ the exterior mass force density (corresponding to gravity). We suppose that the right-hand side of this equation is explicitly considered, assuming the form:

$$\nabla \cdot \sigma = \mathbf{f} \quad \forall (\mathbf{x}, t) \in \Omega(t) \times [0, \Theta] \tag{2.12}$$

We take as hypothesis that the material behaves like a purely viscous fluid. The most general behavior law is, in this case:

$$\sigma = 2\eta\varepsilon(\mathbf{v}) + [\lambda \mathrm{tr}(\varepsilon(\mathbf{v})) - p]\mathbf{I} \tag{2.13}$$

where $\mathbf{I}$ is the identity tensor, η the fluid dynamic viscosity, λ the second viscosity coefficient, and $\varepsilon(\mathbf{v})$ the strain rate deformation tensor, represented by:

$$\varepsilon(\mathbf{v}) = \frac{1}{2}[\nabla \mathbf{v} + \nabla \mathbf{v}^t] \tag{2.14}$$

If we consider that the second viscosity coefficient is a function of the dynamic viscosity (Stokes fluid), $\lambda = -\frac{2}{3}\eta$, which is required by the second law of thermodynamics ($3\lambda + 2\eta \geq 0$, see Appendix B), our behavior law is:

$$\sigma = 2\eta\varepsilon(\mathbf{v}) - p\mathbf{I} - \frac{2}{3}\eta\mathrm{tr}(\varepsilon(\mathbf{v}))\mathbf{I} \tag{2.15}$$

For simplification purpose we will detail our compressible resolution method by supposing that the fluid viscosity is constant, i.e., the fluid is Newtonian. Later, we will extend our approach to the non-linear case, considering the non-isothermal and shear-rate dependent model.

From the conservation equations previously described, we derive the following form of the Stokes compressible problem: *find $\boldsymbol{v} \in \mathcal{C}^2(\Omega)$ and the pressure $p \in \mathcal{C}^1(\Omega)$ such that, $\forall t \in [0, \Theta]$, $\forall x \in \Omega(t)$,*

$$\begin{cases} \nabla \cdot [2\eta(\varepsilon(\mathbf{v}) - \frac{1}{3}\nabla.\mathbf{v}\mathbf{I})] - \nabla p = \mathbf{f} \\[2ex] \nabla \cdot \mathbf{v} + \chi_p \frac{dp}{dt} = \chi_e \frac{de}{dt} \\[2ex] + \text{ boundary and initial conditions} \end{cases} \tag{2.16}$$

Let us consider that our time interval $[0, \Theta]$ is structured as follows: $0 = t^0 < t^1 < ... < t^{N_t}$. We define the time element I by $I^n =]t^n, t^{n+1}[$, such that

$$[0, \Theta] = \bigcup_n I^n \tag{2.17}$$

We observe the presence of a transient term in the equation of mass conservation that corresponds to the partial derivative of the pressure as a function of time. In our case, we consider that velocity and pressure are constant *per* time slab. This means that we can approach the time derivative of the pressure by an Euler implicite scheme in the following way:

$$\begin{cases} \nabla \cdot [2\eta(\varepsilon(\mathbf{v}^n) - \frac{1}{3}\nabla.\mathbf{v}^n\mathbf{I})] - \nabla p^n = \mathbf{f}^n \\[2ex] \nabla \cdot \mathbf{v}^n + \chi_p \frac{p^n}{|I^n|} + \chi_p \mathbf{v}^{n-1} \cdot \nabla p^n = \chi_p \frac{p^{n-1}}{|I^n|} + \chi_e \frac{e^{n-1} - e^{n-2}}{|I^n|} + \chi_e \mathbf{v}^{n-1} \cdot \nabla e^{n-1} \end{cases} \tag{2.18}$$

where $\mathbf{v}^n$ and p^n are the velocity and pressure at the current time element I^n and p^{n-1} the pressure field at the previous time element. We are therefore led to the solution, on each time element, of a problem of the generic form:

$$\begin{cases} \nabla \cdot [2\eta(\varepsilon(\mathbf{v}) - \frac{1}{3}\nabla.\mathbf{vI})] - \nabla p = \mathbf{f} \\ \\ \nabla \cdot \mathbf{v} + \alpha p + \beta \mathbf{v}^{n-1} \cdot \nabla p = C \end{cases} \qquad (2.19)$$

where

$$C = \chi_e \frac{e^{n-1} - e^{n-2}}{\mid I_n \mid} + \chi_e \mathbf{v}^{n-1} \cdot \nabla e^{n-1} \qquad (2.20)$$

Here the velocity used in the convective term will be taken at the previous time step (a classical linearization). Furthermore, the isothermal compressibility coefficient χ_p is, for many materials, pressure-dependent, introducing a strong non-linearity. Nevertheless, it will be treated as constant in subsequent description. A pressure-dependent coefficient will be studied later. Even though inertia effects are often neglected in polymer injection molding, we can take them into account. Their numerical treatment is not considered here, since it has been object of a previous work [Saez, 2003].

Numerical studies of compressible flows generally involve the full compressible Navier-Stokes equations, and applications concern high Mach number flows of non-dilute, compressible fluids. Many of the mathematical issues concerning compressible Navier-Stokes equations will be the same as for incompressible ones. Theorems concerning existence and uniqueness begin with the 1D theory of Kanel [Kanel, 1968] and Kazhikov and Shelukhin [Khazikov and Shelukh, 1977], among others. This approach was extended to two and three dimensions in a series of papers of Matsumura and Nishida [Matsumura and Nishida, 1979]. They prove the global existence of small (close to a constant state) smooth solutions with small, smooth initial data. More recent results relax these restrictions on the initial data. First Lions [Lions, 1993], then Kazhikov and Weigant [Khazikov and Weigant, 1995] apply more modern techniques of weak compactness to obtain global solutions with large initial data in certain cases of barotropic flow ($\rho = \rho(p)$). Then Hoff [Hoff, 1995] analyzes in depth the effect of initial discontinuities for the full (nonbarotropic) compressible Navier-Stokes equations, finding that singularities convect with the flow and decay exponentially in time, more rapidly for small viscosities and larger sound speeds.

In our case, as said previously, we have a slightly-compressible fluid where a high pressure induces a compressible flow. One must point out that the role of pressure is very different in both compressible and incompressible cases. In the later case, p is a function of $\mathbf{v}$, the velocity (through the solution of a Neumman problem). In the compressible case, it is an independent function and one more equation is added. Basically, we note that this equation contains a convective derivative of p and is therefore an hyperbolic equation in p. Thus, even if we neglect mass and inertia forces (classical Stokes problem), the system 2.16 is neither elliptic nor hyperbolic, but contains features of each class of equations. Systems that are of mixed elliptic and hyperbolic type are sometimes called "incompletely elliptic" or, in the time dependent case, "incompletely parabolic" [Kellog and Liu, 1996]. The system differs from the Stokes equations, mainly in the convective derivative of p. Therefore, our finite element method will approach the one used in the Stokes equations by extending it to compressible flow - Stokes compressible equations.

Existence and unicity of solution for finite element formulations of the Stokes problem follows an inf-sup condition. Appropriate pairs of velocity-pressure spaces for the Stokes system and error estimates have been well studied and obtained [Brezzi and Fortin, 1991]. In what concerns the Navier-Stokes problem, Bristeau and co-workers [Bristeau et al., 1990] discussed the numerical simulation of compressible viscous flows by a combination of finite element methods for the space approximation, and

implicit second-order multi-step scheme for time discretization, and generalized minimal residual methods (GMRES) for solving the linearized systems. R. Kellog and B. Liu [Kellog and Liu, 1996] proposed a finite element formulation for the <u>Stokes compressible</u> problem which is uniquely solvable, without requiring any compatibility condition on the subspaces for velocity and pressure, by penalizing the continuity equation [Kellog and Liu, 1997].

Numerical methods used to solve compressible or incompressible problems are often different, for what concerns independent variables, linear system solvers, and numerical stability. Several authors developed in the past unified computational methods for compressible and incompressible viscous flows [Harlow and Amsden, 1971], [Issa et al., 1986], [Yabe and Wang, 1991], [Zienkiewicz and Wu, 1992], [Hauke and Hughes, 1994],[Nonaka and Nakayama, 1996], [Nigro et al., 1997], showing results for a wide range of flow speeds, but in two-dimensional simple geometries.

In the following, we consider finite element methods for the system 2.19, based on the Stokes (or Navier-Stokes) incompressible problem. A weak formulation of the problem is given, such as the pressure subspace consists of continuous functions. The finite element subspaces satisfy the inf-sup condition as it is required for the Stokes system. Consequently, the finite element system has a unique solution and an error bound is obtained for this solution.

To sum up, we solve using the finite element method, at each time step, the problem: find $\boldsymbol{v} \in \mathcal{C}^2(\Omega)$ and the pressure $p \in \mathcal{C}^1(\Omega)$ such that $\forall x \in \Omega$,

$$\begin{cases} \nabla \cdot [2\eta(\varepsilon(\boldsymbol{v}) - \frac{1}{3}\nabla.\boldsymbol{v}\mathbf{I})] - \nabla p = \boldsymbol{f} \\ \\ \nabla \cdot \boldsymbol{v} + \alpha p + \beta \boldsymbol{v}^{n-1} \cdot \nabla p = C \end{cases}$$

2.1.2 Mixed variational formulation and Mixed Finite Element (MFE) discretization

Let us introduce the $L^2(\Omega))$ and $\mathcal{H}^1(\Omega)$ as the classical Sobolev spaces (Lebesgue and Hilbert). Let $\mathcal{V}$ and $\mathcal{Q}$ be Hilbert spaces, and $\mathcal{P}$ a Lebesgue space, $\mathcal{P} = L_2(\Omega)$, with

$$\mathcal{L}^2(\Omega) = \{\mathbf{v} : \Omega \longrightarrow \mathbb{R}; \int_\Omega \mid \mathbf{v} \mid^2 < \propto\} \tag{2.21}$$

We state that $\mathcal{Q} \subset \mathcal{P}$, $\mathcal{Q}$ dense in $\mathcal{P}$, $\|q\|_\mathcal{P} \leq \|q\|_\mathcal{Q}$. We establish the variational form of 2.19: *find $(\boldsymbol{v}, p) \in \mathcal{V} \times \mathcal{Q}$ such that, $\forall(\boldsymbol{w}, q) \in \mathcal{V} \times \mathcal{P}$, for $(\boldsymbol{f}, g) \in \mathcal{V}' \times \mathcal{Q}'$*

$$\begin{cases} \int_\Omega 2\eta(\varepsilon(\mathbf{v}) - \frac{1}{3}\text{tr}(\varepsilon(\mathbf{v}))\mathbf{I}) : \varepsilon(\mathbf{w}) - \int_\Omega p\nabla \cdot \mathbf{w} = -\int_\Omega \mathbf{fw} - \int_{\partial\Omega} p_e(\mathbf{w} \cdot \mathbf{n}) \\ \\ -\int_\Omega q\nabla \cdot \mathbf{v} - \int_\Omega q(\alpha p + \beta\mathbf{v} \cdot \nabla p) = -\int_\Omega qC \end{cases} \tag{2.22}$$

Let a be a bounded bilinear form on $\mathcal{V} \times \mathcal{V}$, let b be a bounded bilinear form on $\mathcal{V} \times \mathcal{P}$, let d be a bounded bilinear form on $\mathcal{Q} \times \mathcal{P}$. We associate to these forms the problem: *for $(\boldsymbol{f}, g) \in \mathcal{V}' \times \mathcal{Q}'$, find $(\boldsymbol{v}, p) \in \mathcal{V} \times \mathcal{Q}$ such that, $\forall(\boldsymbol{w}, q) \in \mathcal{V} \times \mathcal{P}$*

$$\begin{cases} a(\mathbf{v}, \mathbf{w}) + b(\mathbf{w}, p) = \langle\mathbf{f}, \mathbf{w}\rangle \\ \\ b(\mathbf{v}, q) + d(p, q) = \langle C, q\rangle \end{cases} \tag{2.23}$$

Some conditions in the bilinear forms are required. Firstly, a must be coercive on $\mathcal{V}$:

$$\exists \alpha > 0 \quad \text{such that} \quad a(\mathbf{w}, \mathbf{w}) \geq \alpha \|\mathbf{w}\|_{\mathcal{V}}^2, \qquad \forall \mathbf{w} \in \mathcal{V} \tag{2.24}$$

b must satisfy the inf-sup condition on $\mathcal{V} \times \mathcal{P}$:

$$\exists \beta > 0 \quad \text{such that} \quad \inf_{q \in \mathcal{Q}} \sup_{\mathbf{w} \in \mathcal{V}} \frac{b(\mathbf{w}, q)}{\|\mathbf{v}\|_{\mathcal{V}} \|q\|_{\mathcal{P}}} \geq \beta, \quad \forall \mathbf{w} \in \mathcal{V}, \forall q \in \mathcal{Q} \tag{2.25}$$

Finally, we need d to be bounded from below in the norm of P:

$$\exists \gamma > 0 \quad \text{such that} \quad d(q, q) \geq -\gamma \|q\|_{\mathcal{P}}^2, \quad \forall q \in \mathcal{Q} \tag{2.26}$$

It will be necessary to choose γ sufficiently close to zero, or negative. The difference from the Stokes classical problem is the addition of the condition on d, because this bilinear form is not bounded on $\mathcal{P} \times \mathcal{P}$. One needs a space $\mathcal{Q}$ with a norm that controls the convective derivative of p. We can show [Kellog and Liu, 1996] that the solution $(\mathbf{v}, p)$ exists and is unique in the chosen spaces $\mathcal{V} \times \mathcal{Q}$.

Let Ω_h be a discretisation of the spatial domain:

$$\Omega_h = \bigcup_{K \in \mathcal{T}_h(\Omega)} K \tag{2.27}$$

The parameter h denotes mesh spacing, or approximation indicator, on the subspace. It is related with the diameter of the elements by

$$h = \max_{K \in \mathcal{T}_h(\Omega)} \ \text{diam}(K) \tag{2.28}$$

The projection operator from a continuous space $\mathcal{U}$ into a discrete space $\mathcal{U}_h$ may be defined as

$$\Pi_h : \begin{cases} \mathcal{U} \to \mathcal{U}_h \\ \\ u \to \Pi_h u = \arg(\min_{u_h} \| u - u_h \|) \end{cases} \tag{2.29}$$

The elements K of the eulerian mesh $\mathcal{T}_h$ are d-simplexes (triangles in 2D, tetrahedra in 3D). We need to define the functional spaces $\mathcal{V}_h$ and $\mathcal{Q}_h$ of finite dimensions, close to $\mathcal{V}$ and $\mathcal{Q}$ of infinite dimension, such that the solution $(\mathbf{v}, p) \in \mathcal{V} \times \mathcal{Q}$ is close to $(\mathbf{v}_h, p_h) \in \mathcal{V}_h \times \mathcal{Q}_h$. The discrete problem can be written as: *find* $(\boldsymbol{v}_h, p_h) \in \mathcal{V}_h \times \mathcal{Q}_h, \mathcal{V}_h \subset \mathcal{V}, \ \mathcal{Q}_h \subset \mathcal{Q}$ *such that,* $\forall (\boldsymbol{w}_h, q_h) \in \mathcal{V}_h \times \mathcal{P}_h$

$$\begin{cases} a(\mathbf{v}_h, \mathbf{w}_h) + b(\mathbf{w}_h, p_h) = \langle \mathbf{f}, \mathbf{w}_h \rangle \\ \\ b(\mathbf{v}_h, q_h) + d(p_h, q_h) = \langle g, q_h \rangle \end{cases} \tag{2.30}$$

We assume that a, b and d satisfy, in the discrete problem, the same conditions than in the continuous one. We can also prove existence and unicity of solution to the discrete problem [Kellog and Liu, 1996] (see Appendix C):

LEMMA 1. If 2.24, 2.25 and 2.26 are satisfied and if $\gamma \leq \frac{1}{2}\alpha\beta^2\|a\|^{-2}$, then the problem 2.30 has at most one solution.

THEOREM 1. If 2.24, 2.25 and 2.26 are satisfied and if $\gamma \leq \frac{1}{2}\alpha\beta^2\|a\|^{-2}$, then the approximate solution $(\mathbf{v}_h, p_h)$ satisfies

$$\|\boldsymbol{v} - \boldsymbol{v}_h\|_{\mathcal{V}} + \|p - p_h\|_{\mathcal{P}} \leq C[\|\boldsymbol{v} - \boldsymbol{w}_h\|_{\mathcal{V}} + \|p - q_h\|_{\mathcal{Q}}]$$

for all $\boldsymbol{w}_h \in \mathcal{V}_h$ and $q_h \in \mathcal{Q}_h$.

Let d_v be the dimension of $\mathcal{V}_h$, d_p the dimension of $\mathcal{P}_h$ and let us choose $\{\phi_m\}_{m=1,..,d_v}$ a basis of $\mathcal{V}_h$ and $\{\lambda_m\}_{m=1,..,d_p}$ a basis of $\mathcal{P}_h$. We decompose $\mathbf{v}_h$ and p_h on these basis by writing:

$$\mathbf{v}_h = \sum_{m=1}^{d_v} V_m\phi_m \quad \text{and} \quad p_h = \sum_{m=1}^{d_p} P_m\lambda_m \tag{2.31}$$

We can assume that $\mathbf{w}_h = \phi_m$ and $q_h = \lambda_m$. Our variational problem 2.30 is equivalent to the system:

$$\begin{pmatrix} A_{vv} & B_{vp} \\ B_{vp}^t & D_{pp} \end{pmatrix} \begin{pmatrix} V \\ P \end{pmatrix} = \begin{pmatrix} F \\ G \end{pmatrix} \tag{2.32}$$

where $V \in \mathbb{R}^{d_v}$, $V = (V_1, ..., V_{d_v})^t$ is the velocity solution vector, $P \in \mathbb{R}^{d_p}$, $P = (P_1, ..., P_{d_p})^t$ is the pressure solution vector. The operators are defined as:

$$\begin{cases} A \in \mathcal{M}_{d_v,d_v}(\mathbb{R}), A_{pm} = \displaystyle\int_{\Omega_h} 2\eta\varepsilon(\phi_m) : \varepsilon(\phi_p) - \int_{\Omega_h} \frac{2\eta}{3}(\nabla \cdot \phi_m)(\nabla \cdot \phi_p) \\[2mm] B \in \mathcal{M}_{d_v,d_p}(\mathbb{R}), B_{mp} = -\displaystyle\int_{\Omega_h} \lambda_m \nabla \cdot \phi_p \\[2mm] D \in \mathcal{M}_{d_p,d_p}(\mathbb{R}), D_{mp} = -\displaystyle\int_{\Omega_h} \alpha\lambda_m\lambda_p - \int_{\Omega_h} \lambda_m\beta\mathbf{v} \cdot \nabla\lambda_p \end{cases} \tag{2.33}$$

The right-hand side members may be written as:

$$\begin{cases} F \in \mathbb{R}^{d_v}, F_{v_m} = -\displaystyle\int_{\Omega_h} \mathbf{f}\phi_m - \int_{\partial\Omega_h} p_e\phi_m \cdot \mathbf{n} \\[2mm] G \in \mathbb{R}^{d_p}, F_{p_m} = -\displaystyle\int_{\Omega_h} \lambda_m C \end{cases} \tag{2.34}$$

We need now to choose the spaces $(\mathcal{V}_h, \mathcal{P}_h, \mathcal{Q}_h)$. These spaces may be chosen independently one from the other but they must satisfy the same conditions imposed to the discrete problem. Our choice of subspaces $\mathcal{V}_h$ and $\mathcal{P}_h$ was the MINI-element $P1+/P1$, introduced by [Arnold et al., 1984]. This element (figure 2.2) has a linear continuous pressure on Ω_h. The velocity interpolation is also continuous on Ω_h and is the addition of a linear part with a non-linear one called bubble function.
The finite element space $\mathcal{V}_h$ may be written as $\mathcal{V}_h = V_h \oplus B_h$ where

$$V_h = \{\mathbf{w}_h \in \mathcal{C}^0(\Omega_h)^d : \mathbf{w}_h \mid_K \in P1(K)^d\} \tag{2.35}$$

and $P1(K)$ is the space of polynomials of degree inferior or equal to 1. The bubble functional space must verify the compatibility condition 2.24. The bubble function vanishes at the boundary of K and is continuous inside the element, and is defined on K as a polynomial on each of the three sub-triangles
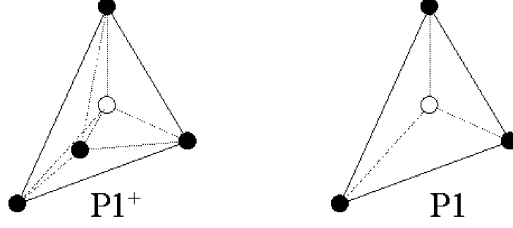
Figure 2.2: *Element P1$^+$/P1, or MINI-element.*

in 2D or four sub-tetrahedra in 3D. It is the pyramidal version of the bubble function, and the discrete space associated is

$$B_h = \{\mathbf{b}_h \in \mathcal{C}^0(\Omega_h)^d : \mathbf{b}_h \mid_{\partial K} = 0 \text{ and } \mathbf{b}_h \mid_{K_i} = 0 \in P1(K_i)^d i = 1, ..., D\} \tag{2.36}$$

where D is the topological dimension, and $(K_i)i = 1, ..., D$ is a decomposition of K in D subsimplex (subtriangle in 2D and subtetrahedra in 3D), that have as common vertex the barycenter of K. Finite element spaces that correspond to pressure may be defined as

$$\mathcal{P}_h = \mathcal{Q}_h = \{\mathbf{q}_h \in \mathcal{C}^0(\Omega_h) : \mathbf{q}_h \mid_K \in P1(K)\} \tag{2.37}$$

We notice that

$$\dim \mathcal{V}_h = d \times (N_n + N_e) \quad \dim \mathcal{P}_h = \dim \mathcal{Q}_h = N_n \tag{2.38}$$

where N_e is the number of elements and N_n the number of nodes of the mesh $\mathcal{T}_h(\Omega)$. The approximation error of this element is of the first order (in $O(h)$). The choice of this element gives rise to the global system to solve

$$\begin{pmatrix} A_{vv} & 0 & B_{vp} \\ 0 & A_{bb} & B_{bp} \\ B_{vp}^t & B_{bp}^t & D_{pp} \end{pmatrix} \begin{pmatrix} V_l \\ V_b \\ P \end{pmatrix} = \begin{pmatrix} F_l \\ F_b \\ G \end{pmatrix} \tag{2.39}$$

where $V_l \in \mathbb{R}^{d \times N_n}$ is the nodal velocity vector, $V_b \in \mathbb{R}^{d \times N_e}$ represents the barycenter velocity vector, and $P \in \mathbb{R}^{N_n}$ is the pressure vector. We note that bubble functions have the following properties [Coupez, 1996]:

- $\int_K q_h \nabla \cdot b_h = -\int_K \nabla q_h \cdot b_h$

- $\int_K \mathbf{C} : \nabla b_h = 0$, for all constant tensor $\mathbf{C}$

Thus matrices B_{vp}, B_{bp} are the same matrices obtained for the Stokes incompressible problem, and A_{vv}, A_{bb} remain similar. By a classical technique, we condensate the bubble function:

$$A_{bb}V_b + B_{bp}P = F_b \implies V_b = A_{bb}^{-1}(F_b - B_{bp}P) \tag{2.40}$$

We obtain a mixed velocity-pressure formulation, with unknowns the nodal velocities and pressures. The final element contribution system is written:

$$\begin{pmatrix} A_{vv} & B_{vp} \\ B_{vp}^t & C_{vb} + D_{pp} \end{pmatrix} \begin{pmatrix} V_l \\ P \end{pmatrix} = \begin{pmatrix} F_l \\ F_p \end{pmatrix} \tag{2.41}$$

with:

$$C_{vb} = -B_{bp}^t A_{bb}^{-1} B_{bp} \text{ and } F_p = G - B_{bp}^t A_{bb}^{-1} F_b \tag{2.42}$$

2.1.3 Local computation of compressibility matrices

We need to determine the form of the matrix D_{pp} identified previously:

$$D \in \mathcal{M}_{d_p,d_p}(\mathbb{R}), D_{mp} = -\int_{\Omega_h} \alpha \lambda_m \lambda_p - \int_{\Omega_h} \lambda_m \beta \mathbf{v} \cdot \nabla \lambda_p \qquad (2.43)$$

where

$$\alpha = \frac{\chi_p}{|I^n|} \qquad \text{and} \qquad \beta = \chi_p \qquad (2.44)$$

The use of classical Galerkin techniques generate numerical instabilities, which can be avoided using several techniques described in the literature, the most well known being the SUPG (Streamline Upwind Petrov Galerkin) or the DG (Discontinuous Galerkin) schemes. These techniques allow an upwind of the convective flow, eliminating the central derivative at the origin of the numerical instabilities.

In our case, we use a DG technique obtained by re-writing our continuous problem using the 3-field form: *find $(\boldsymbol{v}, p, \bar{p})$ such that:*

$$\begin{cases} \nabla \cdot [2\eta(\varepsilon(\mathbf{v}) - \frac{1}{3}\nabla.\mathbf{v}\mathbf{I})] - \nabla p = \mathbf{f} \\[2mm] \nabla \cdot \mathbf{v} + \alpha p + \beta \mathbf{v} \cdot \nabla \bar{p} = C \qquad \text{in } \Omega \\[2mm] \bar{p} - p = 0 \end{cases} \qquad (2.45)$$

We establish the discrete variational of this three-field problem by using the discrete spaces $\mathcal{V}_h$, $\mathcal{P}_h$ and the newly defined $\overline{\mathcal{P}}_h$

$$\overline{\mathcal{P}}_h = \{\bar{p}_h \in \mathcal{L}^2(\Omega_h) : \bar{p}_h \in P0(K), \forall K \in \mathcal{T}_h(\Omega)\} \qquad (2.46)$$

In the absence of mass forces, the corresponding discrete variational form is: *find $(\boldsymbol{v}_h, p_h, \bar{p}_h) \in \mathcal{V}_h \times \mathcal{P}_h \times \overline{\mathcal{P}}_h$ such that, $\forall (\boldsymbol{w}_h, q_h, \bar{q}_h) \in \mathcal{V}_h \times \mathcal{P}_h \times \overline{\mathcal{P}}_h$*

$$\begin{cases} \int_{\Omega_h} 2\eta(\varepsilon\mathbf{v}_h - \frac{1}{3}\text{tr}(\varepsilon(\mathbf{v}))\mathbf{I}) : \epsilon(\mathbf{w_h}) - \int_{\Omega_h} p\nabla \cdot \mathbf{w}_h = -\int_{d\Omega_h} p_e(\mathbf{w}_h \cdot \mathbf{n}) \\[2mm] -\int_{\Omega_h} q_h \nabla \cdot \mathbf{v}_h - \int_{\Omega_h} q_h(\alpha_h p_h + \beta_h \mathbf{v} \cdot \nabla \bar{p}_h) = -\int_{\Omega_h} q_h C \\[2mm] \int_{\Omega_h} \bar{q}_h(\bar{p}_h - p_h) = 0 \end{cases} \qquad (2.47)$$

From the last equation of this system, and since we have chosen $\bar{p}_h$ and $\bar{q}_h$ in $\overline{\mathcal{P}}$, we get to the conclusion that the value of p_h in one element K, p_{h_K} is a function of the nodal pressures of this element through:

$$\bar{p}_{h_K} = \frac{1}{|K|} \int_K p_h = \frac{1}{D} \sum_{i=1}^{D} P_i \qquad (2.48)$$

where $|K|$ is the volume of element K, D is the mesh topological dimension, λ_i the test functions and P_i the local nodal pressures on the element K.

- The first term of the compressible matrix D_{pp} is easily computed, supposing that compressibility coefficients are piecewise constant per element, with value α_K:

$$D^1_{mp} = -\int_{\Omega_h} \alpha \lambda_m \lambda_p = -\sum_{K \in \mathcal{T}_h(\Omega)} \alpha_K \int_K \lambda_m \lambda_p \qquad (2.49)$$

The local contribution to the global matrix of each element K is $D^1_{mp|_K}$, and computed using the Gauss integration rule (since we have a quadratic polynomial on each tetrahedra) such that:

$$D^1_{mp_K} = -\alpha_K \int_K \lambda_m \lambda_p = -|K|\alpha_K \sum_{n=1}^{Ng} \omega_n \lambda_{m_n} \lambda_{m_n} \qquad (2.50)$$

where Ng is the number of Gauss integration points, λ_{i_n} the value of the test function λ_i at the integration point x_n, with weight ω_n. The local coordinates of the integration points and their weights can be found in the literature.

- Computation of the second term of the compressible matrix D_{pp} requires a deeper study. Let us introduce the notation (figure 2.3):

$$-F = F \subset \partial K \quad \text{is a face of the element} K$$
$$-\mathcal{F}(\mathcal{T}_h(\Omega)) = \{F \subset \partial K; \forall \subset \mathcal{T}_h(\Omega)\} \quad \text{are all the faces of the mesh } \mathcal{T}_h(\Omega)$$
$$-\mathcal{K}(F) = \{K \subset \mathcal{T}_h(\Omega); F \subset \partial K\} \quad \text{are all the elements sharing the same face } F$$
$$-\mathbf{n}_K^F \quad \text{is the outward unit normal to face } F \text{ in element } K$$
$$-\mathbf{v}^F \quad \text{is the velocity at the barycenter of face } F$$
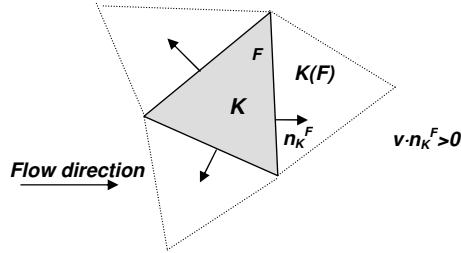
Figure 2.3: *Notation and schematic illustration of the up-winding formulation.*

We remind that the velocity field (known) $\mathbf{v}$ is continuous in Ω. Therefore, the discretized form of the contribution of the pressure convection term may be rewritten (applying the Green formula):

$$\int_{\Omega_h} q_h \mathbf{v}_h \cdot \nabla \bar{p}_h = -\sum_K \left(\int_{\partial K} \bar{p}_h q_h \mathbf{v}_h \cdot \mathbf{n}_K - \int_K \nabla \bar{p}_h \cdot \mathbf{v}_h q_h \right) \qquad (2.51)$$

Let us define the space jump operator $[.]_K^F$ as:

$$[f]_K^F(x) = \sum_{K' \in \mathcal{K}(F)} f_{K'}(x) \mathbf{n}_{K'}^F \mathbf{n}_K^F \qquad (2.52)$$

where K' is an arbitrary element of $\mathcal{K}(F)$. Using this definition, we can write:

$$\int_{\Omega_h} \beta q_h \mathbf{v}_h \cdot \nabla \bar{p}_h = -\sum_{F \in \mathcal{F}} \int_F [\bar{p}]_{K(F)}^F q_h \mathbf{v}_h \cdot \mathbf{n}_K^F + \sum_{K \in \mathcal{T}(\Omega)} \int_K \nabla \bar{p}_h \cdot \mathbf{v}_h q_h$$

being $K(F)$ an arbitrary element of $\mathcal{K}(F)$. Since $\bar{p}_h$ is constant per element, the second term in the right-hand side of the last expression is zero. Decomposing the flux in positive and negative parts, and since only two elements share the same face, we will take into account only the negative flux, $(\mathbf{v} \cdot \mathbf{n}) < 0$, i.e., the flux entering the face F. This technique allows the upwind of the scheme and stabilizes the formulation (figure 2.3). Thus:

$$
\begin{aligned}
\int_F [\bar{p}]_{K(F)}^F q_h \mathbf{v}_h \cdot \mathbf{n}_{K(F)}^F \quad &= [\bar{p}]_{K(F)}^F \int_F q_h (\mathbf{v}_h \cdot \mathbf{n}_{K(F)}^F)^- \\
&= (\bar{p}_K - \bar{p}_{K(F)}) \lambda_m^F |F| (\bar{\mathbf{v}}^F \cdot \mathbf{n}_{K(F)}^F)^-
\end{aligned}
\tag{2.54}
$$

where $\bar{p}_K(F)$ is the pressure in the neighbor element of K through F, $\bar{\mathbf{v}}^F$ is the velocity determined at the barycenter of the face, and λ_m^F is the value of the test function in local coordinates ($\lambda_m^F = \frac{1}{D-1}$) if $m = F$ and zero otherwise. Using equation 2.48, we add the following contributions, for each assembled element K:

$$
D_{mp}^2|_K = \begin{cases} \bar{p}_K \displaystyle\sum_{F \in \partial K} \lambda_m^F |F| (\bar{\mathbf{v}}^F \cdot \mathbf{n}_K^F)^- & \text{if } m = p \\[2mm] 0 \quad \text{otherwise} \end{cases}
\tag{2.55}
$$

and, for each face F

$$
D_{mp}^2|_{K(F)} = \begin{cases} \bar{p}_{K(F)} \lambda_m^F |F| (\bar{\mathbf{v}}^F \cdot \mathbf{n}_K^F)^- & \text{if } m = p \\[2mm] 0 \quad \text{otherwise} \end{cases}
\tag{2.56}
$$

2.1.4 Resolution and optimization

Resolution of the linear system obtained is performed using the PETSC (*Portable, Extensible Toolkit for Scientific Computation*) library, through a preconditionned iterative method. Even if this formulation is purely implicit in pressure, two main inconvenients have to be pointed out:

- before this work, the incompressible Stokes linear system resolution was done through the CR (Conjugated Residual) method with an ILU preconditioning. Since the global matrix D_{pp} is now non-symmetrical, the CR method is no longer adapted. One solution is to choose another solver from the PETSC library (for example, the GMRES iterative solver), and eventually keep the same ILU preconditionner;

- more important, the assembly is performed locally by doing a loop over all the mesh elements. Local matrices are thus dimensioned in $[(D \times D), (D \times D)]$ where D is the topological dimension. Since $D_{mp}^2|_{K(F)}$ is assembled to the neighbor element, we need to change the general assembly procedure.

One way of overcoming the second problem, is to consider explicitly the contribution of the matrix $D_{mp}^2|_{K(F)}$. However, a simpler way is to consider the problem from a different point of view through the variable change:

$$
\nabla p = \rho \nabla p'
\tag{2.57}
$$

We look at the Stokes compressible problem (continuous form, equation 2.16), and we suppose then that the density is piecewise constant in space and p' is approached linearly in space ($p' \in \mathcal{P}$). We re-write: *find* $(\boldsymbol{v}, p)$ *such that* $\forall x \in \Omega$

$$
\begin{cases} \nabla \cdot [2\eta\varepsilon(\mathbf{v}) - \dfrac{2}{3}\eta(\nabla \cdot \mathbf{v})\mathbf{I}] - \rho\nabla p' = 0 \\[4mm] \nabla \cdot (\rho\mathbf{v}) + \chi_p \rho^2 \dfrac{\partial p'}{\partial t} = C' \end{cases}
\tag{2.58}
$$

The terms $\rho\nabla p'$ and $\nabla\cdot(\rho\mathbf{v})$ are now symmetrical. Actually, in the weak form, we have the functions ρ, p' and $\mathbf{w}$ belonging to the appropriate subspaces:

$$(\rho\nabla p', \mathbf{w}) = -(p', \nabla\cdot(\rho\mathbf{w})) \tag{2.59}$$

The resulting matrix is similar to the preceding one (always considering the velocity known), but now the sub-matrix D_{pp} is symmetrical. Finally, we rebuild the pressure on each node through:

$$P = M(\rho)Q \tag{2.60}$$

where Q is the solution vector of the modified nodal pressures (corresponding to p') from the Stokes problem.

Consequently, the two possible resolution algorithms are:

ALGORITHM 1: SEMI-IMPLICIT

for each time step **do**

knowing $(\mathbf{v}^n, p^n)$, compute $(\mathbf{v}^{n+1}, \mathbf{b}^{n+1}, p^{n+1})$ such that

assemble for all elements $K \in \mathcal{T}_h(\Omega)$

$$
\begin{cases}
\displaystyle\int_K 2\eta\varepsilon(\mathbf{v}^{n+1}):\varepsilon(\mathbf{w}) - \int_K \frac{2\eta}{3}(\nabla\cdot\mathbf{v}^{n+1})(\nabla\cdot\mathbf{w}) - \int_K p^{n+1}(\nabla\cdot\mathbf{w}) = -\int_{\partial K} p_e(\mathbf{w}\cdot\mathbf{n}) \\[3mm]
\displaystyle\int_K 2\eta\varepsilon(\mathbf{b}^{n+1}):\varepsilon(\mathbf{b}^*) - \int_K \frac{2\eta}{3}(\nabla\cdot\mathbf{b}^{n+1})(\nabla\cdot\mathbf{b}^*) - \int_K p^{n+1}(\nabla\cdot\mathbf{b}^*) = 0 \\[3mm]
\displaystyle-\int_K q(\nabla\cdot\mathbf{v}^{n+1}) - \int_K q(\nabla\cdot\mathbf{b}) - \alpha_K\int_K qp^{n+1} + \bar{p}_K^{n+1}\sum_{F\in\partial K} q^F|F|(\bar{v}^{n\,F}\cdot\mathbf{n}_K^F)^- = \\[3mm]
\displaystyle-C_K\int_K q + \sum_{F\in\partial K}\bar{p}_{K(F)}^n q^F|F|(\bar{v}^{n\,F}\cdot\mathbf{n}_K^F)^-
\end{cases}
$$

end for

ALGORITHM 2: VARIABLE CHANGE

for each time step **do**

knowing $(\mathbf{v}^n, p'^n)$, compute $(\mathbf{v}^{n+1}, \mathbf{b}^{n+1}, p'^{n+1})$ such that

assemble for all elements $K \in \mathcal{T}_h(\Omega)$

$$
\begin{cases}
\displaystyle\int_K 2\eta\varepsilon(\mathbf{v}^{n+1}):\varepsilon(\mathbf{w}) - \int_K \frac{2\eta}{3}(\nabla\cdot\mathbf{v}^{n+1})(\nabla\cdot\mathbf{w}) - \int_K p'^{n+1}(\nabla\cdot(\rho_K\mathbf{w})) = -\int_{\partial K} p_e(\mathbf{w}\cdot\mathbf{n}) \\[3mm]
\displaystyle\int_K 2\eta\varepsilon(\mathbf{b}^{n+1}):\varepsilon(\mathbf{b}^*) - \int_K \frac{2\eta}{3}(\nabla\cdot\mathbf{b}^{n+1})(\nabla\cdot\mathbf{b}^*) - \int_K p'^{n+1}(\nabla\cdot(\rho_K\mathbf{b}^*)) = 0 \\[3mm]
\displaystyle-\int_K q(\nabla\cdot(\rho_K\mathbf{v}^{n+1})) - \int_K q(\nabla\cdot(\rho_K\mathbf{b})) - \alpha_K\rho_K\int_K qp'^{n+1} = -C_K'\int_K q
\end{cases}
$$

compute the nodal pressures
$p^{n+1} = \rho p'^{n+1}$

update the density on each element
$\rho_K = \rho_K(p^{n+1})$

end for

Both strategies have been considered and compared, with respect to the mass conservation. For that purpose, let us consider the filling and the transition towards post-filling of a cubic part (figure 2.4) with a viscous compressible fluid ($\eta = 1000$ Pas), with a constant isothermal compressibility coefficient. The filling time was 1 s, and the cube's side is 10 mm.

To verify the sensitivity of each numerical scheme to simulation data, two mesh discretisations were considered (Mesh1, coarse and Mesh2, fine), as well as three different isothermal compressibility coefficients and three different time steps. Evaluation of the mass loss is done by comparing the mass entering the cavity at each time step:

$$M_e = -\Delta t \int_{d\Omega_{in}} \rho(\mathbf{v}^* \cdot \mathbf{n}) \tag{2.61}$$

with the difference of mass between each increment:

$$\Delta M = \int_{\Omega} \frac{\partial \rho}{\partial t} = \frac{\partial}{\partial t} \int_{\Omega} \rho = \frac{\partial M(\Omega)}{\partial t} \tag{2.62}$$

Results are presented in figures 2.5 and 2.6. We notice that both algorithms give a correct (linear) evolution of the filling rate. Figure 2.6 shows that algorithm 1 and algorithm 2 give very small mass differences, of the order of the domain discretization. Furthermore, smaller time steps, isothermal compressibility coefficients and mesh sizes allow a better mass conservation, as expected. Nevertheless, in both cases the mass difference remains very small, and Algorithm 1 seems better performing than Algorithm 2 for all conditions. This might be due to the fact that in the last one the density is computed explicitly, from the pressure obtained. Thus, Algorithm 1 is preferred and used in the sequel.

> *The compressible Stokes problem is solved using the Mixed Finite Element Method, with a velocity-pressure formulation, where pressure (and thus density) convection in treated in a semi-implicit way.*
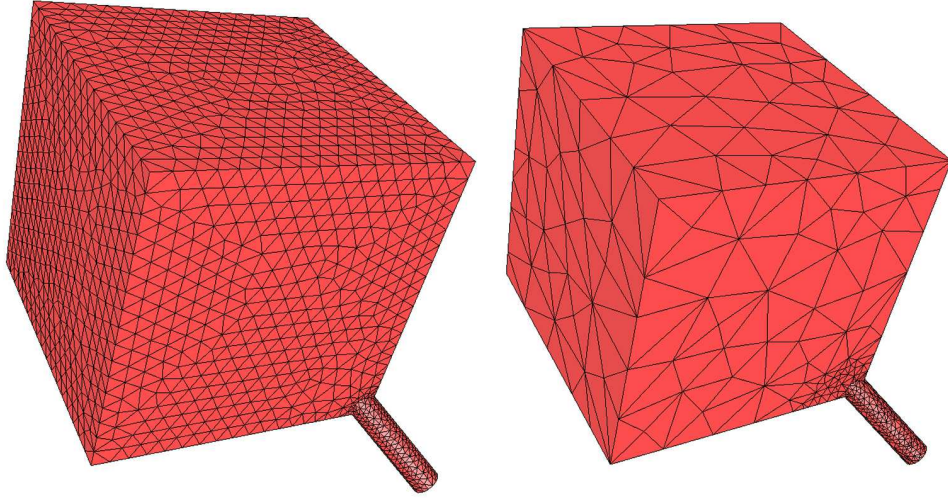
Figure 2.4: *Geometry for the mass conservation test, coarse and fine meshes.*
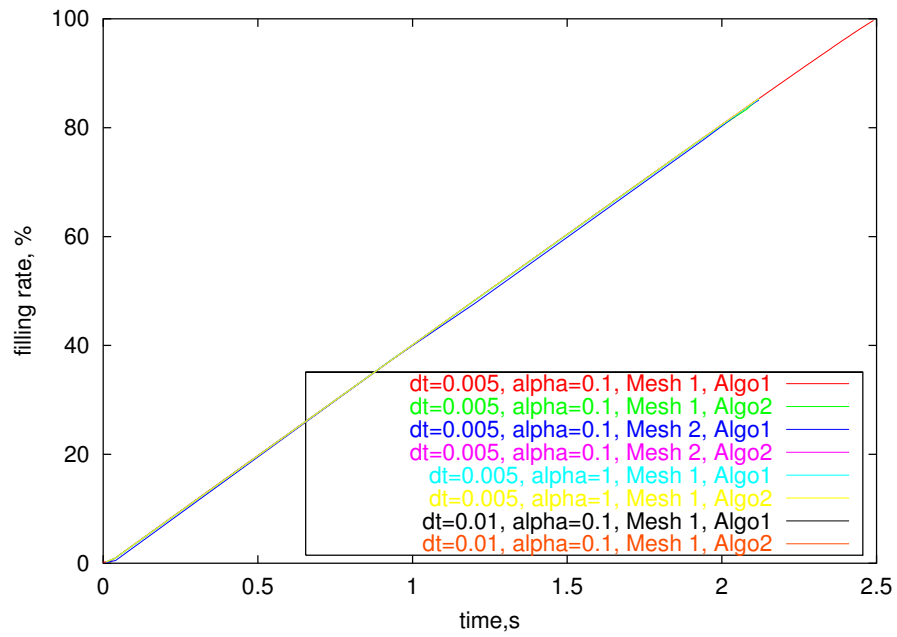
Figure 2.5: *Evolution of the filling rate for different test conditions.*
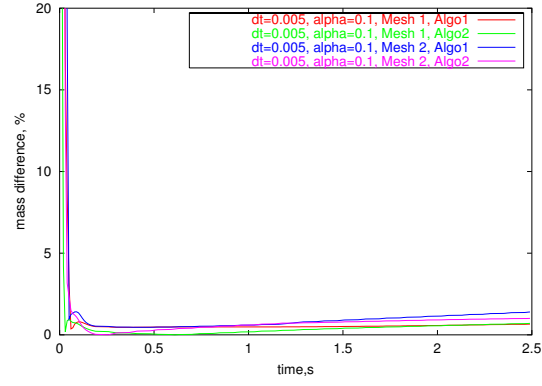
(a)
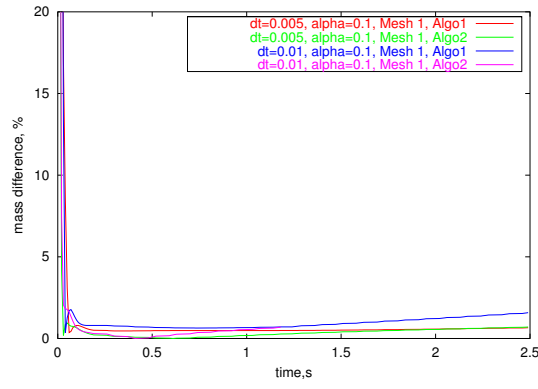
(b)
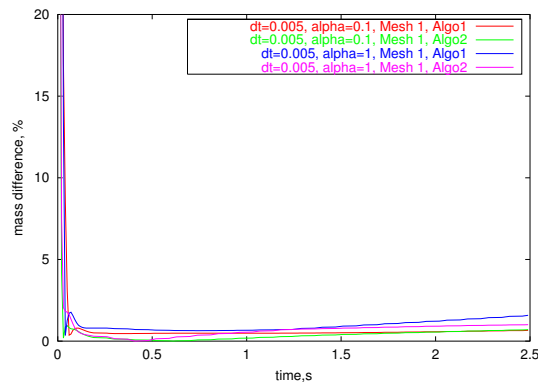
(c)

Figure 2.6: *Results concerning the mass conservation for each resolution method proposed: (a) influence of the mesh (b) influence of the time step (c) influence of the isothermal compressibility coefficient, for both numerical schemes.*

2.1.5 Non-linear compressibility

We consider that the velocity field is known and taken at the preceding time step. We also consider a constant isothermal compressibility coefficient.

The first assumption is justified by the fact that the pressure gradient remains very small during the filling stage and increases significantly at the end of the filling and ant the beginning of the packing stage. At this moment, the velocity field is (and remains) very small, allowing mainly the transport of material from the warmer to the cooler zones.

The second assumption may be kept since polymer's isothermal compressibility coefficient is of the order of 10^{-9} Pa^{-1}, and thus, very small. However, we will show in the following that a simple fixed point iterative scheme can be easily implemented.

Before this work, the viscosity was a function of the strain rate (and eventually, temperature), and the non-linear mechanical problem was solved through a Newton-Raphson scheme. Let us consider this technique applied to the non-linear Stokes compressible problem:

$$\begin{pmatrix} A_{vv}(V_l) & B_{vp} \\ B_{vp}^t & C_{vb} + D_{pp}(P) \end{pmatrix} \begin{pmatrix} V_l \\ P \end{pmatrix} = \begin{pmatrix} F_l \\ F_p \end{pmatrix} \tag{2.63}$$

The residual is built:

$$R(V_l, P) = \begin{pmatrix} A_{vv}(V_l, P) & B_{vp} \\ B_{vp}^t & C_{vb} + D_{pp}(P) \end{pmatrix} \begin{pmatrix} V_l \\ P \end{pmatrix} - \begin{pmatrix} F_l \\ F_p \end{pmatrix} \tag{2.64}$$

Using the Newton's method, we minimize:

$$R(V_l + \delta V_l, P + \delta P) = R(V_l, P) + \frac{\partial R(V_l, P)}{\partial V_l} \delta V_l + O(\delta V_l, \delta P) \tag{2.65}$$

We then need to solve:

$$R(V_l, P) + \frac{\partial R(V_l, P)}{\partial V_l} \delta V_l = 0 \tag{2.66}$$

This new problem is linear and solved as described previously. The value of $(\delta V_l, \delta P)$ is computed with an error tolerance ϵ_r on the residual and we update $(V_l, P) \longleftarrow (V_l, P) + (\delta V_l, \delta P)$. The processus continues until

$$\frac{(\delta V, \delta P)\mid}{\mid (V, P)\mid} < \epsilon_v \tag{2.67}$$

is verified, where ϵ_v is the tolerance on the solution vector. This is basically our Newton-Raphson scheme. We solve then:

$$\frac{\partial R(V_l^k, P^k)}{\partial V_l} \delta V_l^k = -R(V_l^k, P^k) \tag{2.68}$$

and

$$(V_l^{k+1}, P^{k+1}) = (V_l^k, P^k) + (\delta V_l^k, \delta P^k) \tag{2.69}$$

where k is the iteration index, up until convergence. Since the residual $R(V_l^k, P^k)$ has a matrix $D(V_l^k, P^k)$, we note that if the later is recomputed at each iteration until convergence based on the recently obtained values (V_l^k, P^k), we have a classic fixed point iterative scheme on pressure, guaranteeing an improvement in our solution.

2.1.6 Application to the compression of a filled mold

In this section, we validate our numerical scheme by considering the compression of a fluid inside a cavity completely filled [Maillot, 1993]. A constant compression pressure p_e is applied on one side of the plaque and we look at the time, function of the isothermal compressibility coefficient, required to propagate this pressure to the whole plaque. The geometry of the problem is described in figure 2.7. The fluid state law has the simplified form:

$$\rho = \rho_0 \exp[\chi_p(p-p_0)] \quad \text{and} \quad \chi_p = const \tag{2.70}$$

where ρ_0 is the density at the atmospheric pressure p_0. The problem to solve is:

$$\begin{cases} 2\eta\nabla\cdot[\varepsilon(\mathbf{v}) - \dfrac{1}{3}\text{tr}(\varepsilon(\mathbf{v}))\mathbf{I}] - \nabla p = 0 \\ \nabla\cdot(\mathbf{v}) + \chi_p\dfrac{dp}{dt} = 0 \end{cases} \text{ in } \Omega(t)\times[0,\Theta] \tag{2.71}$$

If the viscosity of the fluid is constant ($\eta = 1000$ Pas), and the pressure convection term is neglected, an analytical solution may be found, and defined as [Maillot, 1993]:

$$p(x,t) = p_0 + \frac{2}{L}\sum_{n=0}^{\infty}(-1)^n\frac{h^2}{12\eta\kappa}a_n\cos[a_n(L-x)]e^{-\frac{h^2}{12\eta\kappa}a_n^2 t}\int_0^t (p_e(\tau)-p_0)e^{\frac{h^2}{12\eta\kappa}a_n^2\tau}d\tau \tag{2.72}$$

with

$$a_n = \frac{2n+1}{2L} \quad \text{and} \quad \kappa = \frac{H^2}{12\eta\chi_p} \tag{2.73}$$
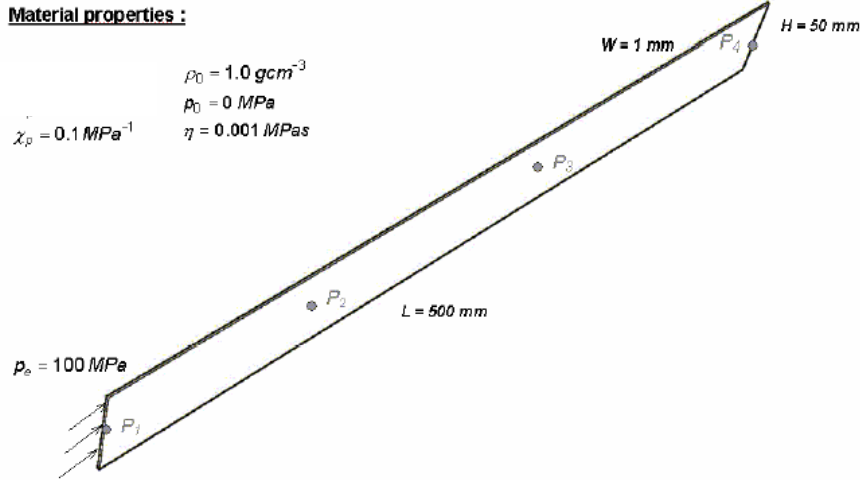
Figure 2.7: *Geometry of the plaque, with localisation of the pressure "numerical" transducers.*

The propagation of pressure and velocity can be observed in figures 2.8 and 2.9. They represent the evolution of pressure and axial velocity distributions in the cavity for successive time steps. On one hand, pressure increases until it reaches the packing imposed pressure. On the other hand, the axial velocity decreases until no more fluid can enter the cavity.
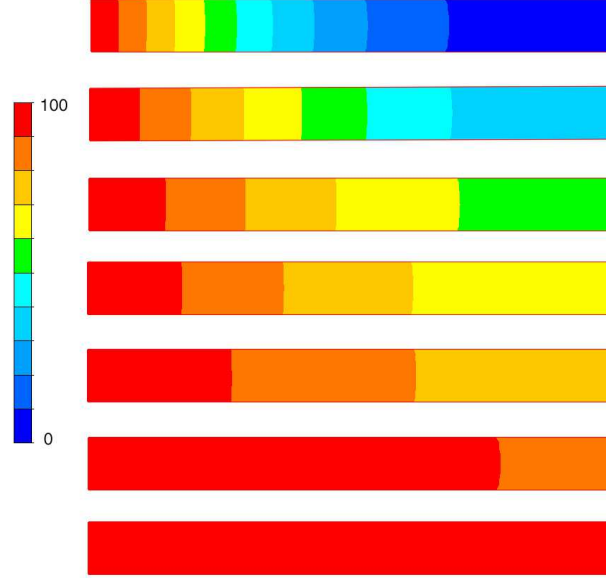
Figure 2.8: *Pressure field in the cavity at different time steps (units MPa).*
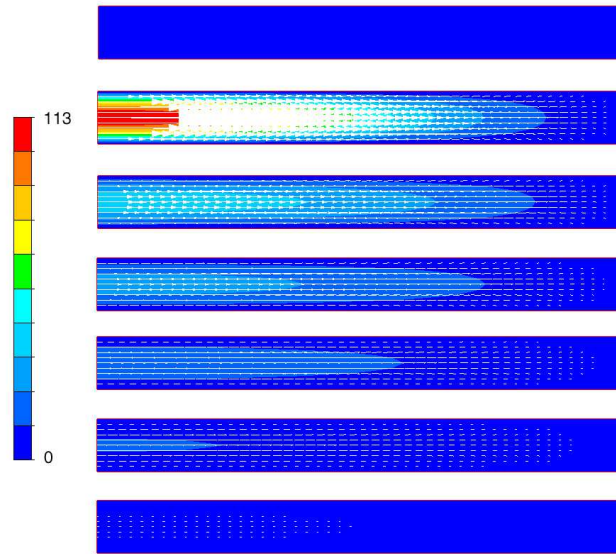
Figure 2.9: *Axial velocity distribution in the cavity at different time steps (units mm/s).*

These results are confirmed by figure 2.10, which compares the numerical and analytical evolution of pressure and velocity as a function of time for all the "numerical" pressure transducers. All the points reach the packing pressure at different instants and there is a good agreement between the analytical and the numerical solutions, showing that the numerical methods used to incorporate compressibility are perfectly adapted to the injection molding regime. We will study in the next paragraphs the sensitivity of these results to the mesh size and time step.
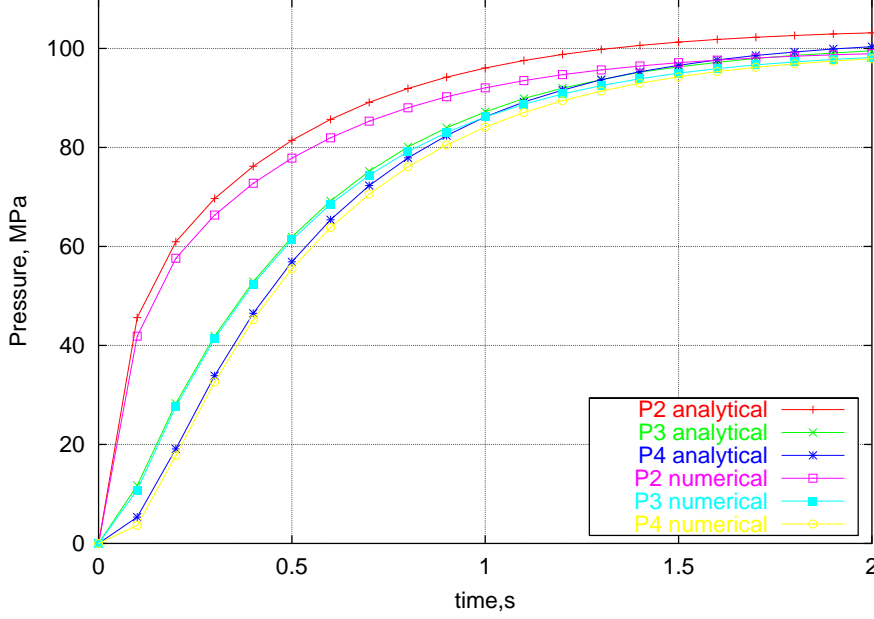
Figure 2.10: *Pressure and velocity function of time for the 4 numerical transducers in the plaque.*

Influence of the mesh

The sensitivity to the mesh size was tested on four different meshes, M_6, M_{12}, M_{24} and M_{48}, for a time step of 0.0005 s. The mesh sizes are: M6 - 684 elements, M12 - 1288 elements, M24 - 2536 elements, and M48 - 5032 elements. The relative error between the analytical solution and the numerical one is measured on each point P_2, P_3 and P_4 and is shown on figure 2.11, as function of time. We remark that there is no particular influence of the mesh, except for the coarser mesh and in the first time steps, when the pressure propagation rate is more important. This can be explained through the fact that the convective pressure remains less important than its temporal variation.

Influence of the time step

The convergence with the time step, when $|I^n| \longrightarrow 0$, was tested (figure 2.12), for three different time steps. On the interval $[0, 0.25]$, the error decreases quickly with $|I^n|$, being after less sensitive to the time step. This may be explained by the fact that an increase of the pressure in P_1 is immediately propagated to P_2 if the time step is very large.

We conclude that compressibility introduces a transient flow behavior. The pressure values are similar to the ones considered in injection molding and the numerical methods developed are efficient. We observe that the spatial evolution of the pressure gradient is less significant that the temporal one, which is reflected in the weak sensitivity of the results to the mesh size. Finally, this sensitivity is more important when we increase the isothermal compressibility coefficient. Nevertheless, for the typical compressibility values encountered in injection molding (0.001 MPa^{-1}) it works well.
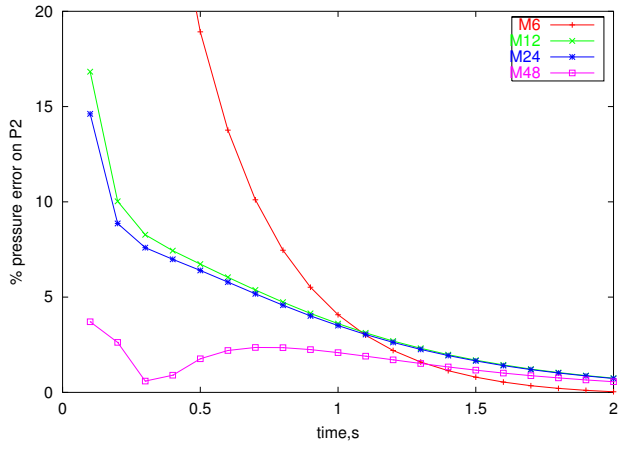
(a)
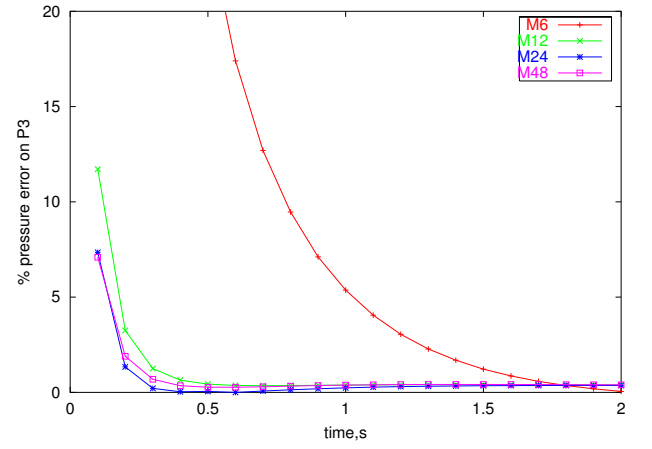
(b)
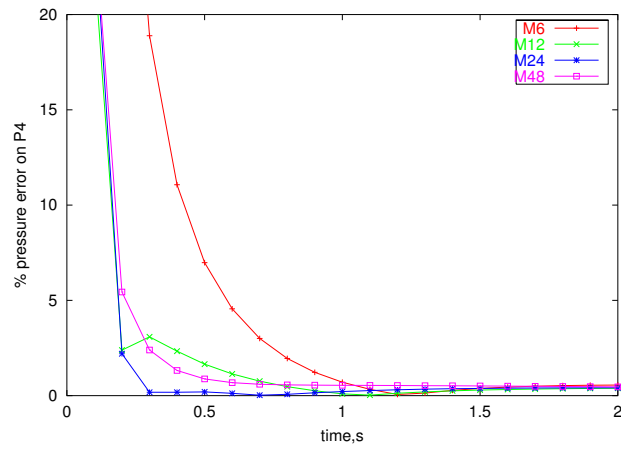
(c)

Figure 2.11: *Error on each point for the different meshes in the full compression benchmark: (a) P2 (b) P3 and (c) P4.*
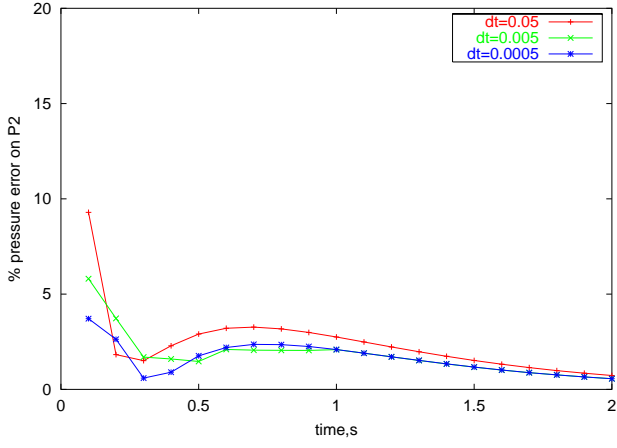
(a)
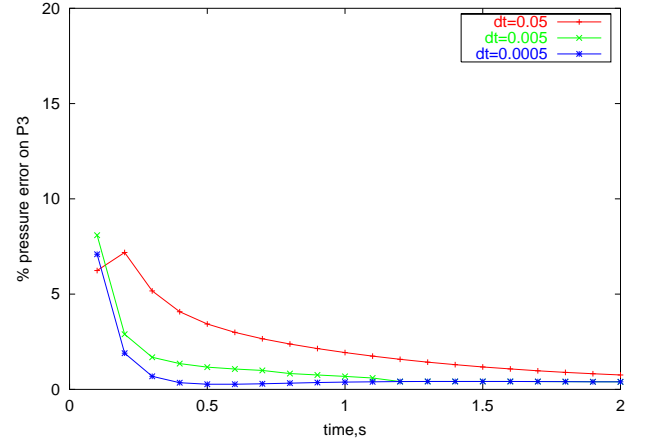
(b)
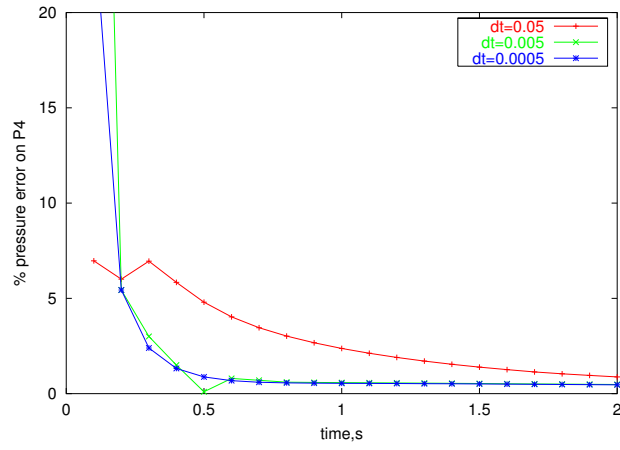
(c)

Figure 2.12: *Error on each point for the different time steps in the full compression benchmark: (a) P2 (b) P3 and (c) P4.*

2.2   Thermal compressibility

2.2.1   Conservation of energy and thermal behavior

The principle of the conservation of energy in a fluid flow can be expressed in the form: the rate of increase of total energy equals the rate of heat addition minus the rate at which work is done by the fluid element, or

$$\frac{dE}{dt} = \frac{dQ}{dt} - \frac{dW}{dt}$$
(2.74)

to a flowing fluid. This law defines the relationship between the internal energy U of a thermodynamic substance and the transfer of heat Q and work W to or from the substance during a process of change. When applied to a moving fluid element, the first law states that the element's total energy E, which is the sum of its internal energy, kinetic energy and potential energy in the earth's gravitational field, is increased by the net amount of heat added to the element and decreased by the amount of work done by the element on its environment. (The thermodynamic convention is that heat added to a fluid element or work done by it on its surroundings is a positive quantity.) Because the first law applies to a fixed amount of matter, it is expressed in Lagrangian form, i.e., it describes the changes to an identified fluid element as it moves through the flow field. Using our previous notation for the material time derivative,
Let e be the internal energy per unit mass due to microscopic motion, and $\frac{\mathbf{v}^2}{2}$ the kinetic energy per unit mass due to macroscopic motion. Using the Reynolds transport theorem, the material derivative of the total energy becomes:

$$\frac{dE}{dt} = \frac{d}{dt} \int_\Omega \rho(e + \frac{\mathbf{v}^2}{2}) + \frac{d}{dt} \int_{\partial\Omega} \rho(e + \frac{\mathbf{v}^2}{2})\mathbf{v} \cdot \mathbf{n}$$
(2.75)

The first term is the rate of accumulation of E within the domain, and the second is the rate of transport of E out of the domain by the fluid flowing across its boundaries. On the other hand, heat is transferred because of temperature differences between adjacent locations in the fluid. For most fluids, the rate of heat flow per unit area across a surface in the fluid, ϕ, is proportional to the temperature gradient according to Fourier's law:

$$\phi = -k\nabla T$$
(2.76)

where $k \geq 0$ represents thermal conductivity of the molten polymer. The rate of heat addition to the fluid is thus the integral of the heat flux over the whole surface:

$$\frac{dQ}{dt} = -\frac{d}{dt} \int_{\partial\Omega} \phi \cdot \mathbf{n}$$
(2.77)

Now we consider the rate at which work is done in the environment by the fluid in the domain as the sum of the rate of work by body forces and rate of work done by surface forces:

$$\frac{dW}{dt} = \frac{d}{dt} \int_\Omega \rho\mathbf{f}\mathbf{v} + \frac{d}{dt} \int_{\partial\Omega} \sigma\mathbf{n} \cdot \mathbf{v}$$
(2.78)

Using the Reynolds transport theorem, the Gauss theorem and re-writing the work done by the surface stress, we obtain, in the differential form:

$$\rho\frac{de}{dt} = -\nabla\cdot\phi + \sigma : \varepsilon(\mathbf{v}) = -\nabla\cdot\phi + \dot{\omega} - p\nabla\cdot\mathbf{v} \quad \forall(\mathbf{x}, t) \in \Omega(t) \times [0, \Theta]$$
(2.79)

where $\dot{\omega} = \tau_s : \varepsilon(\mathbf{v})$ is the heat dissipation. Now we need an expression for the internal energy, according to another state law. This will allow us to transform the energy equation in an equation of the main variables pressure and temperature, with eventual simplification. For example for a perfect

gas, $e = c_v T$ and $p = \rho R T$, where $R = c_p - c_v$, c_v and c_p being specific volumes determined at constant volume and pressure, respectively. This means that we have, for a perfect gas (neglecting its viscosity),

$$\rho c_v \frac{dT}{dt} = -\nabla \cdot \phi - p \nabla \cdot \mathbf{v} \tag{2.80}$$

In the case of a compressible liquid, the internal energy is function of pressure and temperature, $e = e(p, T)$, if we neglect creation terms. From Maxwell relations [Agassant et al., 1986], we can establish that

$$de = c_p dT - p dV - \frac{1}{\rho} \chi_T T dp \tag{2.81}$$

and by replacing in equation 2.79 we obtain

$$\rho c_p \frac{dT}{dt} - p \nabla \cdot \mathbf{v} - \chi_T \frac{dp}{dt} T = -\nabla \cdot \phi + \dot{\omega} - p \nabla \cdot \mathbf{v} \quad \forall (\mathbf{x}, t) \in \Omega(t) \times [0, \Theta] \tag{2.82}$$

The isobar dilatation coefficient, χ_T is also a material property, defined as:

$$\chi_T = -\frac{1}{\rho} \frac{\partial \rho}{\partial T} \tag{2.83}$$

The final form of the energy equation for a compressible liquid is

$$\boxed{\rho c_p \frac{dT}{dt} - \chi_T \frac{dp}{dt} T = -\nabla \cdot \phi + \dot{\omega}} \quad \forall (\mathbf{x}, t) \in \Omega(t) \times [0, \Theta] \tag{2.84}$$

This equation is valid in the whole computational domain $\mathcal{D}$ and is an evolution equation on temperature, which means that it induces a transient behaviour to the material. We notice that the velocity interferes in this equation through the convective and dissipative terms. This means that to solve the thermal problem we need to use a coupled approach (in $(\mathbf{v}, p, T)$). Nevertheless, we use a splitting technique by solving the $(\mathbf{v}, p)$ system considering that T is known, and with the computed velocity, determine the temperature through the heat equation (figure 2.13).
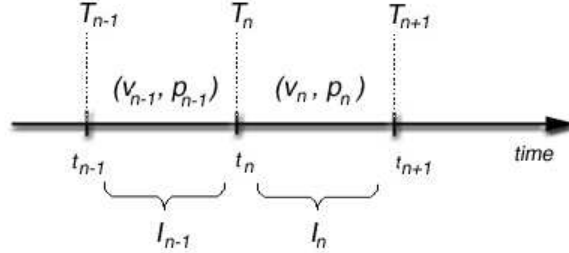
Figure 2.13: *Description of the splitting scheme to decouple temperature from velocity and pressure computation.*

Thus, we solve the following problem in temperature: find the temperature $T \in \mathcal{C}^1(\Omega)$ and the heat flux $\phi \in \mathcal{C}^0(\Omega)$ such that, $\forall t \in]0, \Theta[$, $\forall x \in \Omega(t)$,

$$\begin{cases} \rho c_p \dfrac{dT}{dt} - \chi_T \dfrac{dp}{dt} T = -\nabla \cdot \phi + \dot{\omega} \\[2mm] \phi = -k \nabla T \\[2mm] + \text{ boundary and initial conditions} \end{cases} \tag{2.85}$$

Whereas the initial conditions are related with the initial temperature of the computational domain $(T(x, t_0) = T_0(x), \forall x \in \Omega(t_0))$, the boundary conditions associated to this problem may be of two types:

- in temperature

$$T(\mathbf{x}, t) = T_{imp} \quad \forall(\mathbf{x}, t) \in \partial\Omega_m \times [0, \Theta] \text{ at the inlet or the mold wall} \tag{2.86}$$

- in heat flux

$$\phi \cdot \mathbf{n} = \phi_{imp} \in \partial\Omega_m \times [0, \Theta] \tag{2.87}$$

This problem has been studied by [Batkam et al., 2003] and its resolution will be briefly described, in order to introduce the additional dilatation/contraction term.

2.2.2 Space-time discontinuous Galerkin (STDG) method and resolution of the heat equation

Numerically, the heat equation is a convection-diffusion-reaction equation. Classical Galerkin techniques generate numerical instabilities, while diffusion problems may cause oscillations during the treatment of thermal shocks. To avoid stability difficulties, several techniques are described in the literature: SUPG (Streamline Upwind Petrov Galerkin), CG (Characteristic Galerkin), SGS (Subgrid Scale) or ST-GLS (Space Time / Galerkin Least Squares) methods. Essentially, all these methods consist in the addition of a stabilising term to the original Galerkin formulation of the problem. These methods behave well on high convective problems but are limited by their tendency to denature the solution. Techniques to avoid oscillations during the treatment of thermal shocks are well-known: one must adapt the mesh size or the time step in the direction of the gradient. The method introduced by [Batkam et al., 2003] does not need any stabilization term for highly convection problems and behaves well during the treatment of the thermal shocks, and is based on the Space-Time Discontinuous Galerkin (STDG) method. Resolution of a classical transport equation using this technique is detailed in Appendix A. Since throughout our work this technique has been applied to all evolution equations, a short description of its application to convection-diffusion is given in the following.

Basic description

Basically, a Space-Time method allows a simultaneous resolution in space and in time ($\mathbf{x} = (x, t)$) in the computational domain ($\Omega \times [0, \Theta]$)). Moreover, we choose discontinuous interpolations both in space (low order) and in time (higher order).
In this case, we consider a $(d + 1)$ finite element mesh, where d is the spatial dimension, unstructured in space and structured in time. A discontinuous Galerkin technique using low order P0 elements in space and high order Pk element in time is proposed to discretise all equations, leading to a quite simple scheme that can be solved locally.

Generally, our heat problem is similar to:

$$\begin{cases} \dfrac{\partial T}{\partial t} + \mathbf{v} \cdot \nabla T - bT + \nabla \cdot \phi = f \\ \phi + a\nabla T = 0 \end{cases} \quad \text{in} \quad \Omega(t) \times [0, \Theta] \tag{2.88}$$

In this equation, $\mathbf{v}$ represents a velocity field defined in the whole space-time domain, a is a diffusion coefficient, b a dilatation/contraction coefficient and f is a source term. Note that the diffusion term is expressed here with a two fields formulation. The gradient operator and the velocity components can be extended in the $d+1$ dimension by:

$$\tilde{\mathbf{v}} = \left(\begin{array}{c} \mathbf{v} \\ 1 \end{array} \right) \qquad \text{and} \qquad \tilde{\nabla} = \left(\begin{array}{c} \nabla \\ \frac{\partial}{\partial t} \end{array} \right) \tag{2.89}$$

This means that equation 2.88 takes the form:

$$\left\{ \begin{array}{l} \tilde{\mathbf{v}} \cdot \tilde{\nabla} T - bT + \nabla \cdot \phi = f \\ \phi + a\nabla T = 0 \end{array} \right. \qquad \text{in } \tilde{\Omega} = \Omega(t) \times [0, \Theta] \tag{2.90}$$

The Space-Time finite element method consists in applying the finite element methodology both in space and in time: the space-time domain $\tilde{\Omega}$ is subdivided into slabs $\tilde{K}$. To discretise α we choose a function α_h piecewise continuous on each $\tilde{K}$. Furthermore, we choose a space time mesh which is structured in time: each elementary slab is taken as the Cartesian product of a simplex K and a time interval $]t^n, t^{n+1}[$. This choice involves the orthogonality between the time normal and the space normal. In this space-time context, we define the approximation space for temperature as follows:

$$\mathcal{P}^{0,q} = \{f_h \in \mathcal{L}^2(\tilde{\Omega}) : f_{\tilde{K}} = g(x)h(t) with g \in P0(K) and h \in Pq(I), \forall \tilde{K} = K \times I \in \mathcal{T}_h(\tilde{\Omega})\} \tag{2.91}$$

Thus, the temperature T is approximated by T_h discontinuous on Ω_h and constant per element. As $\mathcal{T}_h(\Omega)$ was defined as the spatial mesh, $\mathcal{T}_h(\tilde{\Omega})$ is the space-time mesh. If we consider a basis of this space as:

$$\mathcal{B}^{0,q} = \{1_{\tilde{K}}(x,t)(t-t_n)^p\}_{\tilde{K} \in \mathcal{T}_h(\tilde{\Omega}); p=1,...,q} \tag{2.92}$$

we may write on each space-time element $\tilde{K}$

$$T_h(x,t) \mid_{\tilde{K}} = \sum_{p=0}^{q} T_{\tilde{K}}^p (t-t_n)^p \tag{2.93}$$

On the other hand, the approximation in space of the flux is built considering that each spatial element K of the mesh is divided into D sub-elements K_f (see figure 2.14). The flux is then approximated in space by a piecewise constant function per sub-element:

$$\mathcal{Q}_h^+ = \{q_h \in \mathcal{L}^2(\Omega_h) : q \mid_{\tilde{K}_i} = g(x)h(t) with g \in P0(K_i) and h \in Pq(I), i = 1, ..., D, \forall \tilde{K}_i = K_i \times I \in \mathcal{T}_h(\tilde{\Omega})\} \tag{2.94}$$

The so-constructed element is said P0/P0+ in T/ϕ. Furthermore, the following condition is imposed to the P0/P0+ element : the jump of T_h is zero across "internal" faces f, and the jump of ϕ_h is zero across the "external" faces F of a space element K. These properties allow to condensate the heat flux, and bring our mixed system to one that has as unknown only the temperature values T_h. More details on the numerical scheme are given in [Batkam et al., 2003] and in its application in **REM3D** in Appendix A. We will focus here on the introduction of the contraction/dilatation term.
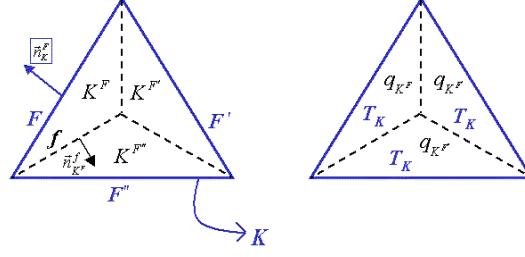
Figure 2.14: *Decomposition of an element in $d+1$ sub-elements and notation introduced.*

Introduction of the contraction/dilatation term

To introduce the term due to compressibility, we need to consider its discrete form:

$$\int_{\tilde{\Omega}} bT_h\varphi_h = \sum_{\tilde{K}} \int_{\tilde{K}} b_{\tilde{K}} T_h \varphi_h \tag{2.95}$$

where the coefficient b is defined constant per space and time elements. If we choose φ_h in the same space basis as T_h, $\varphi_h = 1_{\tilde{K}}(t-t_n)^r$, we have

$$
\begin{aligned}
\int_{\tilde{K}} bT_h\varphi_h &= \int_{\tilde{K}} b_K(t-t_n)^r \sum_{p=0}^{q} T_{\tilde{K}}^p (t-t_n)^p \\
&= |K|b_K \sum_{p=0}^{q} T_{\tilde{K}}^p \int_I (t-t_n)^{r+p} \\
&= |K|b_K \sum_{p=0}^{q} T_{\tilde{K}}^p \frac{|I|^{r+p+1}}{r+p+1}
\end{aligned}
\tag{2.96}
$$

where $|I|$ represents the size of the time element. Basically, if we choose P0 functions in time, and using the usual notation $\Delta t = |I| = \mathrm{diam}(I)$ we have:

$$\int_{\tilde{K}} bT_h\varphi_h = |K|b_K T_{\tilde{K}}\Delta t \tag{2.97}$$

This means that a diagonal component has been added to the linear system issue from the heat equation problem. This reinforcement of the diagonal favors the iterative resolution based on a Gauss-Seidel method.

Remark:

In fact, the density, the specific heat and, more important, the dilatation coefficient χ_T may be temperature dependent, giving a non-linear character to this equation. However, this dependence remains very weak in the case of polymers ($\chi_T \sim 10^{-4}$ K) and thus it has not been treated in this work. The coefficient is thus computed at the previous time step. The general split algorithm is shortly described below.

ALGORITHM: THERMAL COMPRESSIBILITY

for each time step **do**

knowing $(\mathbf{v}^n, p^n, T^n)$

1) compute $(\mathbf{v}^{n+1}, p^{n+1})$ such that

$$\begin{cases} \nabla \cdot [2\eta(\varepsilon(\mathbf{v}^{n+1}) - \dfrac{1}{3} \cdot \mathbf{v}^{n+1}\mathbf{I})] - \nabla p^{n+1} = \mathbf{f} \\ -\nabla \cdot \mathbf{v}^{n+1} - \dfrac{\chi_p^n}{|I^n|}p^{n+1} - \mathbf{v}^n \cdot \nabla p^{n+1} = -\dfrac{\chi_p^n}{|I^n|}p^n - \chi_T^n\dfrac{dT^n}{dt} \end{cases}$$

2) compute (T^{n+1}) such that

$$\rho^n\frac{dT^{n+1}}{dt} - \chi_T^n\frac{dp^{n+1}}{dt}T^{n+1} - k\nabla\cdot(\nabla T^{n+1}) = \dot{\omega}(\mathbf{v}^{n+1}, p^{n+1})$$

3) update material parameters χ_T^{n+1}

end for

2.2.3 Square cavity

Actually, this dilatational behavior does not change a lot the temperature evolution, but plays a more important role in the flow equations. For example, an evolution of the density with temperature will affect inertia/gravity flow.

One of the most popular benchmarks in CFD is the laminar flow in a two-dimensional square cavity with differentially heated sidewalls [Davis, 1983]. This test validates the implementation of a thermal dependent state law. The problem has later been extended to 3 dimensions [Wakashima and Saitoh, 2004]. The cavity is a square of side 1 and is filled with fluid. All surrounding walls are rigid and impermeable. The vertical walls located at $x = 0$ and $x = 1$ are isothermal at different temperatures T_1 and T_2 $(T_1 > T_2)$, respectively. The remaining walls are taken as adiabatic. The buoyancy force due to gravity works downwards (i.e. in negative $z-$direction) (figure 2.15). The fluid is initially at a temperature $T_0 = \frac{T_1+T_2}{2}$ and its behavior is supposed newtonian, with a Boussinesq approximation (the Navier-Stokes equations are solved considering the density variation with temperature only in the volumic forces term). All the other physical parameters remain constant. The state law considered is:

$$\rho(T) = \rho_0[1 - \chi_T(T - T_0)] \tag{2.98}$$

We observe that, due to the temperature gradient, natural convection occurs for a Rayleigh number higher than a critical value, $Ra_c \simeq 1700$. The Rayleigh number represents the ratio between destabilizing and stabilizing convective flows and is defined as:

$$Ra = \chi_T\frac{\rho_0^2 c_p g(T_1 - T_2)L^3}{\eta k} \tag{2.99}$$

where χ_T is the isothermal compressibility, c_p the specific heat, k the conductivity and g the gravity value. The problem is also characterized by the Prandtl adimensional number:

$$Pr = \frac{\eta c}{k} \tag{2.100}$$

Values of the Rayleigh number vary between 10^3 to 10^6 in 2D and the Prandtl number is 0.71, which corresponds to the material data in table 2.1.
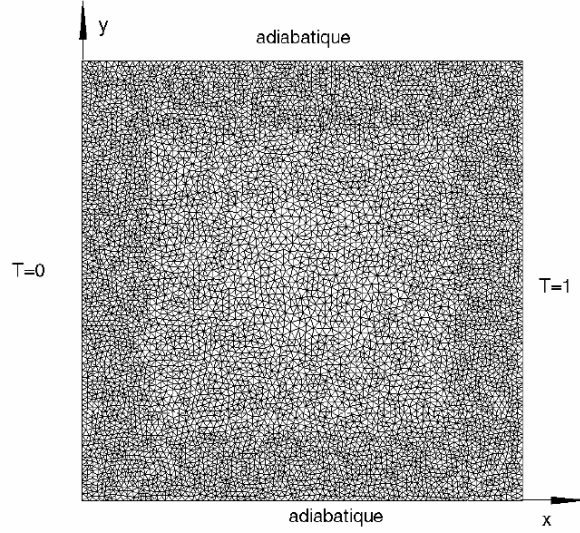
Figure 2.15: *Schematic model for the natural convection in a square cavity: geometry and boundary conditions.*

ρ_0	η	k	c	ΔT	L
1 kg/m^3	0.0071 Pa.s	1 W/mK	100 J/kgK	1 ^{o}C	1 m

Table 2.1: *Material data for the natural convection benchmark.*

The computed results converged to the steady state from initial isothermal and quiescent conditions. Figure 2.16 represents the temperature contours for the different Rayleigh numbers (left and center), and on the right the results from [Davis, 1983]. We notice a good agreement, although for higher Rayleigh numbers it tends to slightly differ. The velocity field on each direction, x and y is represented in figure 2.17, and their extreme values shown in table 2.2. The first line of the table corresponds to the values obtained by [Davis, 1983], from which we can conclude that the results obtained by **REM3D** are comparable to the literature ones.

Ra=1000

Ra=10000

Ra=100000

Ra=1000000
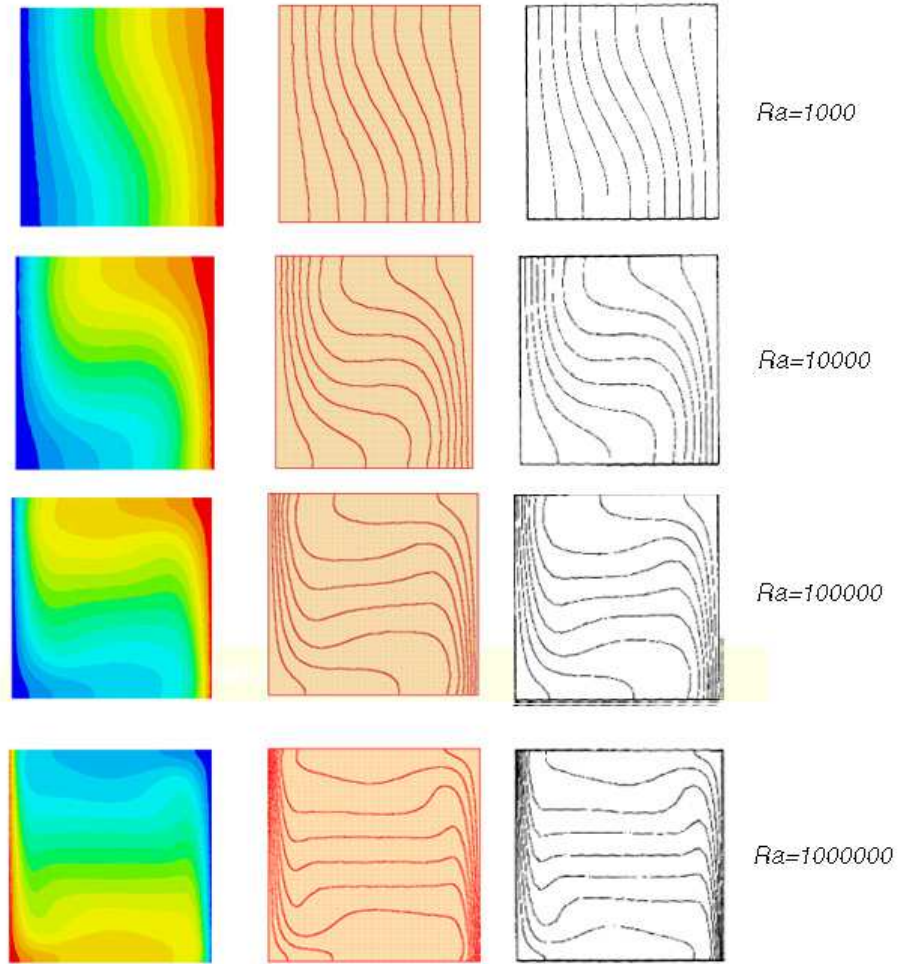
Figure 2.16: *Temperature contours for different Rayleigh numbers; comparison with the solution from* [DeVahlDavis, 1983].
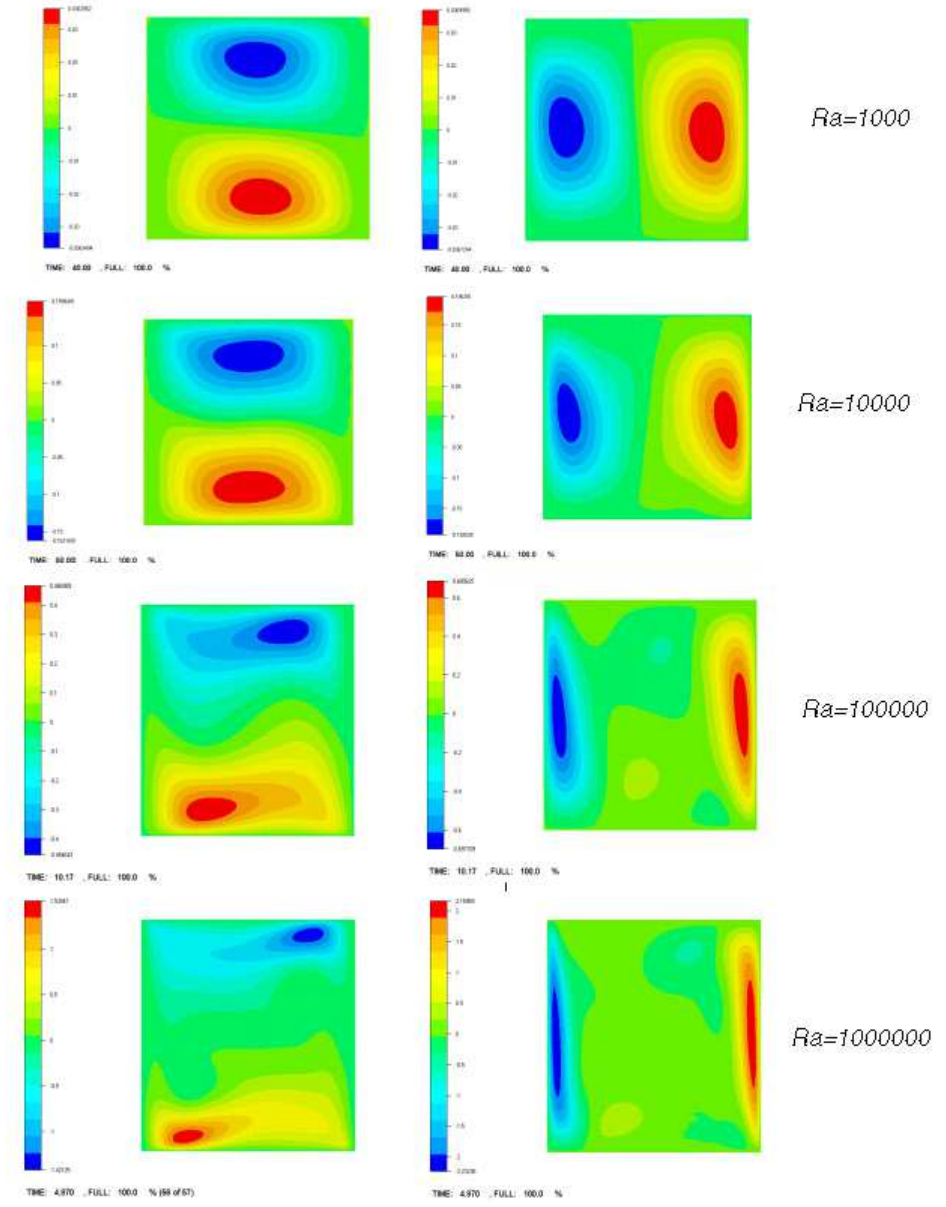
Figure 2.17: *Velocity distributions in x (on the left) and y (on the right) for different Rayleigh numbers.*

Ra	v_x^{max} (m/s) **REM3D**	v_x^{max} (m/s) DeVahlDavis	v_y^{max} (m/s) **REM3D**	v_y^{max} (m/s) DeVahlDavis
10^3	3.70	3.67	3.65	3.63
10^4	19.17	19.55	16.72	15.96
10^5	68.59	68.15	34.73	37.50

Table 2.2: *Maximum velocity on each axis for different Rayleigh numbers.*

2.3   Polymers compressibility

2.3.1   Dynamical behavior

In the previous sections, the non-isothermal compressible flow of a Newtonian fluid was considered. However, polymers are non-Newtonian fluids and their dynamic viscosity is supposed to be function of $\varepsilon(\mathbf{v})$, pressure p and temperature T. Viscoelasticity will be taken into account in the next section. Several laws of the form

$$\eta(\varepsilon(\mathbf{v}), p, T) = \eta_0(p, T) f(\dot{\gamma}) \tag{2.101}$$

may be found in the literature [Agassant et al., 1986], where η_0 is function of pressure and temperature, and f a regular function. In what concerns dependence towards temperature and pressure, we have the following equations:

- Arrhenius law

$$\eta_0(T, p) = K \exp\left[\frac{E}{R}\left(\frac{1}{T} - \frac{1}{T_0}\right)\right] \exp(\kappa p) \tag{2.102}$$

  where E represents the polymer activation energy, R the perfect gas constant, K the viscosity at the reference temperature T_0, and κ a pressure dependent coefficient

- WLF law (Williams, Landel et Ferry)

$$\eta_0(T, p) = D_1 \exp\left[-\frac{A_1(T - T^*)}{A_2 + (T - T^*)}\right] \tag{2.103}$$

  where

$$T^* = D_2 + D_3 p \quad \text{et} \quad A_2(p) = \tilde{A}_2 + D_3 p \tag{2.104}$$

  and D_1, A_1, $\tilde{A}_2$, D_2 and D_3 are polymer dependent parameters.

The coefficients κ and D_3 characterize the dependence of the viscosity towards pressure and are reasonably in agreement with experimental data [Westover, 1992]. Other authors [Mahishi, 1998] define the sensitivity of the viscosity to pressure, a coefficient independent of pressure but affected by temperature (generally it increases when temperature decreases), represented by:

$$\chi_0 = \left(\frac{\partial \eta_0}{\partial p}\right)_T \tag{2.105}$$

If viscosity's dependence on the pressure is not taken into account, the error on the pressure prediction increases at high values, even if the value of this coefficient is very small for polymers (10^{-8} to 10^{-9}). The implementation of a viscosity pressure-dependent is easily done in our fixed point iterative scheme, described previously.

As an example, let us consider the filling of a disk at a constant flow rate. Figure 2.18 shows the difference between a non-pressure dependent fluid and a pressure-dependant one, in terms of evolution of the filling rate and of the pressure at the gate. We observe that the pressure-dependance, does not influence the filling rate, but leads to higher gate pressure values, which may be very important for some mold geometries and molding conditions.
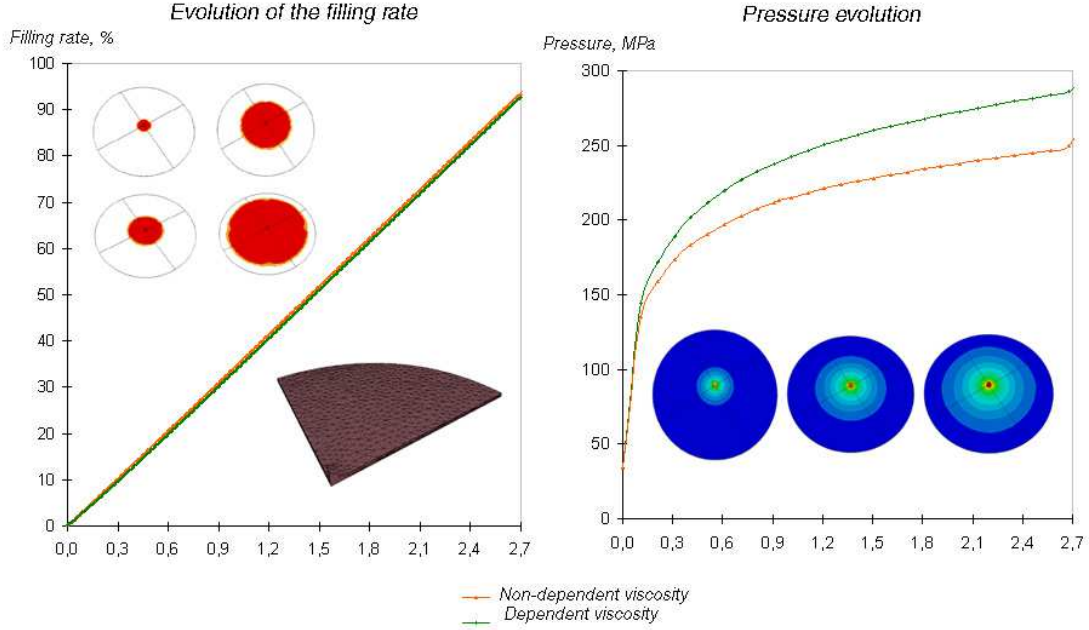
Figure 2.18: *Filling of a disk mold: filling rate and pressure at the gate as function of time.*

2.3.2 Some considerations on the thermal behavior

Some authors [Chiang et al., 1991] consider that polymer's thermal conductivity and heat capacity are function of temperature (even if they often neglect this influence during the filling stage) and represent this variation by an empirical equation. The heat capacity is given by:

$$c(T) = c_1 + c_2\tilde{T} + c_3 \tanh\left(c_4\tilde{T}\right) \tag{2.106}$$

where $\tilde{T} = T - c_5$. For conductivity, a similar relationship is used:

$$k(T) = k_1 + k_2\hat{T} + k_3 \tanh\left(k_4\hat{T}\right) \tag{2.107}$$

with $\hat{T} = T - k_5$. However, it is our opinion that this evolution is mainly due to complete or partial solidification, a behavior that is not considered in this work. Therefore, this influence was not taken into account in the following examples.

2.3.3 State laws and polymer's density evolution

For thermoplastic polymers, the state law is of the type $\rho = \rho(p, T)$, and is generally represented as a PVT diagram, which gives the specific volume as a function of temperature and pressure. Figure 2.19 represents typical PVT diagrams for an amorphous polymer and a semi-crystallin one. In the case of an amorphous material, the specific volume decreases with temperature, with a rupture corresponding to glass transition. For a semi-crystalline polymer, crystallization implies an abrupt decrease of the specific volume at the neighborhood of the transition temperature.

Many theoretical equations were developed to describe polymer's PVT diagrams and are detailed in [Rodgers, 1993]. In certain models, volume changes are taken into account by modifying the size of the regions occupied by polymer chains [Flory et al., 1964], [Dee and Walsh, 1988]. In other models, it is the size of the chain that varies [Simha and Somcynski, 1969]. Nevertheless, the most common equation used to describe the behavior of polymers in the liquid and solid states is the <u>Tait law</u> [Chiang et al., 1991]:

$$v(T, p) = v_0(T)[1 - C \ln\left(1 + \frac{p}{B(T)}\right)] \tag{2.108}$$
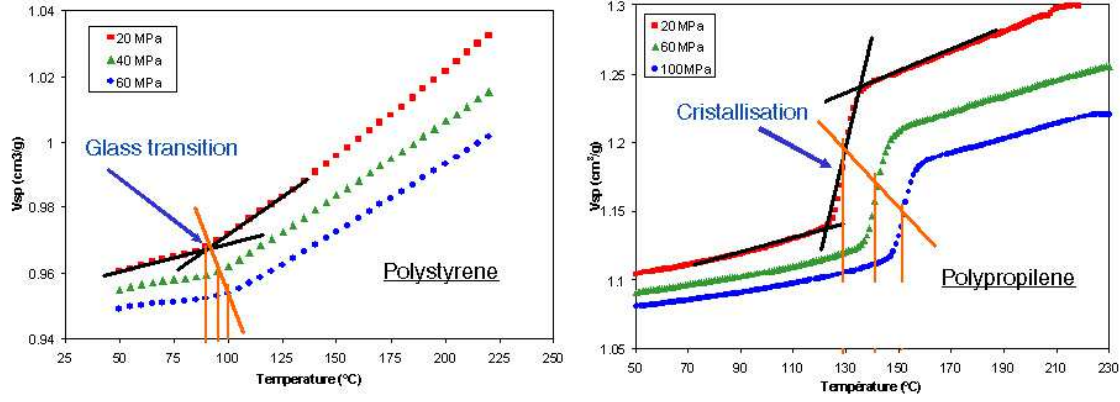
Figure 2.19: *Typical PVT diagrams for amorphous and semi-crystallin polymers [Fulchiron, 2002].*

where $C = 0.0894$ is a constant seen as an universal constant [Fulchiron, 2002]. This equation describes polymer compressible behavior both in the liquid and in the solid state, by representing differently $v_0(T)$ and $B(T)$ for each phase.

$$v_0(T) = \begin{cases} b_{1s} + b_{2s}(T - b_5) & \text{if } T \leq T_t \\ b_{1l} + b_{2l}(T - b_5) & \text{if } T > T_t \end{cases} \tag{2.109}$$

and

$$B(T) = \begin{cases} b_{3s} \exp[-b_{4s}(T - b_5)] & \text{if } T \leq T_t \\ b_{3l} \exp[-b_{4l}(T - b_5)] & \text{if } T > T_t \end{cases} \tag{2.110}$$

The transition temperature (corresponding to the crystallization or glass transition temperature) is assumed to be a linear function of pressure, $T_t = b_5 + b_6 p$. In the case of semi-crystalline polymers, the value of the transition temperature depends on other properties and this remains an active area of research. It is also appropriate to introduce an additional term to handle the sharp density change in the vicinity of T_t for semicrystalline polymers. Equation 2.108 then becomes

$$v(T, p) = v_0(T)[1 - C \ln{(1 + \frac{p}{B(T)})}] + v_t(T, p) \tag{2.111}$$

with

$$v_t(T, p) = \begin{cases} b_7 \exp[b_8(T - b_5) - b_9 p] & \text{if } T \leq T_t \\ 0 & \text{if } T > T_t \end{cases} \tag{2.112}$$

As a consequence, the Tait law requires 10 coefficients for an amorphous polymer and 13 for a semi-crystalline polymer. [Chang, 1994] increased the model's capabilities by introducing the influence of the cooling rate, q_T, through:

$$v_0(T) = \begin{cases} b_{1s} + b_{2s}(T - b_5) + b_{2l}\theta_q \ln(\frac{q_T}{q_{T0}}) & \text{if } T \leq T_t \\ b_{1l} + b_{2l}(T - b_5) + b_{2l}\theta_q \ln(\frac{q_T}{q_{T0}}) & \text{if } T > T_t \end{cases} \tag{2.113}$$

where

$$\theta_q = \frac{dT_g \mid q \mid}{d \log \mid q \mid} \tag{2.114}$$

is a parameter typical for each material. The specific volume of the polymer may also be calculated using the equivalent seven-coefficient formulation [IKV, 2002]:

$$v(T, p) = \frac{K_1}{p + K_4} + \frac{K_2}{p + K_3} T + K_5 \exp[K_6 T - K_7 p] \tag{2.115}$$

This formulation uses different coefficients for the molten and solid states, and the transition temperature is defined as $T_t = K_7 + K_9 p$.

The two laws have been implemented in **REM3D**. At this point, we remind that deriving these empirical equations allows us to obtain the isothermal compressibility and dilatation coefficients, necessary in the mass conservation equation:

$$\chi_T = -\frac{1}{v}(\frac{\partial v}{\partial T}) = \frac{1}{\rho}(\frac{\partial \rho}{\partial T}) \quad \text{and} \quad \chi_p = \frac{1}{v}(\frac{\partial v}{\partial p}) = -\frac{1}{\rho}(\frac{\partial \rho}{\partial p}) \tag{2.116}$$

Both coefficients are function of pressure and temperature, as illustrated for an amorphous polymer in figure 2.20. Nevertheless, we conclude that even though they are dependent on pressure and temperature, giving a non-linear character to our conservation equations, these non-linearities in the mass conservation equation remain very small in the injection molding regime.
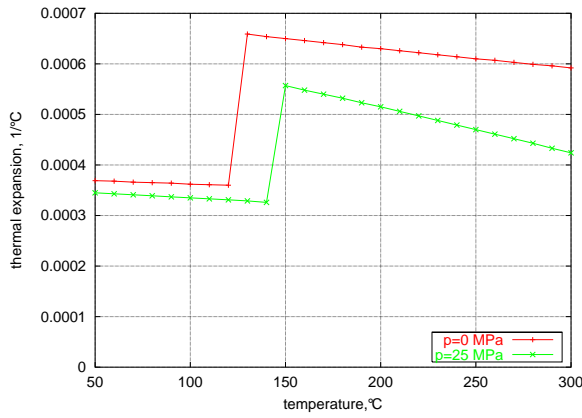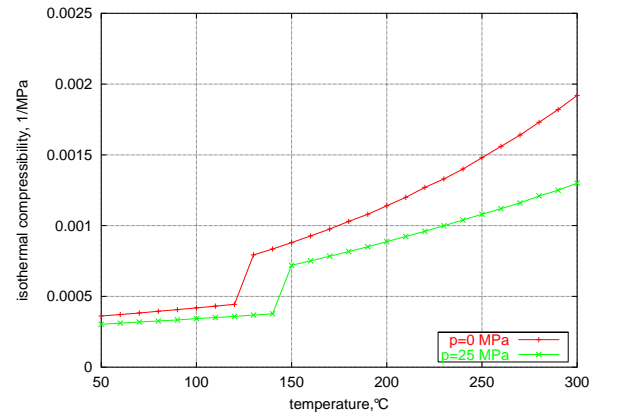
(a)   (b)

Figure 2.20: *Typical diagrams of the thermal expansion and isothermal compressibility coefficients for an amorphous polymer: (a) dilatation coefficients and (b) isothermal compressibility coefficient. Pressure and temperature values correspond to the typical range in injection molding.*

2.3.4   Polymer evolution in a full cavity: the packing stage

A key result emerges from the mass conservation equation: the variation of the volume due to temperature (thermal shrinkage) can be compensated by a pressure increase. Figure 2.21 illustrates how a PVT diagram can help to evaluate the thermal shrinkage during the packing stage of the injection molding cycle. On the right, the evolution of the pressure inside the mold is represented, as well as the mean polymer temperature. At the beginning, the pressure increases strongly until the end of the filling stage, in an almost isothermal way. Afterwards, during the packing stage, we have nearly constant volume on the PVT diagram on the left. Then, the pressure decreases and equalizes the atmospheric pressure; cooling is no longer isochore, but isobar. The specific volume decreases until the polymer part reaches the ambient temperature. The difference of specific volume between the ambient temperature and the one at which the pressure become the atmospheric pressure shows the thermal shrinkage of the polymer. Consequently, the highest the packing pressure is, the lowest the thermal shrinkage will be.
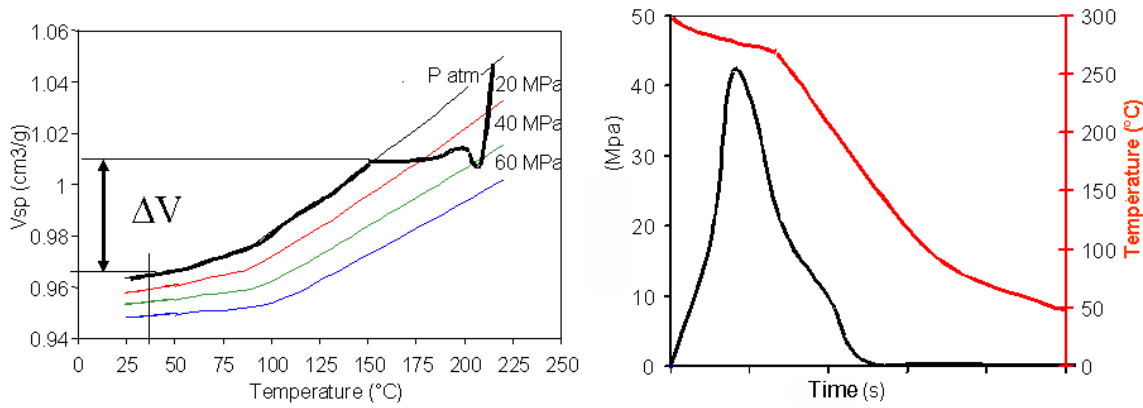
Figure 2.21: *Cavity pressure, temperature and specific volume evolution [Fulchiron, 2002].*

To illustrate this point, let us consider the evolution during cooling of a polymer inside a cavity completely filled. We suppose that its density follows the Tait law, with the parameters for an amorphous polymer. We start from the atmospheric pressure and a temperature of 250°C, and we let the material cool, with a mold temperature of 50°C. Figure 2.22 shows the pressure and temperature fields at $t = 10$s: we notice that pressure has decreased with temperature, and that there is a motion of the material from the warmer zones towards the cooler ones.
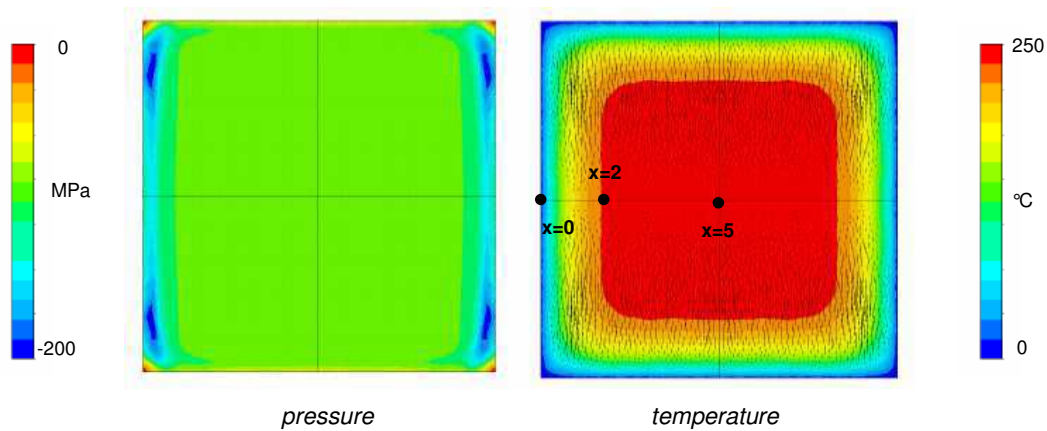
Figure 2.22: *Temperature, pressure and velocity distributions at different time steps.*

One measure of the variation of the specific volume of a material is the <u>shrinkage rate</u>. It illustrates the ability of the material to shrink.

$$\text{shrinkage rate} = 1 - \frac{\rho(p, T)}{\rho(p_{atm}, T_{amb})} \qquad (2.117)$$

The distribution of the shrinkage rate on the part (figure 2.23) gives, at each instant, which zones of the part are more likely to shrink, and therefore to wrap and deform, if at that instant the mold is open.
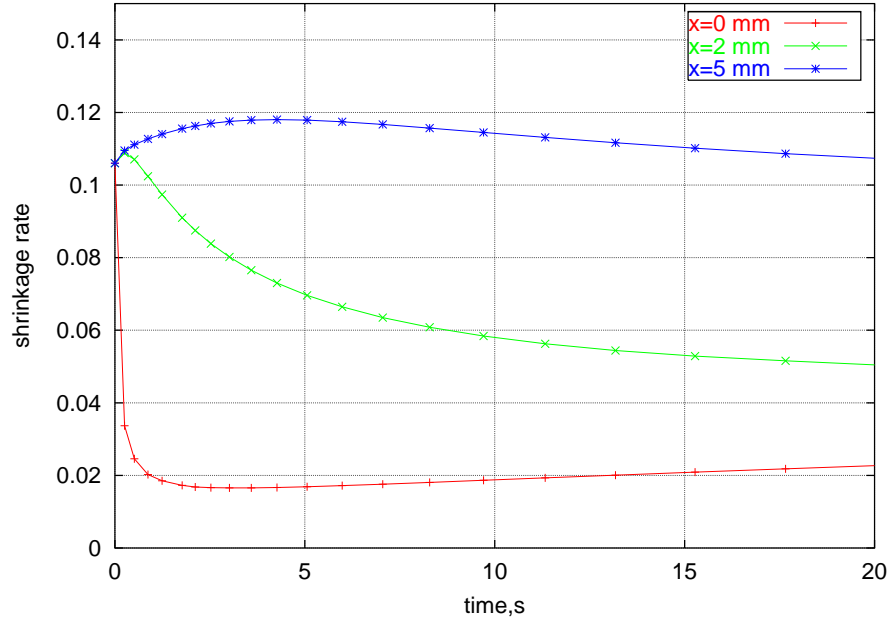
Figure 2.23: *Evolution of the shrinkage rate distribution.*

The same thing happens when we free an edge and let the material enter. In the following figure, one inlet was considered (with $p = 0$ imposed), and the polymer was initially at a temperature superior than the mold temperature, like in the previous case. We observe that inevitably, as the part cools, the polymer enters the cavity (figure 2.24). The pressure distribution indicates points and regions of the part that are in traction (negative pressure). This traction pressure will induce a part deformation once the mold opened.
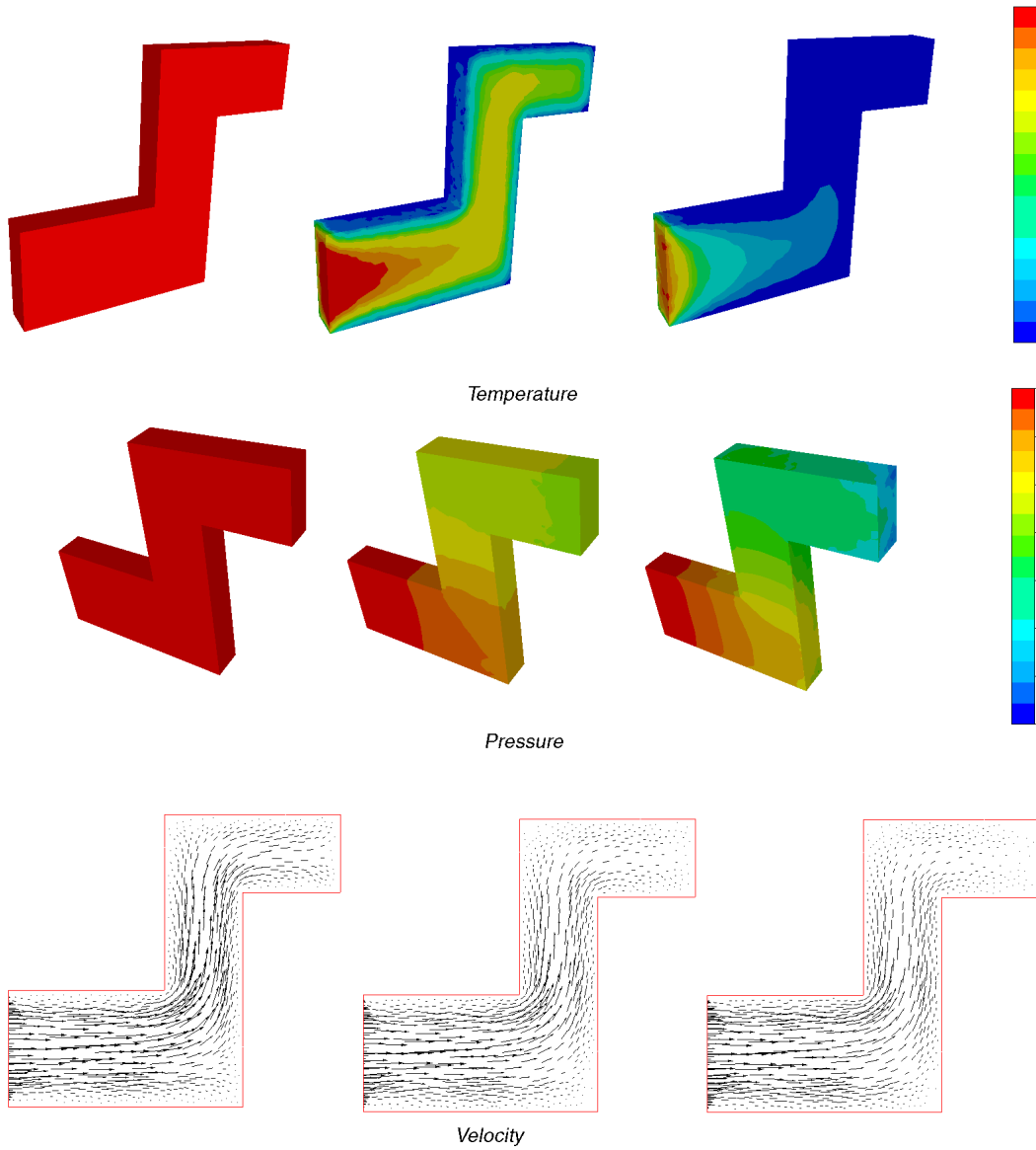
Figure 2.24: *Cooling of a plastic part inside a mold, supposing that the inlet is at zero pressure; temperature and pressure distributions and velocity distributions (truncated scale).*

2.4 Extension to compressible free surface flows

2.4.1 Moving free surfaces and mesh adaptation

In order to calculate a moving free surface (typically a front matter in a 3D mould in injection process) we adopt an eulerian approach. Let us introduce 1_{Ω_f} the characteristic function of the fluid domain Ω_f as an additional unknown in the interval $]t_n, t_{n+1}[$.

> *To identify the region occupied by the fluid, we say that a point $\boldsymbol{x}$ belongs to a domain i if the characteristic function of this domain is 1.*
>
> $$\forall_{t\in\mathbb{R}^+} 1_{\Omega_i}(\boldsymbol{x},t) = \left\{ \begin{array}{l} 1 \; if \, \boldsymbol{x} \in \Omega_i \\ 0 \; if \, \boldsymbol{x} \in \Omega \setminus \Omega_i \end{array} \right.$$
>
> *and the characteristic function obeys a transport equation.*

We can extend each fluid individual problem to the whole computational domain [Pichelin and Coupez, 1998] as follows.

Let us note χ the space containing the whole set of variables (X) of the problem expressed in the fluid, for example $X = (\mathbf{v}, p, T)(x, t)$. The weak form of this problem can be expressed as:

$$\int_{\Omega_f} A(X, Y) = \int_{\Omega_f} L(Y) \tag{2.118}$$

where $(X, Y) \in \chi^2$ and A is the suitable operator. Using the characteristic function 1_{Ω_f}, problem (2.118) can be extended to the whole computational domain:

$$\int_{\Omega} 1_{\Omega_f} A(X, Y) + (1 - 1_{\Omega_f}) a(X, Y) = \int_{\Omega} 1_{\Omega_f} L(Y) \tag{2.119}$$

where a is the generalization to χ of the velocity-pressure extension method developed in [Pichelin and Coupez, 1998], ensuring continuity of the velocity and normal stresses field [Bruchon and Coupez, 2003].

To illustrate this point, let us consider that our computational domain is divided in two subdomains: one fluid viscous and incompressible, and the other fluid viscous and compressible. To determine velocity and pressure, we suppose $\chi = \mathcal{V} \times \mathcal{P}$, and we re-write the variational problems on each domain

find $(\boldsymbol{v}, p) \in \mathcal{V} \times \mathcal{P}$ such that, $\forall (\boldsymbol{w}, q) \in \mathcal{V} \times \mathcal{P}$

$$\left\{ \begin{array}{l} \displaystyle\int_{\Omega_1} 2\eta_1 \varepsilon(\mathbf{v}) : \varepsilon(\mathbf{w}) - \int_{\Omega_1} p\nabla \cdot \mathbf{w} = 0 \\[3mm] \displaystyle -\int_{\Omega_1} q\nabla \cdot \mathbf{v} = 0 \end{array} \right. \tag{2.120}$$

find $(\boldsymbol{v}, p) \in \mathcal{V} \times \mathcal{Q}$ such that, $\forall (\boldsymbol{w}, q) \in \mathcal{V} \times \mathcal{P}$, for $C \in \mathcal{Q}'$

$$\left\{ \begin{array}{l} \displaystyle\int_{\Omega_2} 2\eta_2 (\varepsilon(\mathbf{v}) - \frac{1}{3}\mathrm{tr}(\varepsilon(\mathbf{v}))\mathbf{I}) : \varepsilon(\mathbf{w}) - \int_{\Omega_2} p\nabla \cdot \mathbf{w} = 0 \\[3mm] \displaystyle -\int_{\Omega_2} q\nabla \cdot \mathbf{v} - \int_{\Omega_2} q(\alpha p + \beta \mathbf{v} \cdot \nabla p) = -\int_{\Omega_2} qC \end{array} \right. \tag{2.121}$$

We obtain the extended problem on the whole computational domain: *find $(\boldsymbol{v}, p) \in \mathcal{V} \times \mathcal{P}$ such that, $\forall (\boldsymbol{w}, q) \in \mathcal{V} \times \mathcal{P}$, for $C \in \mathcal{Q}'$*

$$
\begin{cases}
\displaystyle \int_\Omega 1_{\Omega_1} 2\eta_1 \varepsilon(\mathbf{v}) : \varepsilon(\mathbf{w}) - \int_\Omega 1_{\Omega_1} p \nabla \cdot \mathbf{w} = 0 \\[2ex]
\displaystyle \int_\Omega 1_{\Omega_2} 2\eta_2 (\varepsilon(\mathbf{v}) - \frac{1}{3} \mathrm{tr}(\varepsilon(\mathbf{v}))\mathbf{I}) : \varepsilon(\mathbf{w}) - \int_\Omega 1_{\Omega_2} p \nabla \cdot \mathbf{w} = 0 \\[2ex]
\displaystyle -\int_\Omega 1_{\Omega_1} q \nabla \cdot \mathbf{v} - \int_\Omega 1_{\Omega_2} q \nabla \cdot \mathbf{v} - \int_\Omega 1_{\Omega_2} q(\alpha p + \beta \mathbf{v} \cdot \nabla p) = -\int_\Omega 1_{\Omega_2} qC
\end{cases}
\tag{2.122}
$$

Finally, for each material domain, the local matrices are multiplied by the characteristic function of the domain and then assembled to the global system.

2.4.2 Calculating the characteristic function

The characteristic function computation for each time step is not detailed here, since it has been object of a previous work [Batkam et al., 2003], and is given in Appendix A. The characteristic function itself becomes an unknown function which can be approximated by using a finite element technique. For instance, one can choose $1^h_{\Omega_f} = \Pi^h 1_{\Omega_f}$ where Π^h is the projection operator onto the piecewise constant function, which leads to a V.O.F. method : $1^h_{\Omega_f} = vol(K \cap \Omega_f)/vol(K)$.

Finally, free surfaces are moved by solving the transport equation :

$$
\frac{d1_{\Omega_i}}{dt} = 0
\tag{2.123}
$$

by the space-time discontinuous Galerkin formulation.

Although the method performs well, numerical diffusion exists and may give inaccurate rendering of the interface. It is important to have a good description of the interface fluid/fluid, fluid/air, fluid/mold and so, to limit this diffusion, a technique developed in [Bigot and Coupez, 2000] is used. This technique is based on the displacement of mesh nodes without changing the mesh topology: the mesh follows the motions of the fluid by contracting the nodes at the interfaces, regaining its original size once the interface passed. This nodal displacement is implicitly introduces through the mesh velocity, taken into account in all evolution expression (as in a classical ALE technique) as:

$$
\frac{d\alpha}{dt} = \frac{\partial \alpha}{\partial t} + (\mathbf{v} - \mathbf{v}_{mesh}) \cdot \nabla \alpha
\tag{2.124}
$$

where $\mathbf{v}$ is the fluid velocity.

So, considering that our injection molding cavity, partially filled with fluid (with characteristic function 1_{Ω_f}) and partially with air (1_{Ω_a}), we solve, for the duration of the processus Θ:

ALGORITHM: COMPRESSIBLE FREE SURFACE FLOWS

---

for each time step **do**

knowing $(\mathbf{v}^n, p^n, T^n, 1_{\Omega_f}^n)$

1) compute $(\mathbf{v}^{n+1}, p^{n+1})$ such that

$$1_{\Omega_f}^n \begin{cases} \nabla \cdot [2\eta_f(\varepsilon(\mathbf{v}^{n+1}) - \dfrac{2\eta_f}{3}\nabla \cdot \mathbf{v}^{n+1}\mathbf{I})] - \nabla p^{n+1} = \mathbf{f} \\[3mm] -\nabla \cdot \mathbf{v}^{n+1} - \dfrac{\chi_{p_f}}{|I^n|}p^{n+1} - \mathbf{v}^n \cdot \nabla p^{n+1} = -\dfrac{\chi_{p_f}}{|I^n|}p^n - \chi_{T p_f}^n \dfrac{dT^n}{dt} \end{cases}$$

$+$

$$1_{\Omega_a}^n \begin{cases} \nabla \cdot [2\eta_a \varepsilon(\mathbf{v}^{n+1})] - \nabla p^{n+1} = 0 \\[3mm] -\nabla \cdot \mathbf{v}^{n+1} - \dfrac{\chi_{p_a}}{|I^n|}p^{n+1} = 0 \end{cases}$$

2) for each domain i, compute its characteristic function $1_{\Omega_i}^{n+1}$

$$1_{\Omega_i}^{n+1} + \mathbf{v}^{n+1} \cdot \nabla 1_{\Omega_i}^{n+1} = 0$$

3) compute (T^{n+1}) such that

$$\sum_i 1_{\Omega_i}^{n+1}[\rho_i^n c_i \dfrac{dT}{dt}^{n+1} - \chi_{T_i}^n \dfrac{dp}{dt}^{n+1} T^{n+1} - k_i \nabla \cdot (\nabla T^{n+1}) = \dot{\omega}_i(\mathbf{v}^{n+1}, p^{n+1})]$$

end for

The model used in the air is a simplified version of the compressible Stokes equation, described in the following section.

2.5 Applications to more complex systems

In polymer forming processes, evolution of the material density may lead to important shrinkage or expansion rates. The following examples illustrate the importance of the material compressibility in forming situations such as optical lens production and foam molding, where the polymers used present volume variations more important than thermoplastics in injection molding. We observe that in the first case, a chemical reaction (polymerisation) gives rise to an increase of the density ($\frac{d\rho}{dt} > 0$), leading to a reduction of the volume, whereas in the second example a different reaction produces a density decrease and a significant volume increase ($\frac{d\rho}{dt} < 0$). Volume variations are here represented by the evolution of the interfaces between the polymer and the air inside the cavity, or between the polymer and the mold, when the mold is deformable.

2.5.1 Shrinkage of an optical lens

A simple way to obtain the shrinkage of a domain is to consider that its density increases with time: ($\rho = \rho(t)$ and $\frac{d\rho}{dt} > 0$). To test the capacity to induce fluid shrinkage through this simple perturbation of the conservation of mass equation, we consider a box partially filled (90%) with a compressible fluid. No other material is injected (figure 2.25), one symmetry plane is considered, and the fluid is Newtonian, and isothermal flow. A linear and homogeneous density evolution has been considered (shrinkage rate of 10%, shrinkage time of 7200s, initial density of 1 g/cm^3) and we focus on the free surface evolution.
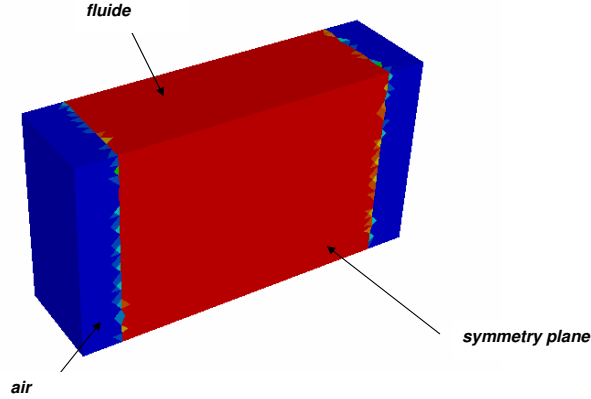
Figure 2.25: *Schematic geometry of the shrinkage test.*

The free surface is determined from the system 3.52, by considering the fluid Ω_f as a compressible viscous fluid, and Ω_a the air in the cavity also compressible, but with a simplified form of the mass conservation equation:

$$\nabla \cdot \mathbf{v} + \alpha p = 0 \ \text{ in } \ \mathbf{x} \in \Omega_a \tag{2.125}$$

with α a constant coefficient, that can be seen as $\alpha = \frac{\chi_p}{|I^n|}$, where χ_p is the isothermal compressibility of the air and $|I^n|$ the time step. Figure 2.26 shows the evolution of the flow front during this density increase, noticing that it leads effectively to a decrease on the volume of the fluid domain. The existence of a velocity field (figure 2.27(a)) and the good correspondance between the theoretical and the numerical computed filling rate (figure 2.27(b)) confirm that the prolongation method chosen, as well as the free surface determination, do not affect the final result.

TIME: 0.000 , FULL: 88.89 %   TIME: 500.0 , FULL: 83.05 %   TIME: 1500. , FULL: 73.96 %   TIME: 2000. , FULL: 69.06 %
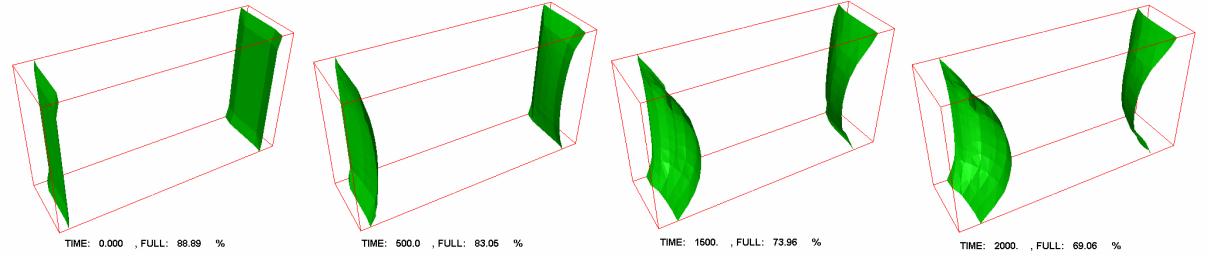
Figure 2.26: *Evolution of the flow front for a compressible fluid with a linear density evolution with time: (a) $t = 3600s$, filling=86% (b) $t = 7200s$, filling=81.8% (c) $t = 10800s$, filling=77.2% and (d) $t = 14400s$, filling=74%.*
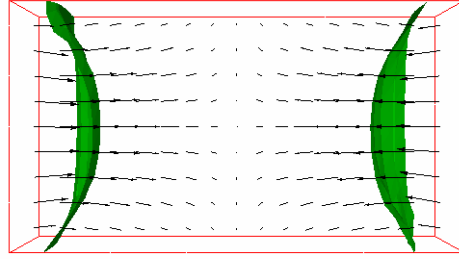
(a)
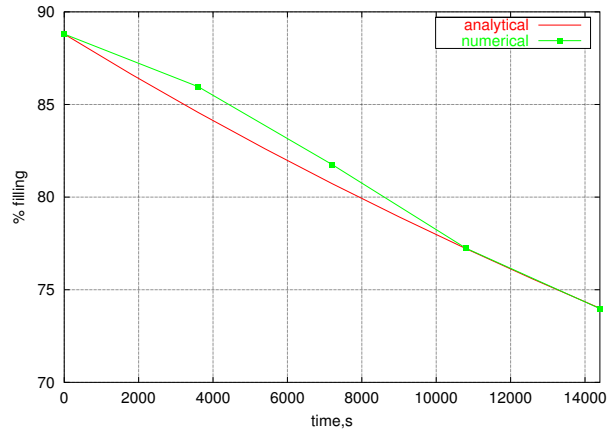
(b)

Figure 2.27: *Velocity field (a) and % of filling versus time(b)*

A more complex illustration of the compressible behavior is the shrinkage of an ophtalmic lens [Hammer, 2001] (figure 2.28(a)). The monomer polymerises inside a deformable mold through curing during several hours. In the referred work C. Hammer used **REM3D** to predict the deformation of the thermoset lens during its curing. The density evolution was:

$$\rho = \rho(t) = A[1-\exp(-at)]+B[1-\exp(-bt)]+C \tag{2.126}$$

where A, B, C, a, b are material parameters. For a given set of parameters ($A = 0.137531$, $B = 0.0172816$, $C = 1.134$, $a = 0.000911878$, $b = 0.00015444$), figure 2.28(b) shows the evolution of the maximum displacement and velocity (representations of the maximum shrinkage) in the lens surface. The agreement is rather good with the experimental data [Hammer, 2001].

(a)

(b)
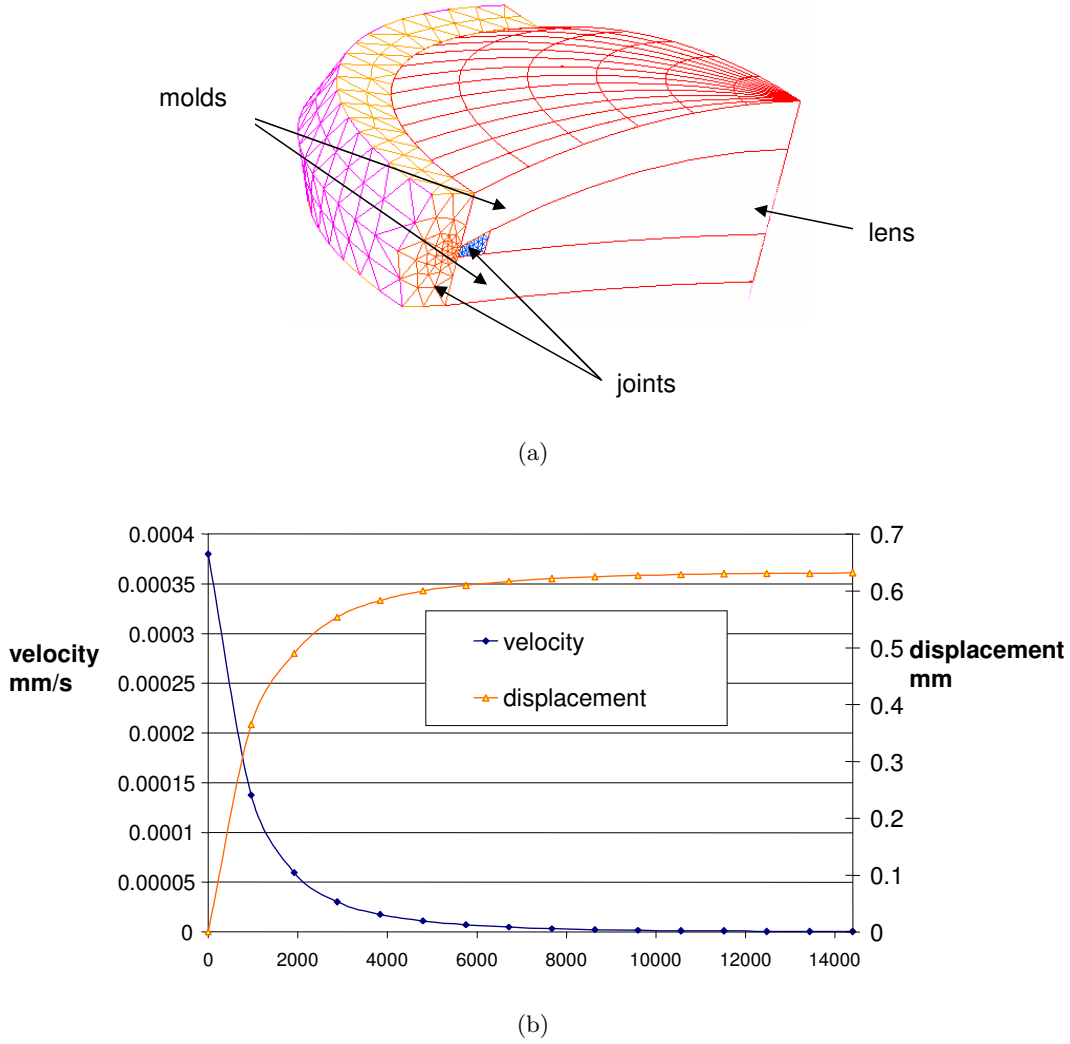
Figure 2.28: *Shrinkage of an ophtalmic lens (a) geometry and (b) maximum displacement and velocities as function of time [Hammer, 2001].*

2.5.2 Expansion of a foam car seat

To obtain the expansion of a fluid domain, we may consider that its density decreases with time: ($\rho = \rho(t)$ and $\frac{d\rho}{dt} < 0$). One important application is the foam expansion (in this case of parts like car seat). Polyurethane foams are produced in an one shot process, with production of carbon dioxide, and foam rise starting a few seconds after mixing and being completed in a matter of minutes. The CO_2 production gives rise to the existence of an homogeneous gas-polymer mixture that induces a compressible behavior.

Let us assume that the reaction producing CO_2 began and that an initial volume of mixture gas/liquid exists in the cavity (Ω is the cavity, Ω_m, the mixture and $| \Omega_m |$ is the volume of the mixture). The gas-fluid mixture is treated as a homogeneous, compressible, viscous fluid, whose density $\rho_m(x,t)$ and viscosity $\eta_m(x,t)$ are function of the volumic gas rate of the mixture. Ω_m expands in the cavity Ω, with an expansion time Θ. The interface mixture/air $\partial\Omega_{fs}$ evolves in time as functions of the velocity field (and of the expansion rate). No-slip conditions are considered in the whole cavity. If we neglect inertia and gravity, as well as surface tension, we have to solve the following problem: *find $\boldsymbol{v} \in \mathcal{C}^2(\Omega)$ and the pressure $p \in \mathcal{C}^1(\Omega)$ such that, $\forall t \in [0, \Theta]$, $\forall x \in \Omega_m(t)$,*

$$
\begin{cases}
\nabla \cdot [2\eta_m(\varepsilon(\mathbf{v}) - \frac{1}{3}\nabla.\mathbf{v}I)] - \nabla p = 0 \\
\nabla \cdot \mathbf{v} + \frac{1}{\rho_m}\frac{d\rho_m}{dt} = 0 \\
+ \text{ boundary and initial conditions}
\end{cases}
\tag{2.127}
$$

This problem is similar to the compressible one described previously. We only need to know how to evaluate ρ_m and its evolution in the mixture. So, let us now consider that the volume $|\Omega_m|$ of the gas-polymer mixture is a diphasic medium Ω_m constituted by the following phases:

- the polymeric phase Ω_l, treated as an incompressible viscous polymer;

- the gas phase Ω_g (constituted for example by the union of N bubbles randomly distributed in the mixture).

We introduce the volumic ratio of each species, α_l and α_g as the volumic ratio of liquid and of gas in the mixture, defined as:

$$
\alpha_i = \frac{|\Omega_i|}{|\Omega|}
\tag{2.128}
$$

Thus, if we consider now the mass conservation equation in the gas-polymer mixture Ω_m, we have:

$$
\frac{1}{\rho_m}\frac{d\rho_m}{dt} = -\frac{1}{1-\alpha_g}\frac{d\alpha_g}{dt}
\tag{2.129}
$$

The global perfect gas behavior and its derivation allows us to write an evolution equation for the gas phase, function of the CO_2 production ($g(t)$) and the flow pressure:

$$
\frac{d\alpha_g}{dt} = \alpha_g(1-\alpha_g)(g(t) - \frac{1}{p}\frac{dp}{dt})
\tag{2.130}
$$

where n_g is the global number of moles at each instant. The liquid is supposed incompressible ($|\Omega_l| = const$), and ρ_l is the liquid's density.

Thus, in the mixture sub-domain, we are led to solve the following problem: *find $\boldsymbol{v} \in \mathcal{C}^2(\Omega)$, pressure $p \in \mathcal{C}^1(\Omega)$ and gas rate $\alpha_g \in \mathcal{C}^1(\Omega)$ such that, $\forall t \in [0, \Theta]$, $\forall x \in \Omega_m(t)$:*

$$
\begin{cases}
\nabla \cdot [2\eta_m(\varepsilon(\mathbf{v}) - \frac{1}{3}\nabla.\mathbf{vI})] - \nabla p = 0 \\[2mm]
\nabla \cdot \mathbf{v} - \frac{1}{1 - \alpha_g}\frac{d\alpha_g}{dt} \\[2mm]
\frac{d\alpha_g}{dt} = \alpha_g(1 - \alpha_g)[g(t) - \frac{1}{p}\frac{dp}{dt}]
\end{cases}
\tag{2.131}
$$

The expansion of the mixture is given by two mechanisms:

- creation of gas in bubbles, which is led by an evolution law on $\dfrac{d\alpha_{CO_2}}{dt}$,

- or difference of pressure between the mixture and the atmospheric pressure, which is led by the dp/dt term (case of free expansion). This term will be obtained by solving the motion equations.

The form of the gas creation term, $g(t)$, has been studied by Lefebvre and co-workers [Lefebvre, 1993] by means of free rise experiments. Assuming that the reaction is not influenced by the local or global pressures, for a constant temperature T_0, the evolution law only depends on a characteristic time of the reaction τ and an exponent of reaction n and can be of the form :

$$
g(t) = \frac{1}{\tau(T_0)}(1 - \alpha_g)^n
\tag{2.132}
$$

In what concerns the resolution, we remark that system (2.131) is highly coupled and non-linear. As previously, a *splitting* technique has been used to decrease the degree of complexity: on one time step (element) knowing α_g, velocity and pressure fields are determined through the mixed finite element method described previously. Velocity is then used to compute the gas expansion rates (through a space-time discontinuous Galerkin technique). The numerical techniques involved are unchanged and detailed in one of the author's submitted paper [Bikard et al., 2004].

An industrial example concerns the molding of an automobile seat in flexible polyurethane foam. Figure 2.29 (top left) shows the initial configuration of the computational domain, where an initial volume of mixture has been considered ($\approx 5\%$ of the total cavity volume). The initial gas rate was supposed to be 0.1%, whereas the liquid is supposed Newtonian, with a viscosity of 710 Pas. The mixture is at rest at the beginning of the computation ($\mathbf{v} = 0$ and $p = 0$) and a no-slip condition was imposed along all the mold walls. Parameters ruling CO_2 creation are determined by considering the initial gas rate (0.1%), the maximum gas rate that can be attained ($\approx 95\%$) and the expansion time ($55s$).

Figure 2.29 illustrates the evolution of the expansion throughout time. We notice that at $t = 26s$, the gas-liquid mixture occupies 54.62% of the part volume. The process finishes when the mold is completely filled. However, residual pressure in the air trapped in the cavity (figure 2.31) does not allow to fully fill the cavity, and at $t = 80s$ computation stopped. Furthermore, at $t = 55s$ mold filing is 87.88%. Empty parts are represented in figure 2.30.

Evolution of the volume and the gas rate (figure 2.32) in one point of the part seem correctly predicted. Volume evolution is linear up until $t = 45s$, for a filling of 82.73%. Then, we observe a decrease of the filling rate, and expansion does not really evolve beyond this point.
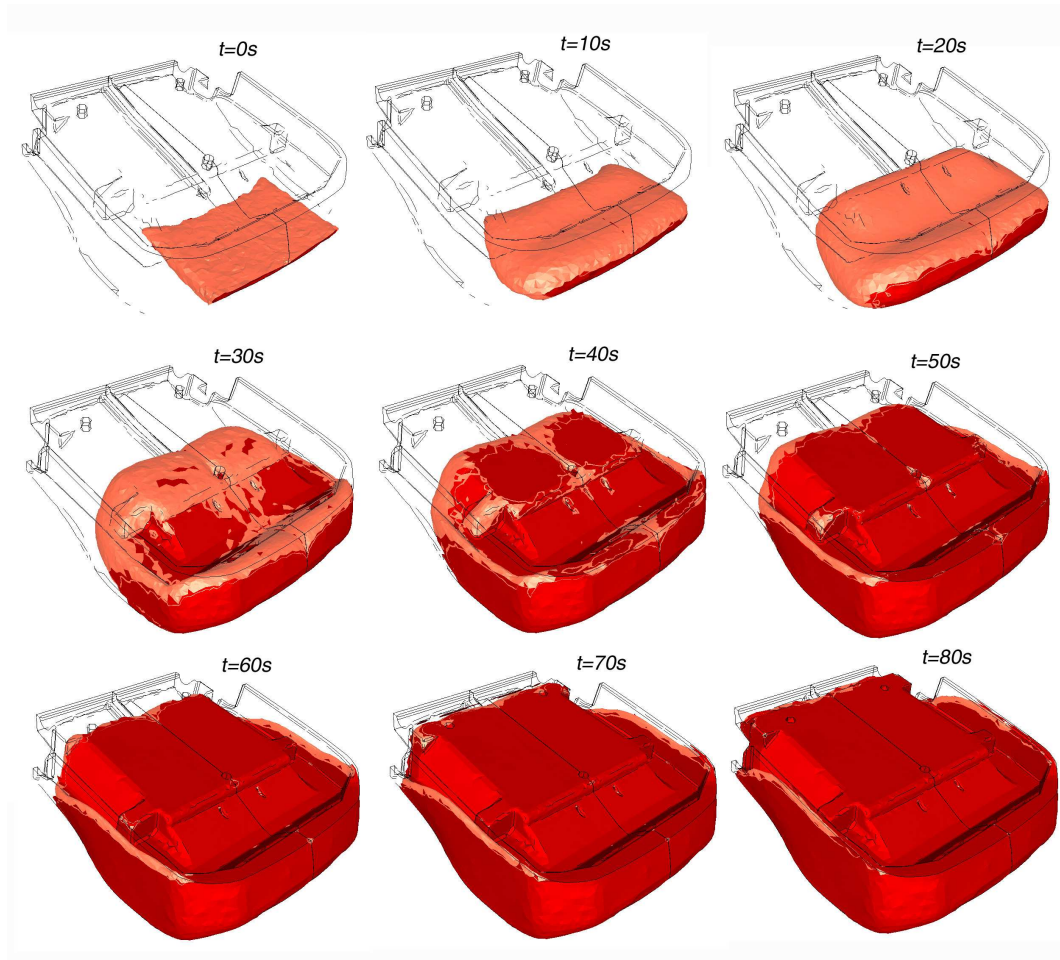
Figure 2.29: *Evolution of the computed foam expansion.*
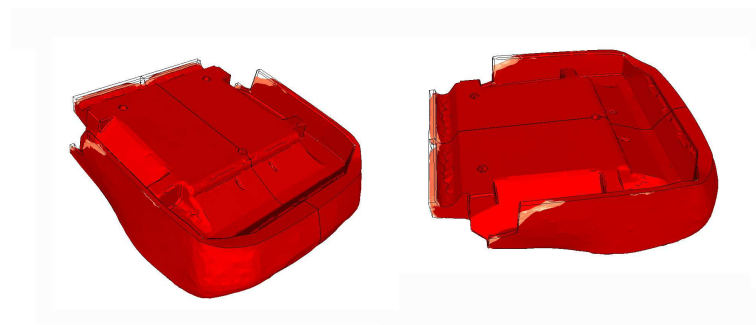
Figure 2.30: *Last regions to become filled.*
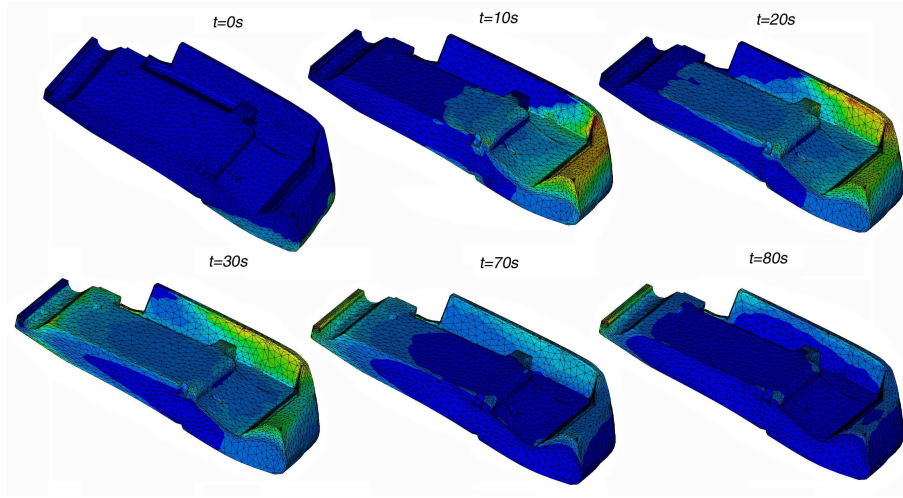
Figure 2.31: *Pressure distribution in the part function of time.*
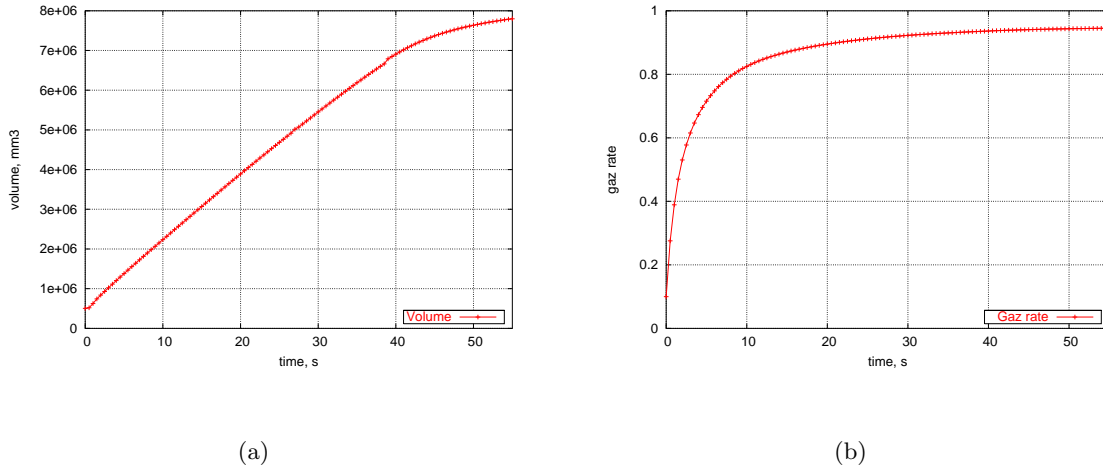
Figure 2.32: *Volume of mixture (a) and gas rate (b) as function of time.*

2.6   Conclusions

A methodology was introduced to compute non-isothermal 3D compressible flows, based on continuum mechanics principles. Compressibility introduces a new unknown: the density. In polymer engineering this density is basically function of temperature and pressure, with opposite effects: increasing temperature decreases density, whereas increasing pressure increases density. Using this basic physical principle we try to maintain the volume of an injected plastic part almost unchanged, reducing drastically the shrinkage rate.

We have also shown that compressibility and thermal shrinkage lead often to stresses trapped in the part. These stresses are generally tractive and are due to the lack of holding pressure or packing time. Stresses may also come from the viscoelastic nature of polymer both at the liquid and at the solid state. The next chapter focus on the description of viscoelastic behavior of polymers at the liquid state, and how it can be modelled efficiently in an 3D injection molding software.

Chapter 3

Viscoelasticity

Contents

In this chapter, a more exact rheological behavior is introduced. Polymers are considered viscoelastic materials and therefore memory dependent. In injection molding, once the material solidifies, the viscoelastic behavior induces stresses that rest frozen in the part. Furthermore, these stresses are strongly related with material's molecular orientation, which influences the part's final mechanical properties.

In the first part of this chapter, a short bibliography on viscoelasticity in injection molding is done. A variant of the Pom-Pom model was chosen [McLeish and Larson, 1998], that behaves well both in elongation and shear, and is numerically acceptable. Furthermore, molecular orientation appears as one mechanism of the model, allowing the numerical developments useful in other applications (such as fiber orientation). The second part is devoted to the numerical resolution of isothermal viscoelastic flows. We extend the mixed finite element method described previously to account for viscoelasticity. The flow solver uses tetrahedral elements and a mixed velocity-pressure-extra stress formulation, using a time marching scheme and a splitting approach. Material behavior constitutive equations were described previously, closing our model. At each time slab, once the velocity has been calculated, all evolution equations associated with the constitutive behavior are solved by a space-time finite element method. Validations tests of the viscoelastic and compressible models implementation are performed, using classical benchmark examples. Results obtained for industrial 3D geometries show the robustness and the efficiency of our approach.

The third part incorporates compressibility, keeping in mind that both effects remain, at this stage, decoupled. A benchmark on compressible viscoelastic flows is used to show the difference between viscoelastic compressible/incompressible behavior.

Finally, thermal viscoelasticity is considered. The subject has not been very well studied up to this date. On one hand, we establish the part of the energy due to extra-stresses that is dissipated and, on the other hand, we define the orientation tensor and molecular stretch freezing conditions. Thus, below a certain temperature, stresses due to viscoelastic behavior are frozen in the material and no longer allowed to evolute. Later examples will illustrate this point, of importance with respect to the part's mechanical properties.

Simple applications in free surface viscoelastic show the potential of the developments performed to applications in injection molding of the following chapter.

3.1 Why considering viscoelasticity in injection molding flows?

3.1.1 Introduction

A part of this work focus on the understanding and the prediction of molecular orientation, which is built-up and frozen-in during the injection process. Orientation affects the physical and mechanical properties, dimensional stability and the aspect of the finished product. It results in anisotropy of mechanical, optical and thermal properties. For example, the anisotropy of the thermal conductivity and the thermal expansion coefficient influences directly the time dependent spatial temperature distribution and subsequently the development of thermal stresses during the entire process. Anisotropy in elastic moduli influences warpage and anisotropy of the refractive index influences birefringence patterns.

Orientation can be seen as the frozen in picture, at a molecular scale, of the deforming material as it existed during processing. The material is oriented when the spatial distribution of chain segments is no longer random. For example, for amorphous polymers, long-range molecular reordering is possible until the glass transition temperature is reached. The spatial distribution of the chain segments will be reached, as it was just before passing T_g. The frozen-in state of orientation, below T_g, is independent of temperature.

From the above description, we conclude that the development of the residual stress field in an injection molded part is rather complex. The flow-induced and thermal-induced stresses are coupled [Isayev, 1987] and no single constitutive equation seems capable of describing the full behavior of the polymer through the injection, packing and cooling stages.

3.1.2 Measuring orientation and flow-induced stresses

Molecular orientation and stresses can be measured through a number of experimental methods, but birefringence remains the most applied one, for transparent materials. Birefringence measurements are based on the fact that a transparent or translucent material changes in the index of refraction, meaning variations in the speed of light through the material. When coming from a beam of polarized light, individual rays take different paths through the material and, when recombining, produce interference patterns (fringes). In classical interpretation, lines of the same birefringence value indicate points in the material at the same stress. This is the principle that underlies the technique of photoelasticity. The empirical stress optical rule relates the residual stresses to birefringence by means of the optical stress coefficient:

$$b_i = C(\sigma_1 - \sigma_2) \tag{3.1}$$

where b_i is the birefringence index, C is the optical stress coefficient and $(\sigma_1 - \sigma_2)$ is the first difference of normal stresses. Flow-induced stresses and molecular orientation distribute differently in the thickness and in the flow length directions. Birefringence measurements provide good information about orientation distribution in the flow direction, being generally more difficult to measure stresses and orientation distributions in the thickness.

First birefringence studies were performed by J. Wales [Wales, 1976], who measured the birefringence distributions from different materials in a slit apparatus; and Isayev and co-workers [Isayev, 1983], who measured birefringence components for strips and runners, investigating the effect of processing conditions.

Later, other authors [Takeshima and Funakoshi, 2001] measures helped to understand the mechanism of formation of flow-induced stresses. Takeshima [Takeshima and Funakoshi, 2001] measured
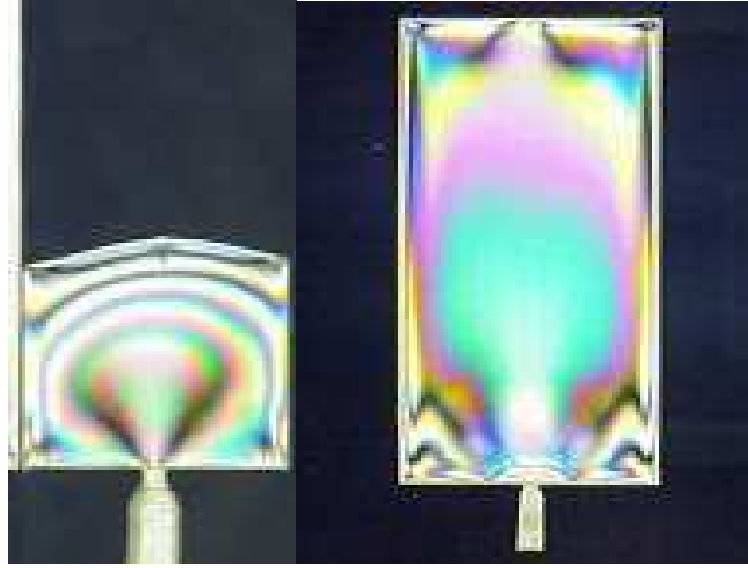
Figure 3.1: *Birefringence fringe patterns in an injection molded part; on the left during filling and on the right after ejection.*

the molecular orientation distribution of injection molded polycarbonate disks at different injection temperatures (for the same other molding conditions). A disk sample was extracted once the part was finished (one for each injection temperature) and birefringence in the flow length and laser-Raman spectroscopy intensity in the thickness were measured (figure 3.2).

The birefringence pattern is shown on figure 3.3(a) as a function of the distance from the gate. The birefringence value decreases gradually with increasing distance, indicating that the molecular orientation is greater near the gate. It can also be seen that the birefringence decreases with increasing injection temperature (T_c). The oriented molecules are relaxed to some extent in the holding period because temperature remains high enough to prevent orientation from being frozen.

Raman spectroscopy is performed illuminating a sample with a laser beam. Light from the illuminated spot is collected with a lens and sent through a monochromator. Wavelengths close to the laser line are filtered out and those in a certain spectral window away from the laser line are dispersed onto a detector, giving the Raman intensity, I. This intensity is function of the angle between polarized light and molecular orientation. The authors [Takeshima and Funakoshi, 2001] measured this intensity ratio along a cross-section perpendicular to the radial section of the disc, at different positions L, corresponding to two different birefringence indexes.
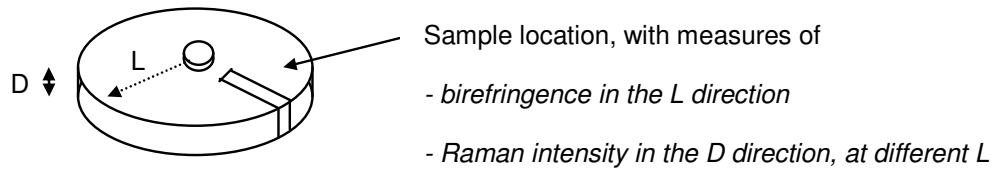
Figure 3.2: *Sample location and measures: birefringence along L, shrinkage as a dimension variation in L and Raman spectroscopy in the thickness direction D.*

Figure 3.3(b) shows the relative Raman spectrum intensity I function of the thickness for three samples with different birefringence, showing that the intensity is higher for the sample with more birefringence.

(a)   (b)
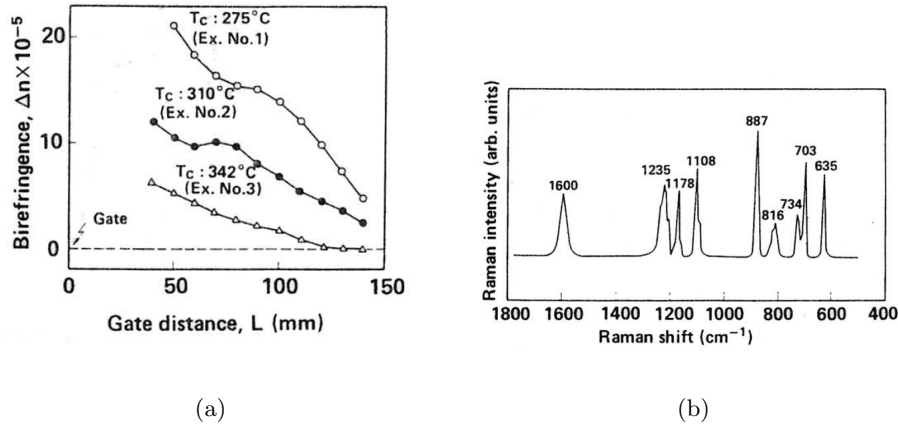
Figure 3.3: *Birefringence, heat shrinkage and polarized laser-Raman spectroscopy results from* [Takeshima, 1986].

Figure 3.4 shows a graphic interpretation of the relative intensity ratio distribution. We identify three zones: a skin zone, a shear zone and a core zone. The skin zone consists of non-oriented molecules. In the core zone, the molecular orientation is considerably relaxed. The shear zone consists of highly oriented molecules. The degree of molecular orientation depends on the molding conditions.
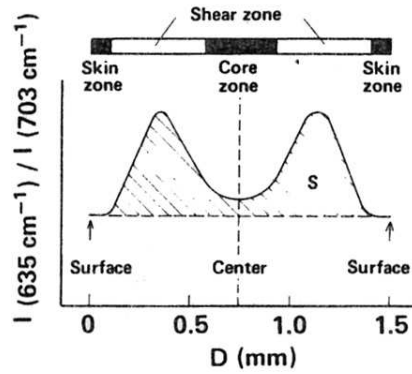
Figure 3.4: *Cross sectional frozen orientation profile* [Takeshima, 1986].

From experimental work, we are able to understand the mechanism of formation of flow-induced stresses in injection molding, as well as to give a qualitative representation of this stresses. The layer in contact with the cold mold wall solidifies rapidly because its cooling rate is very high. Therefore a very thin non-oriented layer is formed as a skin zone. The central layer consists of molecules whose orientation is partly relaxed as a result of annealing because the cooling rate for this layer is lowest. The layer between the skin zone and the core zone consists of highly oriented molecules because it suffers high shear stress due to the solidified skin layer, and the cooling rate is relatively high.

3.1.3   Predicting orientation and flow-induced stresses

One of the first attempts to predict frozen-in orientation and stresses in a quantitative model has been carried out by Tadmor [Tadmor, 1974]. He presented two major sources of orientation in injection molding: the elongational flow at the melt front and the shear flow behind it. He explained the complex orientation distribution using a semi-qualitative model based on macro-molecular theories.

H. Janeschitz [Janeschitz, 1977] derived a simple theoretical description of birefringence in molded parts. Using a temperature dependent Newtonian fluid, he proposed a model for determining the thickness of the frozen layer and he predicted qualitatively the birefringence profiles. These birefringence predictions showed that orientation is introduced not only during filling but also during the post-filling stages of the injection molding process. Dietz and co-workers [Dietz et al., 1978] extended this approach by developing a semi-empirical model for orientation development and relaxation: a linear viscoelastic model was used to describe the non-isothermal stress relaxation after filling. Greener [Greener and Pearson, 1983] followed this same approach but used a viscoelastic equation derived by Marrucci [Marrucci, 1983] to describe the non-isothermal stress relaxation after filling.

A more rigorous model was developed by Isayev [Isayev and Hieber, 1980] using a Leonov constitutive equation during the filling and the cooling stage. The authors described an idealized problem in which a polymer melt at uniform temperature and a fully developed flow between parallel plates have been considered.

Mavridis and colleagues [Mavridis et al., 1988] studied the influence of fountain flow in the frozen-in orientation using the Leonov model.
These models, following the basic paper of Isayev [Isayev and Hieber, 1980] to solve a simplified form of the energy equation. However, the most important limitation of these models is the lack of treatment of the post-filling stage. They all approximate the relaxation of stresses after filling, by the relaxation of stresses upon the cessation of flow. However, due to the density differences in the mold, deformation will still occur until the glass transition temperature is reached. The development and relaxation of stresses during the post-filling stage, when deformation is possible, is totally different from the situation when deformation is prohibited.

Authors like Flaman [Flaman, 1990] and Baaijens [Baaijens, 1991] extended the Leonov model to the compressible case, allowing thus a certain amount of deformation during post-filling.

The Leonov model

The Leonov model [Leonov, 1976] explains the viscoelastic behavior of fluids through a solid mechanics approach. The prime assumption made by Leonov [Leonov, 1976] is that the deformation tensor $\mathbf{F}$ relating the current to the reference configuration can be decomposed in an elastic ($\mathbf{F}_e$) and an irreversible part ($\mathbf{F}_p$), and $\mathbf{F} = \mathbf{F}_e \cdot \mathbf{F}_p$. Secondly, he assumed that the polymer cannot be given a permanent irreversible volume change: $J_p = \det \mathbf{F}_p = 1$ and $J_e = \det \mathbf{F}_e = J$.

To introduce compressibility, Flaman [Flaman, 1990] and Baaijens [Baaijens, 1991], following Simo [Simo, 1987], considered that volumetric changes are separated from the deviatoric responses by the kinematic split

$$\bar{\mathbf{F}}_e = J^{-\frac{1}{3}} \mathbf{F}_e \tag{3.2}$$

They also defined the Finger tensors associated as:

$$\mathbf{B} = \mathbf{F} \cdot \mathbf{F}^T \quad \mathbf{B}_e = \mathbf{F}_e \cdot \mathbf{F}_e^T \quad \bar{\mathbf{B}}_e = \bar{\mathbf{F}}_e \cdot \bar{\mathbf{F}}_e^T \tag{3.3}$$

establishing an evolution equation:

$$\frac{d\bar{\mathbf{B}}_e}{dt} = (\nabla \mathbf{v}_d - \varepsilon(\mathbf{v})_p) \cdot \bar{\mathbf{B}}_e + \bar{\mathbf{B}}_e \cdot (\nabla \mathbf{v}_d^T - \varepsilon(\mathbf{v})_p) \qquad (3.4)$$

where $\nabla \mathbf{v}_d$ is the deviatoric part of the velocity gradient and $\varepsilon(\mathbf{v})_p$ the irreversible part of the strain rate tensor. This last is defined as:

$$\varepsilon(\mathbf{v})_p = \frac{1}{4\theta}(\bar{\mathbf{B}}_e{}^d - \bar{\mathbf{B}}_e{}^{-d}) \qquad (3.5)$$

Thanks to this, the Cauchy stress tensor σ can be split in an elastic part σ_e and an irreversible (plastic) part σ_p. First the elastic stresses are defined, then the irreversible part is given:

$$\sigma = \sigma_e + \sigma_p = -p\mathbf{I} + Gt\bar{B}_e^d + 2\eta\varepsilon(\mathbf{v})^d \qquad (3.6)$$

A thermorheological simple behavior was often assumed, implying that $G = \frac{T}{T_0}G_0$, $\theta = a_T\theta_{ref}$ and $\eta = a_T\eta_{ref}$, where a_T is the shift factor and $()_{ref}$ is the reference value at the reference temperature T_{ref}. Baaijens [Baaijens, 1991] considers that the shift factor is governed by the WLF equation at $T \geq T_g$ while below T_g, $a_T = a_T(T_g)$. The reason for this last choice is that below T_g relaxation processes are extremely slow, hence they take place a time scale beyond current interest.

The author [Baaijens, 1991] considered also a viscoelastic model for the solidified state, supposing that deformations and rotations are small [Baaijens, 1991], and reducing the compressible Leonov model to a linear Maxwell model.

Numerical results

Using this approach for the liquid phase, Flaman [Flaman, 1990] analyzed numerically the buildup and the relaxation of molecular orientation throughout the injection molding process of a plate. Stresses calculated with the model were coupled to birefringence by means of the stress optical rule, and birefringence was used to characterize the molecular orientation. The model was used to investigate the influence of the processing conditions, the mold elasticity, and the pressure dependence of the material on the pressure and birefringence profiles.

During the filling stage, the shear rate and the velocity decrease with increasing time in the vicinity of the wall during mold cooling, resulting in the stress profiles shown in figure 3.5. The normal stress increases from the channel center to the wall until a maximum is reached. Then it decreases again, and the major part of the stress in this region is frozen in. The shear stress is linear in z. Just after filling, when the system changes to the packing stage, it results in a small increase of the normal stress and the shear stress. Then, they relax in the regions where the temperature is still high enough. The stresses at t_6 are the final frozen-in stresses, which also determine the final frozen-in birefringence.

The author [Flaman, 1990] also studied the influence of the processing conditions and material parameters in the frozen-in birefringence (figure 3.6). Generally, the residual birefringence profiles show that, like the stress profiles, there exists a maximum near the surface, zero values at the centerline and significant values in the intermediate zone, which under special conditions change into a second maximum. Figure 3.6(a) shows that the lowest flow rate results in the highest birefringence levels, and the maximum at the wall moves in with decreasing flow rate. Figure 3.6(b) shows that the birefringence level decreases with an increasing melt temperature, leading to more relaxation during the post-filling stage. The influence of mold temperature and packing pressure are not very pronounced (figures 3.6(c) and 3.6(d)).

(a)   (b)
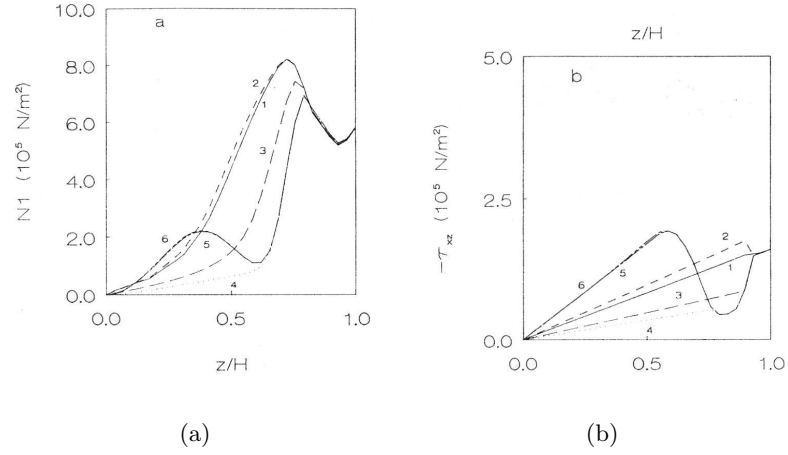
Figure 3.5: *Stresses through the thickness at different instants of the process; z is the half-thickness direction, 1-2 correspond to the filling stage, 3-4 correspond to the packing stage, 5-6 are predictions at the ejection time [Flaman, 1990].*
(a) First normal stress difference through the half-thickness
(b) Shear stress through the half-thickness

(a)   (b)   (c)   (d)
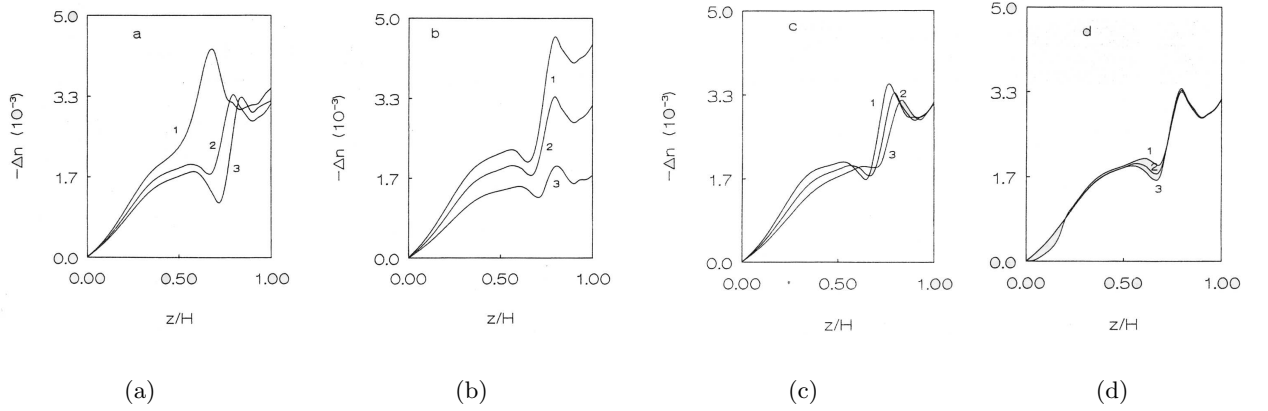
Figure 3.6: *Birefringence index; z is the half-thickness direction, 1-3 correspond to different injection conditions [Flaman, 1990]*
(a) Influence of the flow rate Q, with $Q_1 < Q_2 < Q_3$
(b) Influence of the injection temperature, with $T_1 < T_2 < T_3$
(c) Influence of the packing pressure, with $P_1 < P_2 < P_3$
(d) Influence of the mold temperature, with $T_{m_1} < T_{m_2} < T_{m_3}$

Later, Baaijens [Baaijens, 1991] applied the model described previously to stress computation in a polycarbonate plate. Computation was performed for a section of the plate (representing flow direction versus half-thickness). Figure 3.7 shows the evolution of the first normal stress difference N_1 at 5 successive time steps: at the end of the filling stage $t = 0.67s$, at the end of the packing stage $t = 0.71s$, and at $t = 2.7s$, $t = 3.2s$ and $t = 4.7s$. During the packing stage, most of the flow-induced normal stresses relax because the flow rate is low and the temperature at the core of the cavity is still quite high. This does not apply to regions close to the walls, because there the temperature has dropped below the glass transition temperature and relaxation has virtually stopped. During the post-filling stage shear rates are several orders of magnitude smaller than in the filling stage. However, due to the decreasing temperature as time proceeds , small shear rates may still introduce considerable normal stresses as demonstrated in figures 3.7(b) to 3.7(e). After about $t = 2.5s$ the first normal stress difference attains a very high value, indicating that packing times should be limited if minimal residual birefringence is required.

Figure 3.7 shows the evolution of the principal stress σ_1. Note that its value is positive at the edge, negative near the edge and positive in the core. This stress distribution is markedly different from what is found in free quench experiments. The difference is due to the pressure evolution in the molten part of the product: solidification takes place at elevated temperatures.
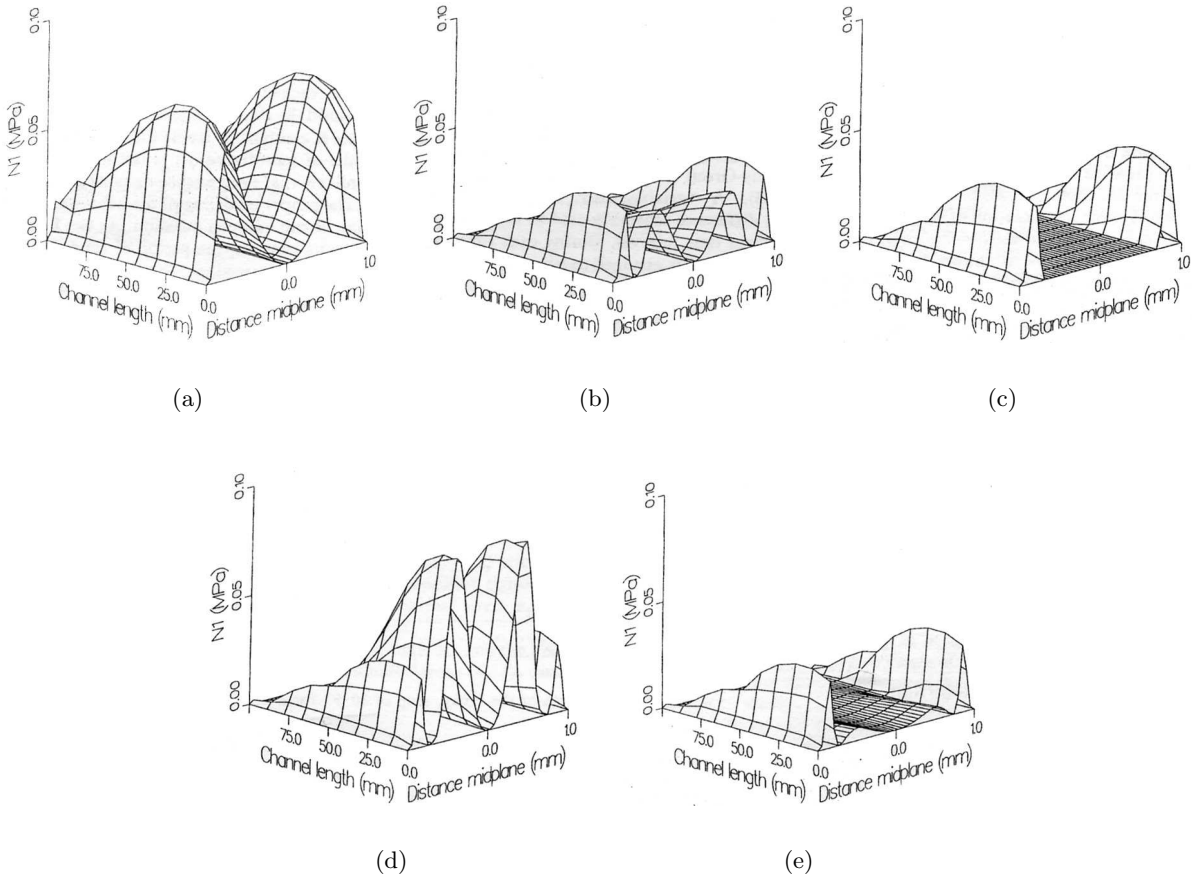
Figure 3.7: *Evolution of the first normal stress difference N_1 at 5 successive time steps: (a) at the end of the filling stage $t = 0.67s$, (b) at the end of the packing stage $t = 0.71s$, and (c) at $t = 2.7s$, (d) at $t = 3.2s$ and (e) at $t = 4.7s$. "Channel length" is the flow length direction, whereas "Distance" is the half-thickness direction [Baaijens, 1991].*

More recently, Kim and co-workers [Kim et al., 1999] used also the Leonov model to describe experimental data of birefringence distribution along the thickness in center-gated polystyrene disks. In the same way, other authors [Shyu et al., 2003] developed a numerical simulation program based on $2D^{1/2}$ finite elements to study the distribution of birefringence in a center-gated disk, considering all three stages of injection molding. The results of numerical simulation were compared with experimental data, for the injection of an optical disk. Figure 3.8 shows the predicted transient development of the first normal stress difference in the filling and packing stages through the part thickness in a cross-section sample:

- during <u>filling</u> stage, the first normal stress difference increases with time with a <u>maximum birefringence index</u> near the surface (but not at the surface) due to the development of a frozen layer, frozen-in stresses that remain through the process;

- during the <u>packing stage</u>, the <u>stresses near</u> the midplane of the disk relax quickly since the flow is very small and the temperature is still high;

- later, when the temperature becomes low and the <u>relaxation time increases</u>, the <u>stresses</u> <u>near the midplane grow again</u> although the flow becomes smaller. We remark that the normal stresses near the cavity wall do not change during the packing stage since the temperature near the wall is lower and the stresses have long been frozen.

The authors studied also the spatial distribution of the birefringence. Figure 3.9 shows the birefringence distribution in the half-thickness at different radial positions at the end of filling and at the end of packing. For all the cross sections analyzed (we observed a similar pattern), with an increase of the birefringence value with the flow length, as observed experimentally by Takeshima [Takeshima and Funakoshi, 2001].

Predicted and measured birefringence at the end of cooling are given in figure 3.10, showing a good agreement between the numerical and experimental results. Differences near the surface may be related with the inaccuracy in shift factors for viscosity and relaxation time at low temperatures.

(a)   (b)
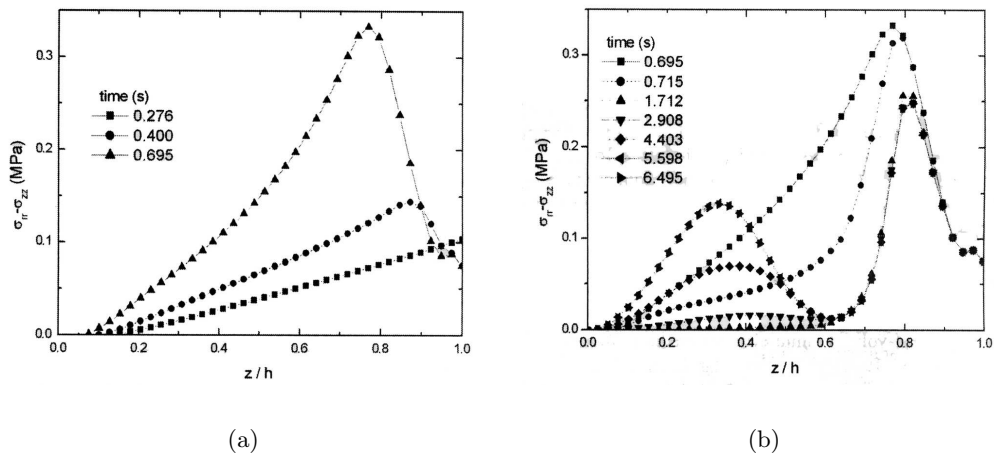
Figure 3.8: *Predicted distributions of the first normal stress difference at different instants of the a) filling and b) post-filling stages for a given radial coordinate* [Shyu, 2003].
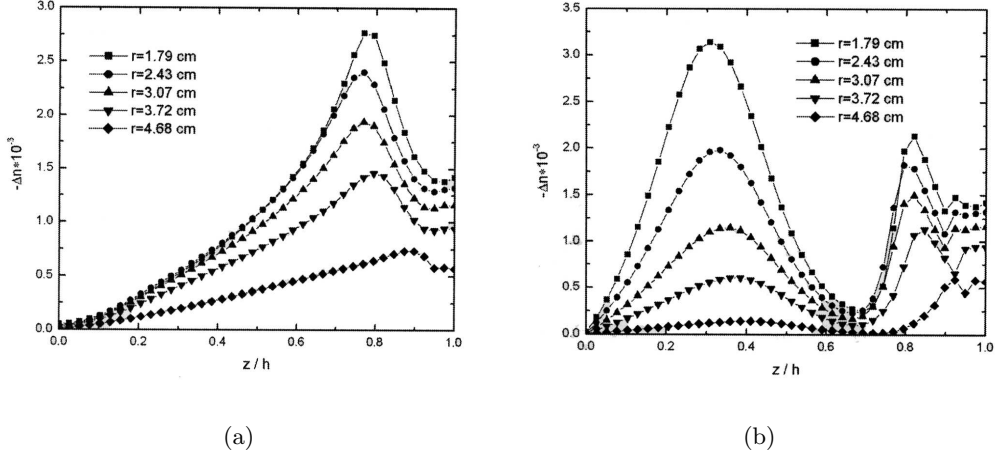
Figure 3.9: *Predicted gapwise distribution of birefringence* Δn *at various radial positions at a) the end of filling and b) the end of packing* [Shyu, 2003].
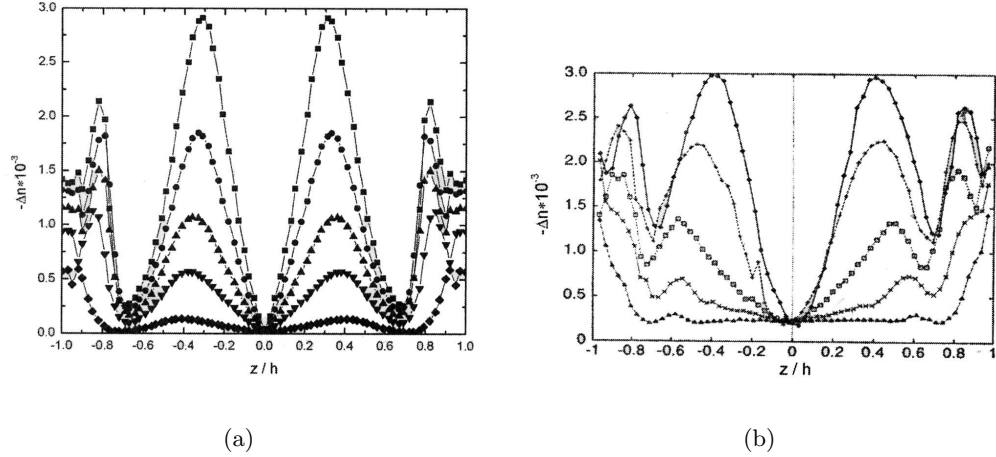
Figure 3.10: *Distribution of birefringence* Δn *at various radial positions at the end of cooling: a) numerical and b) experimental* [Shyu, 2003].

More recently, Pantani and co-workers [Pantani et al., 2004] analyzed the same problem of orientation evolution by applying a simple non-linear dumbbell model, with thermal, pressure and shear rate dependent relaxation times. The authors gathered detailed measurement results, including material characterization, a thorough description of experimental conditions, mold and nozzle geometry. They measured pressure curves, orientation and strain distributions in molded samples.

Simulation results in terms of an orientation parameter ϕ (maximum eingenvalue of the orientation tensor), for the injection molding of a plaque, are compared with final thickness birefringence distributions in the gate and at different positions inside the cavity at the end of cooling (figure 3.11). We remark that the orientation decreases along the flow direction as the distance from the gate increases, with a peak near the wall.
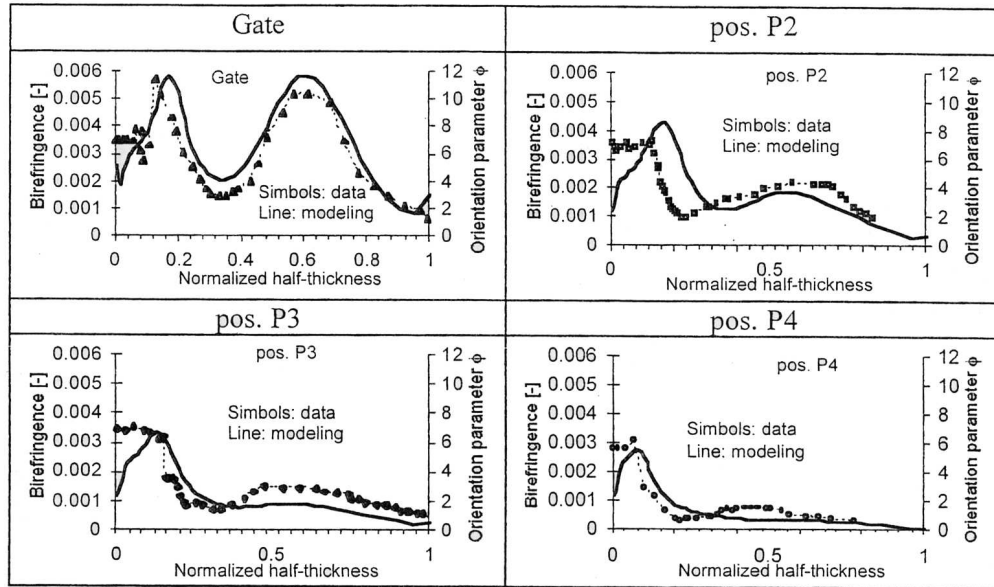
Figure 3.11: *Comparison between predicted distribution of orientation and birefringence measurements at the end of cooling; P4 is the farthest point from the gate[Pantani, 2004].*

3.1.4 Conclusion

Knowledge of residual stresses is essential to predict dimensional and shape accuracies in an injection molded part. Basically, there are two main sources of residual stresses. Firstly, due to the <u>viscoelastic</u> nature of polymers, normal stresses develop during filling and packing/holding stages, usually these <u>flow-induced stresses</u> are relatively small. However, they give rise to large molecular orientations which affect the mechanical and optical behavior of the part. They also influence differences in the shrinkage behavior in directions perpendicular and parallel to the flow direction. The second cause of residual stresses is the rapid increase in rigidity of the material as it passes through the glass transition point. Across the molded part thickness, a highly non-uniform temperature distribution exists. Consequently, each material point solidifies at a different time, leading to differential shrinkage causing thermally induced stresses.

From experimental and previous simulation work, we are able to understand the mechanism of formation of flow-induced stresses in injection molding, as well as to give a qualitative representation of this stresses:
- during <u>filling</u>, the layer in contact with the cold mold wall solidifies rapidly because its cooling rate is very high, but near the surface the molecules are highly oriented due to the high shear rate. In the central layer molecules do not orient since there is no shear rate;
- at the <u>end of filling</u> the molecular orientation relaxes quickly since the flow is very small and the temperature is still high;
- during <u>packing</u> when the temperature becomes low, molecular orientation near the midplane may grow again;
- at the <u>end of cooling</u> very few stresses were relaxed (the relaxation times increase beyond the process scope) and will cause shrinkage and deformation once the part ejected.

We focus on the formation of flow-induced stresses, through the implementation of a viscoelastic material model in **REM3D**.

3.2   Polymer viscoelasticity and viscoelastic models

A great number of viscoelastic models attempt to describe the polymer behavior under all types of solicitation. This description can be done using:

- models obtained from <u>continuum mechanics</u>;

- models obtained from <u>molecular dynamics</u>.

under differential or integral forms. In the first case, the viscoelastic fluid is supposed to have several relaxation times (multimodes) and the extra-stress tensor is an additive composition of all the modes, following each mode an evolution equation on this tensor. Models issued from continuum mechanics are the Maxwell model, the White-Metzner model, the Giesekus model or the PTT model. Nevertheless, these models fail in describing polymers's non-linear behavior, that appears under quick solicitations (high frequencies) or solicitations of great amplitude. It is described by the dependance of the material's response to the amplitude, the rate and the kinetics of the imposed deformation. The main reason for this failure is the fact that they do not take into account that under deformation, there is topological interaction between polymer chains. To consider these interactions, molecular dynamics models were derived. Since in injection molding, polymer flow runs from strong elongation to strong shear, we are particularly interested in the use of a model of this type.

Different molecular approaches correspond to different levels of abstraction (figure 3.12), at five main scales. We underline three main scales: a coarse scale where viscoelasticity is represented by evolution of molecular chain orientation during deformation (linear dumbbell models, represented by 2); a multi-bead chain (for example the non-linear FENE model, illustrated in 3); interaction between chains and possibility of entanglements (for example the Pom-Pom model, schematic representation of a molecule in 4).
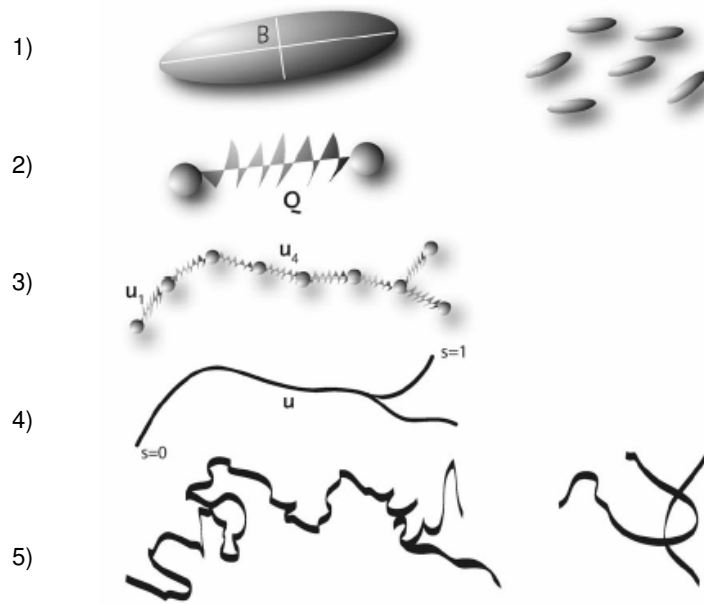
Figure 3.12: *Microscopic models for complex fluids with increasing degree of abstraction and decreasing degrees of freedom (bottom to top) : 5) atomistically detailed polymer which accounts for anisotropic intermolecular interactions, including entanglements 4) coarse grained model via a mapping to a "primitive path" (or tube) 3) further approximated by a multibead chain 2) further coarse grained to a dumbbell which accounts for entropic elasticity and orientation but not for entanglement effects 1) ellipsoids of revolution with spherical or mean field interaction [Kroger, 2004].*

Evolution laws describing the viscoelastic behavior through molecular models derive all from the tube theory, introduced by P.G. de Gennes [Gennes, 1970]. The first model based on this theory is the Doi and Edwards model [Doi and Edwards, 1986], that considers the flow behavior of monodisperse linear polymers. G. Marrucci [Marrucci, 1985] and J. des Cloizeaux [des Cloizeaux, 1989] extended the Doi and Edwards model to polydisperse linear polymers. Finally, the Pom-Pom model [McLeish and Larson, 1998], considers branched polymers. In the last five years different forms of the Pom-Pom model, as well as other models based on orientation and chain stretch evolution. Other authors presented different forms for this tensor, leading to the models: eXtended Pom-Pom XPP (SXPP et DXPP) [Verbeeten et al., 2002], Improved Pom-Pom IPP (DIPP et SIPP) [Ottinger, 2001], Convected Pom-Pom CPP (DCPP) [Clemeur et al., 2002], with shear modification [Bourrigaud et al., 2003]. Model development in Non-Newtonian Fluid Mechanics rests an active area of research.

It is important to take into account for polymer's viscoelastic behavior during injection molding. As we have seen previously, molecular orientation and stresses rest frozen-in the part when it solidifies, inducing anisotropic shrinkage and deformation. To accurately compute this molecular frozen orientation, we use a constitutive law for the stress tensor given by molecular dynamics, considering also possible interaction between chains, entanglements and stretch.

Reptation models [Gennes, 1970],[Doi and Edwards, 1986] consider a constraint limiting the chain's motion due to their environment, represented by a diffusion phenomena in one-dimension along a tube defined by the chain environment and which dimensions (length L and diameter a) are fixed throughout time. To move over large distances, the chain leaves the tube by means of longitudinal motions. Leaving the tube, the chain creates thus a new piece of tube and at the same time destroys part of the tube on the other side. This kind of motion is called reptation. The extra-stress tensor was defined by Doi and Edwards as:

$$\sigma(t) = -p'\mathbf{I} + G \int_{-\infty}^{t} m(t;t')\mathbf{Q}(t;t')\,dt' \tag{3.7}$$

where p' is a pressure, $\mathbf{I}$ is the identity tensor, G is the relaxation modulus, and $m(t;t')$ is a memory function that weights the contribution of the past deformations by $\mathbf{Q}$. The tensor $\mathbf{Q}$ denotes an orientation tensor at time t that measures the average orientation of the tube segments with respect to a reference time t' in the past, given by:

$$\mathbf{Q}(t;t') = \frac{1}{\langle|\mathbf{F}\cdot\mathbf{p}|\rangle}\langle\frac{(\mathbf{F}\cdot\mathbf{p})(\mathbf{F}\cdot\mathbf{p})}{|\mathbf{F}\cdot\mathbf{p}|}\rangle \tag{3.8}$$

where the unit vector $\mathbf{p}$ represents the orientation of a tube segment, the brackets denote the averaging operator, and $\mathbf{F}$ is the deformation gradient. Nevertheless, the Doi and Edwards model does not take into account important phenomena, like for example, the deformation of the tube, underestimating the polymer behavior under strong deformations. The model needs to take into account the fact that the chain is in evolution in a mobile environment, and the influence of this environment is done through a variation of the stress field that involves the chain, and therefore by altering the tube inside the chain that is moving. Furthermore, chain topology may be of great importance: the existence of entanglements allow stretching not taken into account with classical reptation models.

3.2.1 The Pom-Pom model and why?

McLeish and Larson [McLeish and Larson, 1998] considered a viscoelastic polymer melt like a melt of identical molecules with a very simple branching structure. It consists of two-identical q-armed stars, connected by a backbone section (figure 3.13). They supposed that the backbone section is inside a tube (like all reptation models) and each branch (or arm) is considered to be also inside a tube. We observe that diffusion of the gravity center of the main chain by reptation implies the penetration of the lateral arms inside the main chain tube. They suggested that for branched polymers, relaxation is no longer dominated by the reptation of the main chain, but by the relaxation of the lateral branches, according to a mechanism of activated relaxation.
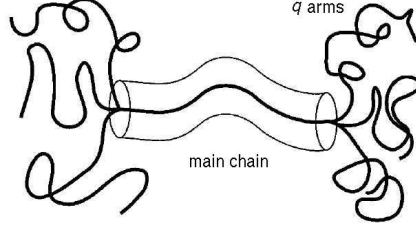
Figure 3.13: *Pom-Pom molecule.*

The molecular model characteristics are: the molecular weight of the backbone, M_b, the molecular weight of the arms, M_a, and the number of arms q. Relaxation dynamics of this molecule is done in three steps: there is *chain stretch* inside the tube, as the entanglement points at the chain ends limit its reptation; then, there is *arm reptation* in their own tube; and finally *chain reptation* is allowed, when the chain has been enough stretched, and arms penetrate inside the backbone tube.

All three relaxation mechanisms have an associated relaxation time: orientation of the backbone tube (orientation relaxation time, θ_b), stretch of the tube (stretch relaxation time θ_s), and penetration of the arms inside the tube (arm relaxation time θ_q). Orientation and stretch relaxation times are function of molecular model characteristics (molecular weights and number of arms), whereas arm relaxation is also function of the amount of arm that penetrates the tube. We may note that the stretch relaxation time is shorter than the orientation one, but longer than the longest arm relaxation time ($\theta_a < \theta_s < \theta_b$).

The polymer molecular configuration at each time step is described by three dynamical variables: tube orientation $\mathbf{s}$, tube stretch λ and arm penetration s_c.

- The tensor $\mathbf{s} = \langle \mathbf{pp} \rangle$ describes the average distribution of backbone tube *orientation*, where $\mathbf{p}$ is a unit vector parallel to a tube segment (similar to the Doi and Edwards model). McLeish and Larson proposed the following differential approximation:

$$\mathbf{s} = \frac{\mathbf{A}}{\text{tr}(\mathbf{A})} \quad \text{and} \quad \frac{\partial \mathbf{A}}{\partial t} + \mathbf{v} \cdot \nabla \mathbf{A} - \nabla \mathbf{v} \cdot \mathbf{A} - \mathbf{A} \cdot \nabla \mathbf{v}^T + \frac{1}{\theta_b}\left(\mathbf{A} - \frac{\mathbf{I}}{3}\right) = 0 \qquad (3.9)$$

In these equations, $\mathbf{A}$ is an auxiliary tensor, and $\text{tr}(\mathbf{A})$ its first invariant of A, defined as the trace of the tensor. It may be re-written in one only equation, in terms of $\mathbf{s}$,

$$\frac{\partial \mathbf{s}}{\partial t} + \mathbf{v} \cdot \nabla \mathbf{s} - \nabla \mathbf{v} \cdot \mathbf{s} - \mathbf{s} \cdot \nabla \mathbf{v}^T + 2[\varepsilon(\mathbf{v}) : \mathbf{s}]\mathbf{s} + \frac{1}{\theta_b I_A}\left(\mathbf{s} - \frac{\mathbf{I}}{3}\right) = 0 \qquad (3.10)$$

- The *stretch* λ is equal to the length of tube occupied by the backbone divided by the equilibrium length. Extension of the chain is not infinite but is limited by the stress generated by the side arms. In addition to the orientation evolution equation, there is one for the backbone extension λ:

$$\frac{\partial \lambda}{\partial t} + \mathbf{v} \cdot \nabla \lambda - \lambda[\varepsilon(\mathbf{v}) : \mathbf{s}] + \frac{1}{\theta_s}(\lambda - 1) = 0 \quad \text{if} \quad \lambda < q \qquad (3.11)$$

- The *length* of the arms drawn into the backbone tube, s_c, complements λ, since they do not vary at the same time. Actually, s_c is zero while $\lambda < q$ and varies once λ has reached the number of arms q, according to the evolution equation:

$$\frac{\partial s_c}{\partial t} + \mathbf{v}\,\nabla s_c = (q\frac{s_b}{2} + s_c)\left[\varepsilon(\mathbf{v}) : \mathbf{s}\right] - \frac{1}{2\theta_a} \quad \text{and} \quad \lambda = q \tag{3.12}$$

  If $\lambda = q$ and $s_c > 0$, the s_c must first relax back to zero before λ can relax.

The total stress, σ is given by (using a simplified notation):

$$\sigma = -p'\mathbf{I} + G(3\lambda^2 + f(s_c))\mathbf{s} \tag{3.13}$$

where G is the relaxation modulus, and $f(s_c)$ is a function of the length of penetration (for more details, see [McLeish and Larson, 1998]).

Model simplifications, advantages, disadvantages and solutions

Despite the achievement of this model, it seams to suffer from a number of mathematical and rheological defects.

First of all, concerning equation 3.9, which governs the tensor A, two critical features are found [Verbeeten et al., 2002]:

- the tensor $\mathbf{A}$ obeys an equation of Maxwellian type. Analytically, a flow problem involving such an equation is well posed under appropriate initial and boundary conditions. However, its numerical treatment may be corrupted by the growth and propagation of numerical oscillations in the vicinity of geometrical singularities;

- the loss of positive-definiteness of $\mathbf{A}$ by successive approximations in a numerical scheme (negative $\mathrm{tr}(\mathbf{A})$) introduces a singular behavior.

The equation in orientation $\mathbf{s}$ may be considered (equation 3.10), even though this latest doesn't have similar asymptotic forms in extension and shear as the integral version, contrary to the equation in $\mathbf{A}$.

Secondly, the stretch λ exhibits features that may hinder a proper treatment, analytically as well as numerically. The associated condition ($\lambda \leq q$) gives to equation (3.11) the attributes of a differential inequality, inducing in an Eulerian scheme a systematic treatment involving sequences of growth and decrease in λ. Blackwell and co-workers [Blackwell et al., 2000] introduced the notion local branch point displacement, a modification of the stretch relaxation time to account for arm penetration, needing no longer to calculate the amount of arm withdrawal s_c. Using this approach, our stretch relaxation time will be:

$$\theta_s = \theta_{0s} \exp\left[-\nu(\lambda - 1)\right] \tag{3.14}$$

In this equation, θ_{0s} is the original relaxation time for the stretch and ν a parameter which is taken to be $2/q$. Alternatively, ν can also be seen as a measure of the influence of the surrounding polymer chains on the backbone tube stretch.

Finally, in what concerns equation 3.13, it is simplified to:

$$\sigma = -p'\mathbf{I} + 3G\lambda^2\mathbf{s} \tag{3.15}$$

However, in static conditions, the extra-stress tensor is not zero, but proportional to a isotropic tensor ($\frac{\mathbf{I}}{3}$), which means that the pressure p' obtained is not the hydrostatic pressure. Therefore, the expression used by [Verbeeten et al., 2002] is also considered here:

$$\sigma = -p\mathbf{I} + G(3\lambda^2\mathbf{s} - \mathbf{I}) \tag{3.16}$$

In addition, we also include a small solvent viscosity, η_s, associated with lower molecular weight material behavior, so that the total stress is finally given by the constitutive equation

$$\sigma = -p\mathbf{I} + 2\eta_s\varepsilon(\mathbf{v}) + G(3\lambda^2\mathbf{s} - \mathbf{I}) \tag{3.17}$$

for a one-mode fluid.

Multi-mode Pom-Pom model

Initially, the Pom-Pom model describes the effect of an imposed deformation on a melt with identical Pom-Pom molecules. Such a model can only be applied to monodisperse polymers. Inkson [Inkson et al., 1999] generalized the approach of McLeish and Larson, considering industrial polymers. They proposed the multi-mode Pom-Pom model. Therefore, accounting for the complex structure of the commercial polymers, the multi-mode model is based on a superposition of Pom-Pom molecules not coupled between themselves, which are characterized by different relaxation times, and different number of arms. The stress is obtained by adding the contribution of each Pom-Pom molecule:

$$\sigma = -p\mathbf{I} + 2\eta_s\varepsilon(\mathbf{v}) + \sum_{i=1}^{m} G_i(3\lambda_i^2\mathbf{s}_i - \mathbf{I}) \tag{3.18}$$

where m is the number of modes.

As a conclusion:

> *To take into account viscoelasticity and orientation effects, we restrain ourselves to a basic form of the multi-mode Pom-Pom model:*
> *- the extra-stress tensor is an additive composition of each mode:*
>
> $$\tau = \sum_{i=1}^{m} \tau_i(\mathbf{s}_i, \lambda_i)$$
>
> *where each extra-stress tensor is function the molecular orientation and stretch distributions*
>
> $$\tau_i = G_i(3\lambda_i^2\mathbf{s}_i - \mathbf{I})$$
>
> *- orientation is determined by solving*
>
> $$\frac{\partial \mathbf{s}_i}{\partial t} + \boldsymbol{v}\cdot\nabla\mathbf{s}_i - [\nabla\boldsymbol{v}\mathbf{s}_i + \mathbf{s}_i\nabla\boldsymbol{v}^T] + 2[\mathbf{s}:\varepsilon(\boldsymbol{v})]\mathbf{s}_i + \frac{1}{\theta_b}(\mathbf{s}_i - \frac{\mathbf{I}}{3}) = 0$$
>
> *- stretch is solution of another evolution equation, where branch point displacement has been introduced*
>
> $$\frac{\partial \lambda_i}{\partial t} + \boldsymbol{v}\cdot\nabla\lambda_i - \lambda_i[\varepsilon(\boldsymbol{v}):\mathbf{s}_i] + \frac{1}{\theta_{si}}(\lambda-1) = 0 \ \textit{with} \ \theta_{si} = \theta_{0si}\exp\left[-\frac{2}{q}(\lambda_i - 1)\right]$$
>
> *The material parameters are the relaxation modulus G, the orientation relaxation time θ_b, the stretch relaxation time θ_{0s}, and the number of arms q (of each mode).*

To summarize: from the evolution equations for orientation and stretch we can determine the extra-stress due to elasticity of the material. Next section will focus on the numerical resolution of these evolution equations and their coupling with flow computation.

3.3   Isothermal viscoelasticity

Computational methods used for viscoelastic flows, and in particular with free surfaces, have been studied for about 30 years and mainly applied to the contraction flow, or die swell or filament stretching problems [Tanner, 1970],[Crochet and Keunings, 1982],[Keunings, 1986],[Keunings and Bousfield, 1987], [Cormenzana et al., 2001]. They remain an active area of research , ([Baaijens, 1998] gives a review of several methods to solve the equations derived for such flows). Most of the techniques are based on differential constitutive equations, because they are easier to implement and require more "standard" numerical methods.

It is not our purpose to develop new numerical techniques to treat viscoelastic flows. We rather adapted the ones described previously to take into account a viscoelastic behavior. Thus, we consider a time step marching scheme allowing to split the system in two subsystems made of the viscoelastic constitutive equation and the flow equations. A stabilisation technique similar to the DEVSS method [Guenette and Fortin, 1995] is used, and the evolution equations are solved through a space-time discontinuous Galerkin technique. We present first a short review on computational methods for viscoelasticity. Next we detail the technique used in our work.

3.3.1   Short review on computational methods used in viscoelastic flow

In the following we consider only one mode. The flows equations are: find $\tau \in \mathcal{C}^2(\Omega)$ and the pressure $p \in \mathcal{C}^1(\Omega)$ such that $\forall (x,t) \in \Omega \times [0,\Theta]$,

$$\begin{cases} -\nabla p + \nabla \cdot \tau = 0 \\ \nabla \cdot \mathbf{v} = 0 \end{cases} \tag{3.19}$$

Since we are dealing with differential models, let us suppose a general form of the evolution equation of the extra-stress tensor [1]:

$$\theta(\frac{d\tau}{dt} - \nabla\mathbf{v}\tau - \tau\nabla\mathbf{v}^T) + f(\tau, \varepsilon(\mathbf{v})) = 2\eta_e\varepsilon(\mathbf{v}) \tag{3.20}$$

where θ is the extra-stress relaxation time, $\eta_e = G\theta$ an "elastic" viscosity, and $f(\tau, \varepsilon(\mathbf{v}))$ a function dependent on the constitutive equation.

Mixed methods

The mixed formulation of the isothermal incompressible viscoelastic flow problem used by Marchal and Crochet [Marchal and Crochet, 1987] is a natural extension of the velocity-pressure problem: *find* $(\boldsymbol{v}, p, \tau) \in \mathcal{V} \times \mathcal{P} \times \mathcal{S}$ *such that*

$$\begin{cases} \int_\Omega \mathbf{w} \cdot (-\nabla p + \nabla \cdot \tau) = 0 \\ \int_\Omega q\nabla \cdot \mathbf{v} = 0 \\ \int_\Omega \phi[\theta(\frac{d\tau}{dt} - \nabla\mathbf{v}\tau - \tau\nabla\mathbf{v}^T) + f(\tau, \varepsilon(\mathbf{v})) - 2\eta_e\varepsilon(\mathbf{v})] = 0 \end{cases} \tag{3.21}$$

The authors introduced finite element spaces $(\mathcal{V}_h, \mathcal{P}_h, \mathcal{S}_h)$ for the 3-field problem that respect the inf-sup condition on $(\mathbf{v}_h, p_h)$ and $(\mathbf{v}_h, \tau_h)$. To treat the convective term in the constitutive equation, the SU (Streamline Upwind) method was used. The main problems associated to this mixed form is that a solvent viscosity needs to be introduced (to give an elliptic contribution to the system) and it gets computationally prohibitive for elements with higher interpolation order.

---

[1]This equation can also describe the evolution of other model variables, such as orientation or chain stretch.

E.V.S.S. (Elastic Viscous Stress Splitting)

One way to overcome the absence of a viscous term is a change of variable, also known as the E.V.S.S. formulation [Beris and Edwards, 1994]. Basically, we replace the extra-stress τ by Σ:

$$\Sigma = \tau - 2\eta_s\varepsilon(\mathbf{v}) \tag{3.22}$$

where η_s is a solvent viscosity. This is equivalent to a decomposition of the extra-stress in a purely viscous $(2\eta_s\varepsilon(\mathbf{v}))$ and a viscoelastic (Σ) parts. We are led to a system of the type: *find* $(\boldsymbol{v}, p, \Sigma) \in \mathcal{V} \times \mathcal{P} \times \mathcal{S}$ *such that*

$$\begin{cases} \int_{\Omega} \mathbf{w} \cdot (-\nabla p + 2\eta_s\nabla\cdot\varepsilon(\mathbf{v}) + \nabla\cdot\Sigma) = 0 \\ \int_{\Omega} q\nabla\cdot\mathbf{v} = 0 \\ \int_{\Omega} \phi\theta(\frac{d\Sigma}{dt} - \nabla\mathbf{v}\Sigma - \Sigma\nabla\mathbf{v}^T) + f(\Sigma, \varepsilon(\mathbf{v})) - 2\eta_e\theta(\frac{d\varepsilon(\mathbf{v})}{dt} - \nabla\mathbf{v}\varepsilon(\mathbf{v}) - \varepsilon(\mathbf{v})\nabla\mathbf{v}^T) = 0 \end{cases} \tag{3.23}$$

Unfortunately, this change of variables does not yield a closed expression for every constitutive equation. Furthermore, depending on the constitutive law, a convective derivative of the strain rate tensor may arise, requiring a third order derivative of the velocity field. To circumvent this problem Rajagopalam and co-workers [Rajagopalam et al., 1990], considered the strain rate tensor as a separate unknown, obtained by an L2-projection of the velocity gradient, whereas [Szadi et al., 1995] developed the EVSS-G/DG methods, computing instead of the strain rate tensor, a velocity gradient field in the same space as Σ. The authors used also a Discontinuous Galerkin technique rather than Streamline Upwind (SU).

D.E.V.S.S. (Discrete Elastic Viscous Stress Splitting)

[Guenette and Fortin, 1995] introduced a modification of the EVSS formulation, known as the Discrete EVSS method (D.E.V.S.S.). Basically, a stabilizing elliptic operator is introduced in the discrete version of the momentum equation, avoiding the use of the objective derivative of the strain rate tensor. The change of variable is done by:

$$\Sigma = \tau - 2\eta_{stab}\varepsilon(\mathbf{v}) \tag{3.24}$$

where η_{stab} is an arbitrary viscosity to be chosen. If the stabilising viscosity is chosen as the solvent viscosity, the problem is: *find* $(\boldsymbol{v}, p, \tau, \mathbf{H}) \in \mathcal{V} \times \mathcal{P} \times \mathcal{S} \times \mathcal{H}$ *such that*

$$\begin{cases} \int_{\Omega} \mathbf{w}[-\nabla p + \nabla\cdot\tau + \nabla\cdot(2\eta_{stab}\varepsilon(\mathbf{v})) - \nabla\cdot(2\eta_{stab}\mathbf{H})] = 0 \\ \int_{\Omega} q\nabla\cdot\mathbf{v} = 0 \\ \int_{\Omega} \phi\theta(\frac{d\tau}{dt} - \nabla\mathbf{v}\tau - \tau\nabla\mathbf{v}^T) + f(\tau, \varepsilon(\mathbf{v})) - 2\eta_e\varepsilon(\mathbf{v}) = 0 \\ \int_{\Omega} \Phi(\mathbf{H} - \varepsilon(\mathbf{v})) = 0 \end{cases} \tag{3.25}$$

An elliptic operator $(2\eta_{stab}(\varepsilon(\mathbf{v}) - \mathbf{H}))$ is introduced where $\mathbf{H}$ is a discrete approximation of the strain rate tensor $\varepsilon(\mathbf{v})$. In analogy with the EVSS-G method, the DEVSS-G method may be defined, where a projection of the velocity gradient is made instead of the strain rate tensor [Baaijens et al., 1998]. All these methods may be coupled to SU, SUPG or DG strategies. Furthermore, Sun [Sun et al., 1996] proposed an Adaptative version of the DEVSS method by choosing η_{stab} in such a way that the elastic

and viscous contributions are of the same amplitude, like in [Bogaerds et al., 1999].

In our case, we will follow a classical mixed formulation of the problem on $(\boldsymbol{v}, p, \tau)$, or $(\boldsymbol{v}, p, \mathbf{s}, \lambda)$. Through a splitting technique, we decouple flow equations from constitutive evolution laws. In what concerns the flow equations, we will show in the following that the choice of the P1+/P1 element for the velocity-pressure problem gives rise to a bubble stabilisation technique similar to the D.E.V.S.S. method. Resolution of the evolution equations through the space-time discontinuous Galerkin method is also detailed.

3.3.2 Numerical resolution of the flow equations and stabilization

We remind that for the isothermal incompressible one-mode fluid, the Cauchy stress tensor is defined as:

$$\sigma = -p\mathbf{I} + 2\eta_s \varepsilon(\mathbf{v}) + \tau = -p\mathbf{I} + 2\eta_s \varepsilon(\mathbf{v}) + G(3\lambda^2 \mathbf{s} - \mathbf{I}) \tag{3.26}$$

The conservation equations to be solved in the whole computational domain are restricted to:

$$
\begin{cases}
\nabla \cdot [2\eta_s \varepsilon(\mathbf{v})] - \nabla p + \nabla \cdot (G(3\lambda^2 \mathbf{s} - \mathbf{I})) = 0 \\[2mm]
\nabla \cdot \mathbf{v} = 0 \\[2mm]
\dfrac{d\mathbf{s}}{dt} - \nabla \mathbf{v} \cdot \mathbf{s} - \mathbf{s} \cdot \nabla \mathbf{v}^T + 2[\varepsilon(\mathbf{v}) : \mathbf{s}]\mathbf{s} + \dfrac{1}{\theta_b}(\mathbf{s} - \dfrac{\mathbf{I}}{3}) = 0 \qquad \text{in } \Omega(t) \times [0, \Theta] \\[2mm]
\dfrac{\partial \lambda}{\partial t} + \mathbf{v} \cdot \nabla \lambda - \lambda[\varepsilon(\mathbf{v}) : \mathbf{s}] + \dfrac{1}{\theta_s}(\lambda - 1) = 0 \\[2mm]
+\text{initial and boundary conditions}
\end{cases}
\tag{3.27}
$$

The weak formulation of our problem is given by considering its product by test functions chosen in adequate spaces, and is thus written as: *find $(\boldsymbol{v}, p, \mathbf{s}, \lambda) \in \mathcal{V} \times \mathcal{P} \times \mathcal{S} \times \mathcal{L}$ such that*

$$
\begin{cases}
\displaystyle\int_\Omega 2\eta_s \varepsilon(\mathbf{v}) : \varepsilon(\mathbf{w}) - \int_\Omega p\nabla \cdot \mathbf{w} + \int_\Omega (G(3\lambda^2 \mathbf{s} - \mathbf{I}) : \varepsilon(\mathbf{w})) = 0 \\[2mm]
\displaystyle\int_\Omega q\nabla \cdot \mathbf{v} = 0 \\[2mm]
\displaystyle\int_\Omega \phi[\dfrac{d\mathbf{s}}{dt} - \nabla \mathbf{v} \cdot \mathbf{s} - \mathbf{s} \cdot \nabla \mathbf{v}^T + 2[\varepsilon(\mathbf{v}) : \mathbf{s}]\mathbf{s} + \dfrac{1}{\theta_b}(\mathbf{s} - \dfrac{\mathbf{I}}{3})] = 0 \\[2mm]
\displaystyle\int_\Omega \varphi[\dfrac{\partial \lambda}{\partial t} + \mathbf{v} \cdot \nabla \lambda - \lambda[\varepsilon(\mathbf{v}) : \mathbf{s}] + \dfrac{1}{\theta_s}(\lambda - 1)] = 0
\end{cases}
\tag{3.28}
$$

$\forall(\mathbf{w}, q, \phi, \varphi) \in \mathcal{V} \times \mathcal{P} \times \mathcal{S} \times \mathcal{L}$, and considering only Dirichlet boundary conditions in velocity. We define the functional spaces of orientation $\mathcal{S}$ and stretch $\mathcal{L}$ as:

$$
\begin{aligned}
\mathcal{S} &= \{\tau \in L^2(\Omega)^{d \times d} \times [0, \Theta] \ , \tau_{ij} = \tau_{ji}\} \\
\mathcal{L} &= \{\lambda \in L^2(\Omega) \times [0, \Theta] \}
\end{aligned}
\tag{3.29}
$$

The spatial discretization, $(\mathbf{v}, p, \mathbf{s}, \lambda)$ must satisfy stability conditions [Marchal and Crochet, 1987]:

- the discrete subspaces of approximation must verify the same Brezzi-Babuska conditions than the Stokes classical formulation (see Chapter 2, equations 2.24 and 2.25);

- a sufficient condition (but not necessary) for satisfying the *inf-sup* condition between $\mathcal{S}_h$ and $\mathbf{v}_h$ is:

$$\mathbf{v}_h \in \mathcal{V} \Longrightarrow \nabla \mathbf{v}_h \in \mathcal{S}_h \tag{3.30}$$

A continuous approximation in velocity and extra-stress does not check generally this last condition. A discontinuous stress and a continuous velocity makes it easily. Since we have chosen a linear approximation for velocity and pressure with bubble enrichment for velocity, the $P1 + /P1$ element, described in the previous chapter, a discontinuous approximation for the extra-stresses is added. Approximation subspaces for orientation ($\mathcal{S}_h$) and stretch ($\mathcal{L}_h$) are defined discontinuous and piecewise constant per element:

$$
\begin{aligned}
\mathcal{S}_h &= \{\tau_h \in L^2(\Omega)^{3\times 3}, \tau_h \in \text{P0}(K)^{d\times d}\} \\
\mathcal{L}_h &= \{\lambda_h \in L^2(\Omega), \lambda_h \in \text{P0}(K)\}
\end{aligned}
\tag{3.31}
$$

The system is highly non linear. Therefore, the problem is solved by splitting the system in two sub-systems : knowing the configuration of our computational domain (orientation distribution and stretch) we solve conservation equations; then, knowing $\mathbf{v}$ and p, we calculate $\mathbf{s}$ and λ. The global problem, with a large number of unknowns, and therefore large-consuming memory, is broken up into smaller systems: a Stokes system augmented with an elastic term, and the non-linear evolution equations that allow the determination of τ. Furthermore, each problem can be treated taking into account its mathematical type as the Stokes problem is elliptic and linear, whereas orientation and stretch problems involve non-linearities and convection.

---

initial conditions: $\mathbf{s}^0(\Omega), {}^0\Omega$

for each time step $[t^n, t^{n+1}]$ **do**

knowing $(\tau^n(\Omega))$, find $(\mathbf{v}^{n+1}, p^{n+1})$ such that

$$
\begin{cases}
\nabla \cdot [2\eta_s \varepsilon(\mathbf{v}^{n+1})] - \nabla p^{n+1} + \nabla \cdot \tau^n = 0 \\
\nabla \cdot \mathbf{v}^{n+1} = 0 \\
+\text{boundary conditions}
\end{cases}
$$

with the recent computed velocity field $\mathbf{v}^{n+1}$, find $(\mathbf{s}^{n+1}, \lambda^{n+1})$ such that

$$
\begin{cases}
\dfrac{d\mathbf{s}}{dt}^{n+1} - \nabla\mathbf{v}^{n+1} \cdot \mathbf{s}^{n+1} - \mathbf{s}^{n+1} \cdot \nabla\mathbf{v}^{n+1}{}^T + 2[\varepsilon(\mathbf{v}^{n+1}):\mathbf{s}^{n+1}]\mathbf{s}^{n+1} + \dfrac{1}{\theta_b}(\mathbf{s}^{n+1} - \dfrac{\mathbf{I}}{3}) = 0 \\
\dfrac{d\lambda}{dt}^{n+1} - \lambda^{n+1}[\varepsilon(\mathbf{v}^{n+1}):\mathbf{s}^{n+1}] + \dfrac{1}{\theta_s}(\lambda^{n+1} - 1) = 0 \\
+\text{boundary conditions}
\end{cases}
$$

update the extra-stress tensor τ^{n+1}

$$
\tau^{n+1} = G[3(\lambda^{n+1})^2\mathbf{s}^{n+1} - \mathbf{I}]
$$

end for

How stable is the formulation

In our formulation, we included an arbitrary solvent viscosity, that may pollute the solution. Some authors completely eliminate it, by using stabilisation methods like the EVSS or the DEVSS formulations, described previously. In our case, we maintain a solvent viscosity, but it can be chosen very small because our bubble stabilization procedure is approaching the DEVSS method of Guenette and Fortin [Guenette and Fortin, 1995]. As shown previously, applying this method to our simple incompressible viscoelastic flow problem leads to: *find* $(\boldsymbol{v}, p, \mathbf{H}) \in \mathcal{V} \times \mathcal{P} \times \mathcal{H}$ *such that*

$$
\begin{cases}
\int_\Omega \mathbf{w}[\nabla \cdot (2\eta_s \varepsilon(\mathbf{v})) - \nabla p + \nabla \cdot (2\eta_{stab}\varepsilon(\mathbf{v})) - \nabla \cdot (2\eta_{stab}\mathbf{H})] = -\int_\Omega \mathbf{w}\nabla \cdot \tau \\
\int_\Omega q\nabla \cdot \mathbf{v} = 0 \\
\int_\Omega \Phi : (\mathbf{H} - \varepsilon(\mathbf{v})) = 0
\end{cases}
\tag{3.32}
$$

where τ is the extra-stress, here known. Let us consider $\mathbf{v}_h = \mathbf{u}_h + \mathbf{b}_h$. The discrete variational form for this problem is: *find* $(\boldsymbol{u}_h, \boldsymbol{b}_h, p_h, \mathbf{H}_h) \in (\mathcal{V}_h \oplus \mathcal{B}_h) \times \mathcal{P}_h \times \mathcal{H}_h$ *such that*

$$
\begin{cases}
\int_{\Omega_h} 2(\eta_s + \eta_{stab})\varepsilon(\mathbf{v}_h) : \varepsilon(\mathbf{w_h} + \mathbf{b_h^*}) - \int_{\Omega_h} p_h \nabla \cdot (\mathbf{w_h} + \mathbf{b_h^*}) \\
- \int_{\Omega_h} 2\eta_{stab}\mathbf{H}_h : \varepsilon(\mathbf{w_h} + \mathbf{b_h^*}) = -\int_{\Omega_h} \tau_h : \varepsilon(\mathbf{w_h} + \mathbf{b_h^*}) \\
\int_{\Omega_h} q_h \nabla \cdot \mathbf{v}_h = 0 \\
\int_{\Omega_h} (\mathbf{H}_h - \varepsilon(\mathbf{v}_h)) : \Phi_h = 0
\end{cases}
\tag{3.33}
$$

$\forall (\mathbf{w}_h + \mathbf{b}_h^*, q_h, \Phi_h) \in (\mathcal{V}_h \oplus \mathcal{B}_h) \times \mathcal{P}_h \times \mathcal{H}_h$. The last equation means that $\mathbf{H}_h$ is the projection of $\varepsilon(\mathbf{u}_h)$ in $\mathcal{H}_h$:

$$
\mathbf{H}_h = \mathcal{P}_{\mathcal{H}_h} \varepsilon(\mathbf{u}_h)
\tag{3.34}
$$

where $\mathcal{P}_{\mathcal{H}_h}$ is the projection operator. The subspace $\mathcal{H}_h$, must not be entirely representative of the space defining $\varepsilon(\mathbf{v}_h)$. If we consider simply the linear part of the velocity's interpolation, $\mathbf{u}_h$ ($\mathcal{H}_h = \varepsilon(\mathcal{V}_h)$):

$$
\mathbf{H}_h = \varepsilon(\mathbf{v}_h)
\tag{3.35}
$$

The first equation in (3.24) may be re-written as [2]:

$$
\int_{\Omega_h} 2\eta_s \varepsilon(\mathbf{u}_h) : \varepsilon(\mathbf{w_h}) + \int_{\Omega_h} 2(\eta_s + \eta_{stab})\varepsilon(\mathbf{b}_h) : \varepsilon(\mathbf{b_h^*}) - \int_{\Omega_h} p_h \nabla \cdot \mathbf{w}_h \\
- \int_{\Omega_h} p_h \nabla \cdot \mathbf{b}_h^* = -\int_{\Omega_h} \tau_h : \varepsilon(\mathbf{w_h})
\tag{3.36}
$$

---

[2]Thanks to the properties of the bubble function chosen, see previous chapter.

Let us now consider our simple problem, without applying the D.E.V.S.S. method. Its discrete formulation may be written: *find* $(\boldsymbol{u}_h, \boldsymbol{b}_h, p_h) \in (\mathcal{V}_h \oplus \mathcal{B}_h) \times \mathcal{P}_h$ *such that*

$$
\begin{cases}
\displaystyle\int_{\Omega_h} 2\eta_s \varepsilon(\mathbf{u}_h) : \varepsilon(\mathbf{w}_h) + \int_{\Omega_h} 2\eta_s \varepsilon(\mathbf{b}_h) : \varepsilon(\mathbf{b}_h^*) - \int_{\Omega_h} p_h \nabla \cdot \mathbf{w}_h \\
\displaystyle - \int_{\Omega_h} p_h \nabla \cdot \mathbf{b}_h^* = - \int_{\Omega_h} \tau_h : \varepsilon(\mathbf{w}_h) \\
\displaystyle \int_{\Omega_h} q_h \nabla \cdot \mathbf{u}_h + \int_{\Omega_h} q_h \nabla \cdot \mathbf{b}_h = 0
\end{cases}
\tag{3.37}
$$

Comparing equations 3.36 and 3.37 it appears that increasing the viscosity in the bubble matrix term (by an additive factor η_{stab}) stabilises the system as a D.E.V.S.S. method, and furthermore, without affecting the final result.

Computing local matrices

After bubble condensation (see chapter 2) and using a matricial notation, we obtain a similar system as the Stokes compressible problem, with a right-hand side dependent on the element's extra-stress tensor:

$$
\begin{pmatrix} A_{vv} & B_{vp} \\ B_{vp}^t & C_{vb} \end{pmatrix} \begin{pmatrix} V_l \\ P \end{pmatrix} = \begin{pmatrix} F_\tau \\ F_p \end{pmatrix}
\tag{3.38}
$$

Since τ's interpolation has been chosen constant per element, and velocity's linear, we can write:

$$
\int_{\Omega_h} \tau_h : \varepsilon(\mathbf{w}_h) = \sum_{K \subset \Omega_h} \int_K \tau_K : \varepsilon(\mathbf{w}_K)
\tag{3.39}
$$

Applying Green's formula, we obtain the value of the additional force:

$$
\int_{\Omega_h} \tau_h : \epsilon(\mathbf{w_h}) = \sum_{K \subset \Omega_h} \int_{\partial K} (\tau_K \cdot \mathbf{n})\mathbf{w} = \sum_{K \subset \Omega_h} \sum_{F \in \partial K} \alpha_K^F [\tau]_K^F \cdot \mathbf{n}_K^F \int_F \mathbf{w}
\tag{3.40}
$$

In these equations, K is the index on the value on element K, $[\tau]_K^F$ is the jump of τ_K through the face F and is defined as:

$$
[\tau]_K^F = \tau_K - \tau_{K(F)}
\tag{3.41}
$$

where $\tau_{K(F)}$ an index of the value of τ on the adjacent element to the face F, ∂K is the boundary of the element K, $\mathbf{n}$ is the outward unit normal vector to ∂K.

3.3.3 Numerical resolution of the orientation and stretch equations

Once the velocity field has been calculated, we need to update the orientation and stretch. These equations are solved using a Space-Time Discontinuous Galerkin method, whose basis are described in Appendix A applied to a general transport equation. On the element $\tilde{K}$, orientation and stretch are approximated piecewise constant in space, $P0(K)$, and polynomial (degree n) and discontinuous in time $(Pn(]t^n, t^{n+1}[))$. Hence, orientation and stretch may be approximated onto the whole element K as

$$
\begin{aligned}
\mathbf{s}_K(t) &= \sum_{p=0}^{n} \mathbf{s}_K^p (t - t_n)^p \\
\lambda_K(t) &= \sum_{p=0}^{n} \lambda_K^p (t - t_n)^p
\end{aligned}
\qquad \forall K \in \Omega_h
\tag{3.42}
$$

where $\mathbf{s}_K^p$ is the approximation of $\mathbf{s}$ over K, unknown of our problem. The discrete variational form of our problems is: *find* $\mathbf{s}_h \in \mathcal{S}_h$ *and* $\lambda_h \in \mathcal{L}_h$ *such that*

$$\int_\Omega (\frac{\partial \mathbf{s}_h}{\partial t} + \mathbf{v} \cdot \nabla \mathbf{s}_h - [\nabla \mathbf{v} \mathbf{s}_h + \mathbf{s}_h \nabla \mathbf{v}^T] + 2[\mathbf{s}_h : \varepsilon(\mathbf{v})]\mathbf{s}_h + \frac{1}{\theta_b}\mathbf{s}_h)\Phi = -\int_\Omega \frac{\mathbf{I}}{3\theta_b}\Phi$$
$$\int_\Omega [\frac{\partial \lambda_h}{\partial t} + \mathbf{v} \cdot \nabla \lambda_h - \lambda[\varepsilon(\mathbf{v}) : \mathbf{s}_h] + \frac{1}{\theta_s}\lambda_h]\varphi = \int_\Omega \frac{1}{\theta_s}\varphi$$

(3.43)

$\forall \Phi \in \mathcal{S}_h$ and $\varphi \in \mathcal{L}_h$.

The STDG method is applied to our two evolution equations, and we consider the following assumptions:

- the stretch equation is linearised supposing that the orientation is known: first we determine the distribution of orientation, then we use its value to determine stretch in this orientation direction;

- the orientation equation is linearised; by computing the closure term at the previous time step $[\mathbf{s}^n : \varepsilon(\mathbf{v})] : \mathbf{s}^{n+1}$.

We remark that since $\mathbf{s}$ is symmetrical, the total number of unknowns is:

$$\sum_{K \subset \Omega_h} \frac{d(d+1)}{2}(n+1) + (n+1)$$

(3.44)

where n the interpolation order in time and d is the spatial dimension.

To synthesize, on one time slab $I^n =]t^n, t^{i+1}[$, the Stokes problem is solved determining $(\mathbf{v}^{n+1}, p^{n+1})$ constant on this interval for a known extra-stress configuration $(\mathbf{s}^n, \lambda^n)$. Afterwards, orientation and stretch are updated $(\mathbf{s}^{n+1}, \lambda^{n+1})$ with $\mathbf{v}^{n+1}$. To capture the different phenomena that we described previously, fine meshes are required, and therefore computation involves a large number of degrees of freedom $4 \times$ (number of nodes) $+ 7 \times$ (number of elements) $\times (number of modes) +$ (number of elements) per time slab), and parallel computation is obviously required. The parallel strategy adopted [Digonnet and Coupez, 2003] uses the MPI standard programming library and will not be described here. We can briefly refer that it is based on a global master-slave program, where SPMD modules were introduced. In our case, we developed an SPMD module capable of computing an extra-stress tensor of viscoelastic origin. Resolution of the non-symmetrical systems resulting from our formulation are done in parallel, using the PETSC (*Portable, Extensible Toolkit for Scientific Computation*) library, using the GMRES method, with an ILU preconditionning.

3.3.4 Analysis of the model in simple flows

Solutions to the orientation equation

The orientation equation may be solved analytically for simple shear, and planar extension [Graham et al., 2001]. Throughout this section, we will consider the solution for pure shear flows, and we suppose that the flow is in the x-direction and the velocity gradient is in the y-direction.

In shear flows, the rate at which the flow stretches the backbone segments $(\varepsilon(\mathbf{v}) : \mathbf{s})$ is equal to $\dot{\bar{\gamma}} \mathbf{s}_{xy}$, where $\dot{\bar{\gamma}}$ is the shear rate. The shear stress will be directly related with the orientation component $\mathbf{s}_{xy}$. In simple shear, the different components of the orientation tensor tend to the following values, when $t \to \infty$:

$$
\begin{aligned}
s_{xx} &\to \frac{1 + 6\theta_b \dot{\bar{\gamma}} s_{xy}}{3 + 6\theta_b \dot{\bar{\gamma}} s_{xy}} \\
s_{xy} &\to -\frac{1}{3\theta_b \dot{\bar{\gamma}} s_{xy}} + \frac{1}{6\theta_b \dot{\bar{\gamma}} s_{xy}} (b^{\frac{1}{3}} + b^{-\frac{1}{3}}) \\
s_{yy} = s_{zz} &\to \frac{1}{3 + 6\theta_b \dot{\bar{\gamma}} s_{xy}} \\
s_{xz} = s_{yz} &\to 0
\end{aligned}
\tag{3.45}
$$

where

$$
b = 1 + 9(\theta_b \dot{\bar{\gamma}})^2 + 3\theta_b \dot{\bar{\gamma}} \sqrt{2 + 9(\theta_b \dot{\bar{\gamma}})^2}
\tag{3.46}
$$

Figure 3.14 shows the value of s_{xy} for a fixed shear rate computed with **REM3D**, as well as the steady-state analytical solution, for various values of θ_b. We observe that there is a good agreement between the numerical steady-state solution (when it is reached) and the analytical one. For relaxation times $\theta_b > \frac{1}{\gamma}$, s_{xy} rises to a maximum before approaching its steady-state value. By maximising $lim_{t\to\infty} s_{xy}(t)$ with respect to θ_b, the value of θ_b which produces the largest steady-state value of s_{xy} can be shown to be:

$$
\theta_b^{max} = \frac{\sqrt{3/2}}{\dot{\bar{\gamma}}}
\tag{3.47}
$$

When $\theta_b < \theta_b^{max}$, the rapid reptation means that the flow is not fast enough to orient the backbones significantly before they relax. In the case $\theta_b > \theta_b^{max}$ the backbones are oriented at the optimum angle but the flow then continues to orient them towards the x-axis before the slow orientation relaxation produces a dynamic equilibrium. The contribution of a single backbone is maximised when it lies in the x-y plane, making an angle of $45°$ with the x-axis. At this angle, the contribution to s_{xy} is $1/3$. Note than even in the affine case $(\theta_b \to \infty)$ s_{xy} never reaches this value since, due to the isotropic initial distribution of backbones, all of the backbones will never simultaneously point in the same direction.

Another validation example, is given by orientation under pure shear flow [Chinesta et al., 2000]. We consider a square domain $[0,1] \times [0,1]$, with an imposed linear velocity field, $\mathbf{v} = (0.01 + y, 0)$. On the inflow boundary $(\partial\Omega^-, x = 0)$, an isotropic orientation is prescribed, $\mathbf{s} = \mathbf{I}/2$. To represent the orientation state at each element, we use an ellipse whose semiaxes lengths are the eigenvalues of the associated orientation tensor, and whose directions correspond to its eigenvectors. Relaxation time was considered sufficiently large $(1000s)$, so that the equation to be solved is similar to the one from the authors (who consider orientation of fiber like particles):

$$
\frac{\partial \mathbf{s}}{\partial t} + \mathbf{v} \cdot \nabla \mathbf{s} - \nabla \mathbf{v} \cdot \mathbf{s} - \mathbf{s} \cdot \nabla \mathbf{v}^T + 2[\varepsilon(\mathbf{v}) : \mathbf{s}]\mathbf{s} = 0
\tag{3.48}
$$
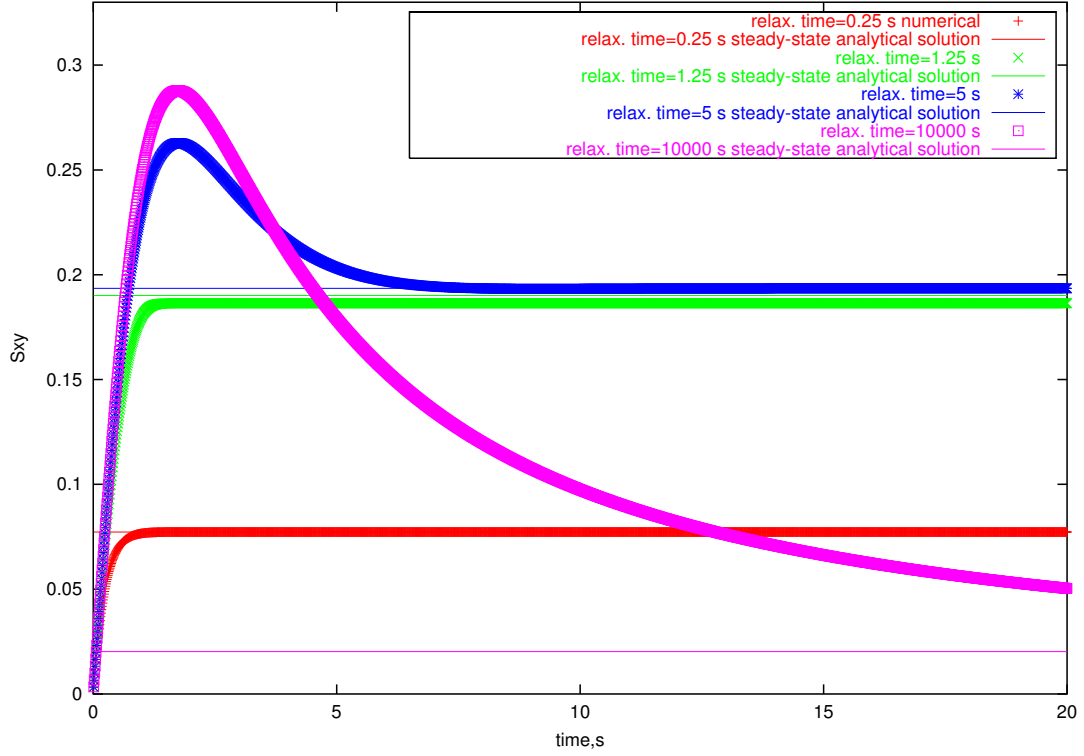
Figure 3.14: *Component s_{xy} of the orientation tensor in a shear flow with $\dot{\gamma} = 1\ s^{-1}$; numerical transient and analytical steady-state solutions.*

In figure 3.15 we observe that our solution is in agreement with the one obtained by Chinesta [Chinesta et al., 2000] with a semi-lagrangian strategy, which is quite good, despite of the use of a coarse mesh, since particles tend to be oriented in the direction of the flow, as expected in a shear flow. On the right, the results for a similar 3D test case.
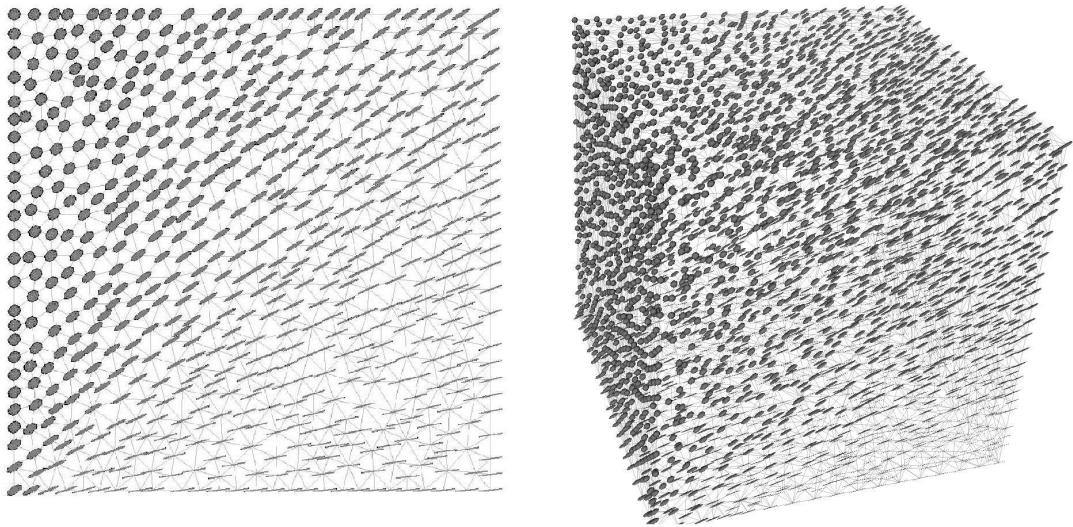
Figure 3.15: *Orientation solutions.*

Solutions to the stretch equation

Figure 3.16 shows the results obtained with **REM3D** in simple shear, for fixed orientation and stretch relaxation times and different shear rates. We notice that stretch increases with the shear rate. Furthermore, for small shear rate values ($\dot{\bar{\gamma}} \leq \frac{1}{\theta_b}$) a stretch overshoot is reached.
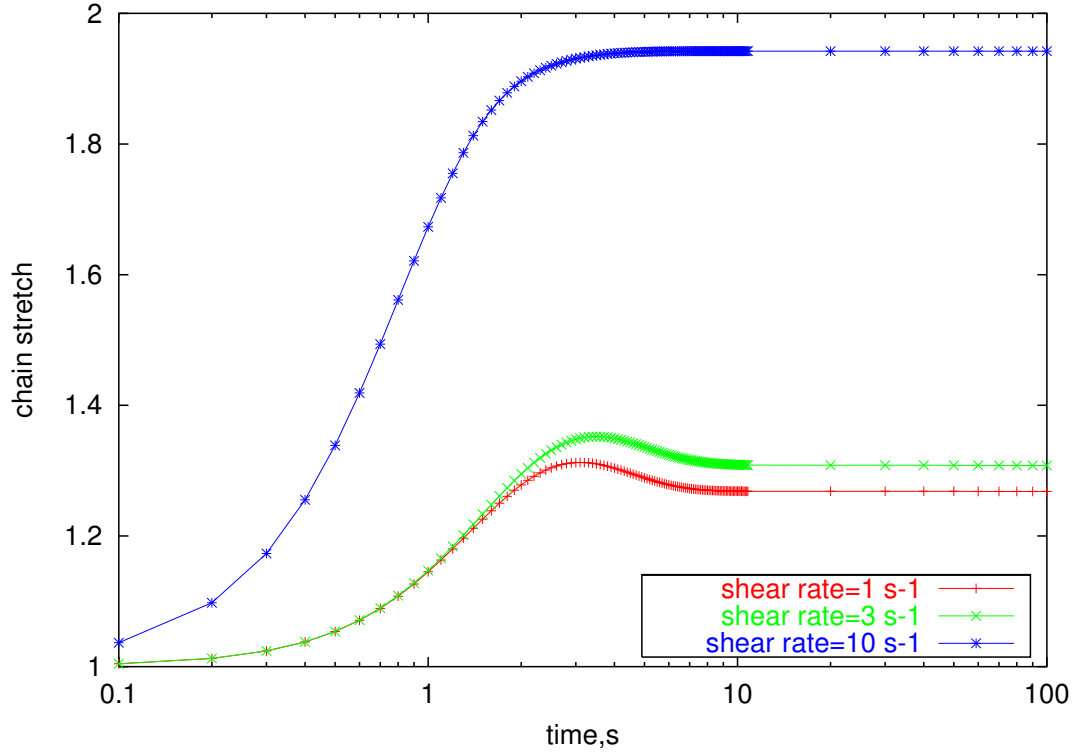
Figure 3.16: *Evolution of stretch in shear flow for different shear rates $\theta_b = 3s$, $\theta_s = 1s$ and $q = 5$, being q the number of arms.*

3.3.5 Numerical efficiency: 2D contraction flow test and 3D extrusion

Viscoelasticity in complex flows involves obsviously a large number of degrees of freedom. In this section we test the numerical efficiency of the methods implemented through two examples. The first one is a classical benchmark from the literature for viscoelastic flow: the 2D contraction flow. Afterwards, a 3D extrusion example is considered, where flow complexity and computational capacities of the numerical and implementation methods described previously are shown.

<u>**Contraction flow**</u>

Let us start by studying the behavior of our implementations in the steady flow in a sudden planar contraction. This kind of flow was chosen as a classical benchmark example, studied exhaustively by other authors and the values considered here were taken from [Beraudo et al., 1998; Sirakov, 2000]. The upstream and downstream half heights of the geometry are $h = 1.25$ mm and $H = 10$ mm, giving a contraction ratio of 8. A flow rate is imposed at the inlet, located at $x/h = -20$, corresponding to a mean velocity of 1 mm/s, whereas zero normal stress is considered at the outlet ($x/h = 20$). The polymer melt used in this work was a low density polyethylene (LDPE). Values at the reference temperature of 160^oC are given in table 3.1, and the solvent viscosity considered is 50 Pas. No-slip boundary conditions are imposed elsewhere, as well as a zero normal velocity for the symmetry plane.

i	$\theta_{b,i}$ (s)	G_i (MPa)	q_i	$\theta_{b,i}/\theta_{s,i}$
1	6.25E-04	6.327E+00	1	2
2	5.35E-03	5.340E-02	1	2
3	2.85E-02	2.700E-02	1	2
4	1.55E-02	1.400E-01	1	2
5	8.91E-01	7.250E-03	3	2
6	4.58E+00	2.660E-03	4	2
7	2.34E+01	5.660E-04	8	1.35
8	1.18E+02	6.183E-05	12	1.9

Table 3.1: Non-linear parameters of LDPE at 160°C [Sirakov, 2000].

Computations were performed on two different meshes: coarse (7478 nodes 14954 elements) and fine (28470 nodes and 56938 elements), represented in figure 3.17.

To analyze the performance of the developed solvers, computations were performed in 1, 2, 4, 8 and 16 processors. Each processor is a Pentium III with 1GHz and 512Mb RAM, linked to the other processors by a Myrinet network. The partitions obtained (figure 3.18) are quite similar for coarse and refined meshes for a small number of processors, whereas for a large number of processors, we observe differences in the refined zones. To reach the steady state, the number of time elements (of different sizes) was 10000, starting with a dimension of 10^{-4}.

Figure 3.17: *Meshes used in the contraction test for numerical performance.*

Figure 3.18: *Partitions of both meshes, coarse on the left and fine on the right (2,4,8 and 16 processor from the top to the bottom).*

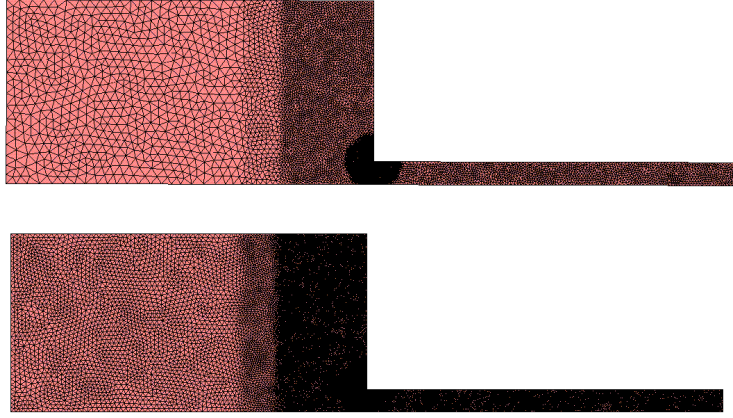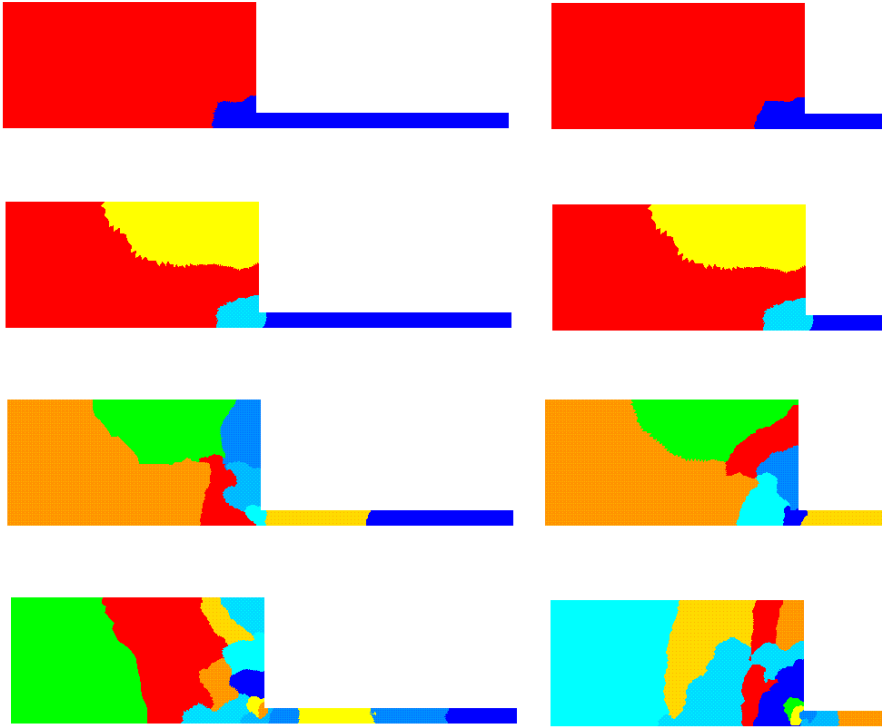Tables 3.2 and 3.3 illustrate the time spent by the software in partitioning the mesh (at the beginning), computing the flow (each time step), storing (each 100 time steps) and the total time. The only sequential operation remains the storage of the results, since they are all gathered in one of the processors. We observe a reduction of the computation and global execution times when the number of processors increases as expected, whereas the storage time is the same and the partitioning time increases. The accelerations obtained are very encouraging, especially in the case of the finer mesh, reaching 14 on 16 processors (corresponding to an efficiency of 0.876), even if a larger time is spent in results storage.

We underline that we consider 8 modes, and there are consequently 8 orientations and stretches to compute, as well as the velocity-pressure field, that correspond to about 1.5 million degrees of freedom per time slab.

Number of processors	1	2	4	8	16
Partitioning time, s	0.6	1.3	2.2	3.5	5.0
Computation time, s	195123	102495	53140	28512	17048
Storage time, s	641	684	683	680	682
Execution time, s	195765	103180	53824	29195	17735
Computation speed-up (efficiency)	1	1.903 (0.952)	3.672 (0.928)	6.843 (0.855)	11.445 (0.715)
World-clock speed-up (efficiency)	1	1.897 (0.948)	3.637 (0.932)	6.705 (0.838)	11.038 (0.690)

Table 3.2: Times for partitioning, computation and storing, as well as total time, speed-up and efficiency in the coarse mesh.

Number of processors	1	2	4	8	16
Partitioning time, s	2.3	9.3	14.5	16.9	23.1
Computation time, s	1309432	659500	356803	178374	93458
Storage time, s	2616	2636	2621	2619	2624
Execution time, s	1312051	662146	359439	181011	96106
Computation speed-up (efficiency)	1	1.986 (0,993)	3.670 (0.918)	7.341 (0.917)	14.011 (0.876)
World-clock speed-up (efficiency)	1	1.981 (0,990)	3.650 (0.912)	7.248 (0.906)	13.652 (0.853)

Table 3.3: Times for partitioning, computation and storing, as well as total time, speed-up and efficiency in the coarse mesh.

Qualitative results can be seen in the following figures. The evolution of the velocity field is in agreement with literature: the streamlines obtained are represented in figure 3.19, showing that the velocity field changes throughout time, seen by a large recirculation zone. On the right, we observe a detail near the singular point of the contraction, where one smaller recirculation appears. We conclude that the use of finer meshes and methods to solve large scale systems allow to capture these kind of small scale phenomena.

To characterize flow elasticity, we define the averaged Weissenberg number:

$$We = \overline{\theta}_b \dot{\gamma} \tag{3.49}$$

Here $\overline{\theta}_b$ is the averaged orientation relaxation time for the material, and $\dot{\overline{\gamma}}$ is the averaged shear rate.

$$\overline{\theta}_b = \frac{\sum_{i=1}^{m} \theta_{bi}^2 G_i}{\sum_{i=1}^{m} \theta_{bi} G_i} \tag{3.50}$$
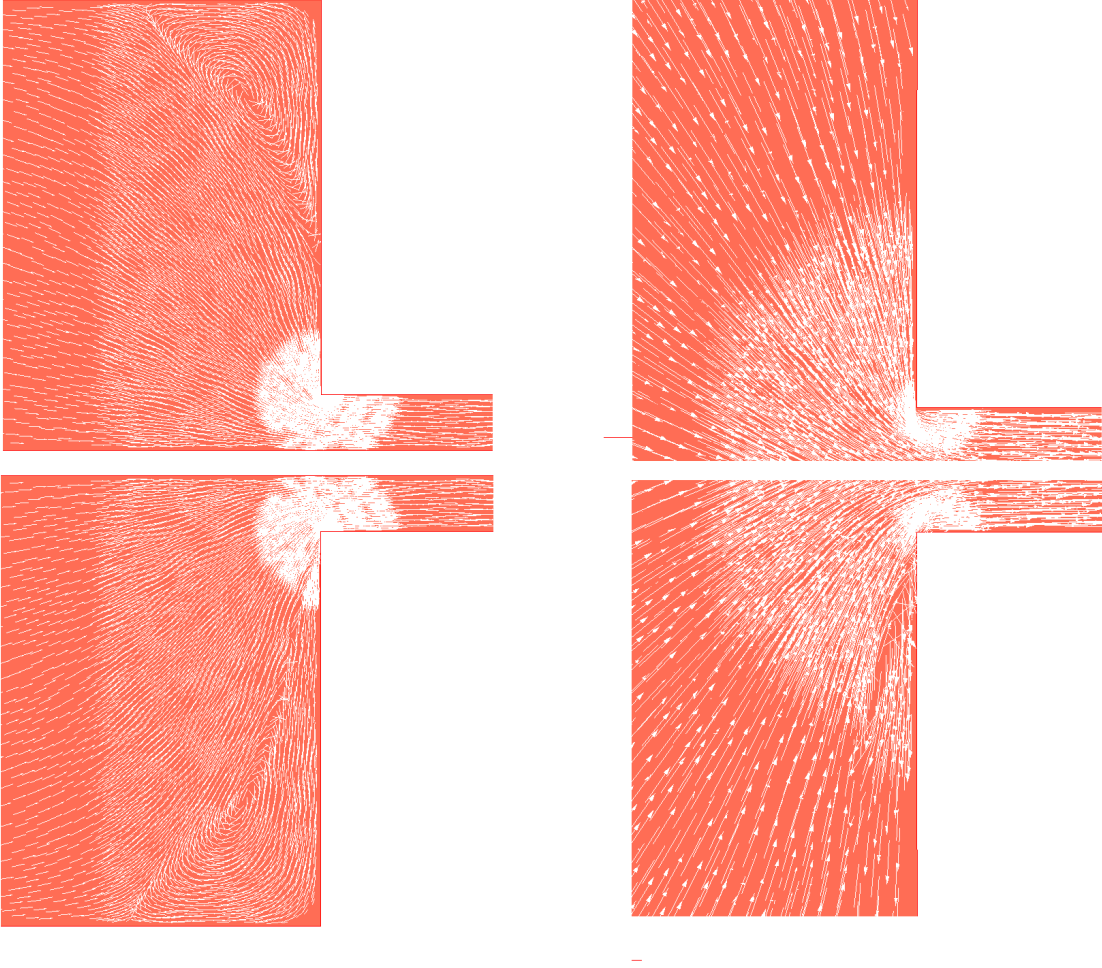
Figure 3.19: *Velocity field in the planar contraction test; on the right a detail of the singular zone.*

In 3D complex flows, a Weissenberg number cannot be easily defined. From the values given above, the averaged Weissenberg number reaches 16.8, but it is much higher locally. A second way to further validate numerical developments is the comparison to measured isochromatic fringe patterns. Assuming the validity of the stress optical rule, birefringence b_i has a linear relationship with the first difference of principal stresses $(\sigma_1 - \sigma_2)$, through the stress optical coefficient, C:

$$b_i = C(\sigma_1 - \sigma_2) \tag{3.51}$$

The computed isochromatic fringe patterns are shown in figure 3.20. It provides a good representation of expected fringe patterns: a "butterfly" shaped region just before the contraction, with a reasonable recirculation shape and size. These results are quite comparable to those obtained by [Beraudo et al., 1998].
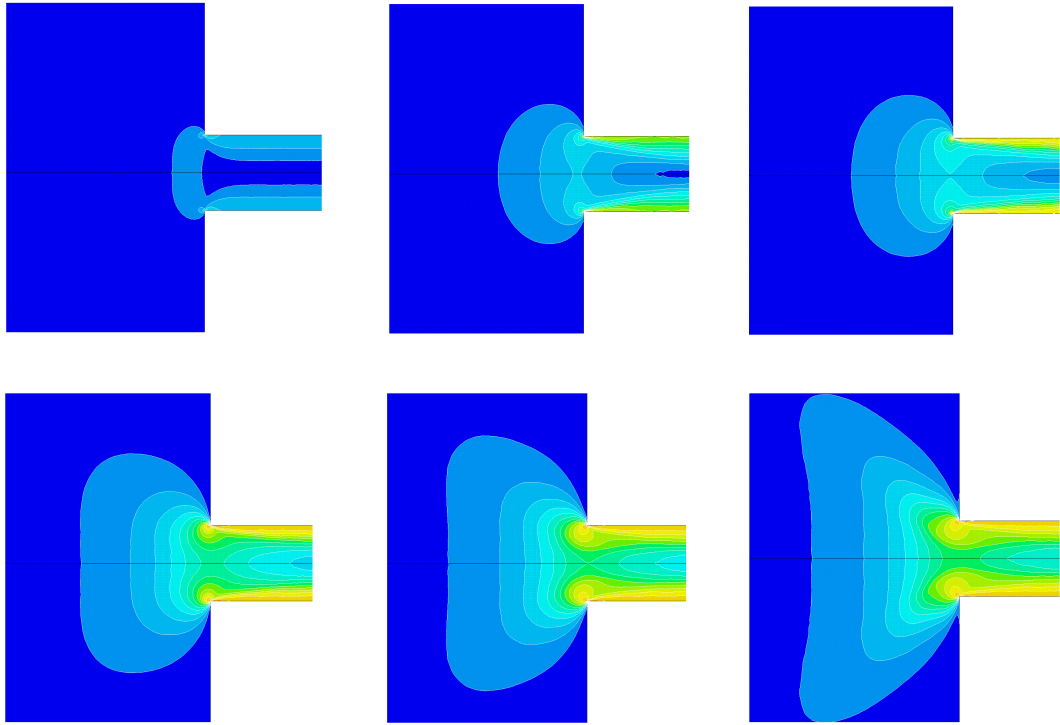
Figure 3.20: *Birefringence pattern development as function of time for the planar contraction test.*

3D extrusion

We now consider a more industrial test case: the extrusion of a complex part, needing a three-dimensional representation (figure 3.21). Boundary conditions are similar to the preceding case: a flow rate is imposed at the inlet, corresponding to a mean velocity of 1 mm/s, whereas zero normal stress is considered at the outlet; no-slip boundary conditions are imposed elsewhere. The polymer used in this study is the same LDPE, but only 4 modes are taken into account.
In what concerns computation data, we performed 1000 time steps to reach the steady-state, for a computation time of 3h 27min 32s on 10 processors. This computation time remains reasonable, although for this mesh size (nodes and elements), we could not perform this computation on a single processor. In figure 3.22 we display the steady-state streamlines, which points out the complexity of the flow. We notice a 3D recirculation with a non-uniform size.

Figure 3.23 shows on the left a cut of the part and the birefringence pattern, and on the right a distribution of the local Weissenberg number, providing a more quantitative information.
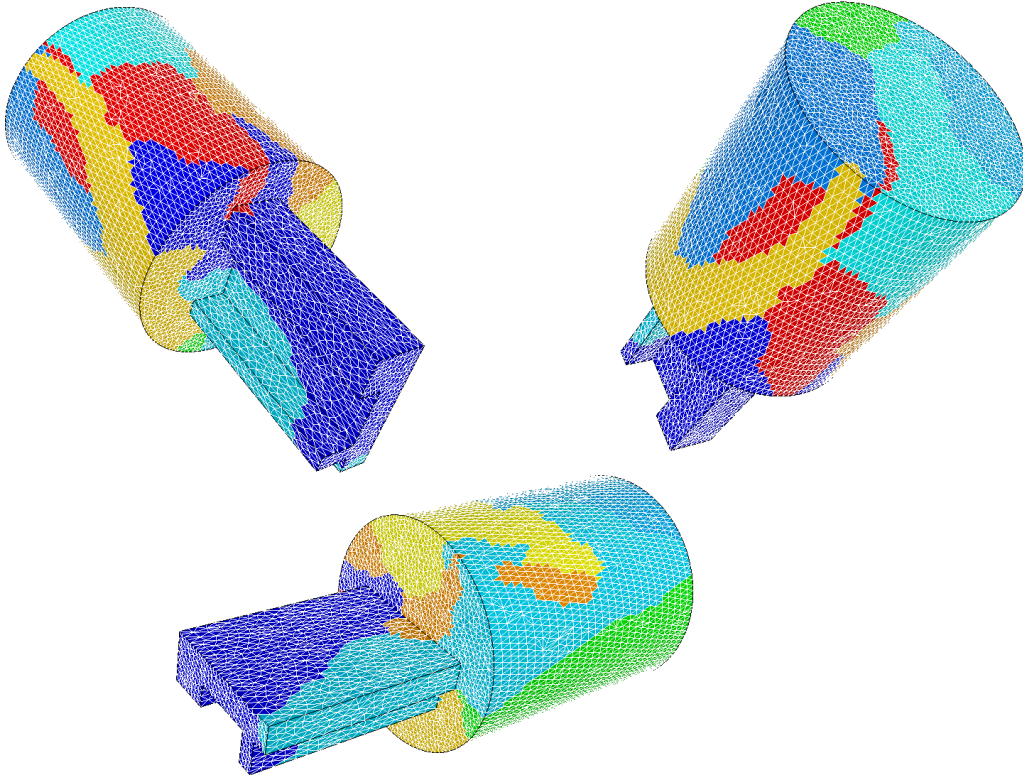
Figure 3.21: *3D partition of the mesh.*
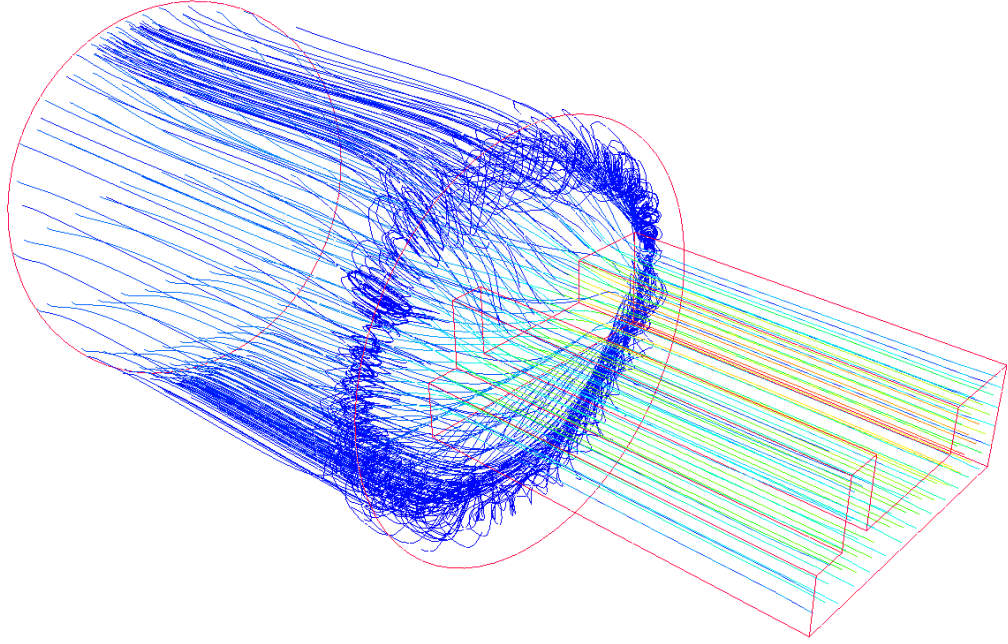
Figure 3.22: *Complexity of the flow in 3D.*
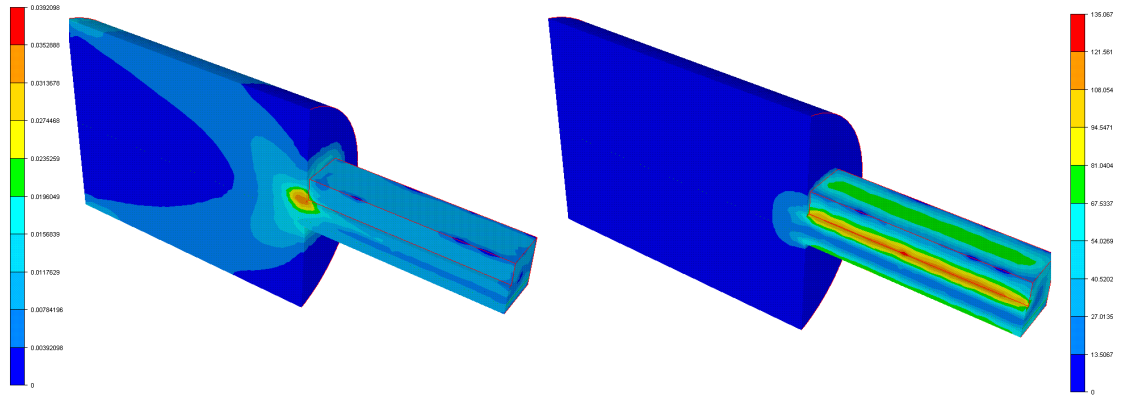
Figure 3.23: *Birefringence pattern in 3D (on the left) and weissenberg distribution (on the right).*

3.4 Compressible viscoelasticity

Compressible viscoelasticity remains an active research area. At this date, there are some theoretical studies concerning existence and uniqueness of the solution [Matusu-Necasova et al., 1999] and stability [Kwon, 1996] of compressible viscoelastic constitutive equations, as well as applications in bubble dynamics [Brujan, 2001]. More recently, [Keshtiban et al., 2004] studied viscoelastic compressible contraction flows using a modified Tait equation and the Oldroyd-B model, and [Valette, 2003] compared experimental and numerical results for this type of flow in the multipass rheometer using the PomPom model (see next section). Since our objective remains the application of this kind of models for industrial problems, we split the compressible and viscoelastic effects by considering that each brings its contribution to the stress determination: compressibility is taken into account classically through a state equation (the Tait law), whereas viscoelasticity is determined through the evolution of the extra-stress tensor. This section provides an application example.

We now consider the start-up flow through a planar 6:1:6 constriction, with small height $h = 0.75$ mm. The upstream and downstream regions have lengths of $L = 20$ mm, and at the inlet, we impose a flow rate and zero normal stress at the outlet ($x/h = 30$). No-slip boundary conditions are specified at the wall and symmetry at the centerline. Schematic geometry and mesh are shown in figure 3.24 (with 4609 nodes and 12932 elements). The material (LLDPE) is considered as compressible and viscoelastic, model parameters are detailed in table 3.4. In what concerns computation data, we performed 705 time steps to reach 4 s, with a computation time of 3h 27min 32s. The flow rate is imposed during 2.8 s, and then we stopped feeding, letting the polymer relax back to equilibrium.

- Streamlines

  In figure 3.25 we display the steady-state streamlines. At the averaged Weissenberg number reached ($We = 42.1$), the downstream vortex decreases, whereas the upstream vortex increases in size. Here again our results are in good agreement with experimental observations and numerical results given in [Lee et al., 2001] and presented by [Valette, 2003].

- Pressure

  The influence of the compressible behavior of the material can be observed through the pressure plot profile (figure 3.26). In start-up, a certain time to reach the steady-state is required, which depends on the viscoelastic component, but also on the isothermal compressible coefficient. Furthermore, a viscous incompressible versus viscoelastic compressible comparison was performed, using a Carreau law fitting. We observe that the amplitude of the time interval to reach the steady-state is largely underestimated in the viscous incompressible computation.

- Birefringence, orientation and stretch

  Figure 3.28 shows a comparison between experimental results (courtesy of R. Valette) and numerical computation of the birefringence patterns. We notice that in the entrance region the computed pattern fits rather well, whereas at the exit it is less accurate. Orientation (figure 3.29) and stretch (figure 3.27) of the different modes are illustrated, where we can see their increase and subsequent relaxation. We remark that at $t = 4$ s some modes have not completely relaxed, whereas others have reached equilibrium.

N	$\theta_{b,i}$ (s)	G_i (MPa)	q_i	$\theta_{b,i}/\theta_{s,i}$
1	1.14E-02	9.89E+00	1	2
2	5.60E-02	3.77E+00	1	2
3	2.35E-01	7.48E-01	2	2
4	1.07E+00	1.40E-01	4	2
5	4.84E+00	1.52E-02	5	2
χ_p (constant)	1.50E-05	MPa^{-1}		

Table 3.4: *Non-linear parameters of the LLDPE at 160° C [Lee et al., 2001].*
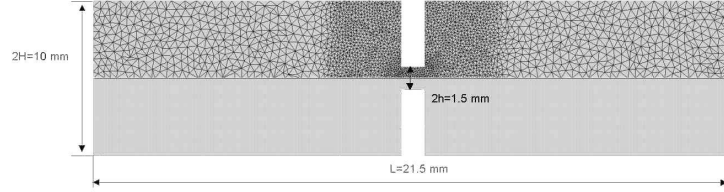
Figure 3.24: *Geometry and mesh of the contraction/expansion test.*
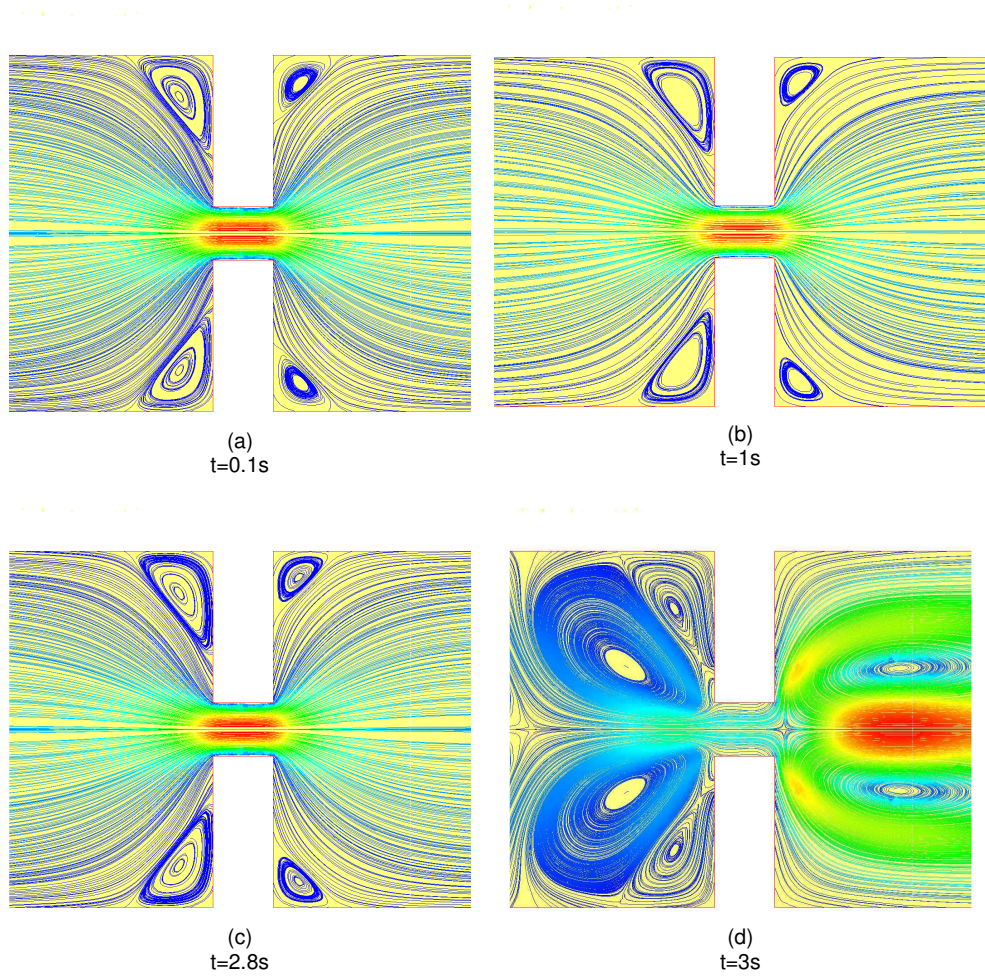
Figure 3.25: *Streamlines for the contraction/expansion test, at different time steps (a) $t = 0$, b) $t = \theta_b$, c) $t = 10\theta_b$, d) relaxation).*
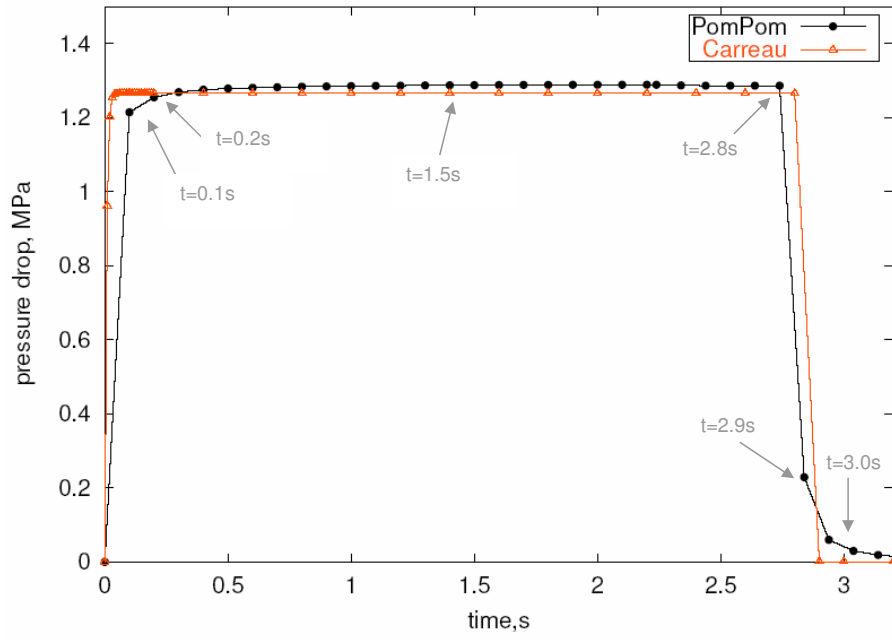
Figure 3.26: *Pressure drop throughout time for the contraction/expansion test.*
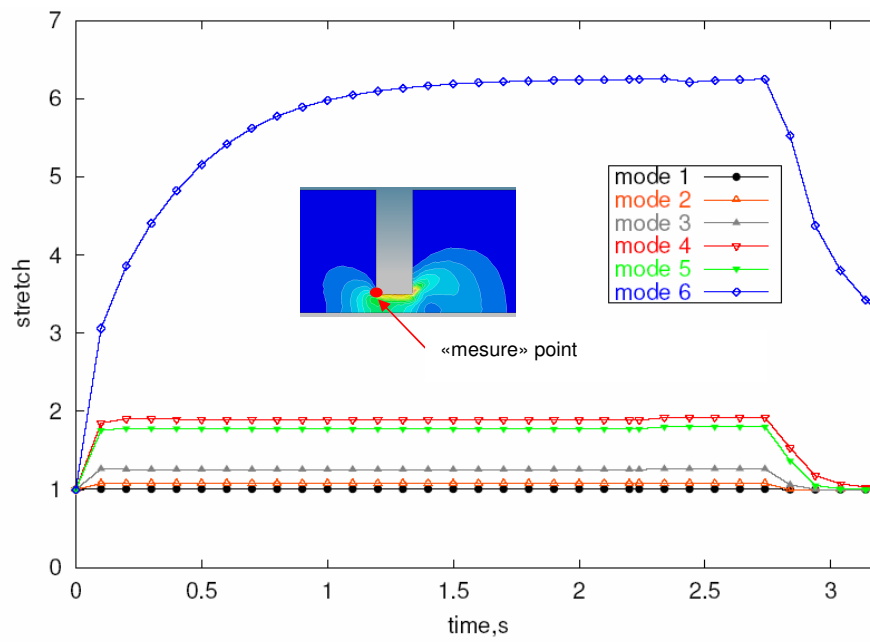
Figure 3.27: *Stretch evolution in the multipass device, for the different modes.*
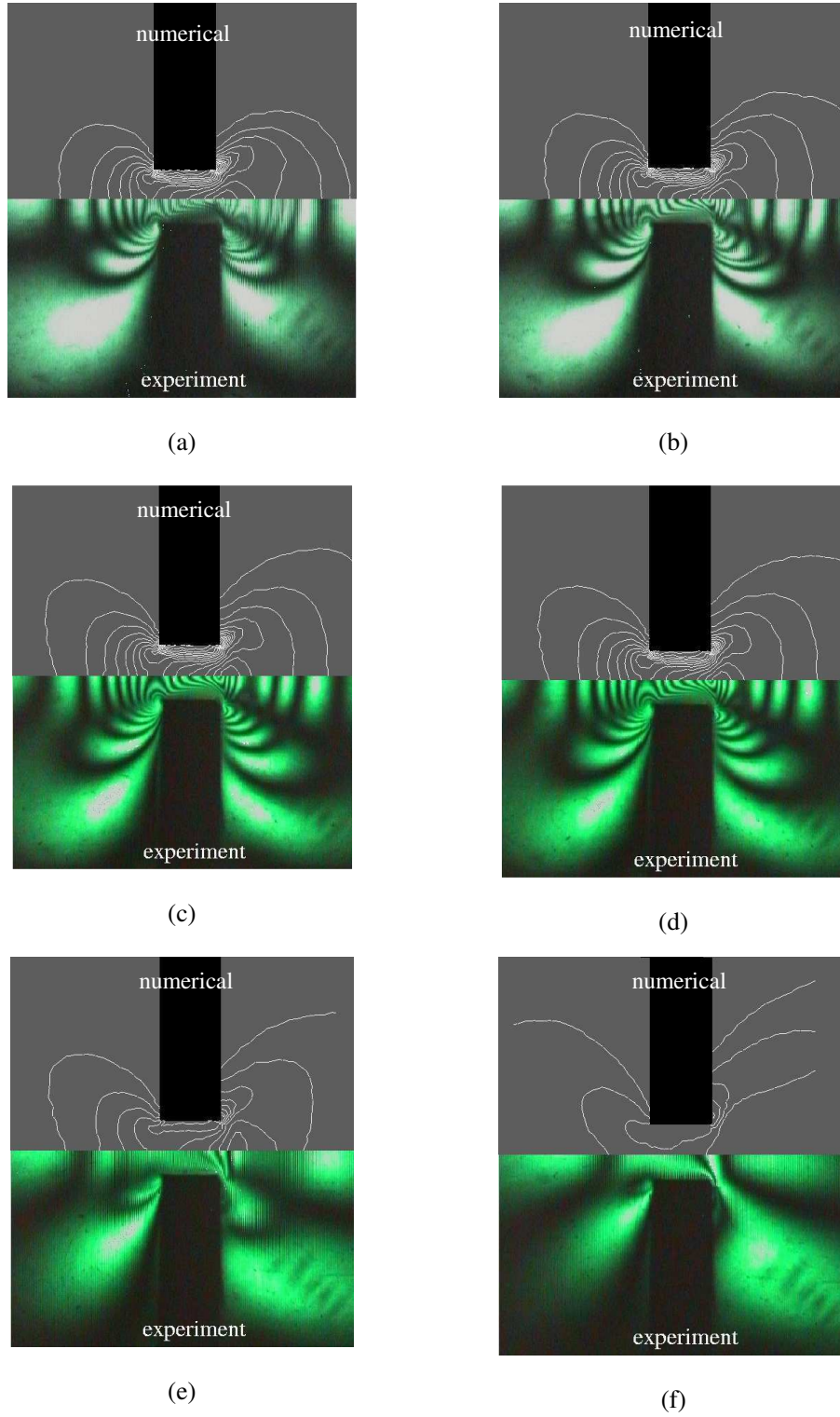
Figure 3.28: *Comparison between experimental and numerical birefringence patterns for different time steps (experimental patterns are a courtesy of Rudy Valette).*
(a) t=0.1s , (b) t=0.2s , (c) t=1.5s , (d) t=2.8s (e) t=2.9s (f) t=3.0s
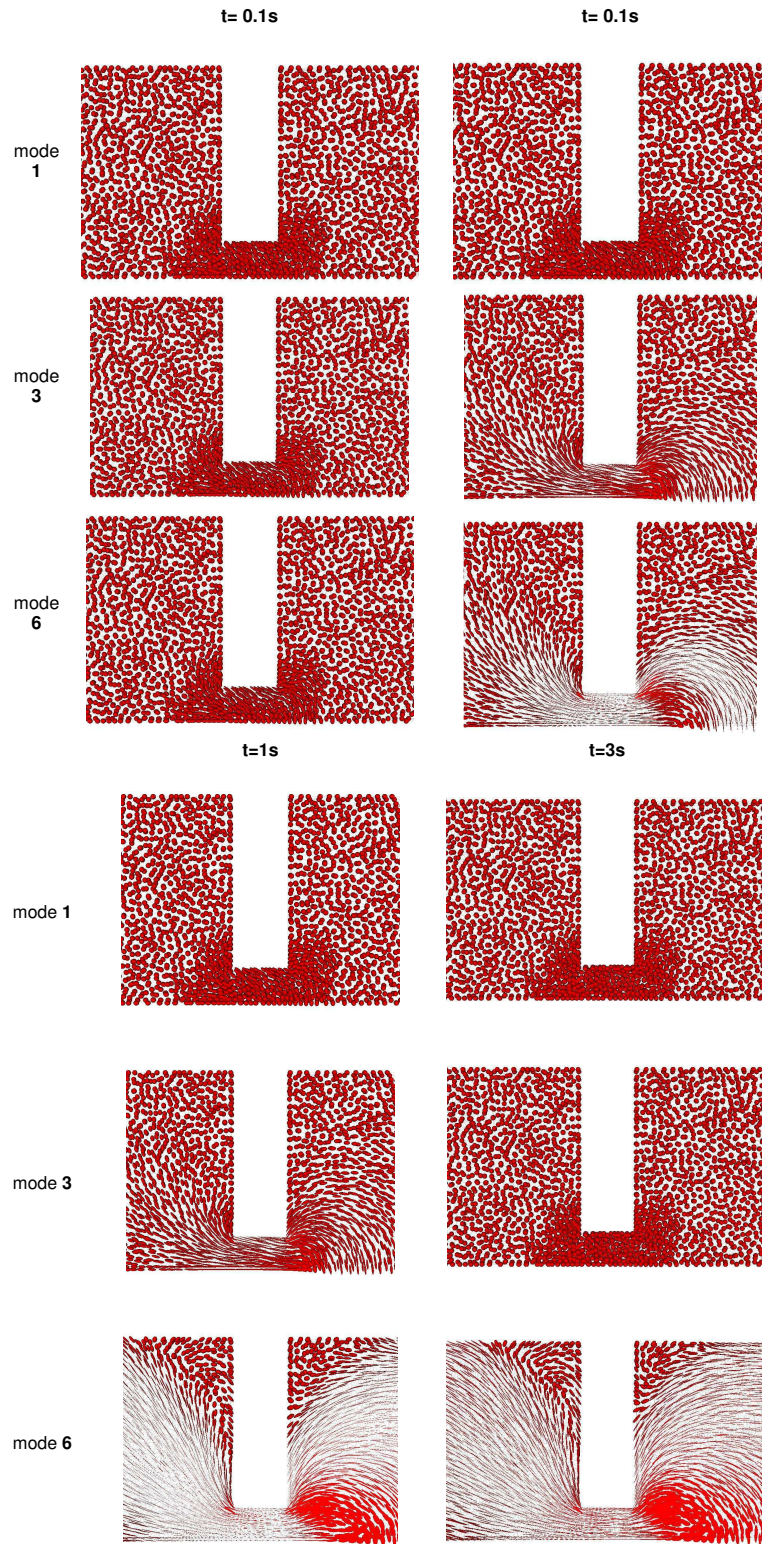
Figure 3.29: *Orientation profile evolution in the multipass device, for three different modes.*

3.5 Applications in viscoelastic free surface flows

In this section, numerical methods described previously are used in two classical tests for viscoelastic flows: the extrudate swell problem and jet buckling. Several methods are proposed in the literature to solve this type of problems (see [Tanner,1992] for a review). In both cases, the free surface determination and extended velocity-pressure formulation is applied, in this case to a viscoelastic fluid.

The results presented were obtained by using directly the model implemented. Although the purpose of this work is to determine internal stresses and potential anisotropy of the mechanical properties in injection molded parts, the capability of our approach to deal with moving fronts can be shown on extrusion type flows involving free surfaces.

3.5.1 Extrudate swell

The extrudate swell problem is a classical free surface benchmark in polymer processing (mainly in extrusion). Generally, the polymer melt is introduced in the die and extruded at a constant flow rate. At the die entrance, the melt is submitted to both elongational and shear flows, whereas at the capillary we have a shear predominant flow. At the exit of the capillary, elastic relaxation and velocity field reorganization lead to a swell phenomena. The polymer is then drawn at a constant tension.
Problem geometry is described in figure 3.30. The contraction ratio is of 8:1 in the die, and the die length of 5 mm (L/D=2, short die). The die width was supposed very large, leading to the bi-dimensional problem studied by C. Beraudo [Beraudo et al., 1998] and I. Sirakov [Sirakov, 2000] (even if we use a 3D-model, with two symmetry planes). Computations were performed with a LDPE polymer (with properties at the reference temperature of 360°C given in table 3.1).
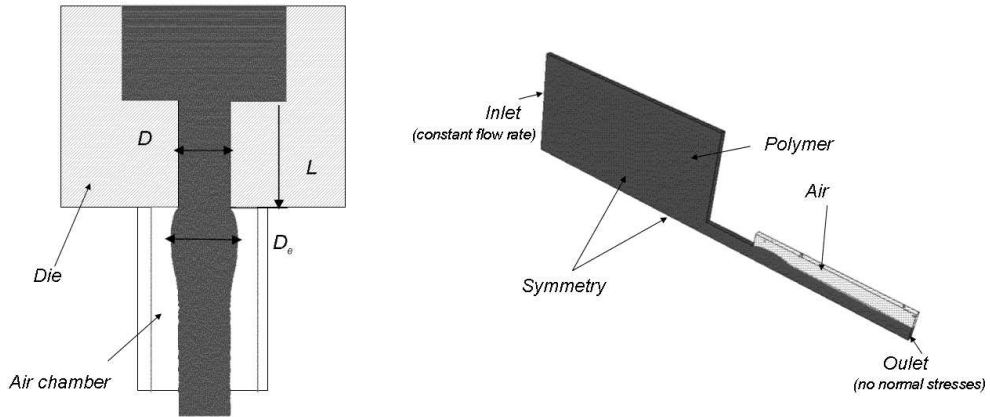
Figure 3.30: *Geometry of the extrudate swell problem: on the left the process description, on the right a schematic geometry of the test case.*

First results concern the swell ratio for both flow rates. Figure 3.31 show the results obtained by [Beraudo et al., 1998] in a similar geometry, both experimentally and numerically. The author used the PTT model. On the right (figure 3.31), we show the results obtained with **REM3D**. We notice that the swell ratio is in agreement with the results of the preceding authors. However, we notice a decrease of this ratio far away in the air chamber. This result is confirmed with the axial velocity profile, measured at the symmetry plane (y=0), that increases slightly from the die exit to the outlet of the air chamber. This increase is due to the fact that the normal stress is not exactly zero at the outlet, but influenced by the extra-stress interpolation (P0 type), and thus constant per element.
Evolution of both orientation and extra-stress components (axial and shear component) for the smallest flow rate are shown in figure 3.33. Orientation is illustrated with ellipsoids and for both smaller and
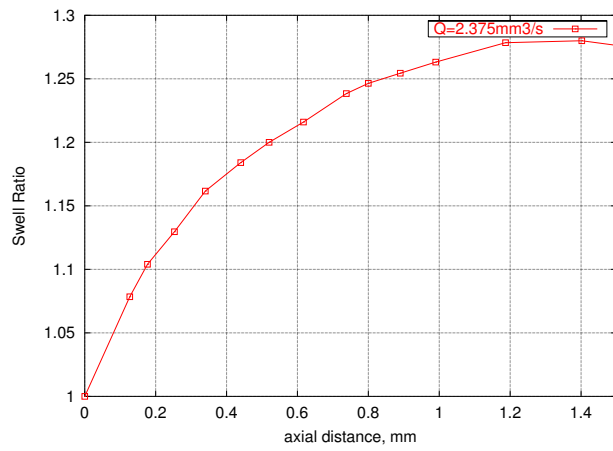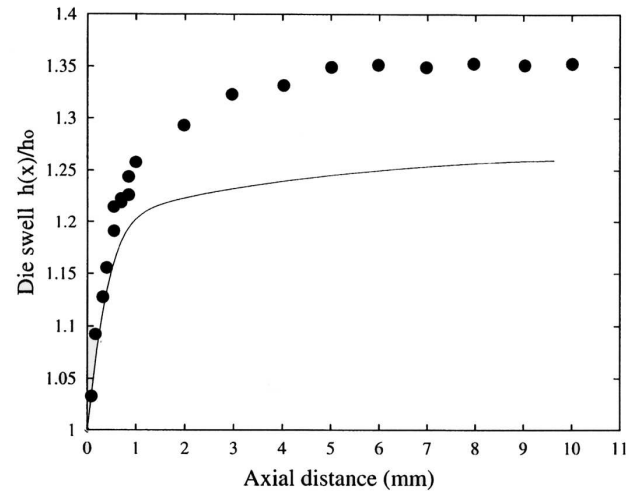
Figure 3.31: *Results concerning the swell ratio: (a) results from [Beraudo* et al, *1998] (b) results of* **REM3D**.
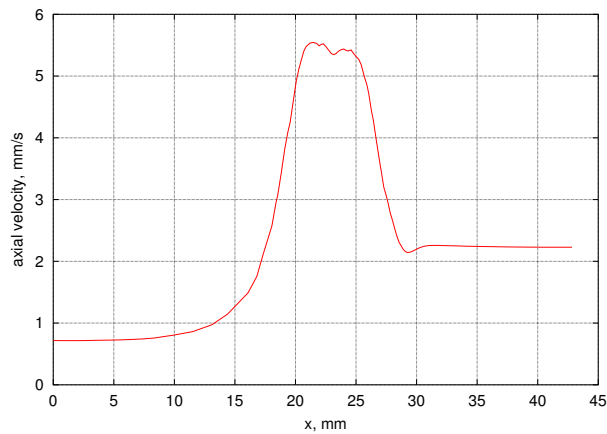
Figure 3.32: *Axial velocity profile, at $y = 0$ mm.*

highest relaxation mode (smaller and highest relaxation times). The minimum and maximum values of the first normal stress difference are also detailed in each picture. We notice that for small relaxation times, orientation relaxes quickly and there is almost any direction in space that is preferred (seen also by the first normal stress maximum value). For the highest mode, molecules are highly oriented. We remark that they are perpendicular to the interface air/polymer, as expected.
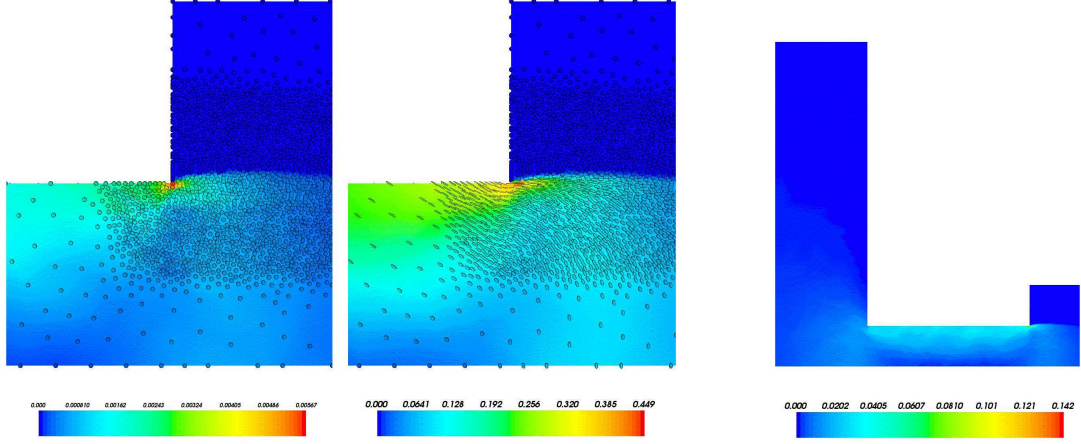
Figure 3.33: *Results concerning on the left orientation of the first mode; at the center of the last mode and on the right the equivalent extra-stress; the scalar values represent the equivalent orientation and extra-stress, being red values the highest attained.*

3.5.2 Swell by gravity

In the previous example, we considered both fluid inlet and outlet. To get closer to injection, we present the flow of a planar jet emerging from a slit. We consider that the fluid falls by gravity into an air-filled cavity of rectangular shape section. The no-slip condition is imposed on the wall of the slit. Geometry test data is pictured in figure 3.34(a) as well as its finite element discretization (mesh of 13750 nodes and 69395 elements). Two symmetry plans were taken into account, since our purpose was not to capture eventual instabilities, but to compare the response of two types of materials under this situation. Two different materials were thus considered: a viscoelastic versus a viscous fluid. Mass forces were taken into account. Gravity was considered to be acting in the negative $z-$direction. Thus, we consider a viscoelastic compressible flow with inertia effects, and a free surface. Numerical resolution of the Navier-Stokes problem and inertial terms introduction was widely studied by [Saez, 2003] and will not be described here.

The degree of swelling obtained numerically in both cases is shown in figure 3.35. We observe that when the fluid is still inside the slit, the difference between the two cases is very small. Nevertheless, at a later time, after exiting the outflow boundary, differences become noticeable. Furthermore, the effect of gravity is present in both situations: it pulls the fluid down, causing a downstream reduction in the jet diameter.

viscous fluid	viscoelastic
$\rho =$1 g/cm^{-3}	$\rho =$1 g/cm^{-3}
$\eta =$10 Pas	$\eta =$10 Pas
	$G =$1 kPa
	$\theta_b =$5.0E-03 s
	$\theta_s =$2.5E-03 s
	$q =$5

(b)
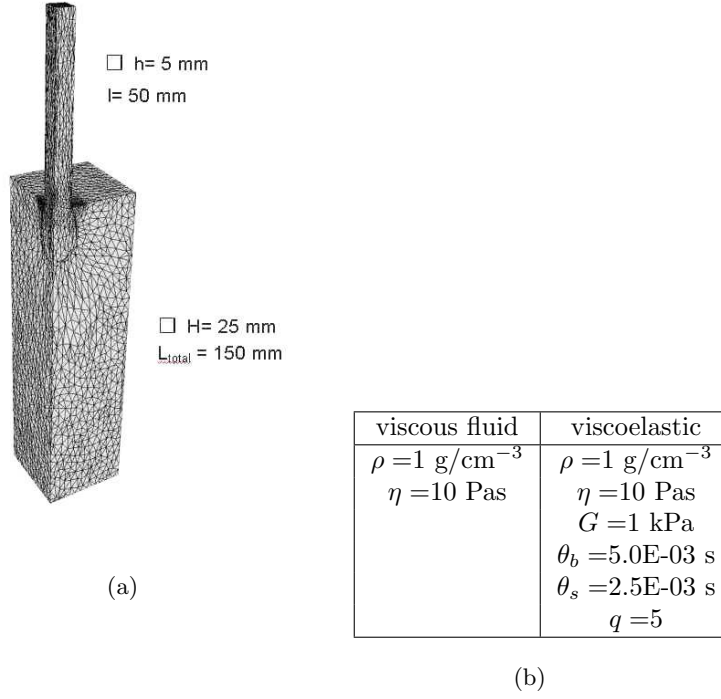
Figure 3.34: *Geometry of the swell under gravity test, as well as material parameters used.*

3.5.3 Jet buckling

To demonstrate that the numerical methods developed can cope with viscoelastic fluids we present a simulation of the buckling of a viscoelastic jet hitting a rigid plate. The equivalent Newtonian problem has been investigated by a number of researchers, and in particular Cruickshank and Munson [Cruickshank and Munson, 1981] have presented numerical results where they argue that a planar jet will buckle if the following restrictions are satisfied

$$Re < 0.56 \qquad \text{and} \qquad \frac{H}{D} > 3\pi \tag{3.52}$$

where Re is the Reynolds number based on the slit width D, and H the height of the inlet above the plate.

In what concerns our computation, the difference from the previous swell example is that there is no symmetry plane - the whole geometry must be taken into account to observe eventual instabilities. Calculations concern a jet injected in a cylindrical cavity of 10 mm of diameter and 15 mm of height, with the inlet slot size of 1mm (so that $\frac{H}{D} = 15$). The material used was the same as for the previous example (see figure 3.34(a)). At the inlet we imposed a constant flow rate of 500 mm3/s, and the components of the extra-stress term was set to zero (corresponding to an isotropic orientation and stretch equal to 1).

Figure 3.36 displays the evolution of the jet. We notice that instabilities occur before the jet hits the plate (as it would not occur, for example, for small viscosity materials). The origin of this instability may be related with a non symmetry of the orientation field towards the revolution axis of the cylinder. This anisotropy induces a dissymmetry in the velocity leading to the buckling initiation. We observe that once the jet has hit the plate, it produces a sort of wave moving upwards and enhancing the buckle. This acceleration thickens the jet producing at the end several folds.
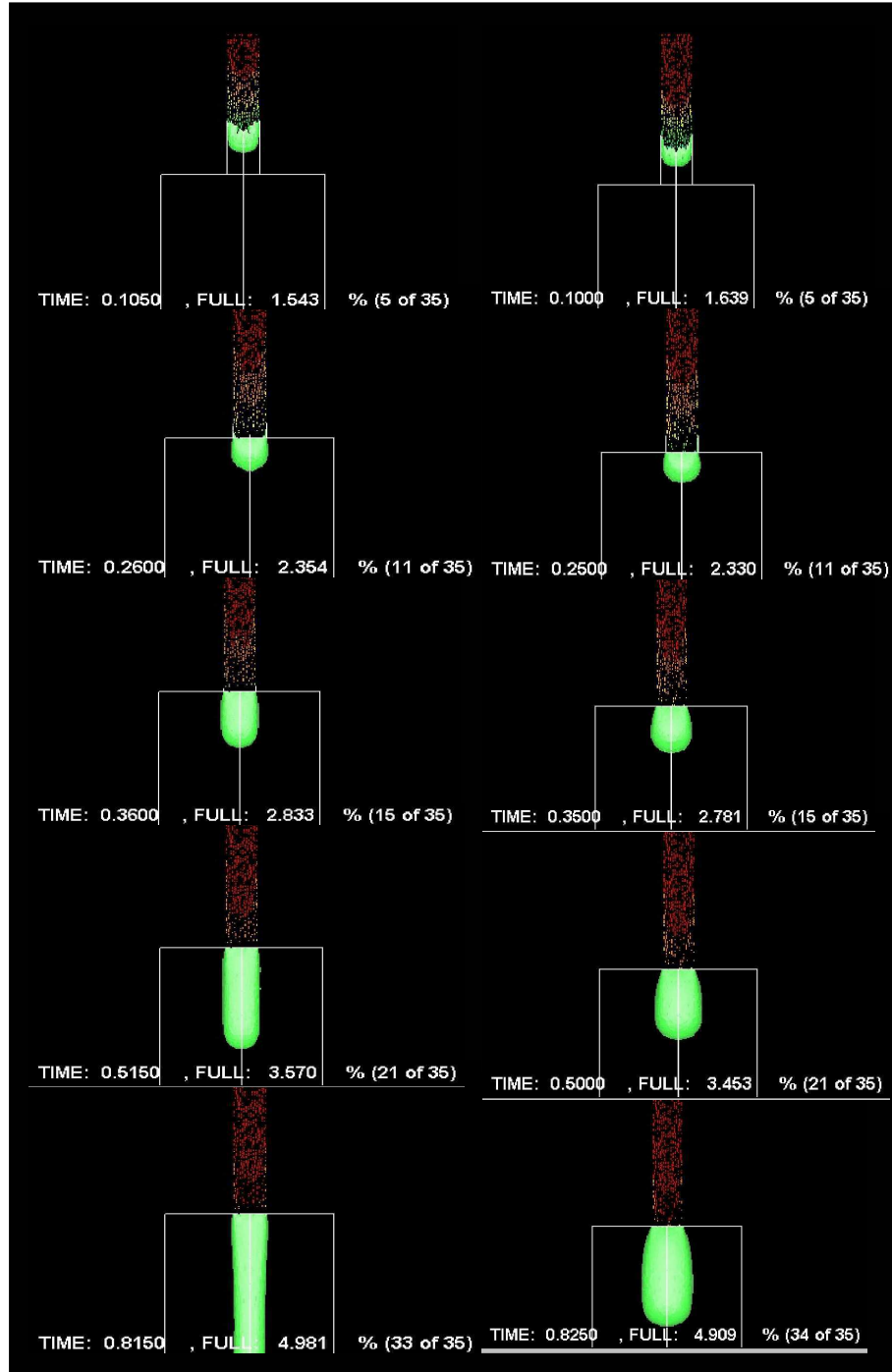
Figure 3.35: *Evolution of the flow front throughout time for the swell test. On the left, the viscoelastic solutions, on the right the newtonian ones.*

(a)　　　　　　　(b)　　　　　　　(c)

(d)　　　　　　　(e)　　　　　　　(f)

(g)　　　　　　　(h)　　　　　　　(i)
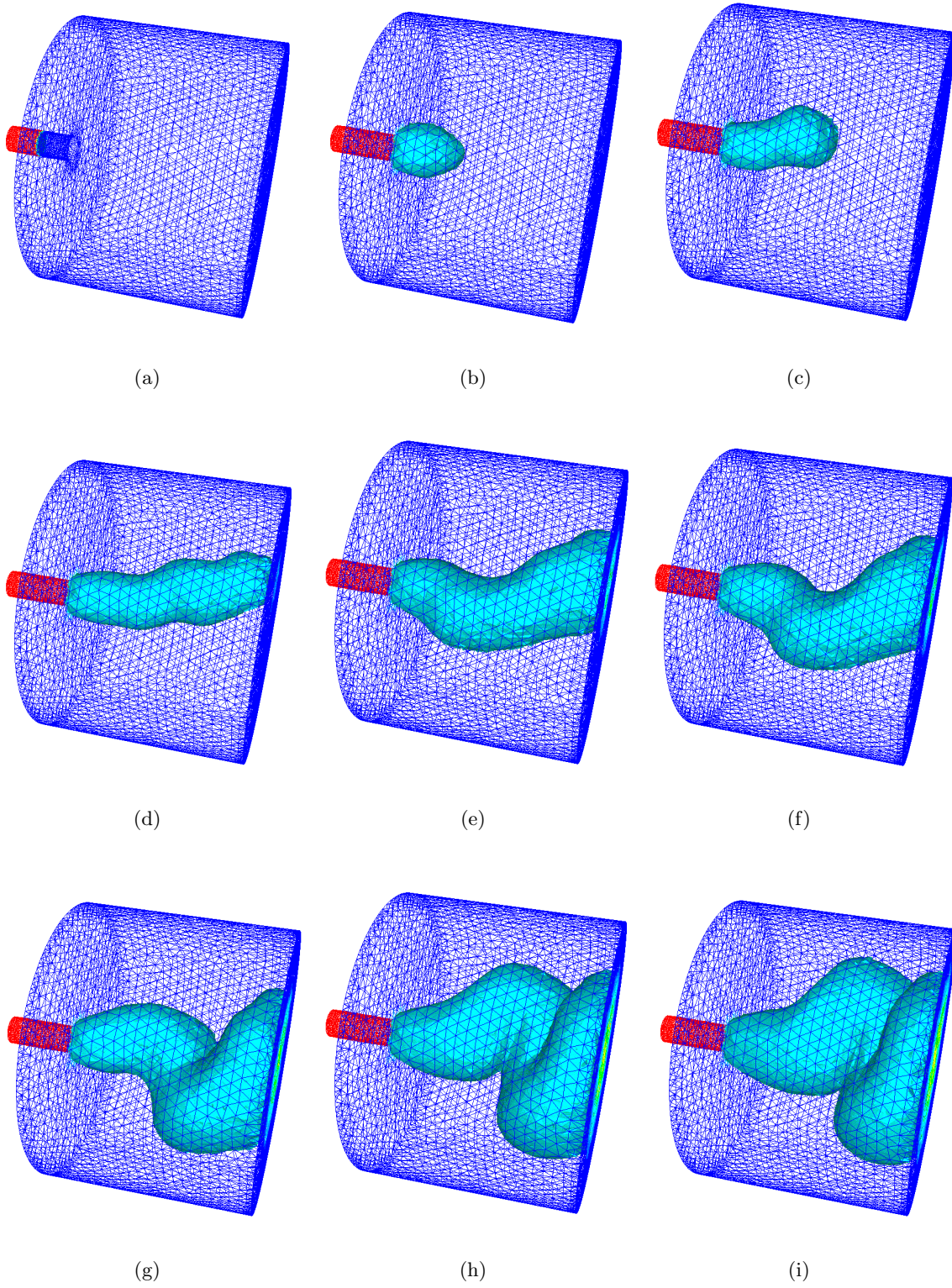
Figure 3.36: *Evolution of the free surface during jet buckling*

3.6   Some remarks on thermal viscoelasticity

Since in injection molding are non-isothermal flows, energy balance for a viscoelastic compressible fluid must be taken into account. However, even if several theoretical works have been done on the subject, each suffer from limitations of universality and/or practicality which can only be overcome by unifying all in a practical entity [Dressler et al., 1999].

In this work, we propose a simple, but coherent thermodynamical model for viscoelastic compressible flow, where the viscoelastic behavior is given by a modified version of the Pom-Pom model.

The main difficulty with the establishment of the energy equation for this particular case is that a part of the energy is stored and a part of it is dissipated. A short review of the most important works in this field is synthesized, followed by thermodynamical considerations, and our approach.

3.6.1   Thermodynamic point of view of non-isothermal viscoelasticity and state of the art

First thermomecanical models were derived from the Leonov model and the deformation field method. As in [Leonov, 1976], let us introduce the material's reference (Ω_0), current ($\hat{\Omega}$) and relaxed (Ω) configurations. The prime assumption made by Leonov [Leonov, 1976] was that the deformation tensor $\mathbf{F}$ relating the current to the reference configuration can be decomposed in an *elastic* or recoverable ($\mathbf{F}_e$) and an *irreversible* part ($\mathbf{F}_p$), such that

$$\mathbf{F} = \mathbf{F}_e \cdot \mathbf{F}_p \tag{3.53}$$

Associated with $\mathbf{F}$, $\mathbf{F}_e$ and $\mathbf{F}_p$, the corresponding Finger tensors are:

$$\mathbf{B}_e = \mathbf{F} \cdot \mathbf{F}^T \quad \text{and} \quad \mathbf{B}_e = \mathbf{F}_e \cdot \mathbf{F}_e^T \tag{3.54}$$

In this, $\mathbf{B}_e$ represents the Finger strain tensor of the current configuration with respect to the relaxed configuration. Let $\nabla \mathbf{v}$ be the global velocity gradient tensor. $\nabla \mathbf{v}$ is decomposed in an elastic and an irreversible part:

$$\nabla \mathbf{v} = \nabla \mathbf{v}_e + \nabla \mathbf{v}_p \tag{3.55}$$

and it can be derived:

$$\frac{\partial \mathbf{B}_e}{\partial t} = \nabla \mathbf{v}_e \cdot \mathbf{B}_e + \mathbf{B}_e \cdot \nabla \mathbf{v}_e^T \tag{3.56}$$

In the incompressible case, volumetric changes may be separated from deviatoric responses by the kinematic split [Simo, 1987]:

$$\bar{\mathbf{F}}_e = J^{-\frac{1}{3}} \mathbf{F}_e \tag{3.57}$$

to obtain an evolution equation in the volumetric part of the Finger strain tensor, $\mathbf{B}_e$, as it has been done in [Flaman, 1990] and [Baaijens, 1991], for example. From this approach, a constitutive law can be obtained as well as a specific form of the energy equation. However, it remains close to solid mechanics formulation, adequate in a Lagrangian context resolution.

More recent work [Peters and Baaijens, 1997], [Wapperon and Hulsen, 1998], [Ottinger, 2001] and [Ammar, 2001], use a thermodynamical approach to derive an appropriate form of the energy equation, using molecular models.

[Peters and Baaijens, 1997] and [Wapperon and Hulsen, 1998] used the *the conformation tensor* ($\mathbf{c} = <\mathbf{pp}>$) as variable, in analogy to the Finger elastic tensor. [Peters and Baaijens, 1997] considered that the end-to-end vector $\mathbf{p}$ of a polymer molecular chain follows an evolution equation of the type

$$\frac{d\mathbf{p}}{dt} = \nabla \mathbf{v} \mathbf{p} - \mathbf{L} \mathbf{p} \qquad (3.58)$$

where $\mathbf{L}$ is a function of averaged (thus macroscopic) variables, i.e., stress, strain or strain rate. The term $-\mathbf{L}\mathbf{p}$ represents the slippage of the molecular element with respect to the continuum, and $\mathbf{L}$ is often referred as the slip tensor. In practice, $\mathbf{L}$ depends on the chosen constitutive equation (for example, $\mathbf{L} = \mathbf{0}$ corresponds to an hyperelastic behavior). [Peters and Baaijens, 1997] were led to a Phan-Thien-Tanner (PTT) constitutive model, and to the energy equation:

$$\rho c_p \frac{dT}{dt} = -\nabla \cdot \phi + \alpha \tau : \varepsilon(\mathbf{v}) + (1 - \alpha) \frac{\text{tr}(\tau)}{2\theta} \qquad (3.59)$$

where ϕ is the heat flux, $\alpha \tau : \varepsilon(\mathbf{v})$ corresponds to the elastic entropy and $(1 - \alpha)\frac{\text{tr}(\tau)}{2\theta}$ expresses the distribution of the elastic energy. The authors considered also that the relaxation times depend on temperature, i.e., $\theta = \theta(T)$.

[Wapperon and Hulsen, 1998] extended [Peters and Baaijens, 1997] approach to compressible materials, without directly coupling compressibility and viscoelasticity.

[Ottinger, 2001] presented a more generic form by considering that the thermodynamical state of a system is described through a vector of state variables $\mathbf{y}$:

$$\mathbf{y} = (\rho, \mathbf{v}, e, \mathbf{c}) \qquad (3.60)$$

The authors deduced that the time evolution of any isolated thermodynamic system is given in the form:

$$\frac{d\mathbf{y}}{dt} = \mathbf{L}\frac{\partial E(\mathbf{y})}{\partial \mathbf{y}} + \mathbf{M}\frac{\partial S(\mathbf{y})}{\partial \mathbf{y}} \qquad (3.61)$$

where E represents the total energy of the system and and S its total entropy, both expressed in terms of the state variables ($\mathbf{y}$). $\mathbf{L}$ and $\mathbf{M}$ are the Poisson and friction matrices, chosen in such a way that:

- the first equation of system 3.61 expresses incompressibility;

- the second equation gives the Navier-Stokes equations;

- the third equation provides the first principle of thermodynamics and thus, the energy equation;

- the last one represents the constitutive equation for the material's viscoelastic behavior. We notice that the model approaches the Pom-Pom model of [McLeish and Larson, 1998], and the authors called it the "Pom-Pon model".

Finally, A. Ammar [Ammar, 2001] defined a thermodynamical formalism to describe a viscoelastic incompressible behavior with the Pom-Pom model. Basically, the author considered an eulerian configuration and the definition of a material element conservative transformation. This transformation gives the expression of the conjugate forces, that, on the other hand allow the definition of the Helmoltz free energy and the dissipation pseudo-potential. Since this approach, even with some approximations, is close to the model chosen, we need to generalize it to compressible materials. To better understand the associated thermodynamical formalism associated, we introduce its basis in Appendix B, generalizing to all types of materials.

In this section, we derive the heat equation for a viscoelastic compressible material, using the definitions above. The procedure followed is:

- definition of the internal variables (the temperature and the mechanical state variables), (T, z_i);

- definition of the mechanical entropy production Π_s, where $T\Pi_s = \sigma : \varepsilon(\mathbf{v}) - \mathbf{Z} : \dfrac{d\mathbf{z}}{dt}$;

- determination of the conjugate forces Z_i, by considering the extreme case $T\Pi_s = 0$;

- verification of the second principle of thermodynamics;

- from the Gibbs equation, and the variation of entropy we obtain the variation of internal energy
$$\rho T\frac{\partial s}{\partial T}\frac{dT}{dt} + \mathbf{Z} : \frac{d\mathbf{Z}}{dt} - T\frac{\partial \mathbf{Z}}{\partial T} : \frac{d\mathbf{z}}{dt};$$

- using the conservation of energy equation (equation B.6, Appendix B) we derive the heat equation.

3.6.2 Temperature equation for viscoelastic compressible flows

Formulation of the Pom-Pom model with a conformation tensor

Let us consider a single Pom-Pom molecule (figure 3.13). A part of the backbone tube is defined as the dimensionless connector vector $\mathbf{u}$, with a dimensionless length or stretch λ in the direction $\mathbf{p}$.

$$\mathbf{u} = \Lambda\mathbf{p} \tag{3.62}$$

We define the conformation tensor $\mathbf{c}$ as the average of all the connector vectors $\mathbf{u}$ over the distribution space:

$$\mathbf{c} = \langle\mathbf{u}\mathbf{u}\rangle = \langle\lambda\mathbf{p}\lambda\mathbf{p}\rangle = \lambda^2\langle\mathbf{p}\mathbf{p}\rangle = \lambda^2\mathbf{s} \tag{3.63}$$

with $\mathbf{s}$ the orientation tensor, previously defined. The extra-stress tensor definition can be rewritten as:

$$\tau = G(3\lambda^2\mathbf{s} - \mathbf{I}) = G(3\mathbf{c} - \mathbf{I}) \tag{3.64}$$

Furthermore, we know that:

$$\mathbf{s} = \frac{\mathbf{c}}{\lambda^2} = \frac{\mathbf{c}}{\mathrm{tr}(\mathbf{c})} \tag{3.65}$$

Using this expression and the evolution equation of the orientation, we obtain the evolution equation of the conformation tensor:

$$\frac{1}{\mathrm{tr}(\mathbf{c})}\frac{d\mathbf{c}}{dt} - \frac{\mathbf{c}}{\mathrm{tr}(\mathbf{c})^2}\frac{d\mathrm{tr}(\mathbf{c})}{dt} - [\nabla\mathbf{v}\frac{\mathbf{c}}{\mathrm{tr}(\mathbf{c})} - \frac{\mathbf{c}}{\mathrm{tr}(\mathbf{c})}\nabla\mathbf{v}^T] + 2[\frac{\mathbf{c}}{\mathrm{tr}(\mathbf{c})} : \varepsilon(\mathbf{v})]\frac{\mathbf{c}}{\mathrm{tr}(\mathbf{c})} + \frac{1}{\theta_b}(\frac{\mathbf{c}}{\mathrm{tr}(\mathbf{c})} - \frac{\mathbf{I}}{3}) = 0$$

or

$$\frac{d\mathbf{c}}{dt} - \nabla\mathbf{v}\mathbf{c} - \mathbf{c}\nabla\mathbf{v}^T + \frac{1}{\theta_b}(\mathbf{c} - \mathrm{tr}(\mathbf{c})\frac{\mathbf{I}}{3}) = \frac{\mathbf{c}}{\mathrm{tr}(\mathbf{c})}(\frac{d\mathrm{tr}(\mathbf{c})}{dt} - 2[\mathbf{c} : \varepsilon(\mathbf{v})])$$

$$\tag{3.66}$$

The first term in the right-hand side of the last equation is identical to (considering large stretch relaxation values):

$$\frac{d\mathrm{tr}(\mathbf{c})}{dt} = 2\lambda\frac{d\lambda}{dt} = -2[\mathbf{c} : \varepsilon(\mathbf{v})] \tag{3.67}$$

and therefore the global right-side is zero. The evolution equation for the conformation tensor of our Pom-Pom model is written:

$$\frac{d\mathbf{c}}{dt} - \nabla\mathbf{v}\mathbf{c} - \mathbf{c}\nabla\mathbf{v}^T + \frac{1}{\theta_b}(\mathbf{c} - \mathrm{tr}(\mathbf{c})\frac{\mathbf{I}}{3}) = 0 \tag{3.68}$$

Temperature equation of a one-mode fluid

Let us also suppose that we have one only mode, and thus one conformation tensor, whose evolution satisfies equation 3.68. For a viscoelastic compressible material, the state variables are the temperature T, the density ρ, and the conformation tensor $\mathbf{c}$. The Gibbs equation is:

$$\rho\frac{de}{dt} = \rho T\frac{ds}{dt} + \frac{p}{\rho}\frac{d\rho}{dt} + \mathbf{Z_c} : \frac{d\mathbf{c}}{dt} \tag{3.69}$$

and the equations of state for the conjugate variables

$$s = -\frac{\partial f}{\partial T} \quad p = -\rho^2\frac{\partial f}{\partial \rho} \quad \mathbf{Z_c} = \rho\frac{\partial f}{\partial \mathbf{c}} \tag{3.70}$$

The entropy production is, in this case (see Appendix B, equation B.47):

$$T\Pi_s = -\frac{\phi}{T}\cdot\nabla T + \tau_s : \varepsilon(\mathbf{v}) + \tau : \varepsilon(\mathbf{v}) - \mathrm{tr}(2\mathbf{Z_c}\cdot\varepsilon(\mathbf{v})) + \frac{1}{\theta_b}\mathrm{tr}(\mathbf{Z_c}\cdot[\mathbf{c} - \mathrm{tr}(\mathbf{c})\frac{\mathbf{I}}{3}]) \tag{3.71}$$

where τ_s represents the contribution of the solvent part to the mechanical dissipation. Considering that in the high elasticity extreme state ($\theta_b \to \infty$) there is no mechanical dissipation at equilibrium, we obtain a zero mechanical dissipation from equation 3.71, $\forall\nabla T, \forall\varepsilon(\mathbf{v})$, if:

$$\tau = 2\mathbf{Z_c}\mathbf{c} \quad \text{and} \quad \mathbf{Z_c} = \frac{1}{2}(3\mathbf{I} - \mathbf{c}^{-1}) \tag{3.72}$$

To verify if the second thermodynamical principle is respected, we need to checkout that:

$$\frac{1}{\theta_b}\mathrm{tr}(\mathbf{Z_c}\cdot[3\mathbf{c} - \mathbf{I}]) \geq 0 \tag{3.73}$$

In fact,

$$\frac{1}{\theta_b}\mathrm{tr}(\mathbf{Z_c}\cdot[3\mathbf{c} - \mathbf{I}]) = \frac{G}{2\theta_b}[\frac{1}{3}\mathrm{tr}(\mathbf{c})\mathrm{tr}(\mathbf{c}^{-1}) - 3] \tag{3.74}$$

We can easily prove that $[\frac{1}{3}\mathrm{tr}(\mathbf{c})\mathrm{tr}(\mathbf{c}^{-1}) - 3] \geq 0$, and thus that the mechanical dissipation is also positive or zero. Figure 3.37 is a representation of the function $f(x, y) = \frac{1}{3}(x+y+z)(1/x+1/y+1/z)-3$ for $z = 0.1$, with $x, y, z > 0$ being the eigenvalues of $\mathbf{c}$, and thus $\mathrm{tr}(\mathbf{c}) = x + y + z$.
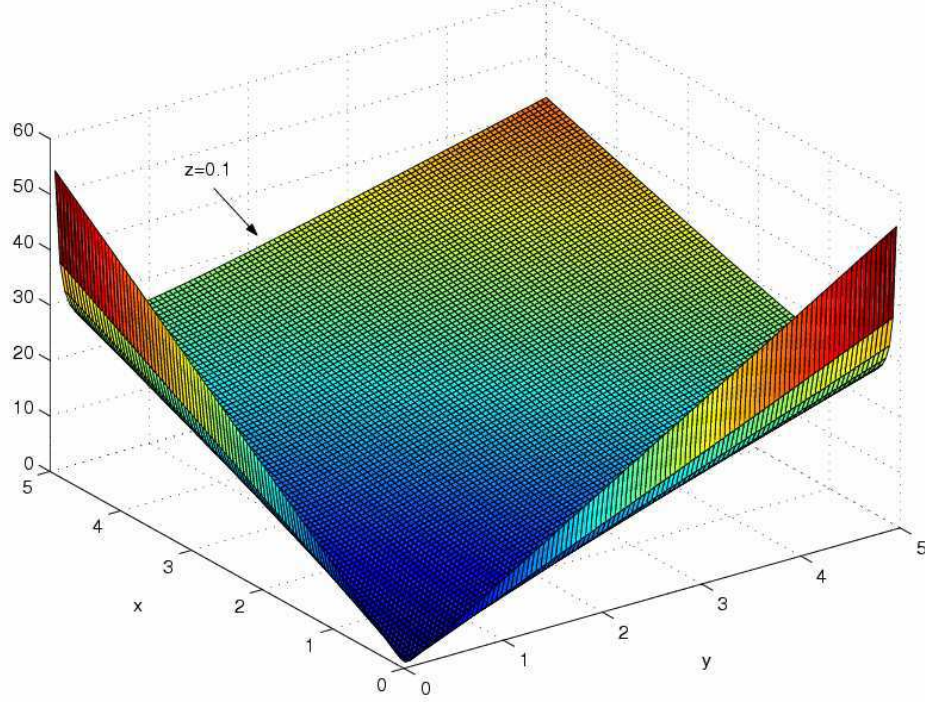
Figure 3.37: *Representation of the function $f(x,y) = \frac{1}{3}(x + y + z)(1/x + 1/y + 1/z) - 3$ for $z = 0.1$.*

We introduce the following material parameter definitions:

$$c_p = T(\frac{\partial s}{\partial T})_{p,\mathbf{c}} \quad \chi_T = -\frac{1}{\rho}(\frac{\partial \rho}{\partial T})_{p,\mathbf{c}} \tag{3.75}$$

where c_p is the heat capacity at constant pressure and conformation tensor $\mathbf{c}$, and χ_T is the thermal expansion coefficient. The internal energy variation is given by the Gibbs equation and the variation of entropy definition, as in Appendix B, equation B.54:

$$\rho\frac{de}{dt} = \rho c_p\frac{dT}{dt} - p\nabla\cdot\mathbf{v} - T\chi_T\frac{dp}{dt} + \mathbf{Z_c} : \frac{d\mathbf{c}}{dt} - T\frac{\partial\mathbf{Z_c}}{\partial T} : \frac{d\mathbf{c}}{dt} \tag{3.76}$$

The temperature equation is obtained through the energy balance equation

$$\rho c_p\frac{dT}{dt} - p\nabla\cdot\mathbf{v} - T\chi_T\frac{dp}{dt} + \mathbf{Z_c} : \frac{d\mathbf{c}}{dt} - T\frac{\partial\mathbf{Z_c}}{\partial T}\frac{d\mathbf{c}}{dt} = -\nabla\cdot\phi + \sigma : \varepsilon(\mathbf{v}) \tag{3.77}$$

or

$$\rho c_p\frac{dT}{dt} - T\chi_T\frac{dp}{dt} - T\frac{1}{G}\frac{\partial G}{\partial T}(\tau : \varepsilon(\mathbf{v})) = -\nabla\cdot\phi + \tau_s : \varepsilon(\mathbf{v}) + \frac{G}{2\theta}[\frac{1}{3}\mathrm{tr}(\mathbf{c})\mathrm{tr}(\mathbf{c}^{-1}) - 3] \tag{3.78}$$

Remarks:

On the left-hand side we have the change of internal energy stored (or released) by the material. If the elastic modulus G is not dependent on the temperature, and the mechanical energy is stored (or released) as internal energy. The material is then said *energy elastic* [Wapperom, 1996]. If the elastic modulus G is linearly dependent on the temperature, $G = G(T)$, the fluid is said *entropy elastic* [Wapperom, 1996]. The reversible part of the internal energy is stored as entropy, which is reached with a (reversible) temperature rise.

Furthermore, the added term is finally similar to the dilatation contraction one introduced in Chapter 2, and we can simplify:

$$T\chi_T \frac{dp}{dt} + T\frac{1}{G}\frac{\partial G}{\partial T}(\tau : \varepsilon(\mathbf{v})) = [\chi_T \frac{dp}{dt} + \frac{1}{G}\frac{\partial G}{\partial T}(\tau : \varepsilon(\mathbf{v}))]T = bT$$

where b is explicitly computed at each time step, and chose piecewise constant per element.

> *The temperature equation for a viscoelastic compressible material, with a constitutive law of the Pom-Pom type $\tau = G(3\lambda^2\mathbf{s} - \mathbf{I})$, may be written:*
>
> $$\rho c_p \frac{dT}{dt} - T\chi_T \frac{dp}{dt} - T\frac{1}{G}\frac{\partial G}{\partial T}(\tau : \varepsilon(\boldsymbol{v})) = -\nabla\cdot\phi + \tau_s : \varepsilon(\boldsymbol{v}) + \frac{G}{2\theta}[\frac{1}{3}tr(\mathbf{c})\,tr(\mathbf{c}^{-1}) - 3]$$

3.6.3 Extension to a multi-mode constitutive equation

We suppose that there is no interdependence between the different modes of the model. Thus, we can define one internal variable corresponding to the internal conformation tensor of each mode: $\mathbf{c}_i = \lambda_i\mathbf{s}_i$. The temperature equation is:

$$\rho c_p \frac{dT}{dt} - T\chi_T \frac{dp}{dt} - T\sum_i^m \frac{1}{G_i}\frac{\partial G_i}{\partial T}(\tau_i : \varepsilon(\mathbf{v})) = -\nabla\cdot\phi + \tau_s : \varepsilon(\mathbf{v}) + \sum_i^m \frac{G_i}{2\theta_i}[\frac{1}{3}tr(\mathbf{c}_i)tr(\mathbf{c}_i^{-1}) - 3] \quad (3.79)$$

where m is the number of modes.

3.6.4 Thermorheological simple behavior

The material coefficients and the rheological parameters may depend on the state variables. [Wapperom, 1996] suggests the following relations for the different parameters (only in the temperature region $T > T_g$, and for amorphous polymers):

- *Temperature dependence of the relaxation time and viscosity*
  The viscosity and the relaxation time have almost the same behavior for different temperatures. It can be described by a shift factor a_T, which is an exponential function of temperature:
  1) the WLF shift factor, $a_T = \exp{(-C_1\frac{T - T_{ref}}{C_2 + T - T_{ref}})}$
  2) the Arrhenius shift factor, $a_T = \exp{[C_1(\frac{1}{T} - \frac{1}{T_{ref}})]}$

- *Temperature dependence of the relaxation modulus*
  The relaxation modulus, $G = \frac{\eta}{\theta}$ is only a weak function of temperature. From the kinetic theory of elastic dumbells, the relaxation modulus needs to be scaled by:
  $$G = G(\rho, T) = \frac{\rho T}{\rho_{ref} T_{ref}} G_{ref}$$

In our case, the solvent viscosity and the relaxation modulus are supposed function of the temperature either by the WLF and the Arrhenius law, for temperatures greater than the solid-liquid transition temperature.

For smaller temperatures, we need to consider a more complex behavior of the solid state, not included in this work. In our case, we simply freeze the conformation tensor.

For $T > T_t$

$$\eta(T) = \eta(T_{ref}) a_T(T)$$

$$\theta(T) = \theta(T_{ref}) a_T(T)$$

$$G(T) = G(T_{ref}) \frac{\rho(T) T}{\rho_{ref} T_{ref}}$$

$$\frac{d\mathbf{s}}{dt} - \nabla \boldsymbol{v} \mathbf{s} - \mathbf{s} \nabla \boldsymbol{v}^T + 2[\varepsilon(\boldsymbol{v}) : \mathbf{s}]\mathbf{s} + \frac{1}{\theta_b}(\mathbf{s} - \frac{\mathbf{I}}{3})$$

$$\frac{d\lambda}{dt} - \lambda[\varepsilon(\boldsymbol{v}) : \mathbf{s}] + \frac{1}{\theta_s}(\lambda - 1) = 0$$

For $T < T_t$

$$\eta(T) = \eta(T_{ref}) a_T(T_t)$$

$$\theta(T) = \theta(T_{ref}) a_T(T_t)$$

$$G(T) = G(T_{ref}) \frac{\rho(T) T}{\rho_{ref} T_{ref}}$$

$$\frac{d\mathbf{s}}{dt} - \nabla \boldsymbol{v} \mathbf{s} - \mathbf{s} \nabla \boldsymbol{v}^T + 2[\varepsilon(\boldsymbol{v}) : \mathbf{s}]\mathbf{s} = 0$$

$$\frac{d\lambda}{dt} - \lambda[\varepsilon(\boldsymbol{v}) : \mathbf{s}] = 0$$

where T_t is the liquid-solid transition temperature (T_g in the case of an amorphous material).

We remark that the relaxation modulus is function of the density, translating a small coupling between compressibility and viscoelasticity.

This rests a simple thermoviscoelastic model implemented in **REM3D**. We are aware that a deeper study (namely on the quality of the results obtained, and the sensitivity to the material parameters) need to be performed.

3.7   Conclusions

We conclude that an efficient viscoelastic compressible flow model was introduced than **REM3D**. We sintethize the material behavior modelling, by drawing the basic features of the multi-mode Pom-Pom model, that has been implemented to treat the non-linear viscoelastic behavior; the computational methods used to solve the viscoelastic compressible flow problem were also detailed. Two basic problems appeared demanding solution: the present of convective terms in constitutive equations, and strong non-linearity when we consider the coupled problem. A splitting method allows separate resolution of the evolution equations (through a Space-Time Discontinuous Galerkin finite element method) from the flow equations, using mixed finite elements. Validation tests performed on 'benchmark' geometries (like the contraction or contraction/expansion flow) were analyzed.

Extension to free surface flows was illustrated through several examples, giving also a measure of the potential of the models implemented, and the perspectives of future works. In the next chapter, we will show the application in injection molding flows.

Chapter 4

Applications in injection molding

Contents

Injection molding can be studied by considering the non-steady flow of a viscous or viscoelastic polymer. In this chapter we approach the real injection molding situation. Validation tests and injection molding comparisons illustrate this point.

The first part concerns injection molding of viscous compressible fluids. Comparison with the literature and experiments through the pressure plots provide a good information about the models implemented.

The second part of this chapter gives a more qualitative information about the state of the part at the end of the injection molding cycle, specially for viscoelastic material behavior.
Finally, we conclude on the quality and the utility of the results obtained.

4.1   The general injection molding problem

As said previously, the main purposes in our injection molding examples are the determination of:

1) the position of the flow front;
2) the thermodynamical state of the material represented by the pressure distribution and traces throughout the process, the temperature distribution and the molecular conformation (orientation and stretch);
3) a measure of the distribution of the shrinkage rate in the part at the moment of the ejection;
4) a measure of the stress distribution.

Thus, viscoelastic and compressible models implemented and described previously need to be fitted in an injection molding context. Evolution of the polymer inside the mold cavity is computed using a multi-domain formulation: let us consider a global computational domain $\Omega \subset \mathbb{R}^d$ (d is the spatial dimension) that is composed by several subdomains $\Omega_i(t) \subset \Omega$ closed and bounded: $\Omega_f(t)$ is the subdomain occupied by the polymer, $\Omega_a(t)$ is the subdomain corresponding to the air, $\Omega_m(t)$ is the subdomain corresponding to the mould. Each domain evolves throughout time, so that our true computational domain is $\mathcal{D} = \Omega \times [0, \Theta]$. The spatial boundaries $\partial\Omega_i$ move with the velocity of the fluid particles at each boundary, giving $\partial\Omega(t)$.
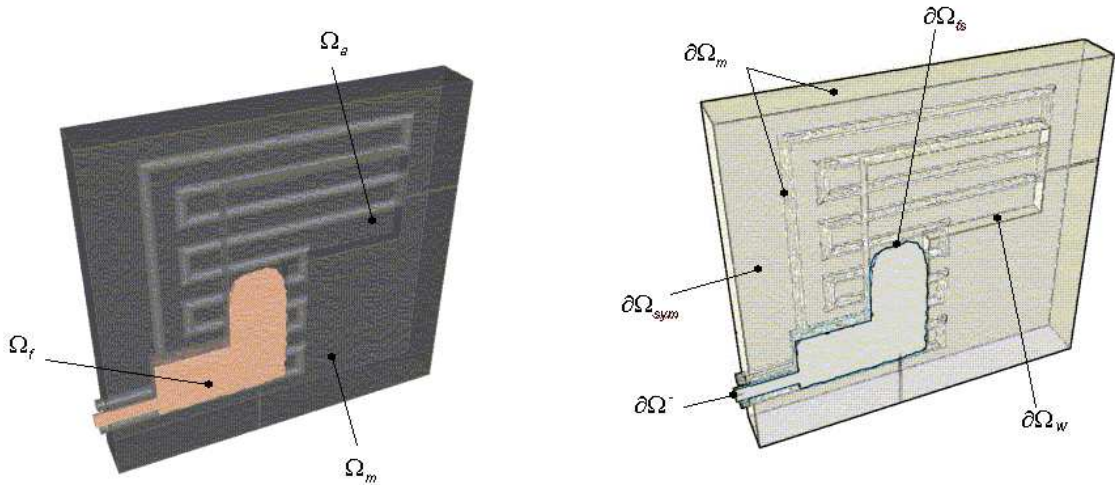
Figure 4.1: *Spatial computational domain Ω, subdivided in polymer Ω_f, mold Ω_m or air Ω_a.*

Equations ruling the behavior of the material behavior of the polymer have been introduced in the previous chapter, applied to the polymer domain. We consider a viscoelastic compressible behavior and *we want to compute* $(\boldsymbol{v}, p, T, \mathbf{s}, \lambda)(x, t), \forall \Omega_f \times [0, \theta]$.

We remark that models implemented rest valid in the liquid state. Once the polymer has solidified, a simple behavior has been assumed, and will be object of future works.

STRUCTURE FOR AN INJECTION CYCLE COMPUTATION

Initialisations
read geometry data
read material data
read boundary conditions
read initial conditions
read simulation data

for each time step **do**

    knowing the initial configuration, compute velocity and pressure
    compute mesh velocity
    compute evolution of the flow front
    compute temperature
    compute extra-stress tensor
    compute orientation
    compute stretch

    check commutation
    update boundary conditions
    update time step

end for

4.2   Comparison with the literature

A first numerical test case concerns the injection of a plaque (length=76.2 mm, width=32.1 mm, height=2.54 mm), which has been studied both experimentally and numerically [Chiang et al., 1991]. Figure 4.2 describes the plaque geometry, preceded by a reservoir of large size, fed by a circular section channel. Three pressure measure points have been considered: one in the feeding zone, and two in the plaque located at 25.4 mm and 61.6 mm of the cavity entrance. The material is a polypropylene, Profax 6323 from Himont, with properties detailed in table 4.1.
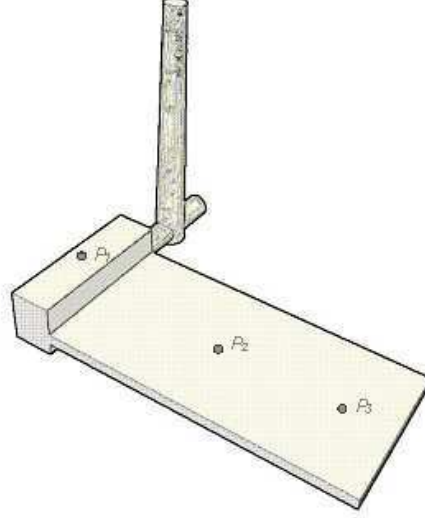
Figure 4.2: *Plaque geometry and location of pressure transducers.*

The polymer was injected at constant flow rate (filling time Δt=0.69s) and kept at constant pressure during the packing stage. Two different packing pressures are considered: 50 and 25 MPa. The holding time is 10 s or 15 s, the injection temperature is 200°C, and the mold temperature is 20°C. Computations were performed using a mesh with 16526 elements and 91075 nodes.

Viscosity		
m	0.3135	
τ^*	1.10E+04	Pa
D_1	1.96E14	Pas
D_2	-10.0	^oC
D_3	1.3E07	$^oC/Pa$
A_1	30.9	
$\widetilde{A}_2$	51.6	^oC
Specific heat		
c	2280	J/kg^oC
Conductivity		
k_1	0.196	W/m^oC

Density		
b_{1_l}	1.246E-03	m^3/kg
b_{2_l}	9.03E-07	m^3/kg^oC
b_{3_l}	9.28E7	Pa
b_{4_l}	4.07E-03	$^oC^{-1}$
b_{1_s}	1.16E-03	m^3/kg
b_{2_s}	3.57E-07	m^3/kg^oC
b_{3_s}	2.05E08	Pa
b_{4_s}	2.49E-03	$^oC^{-1}$
b_5	123.0	^oC
b_6	2.25E-07	$^oC/Pa$
b_7	8.70E-05	m^3/kg
b_8	5.37E-01	$^oC^{-1}$
b_9	1.26E-07	Pa^{-1}

Table 4.1: *PP (Profax6323) material properties.*

Numerical short-shots

Figure 4.3 shows the evolution of the flow front during the filling stage. The polymer enters the reservoir and fills the plaque uniformly. The filling pattern is as expected, with a well-defined 3D flow front region.

Pressure traces and sensitivity to the packing pressure

Figure 4.4 illustrates the pressure traces obtained by H. Chiang and co-workers [Chiang et al., 1991]. It shows the pressure on the three transducers as a function of time, and comparisons with our calculation. The continuous lines represent their experimental results, the black points the authors' numerical ones, and the colored points represent **REM3D** results.

The agreement is fair and comparable with the literature. We notice that **REM3D** values are close to the ones obtained numerically by the referred authors, except for transducer P1, for which H. Chiang did not present any result. In what concerns comparison with the experiments, we show a good tendency, being P2 quite well approximated.

For a thermoplastic semi-crystalline polymer, results concerning the pressure distribution obtained by **REM3D** *are in agreement with the literature. We conclude on the validity of the numerical methods implemented to extend* **REM3D** *from filling to the post-filling stage in this type of materials.*

(a)	(b)	(c)
(d)	(e)	(f)
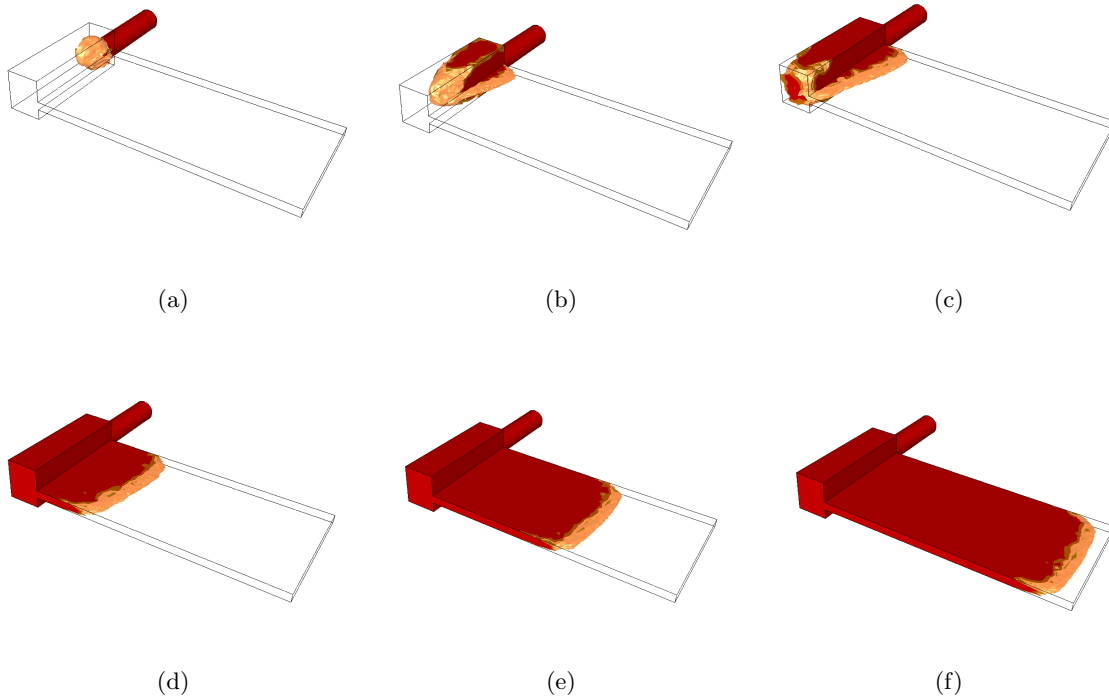
Figure 4.3: *Filling of the plaque.*
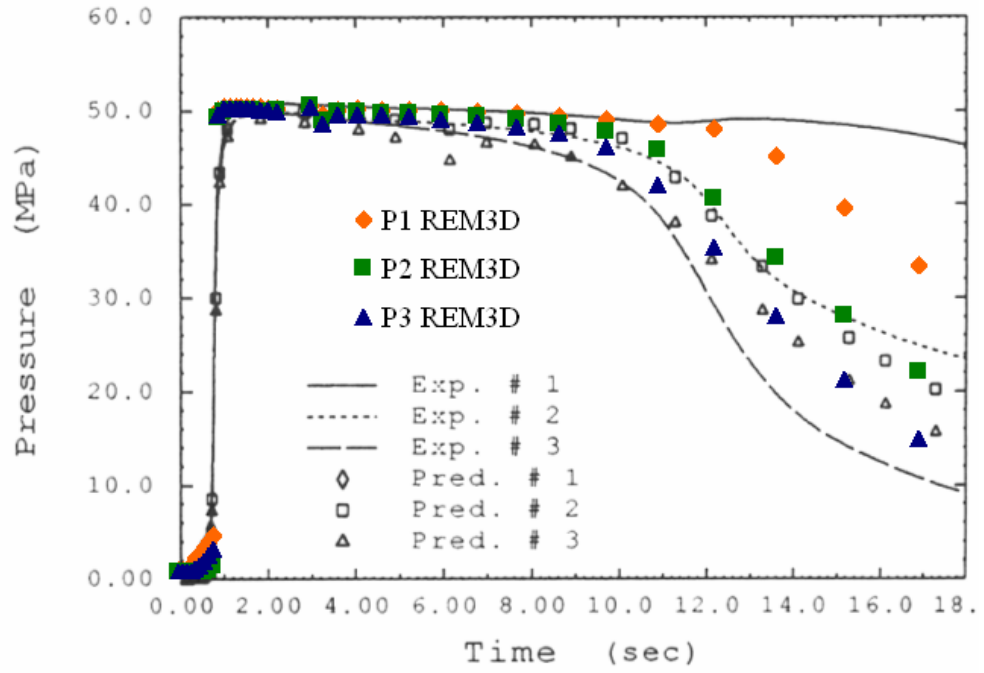
(a)
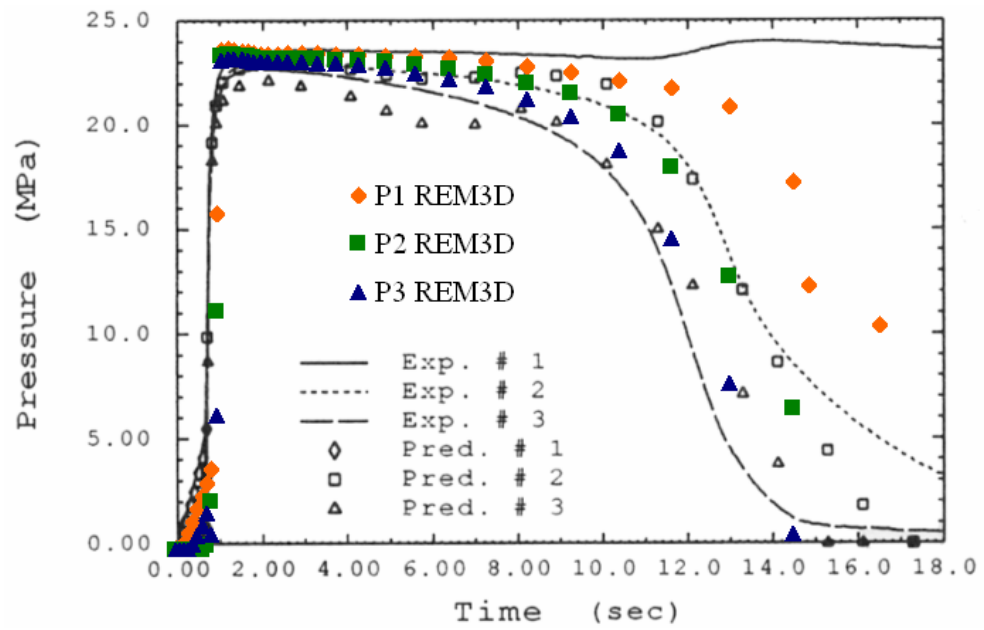
(b)

Figure 4.4: *Pressure in the transducers for two different holding pressures: (a) 50 MPa and (b) 25 MPa.*

4.3 Experimental results and comparison with simulation

To validate the numerical developments presented before on injection molded samples, we performed experiments on one industrial part at the CERDATO (Centre de Recherche Atofina).

For the geometry considered, two different materials were chosen, and tested under several injection conditions.
Numerical simulation for certain molding conditions was performed, and compared with the experimental results obtained.

4.3.1 Molds and equipment

The mold used in these experiments has been proposed by Schneider Electric. It is representative of electrical devices with difficulties encountered during its molding, like thin side walls or contraction-expansion zones (figure 4.5). The mold has a double-cavity, but only one was used in this study (the entry to the other cavity was blocked). The mold was equipped with one pressure transducer (figure 4.5).

transducer location

blocked cavity entry
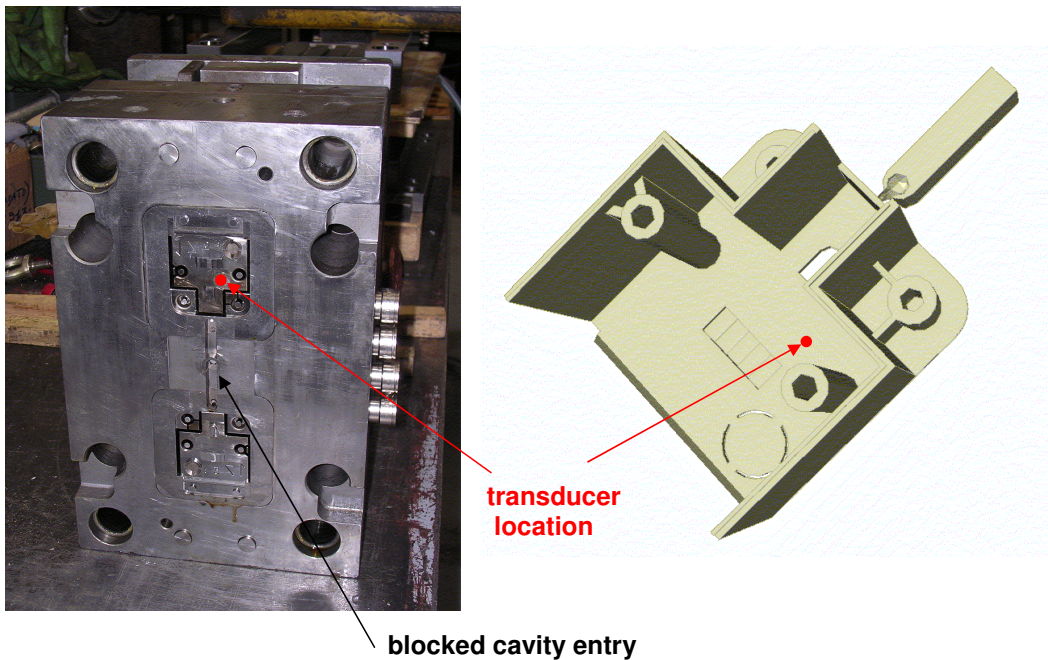
Figure 4.5: *Geometry of the Schneider prototype part, mold cavity, schematic cavity geometry and transducer location.*

The monitoring of pressure was done through a instrumentation system using one pressure sensor in the cavity (Kistler 6157A).

The acquisition and monitoring of the signal measured by the sensors was based on a data acquisition board and the ATS software for data handling and visualization of the signal and its condition, and amplifiers.

In each cycle the monitoring process was triggered by a switch activated by the operator. The pressure data were recorded at 10 tests/condition, and at a velocity of 100 data acquisitions per second.
A typical result of the pressure evolution measured in the mold during the filling and post-filling stages is shown on figure 4.6, for both materials. Results concerning the sensitivity of this trace to the processing conditions will be shown later in this chapter.

We notice that for polystyrene there is a great increase in the pressure at the end of the filling stage, followed by a holding period where the pressure decays slowly. When the gate freezes, we observe an abrupt decrease. For polypropylene, during the holding period, the pressure is uniform without any decrease, and it abruptly lowers once the gate frozen.
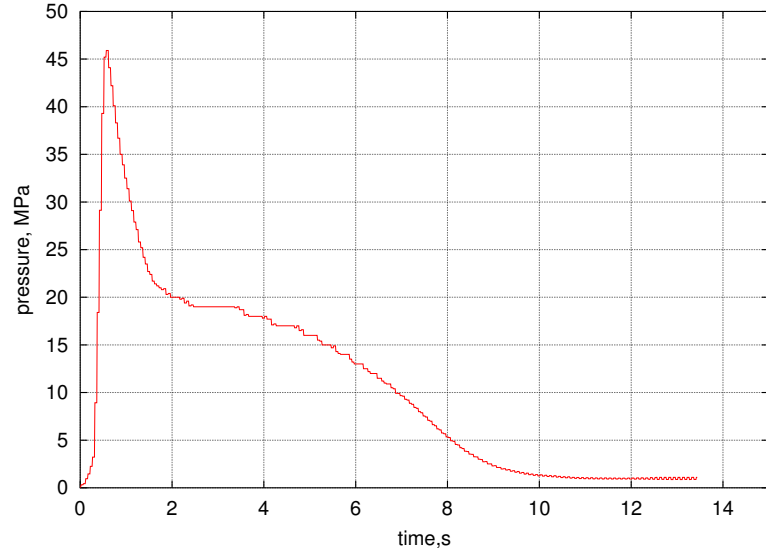
(a)
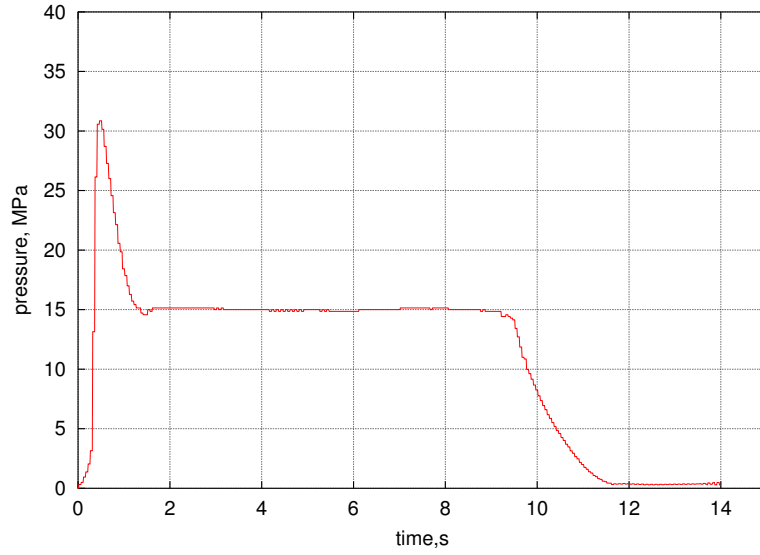
(b)

Figure 4.6: *Typical pressure evolution along the molding cycle: (a) schneider polystyrene molded part and (b) schneider polypropylene molded part.*

4.3.2 Materials characterization

The materials used in the experiments were a polystyrene (PS Lacqrene 7240) and a polypropylene (PP H 7060).

Polystyrene

Polystyrene's grade used here is a non-reinforced polymer from ATOFINA, Lacqrene 7240. This is a super-shock grade destined to extrusion, and formulated especially to be diluted in other grades to obtain sheets for rigid thermoformed shock-resistant packages. The relevant physical, mechanical, thermal and processing characteristics of the Lacqrene 7240 as quoted by ATOFINA, are presented in table 4.2.

Polypropylene

The polypropylene PPH 7060 is a a semicrystalline homopolymer from ATOFINA. This special grade is intended for the injection molding of packaging containers, toys, domestic appliances, garden furniture, caps and closures. Some relevant physical, mechanical, thermal and processing characteristics of PPH 7060 as quoted by the manufacturer are summarised in table 4.3.

Physical property	Method	Value	Unit
Density	ISO 1183	1.04	g/cm^3
Bulk density	ISO 1183	0.525	g/cm^3
Mechanical property	**Method**	**Value**	**Unit**
Tensile strength at yield	ISO 527-2	21	MPa
Elongation at yield	ISO 527-2	60	%
Tensile modulus	ISO 527-2	1950	MPa
Flexural modulus	ISO 178	1850	MPa
Izod impact strength at 23^oC	ISO 180	11	kJ/m^2
Thermal property	**Method**	**Value**	**Unit**
Melting point	ISO 3146	165	C
VICAT softening point (50C/h 50 N)	ISO 306	87	C
Heat deflection temperature (1.80 MPa)	ISO 75-2	74	C
Processing characteristics	**Method**	**Value**	**Unit**
Melt flow index (200C/5 kg)	ISO 1133	4.5	g/10 min
Injection temperature range		270-310	C
Mould temperature range		70-100	C
Maximum shear stress		0.5	MPa
Maximum shear rate		40000	s^{-1}

Table 4.2: *General properties of Lacqrene 7240.*

4.3.3 Experimental set-up and molding programme

The injection molding experiments were performed with a 140 ton injection molding machine (Billion - Hercule 470) with a 40 mm diameter screw and a shot size of approximately 100 ton/mm. The material was injected at a constant injection speed during the filling stage and subsequently hold at a constant hydraulic pressure during the post-filling stage. The mold wall temperature was regulated by a circulating water system, with a temperature controller.

The various processing conditions are given in table 4.4. Taking condition 1 of each material as reference, the remaining cases are used to assess the effects of holding pressure, holding time, injection temperature, mold temperature and inlet flow rate. The cycle time was considered the same (20 s for the PS and 26 for the PP), by varying cooling duration when changing holding time. The quoted mold temperatures refer to values given by the water regulation system. The holding pressure was determined from the hydraulic pressure, through the press guide.

Part weight was measured one hour after ejection at a room temperature of 15-20°C, and the results of these measurements were averaged over 5 consecutive moldings for each combination of molding conditions. In the experimental runs with the above molds, the main output was the pressure traces as recorded by the mounted transducers, at different locations in the cavity.

4.3.4 Experimental results and discussion

The pressure evolution during the production of the samples is presented in this section. The experimental pressure evolution is used to obtain objective information about the flow rate, the extent of the filling, cooling and packing progress, and to validate simulation in the following sections.

Results obtained for the different test conditions are shown in figures 4.7 to figure 4.16. The most influent parameters are the packing pressure and the injection rate. We notice a sharp pressure increase during the filling stage followed by a pressure decrease at the beginning of the packing stage. During this packing stage, the pressure plateau is below the imposed packing pressure, which may be related to the small gate geometry (figure 4.5).

On figure 4.7 we observe that the packing plateau pressure is always smaller than the imposed one. When the packing pressure is low (6 MPa, figure 4.7) the pressure decreases to zero at the beginning of the packing holding time, which means that the packing pressure is not sufficient to induce a packing flow in the mold. Figure 4.9 shows no difference between a packing holding time of 9 s or 13 s. When shorter (6 s), the packing pressure starts to decrease earlier. Figure 4.10 shows that increasing the mold temperature delays the gate freezing and allows to maintain the packing pressure inside the cavity for a longer time step. There is no significant influence of the polymer's injection temperature (figure 4.11). Varying the injection rates modifies the initial pressure peak (it decreases with the flow rate) but the remaining part of the pressure trace remains identical (figure 4.8).

In the case of PP, the same remarks are valid, with a more strong influence of the mold temperature in the pressure holding value attained. This may be justified by the fact that shrinkage is more important in PP than in the PS and greater for lower cooling rates.

Physical property	Method	Value	Unit
Density	ISO 1183	0.905	g/cm^3
Bulk density	ISO 1183	0.525	g/cm^3
Mechanical property	**Method**	**Value**	**Unit**
Tensile strength at yield	ISO 527-2	32	MPa
Elongation at yield	ISO 527-2	10	%
Tensile modulus	ISO 527-2	1550	MPa
Flexural modulus	ISO 178	1450	MPa
Izod impact strength at 23°C	ISO 180	3.5	kJ/m^2
Thermal property	**Method**	**Value**	**Unit**
Melting point	ISO 3146	165	C
VICAT softening point (50C/h 50 N)	ISO 306	87	C
Heat deflection temperature (1.80 MPa)	ISO 75-2	55	C
Processing characteristics	**Method**	**Value**	**Unit**
Melt flow index (230C/2.16 kg)	ISO 1133	12	g/10 min
Injection temperature range		270-310	C
Mould temperature range		70-100	C
Maximum shear stress		0.5	MPa
Maximum shear rate		40000	s^{-1}

Table 4.3: *General properties of PPH 7060.*

Lacqrene7240 and PPH 7060

Condition	Fill time (s)	Hydraulic pressure (MPa)	Holding duration (s)	Melt temperature (^oC)	Mold temperature (^oC)
PS_1	0.5	33.75	9	245	20
PS_2	0.5	6.750	9	245	20
PS_3	0.5	20.25	9	245	20
PS_4	0.5	27.00	9	245	20
PS_5	1.0	33.75	9	245	20
PS_6	0.25	33.75	9	245	20
PS_7	0.5	33.75	5	245	20
PS_8	0.5	33.75	13	245	20
PS_9	0.5	33.75	9	225	20
PS_{10}	0.5	33.75	9	245	40
PP_1	0.5	22.95	9	245	20
PP_2	0.5	6.750	9	245	20
PP_3	0.5	13.50	9	245	20
PP_4	1.0	22.95	9	245	20
PP_5	0.35	22.95	9	245	20
PP_6	0.5	22.95	5	245	20
PP_7	0.5	22.95	13	245	20
PP_8	0.5	22.95	9	225	20
PP_9	0.5	22.95	9	245	40

Table 4.4: *Processing conditions for the injection molding experiments for both PS and PP with the Schneider prototype mold.*

Figure 4.7: *Pressure evolution for different holding conditions for the polystyrene: influence of the packing pressure.*
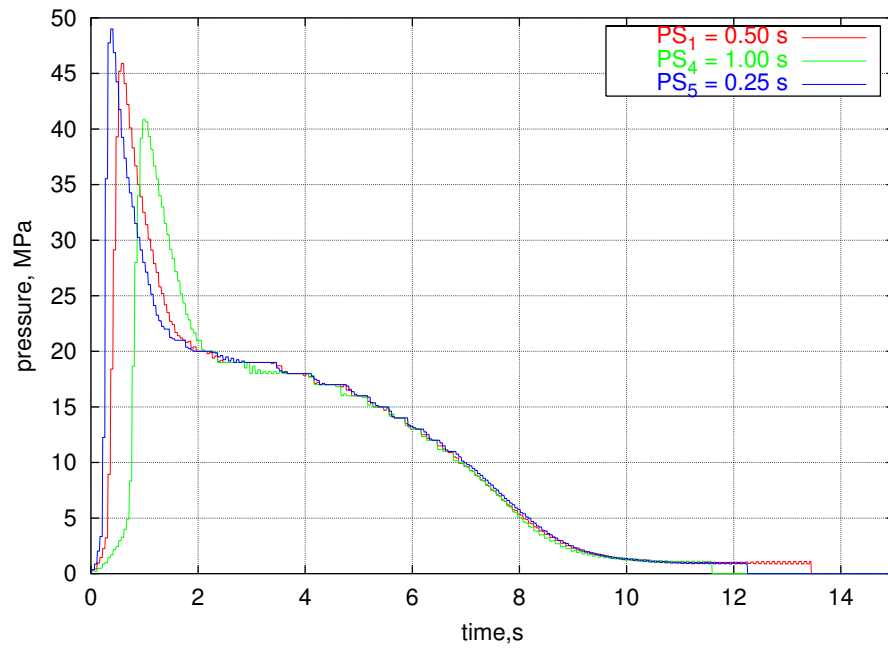
Figure 4.8: *Pressure evolution for different holding conditions for the polystyrene: influence of the flow rate. The legend concerns the filling times*
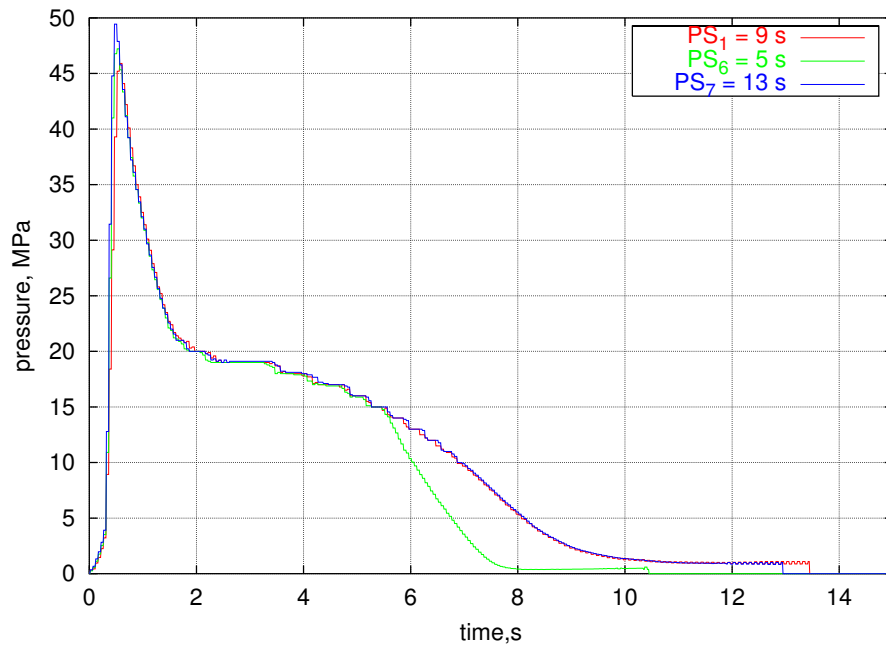
Figure 4.9: *Pressure evolution for different holding conditions for the polystyrene: influence of the holding time.*
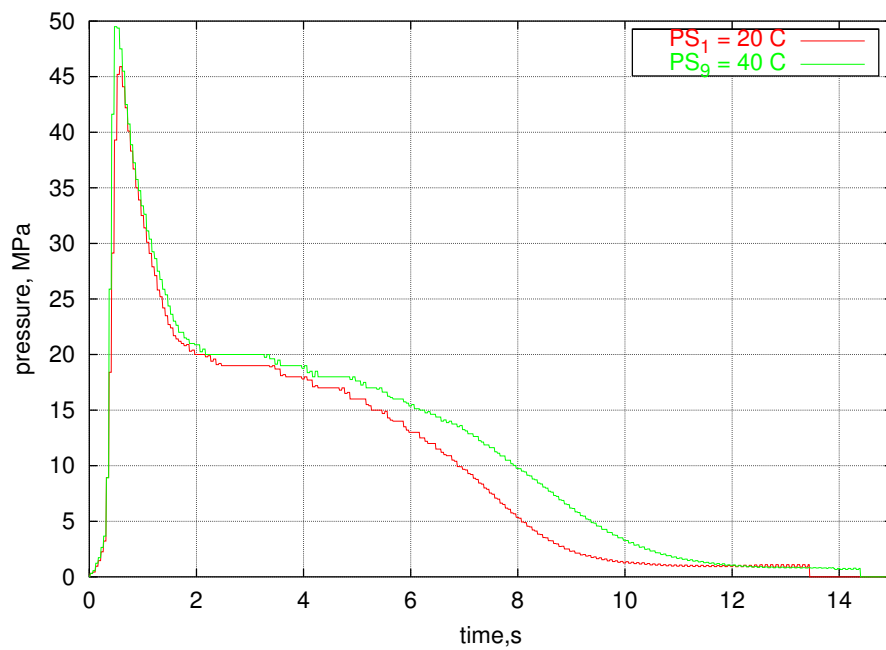
Figure 4.10: *Pressure evolution for different holding conditions for the polystyrene: influence of the mold temperature.*
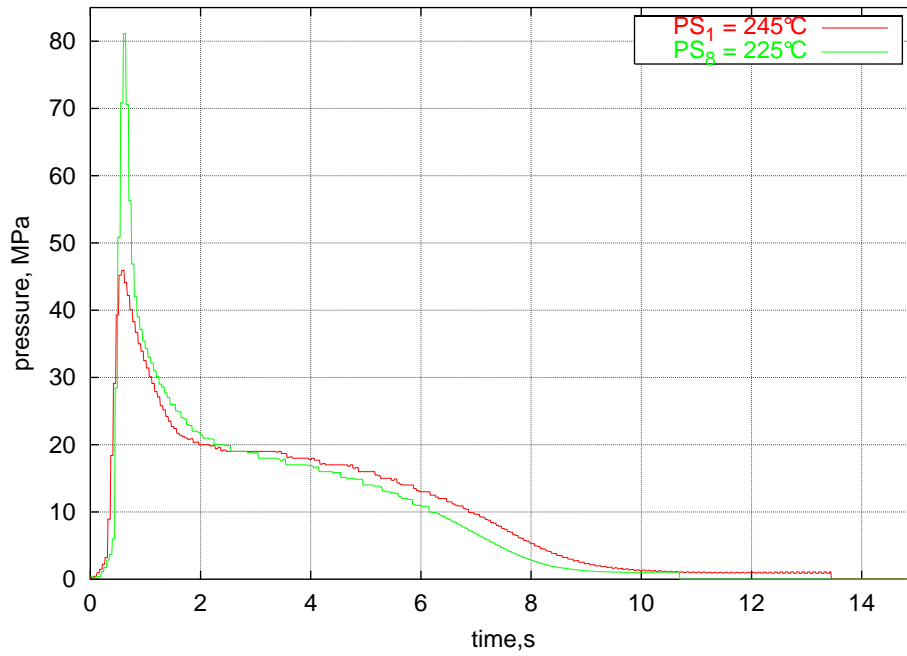
Figure 4.11: *Pressure evolution for different holding conditions for the polystyrene: influence of the injection temperature.*
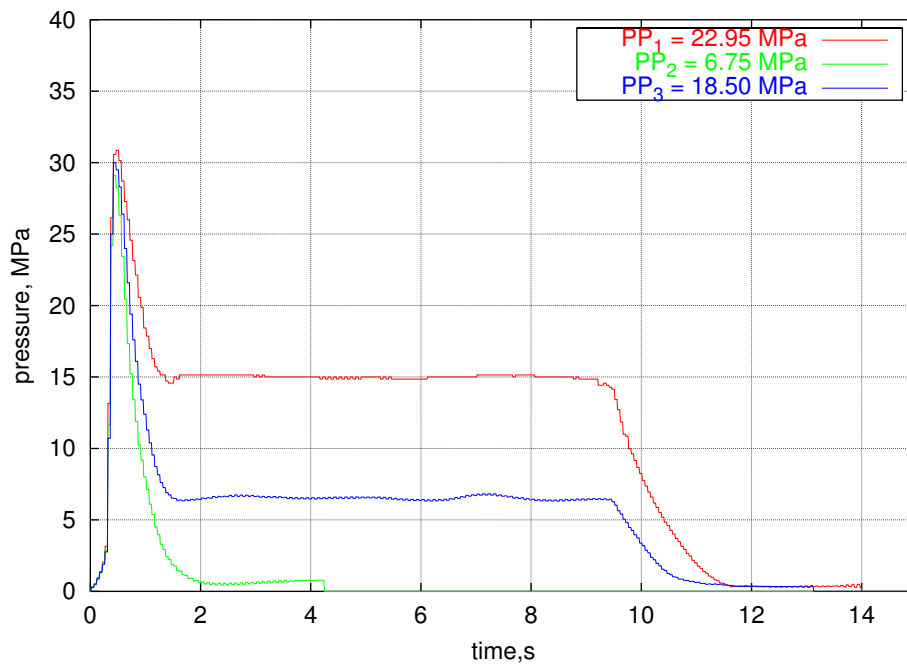
Figure 4.12: *Pressure evolution for different holding conditions for the polypropylene: influence of the packing pressure.*
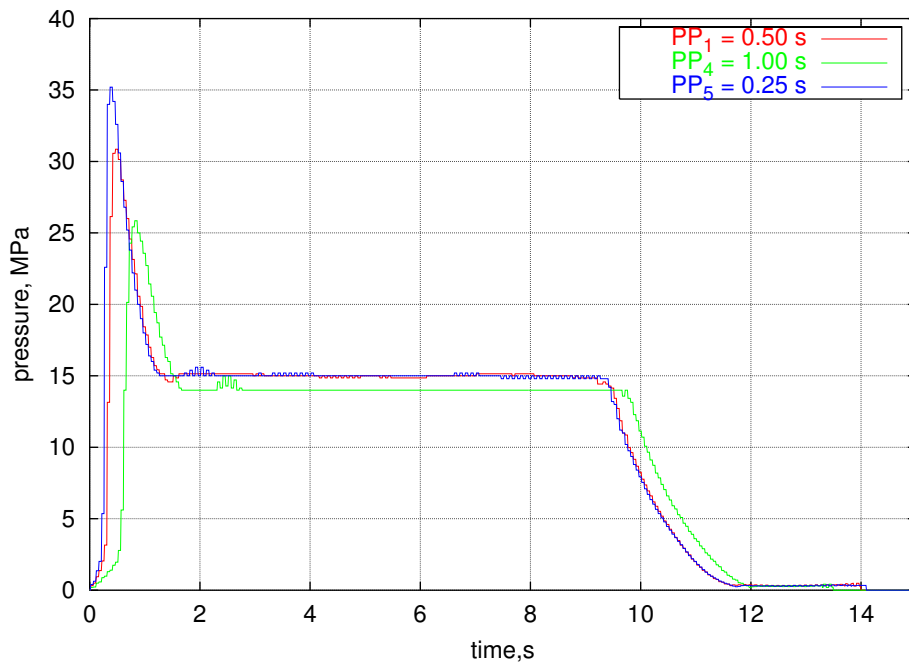
Figure 4.13: *Pressure evolution for different holding conditions for the polypropylene: influence of the flow rate. The legend concerns the filling times.*
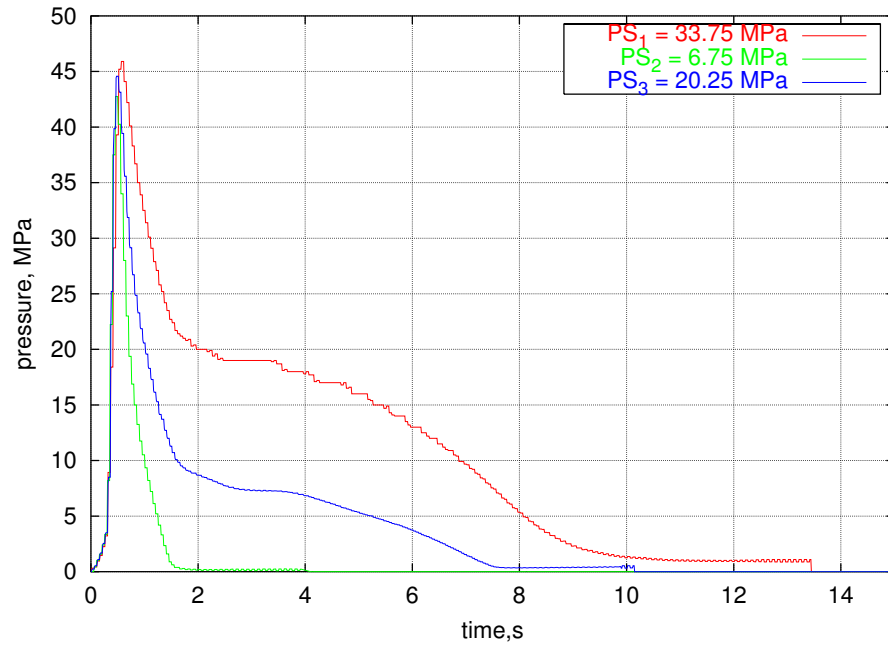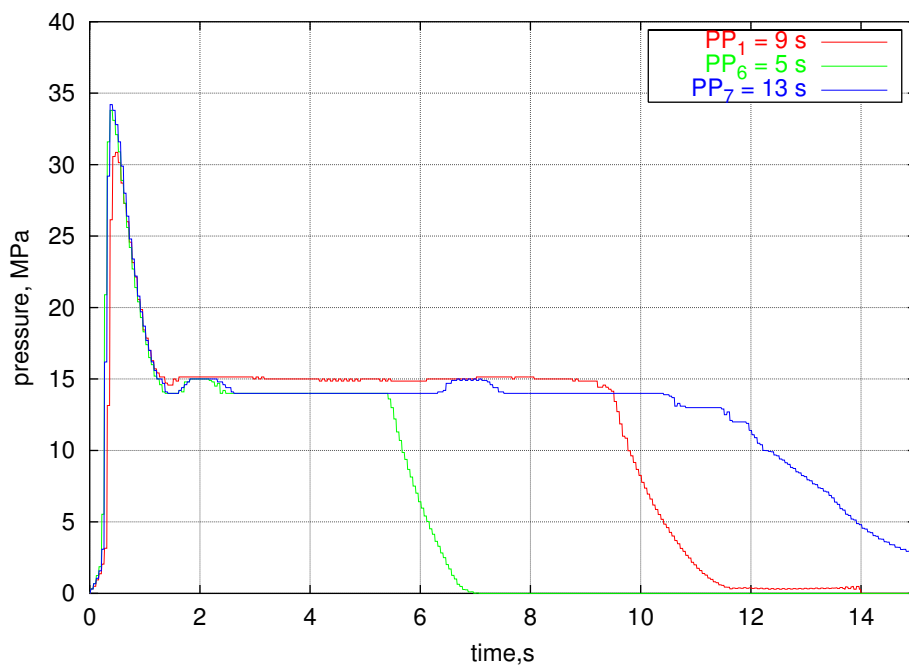

Figure 4.14: *Pressure evolution for different holding conditions for the polypropylene: influence of the holding time.*
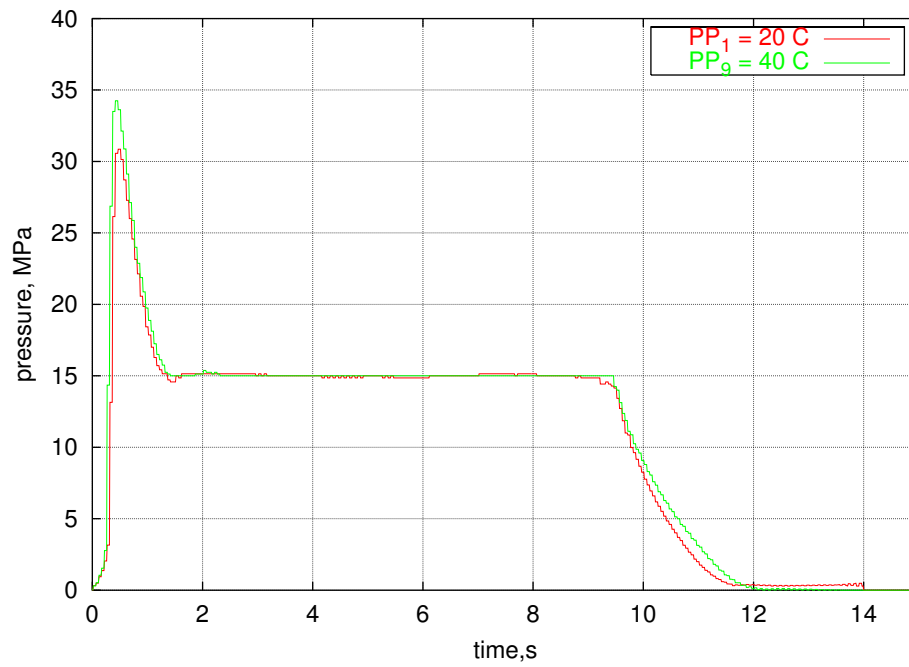
Figure 4.15: *Pressure evolution for different holding conditions for the polypropylene: influence of the mold temperature.*
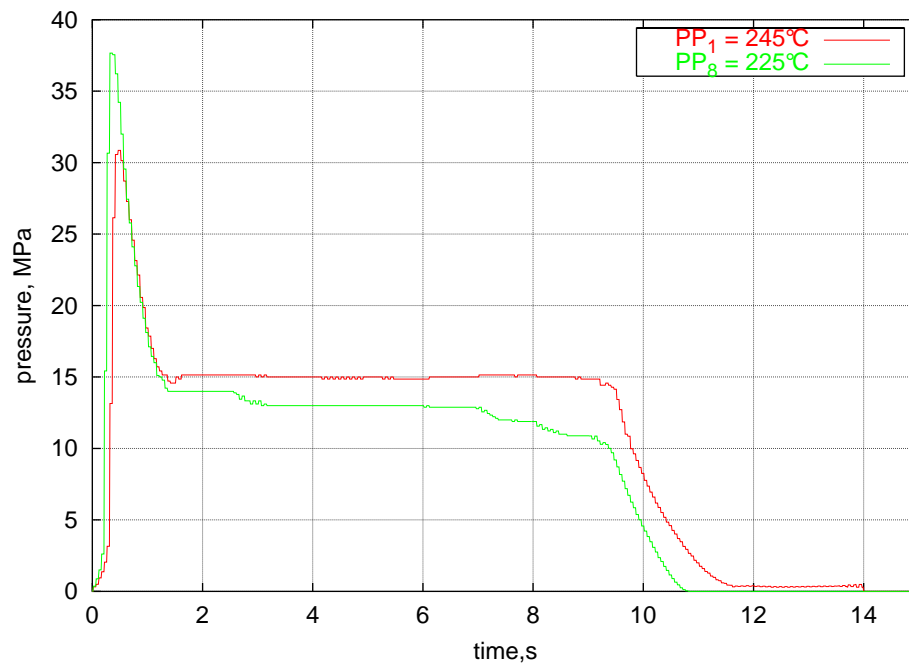
Figure 4.16: *Pressure evolution for different holding conditions for the polypropylene: influence of the polymer's injection temperature.*

4.3.5   Comparison between numerical and experimental results

For our numerical simulations, both polymers' rheologies were characterized at the CERDATO, as well as their PVT behaviour. Although thermal conductivities and specific heats were found to vary with temperature, they were supposed constant in this study.

Viscosity was fitted with a Cross-WLF model (seven-constant representation), whereas PVT data were curve-fitted using the modified double domain Tait equation. Resulting model constants are tabulated in tables 4.5, 4.6 and 4.7. The subscripts l and s in the state law denote liquid and solid values, respectively.

Material	PS Lacqrene 7240	PP H 7040
m	2.740E-01	0.277
τ^* (Pa)	2.484E04	3.700E+04
D_1 (Pas)	1.812E13	4.120E15
D_2 ^oC	3.731E02	-10.0
D_3 $^oC/Pa$	0.000E00	0.000E00
A_1	3.062E01	3.590E01
$\widetilde{A}_2$ ^oC	5.160E01	5.160E01

Table 4.5: *Viscosity model constants for PS and PP from Atofina.*

Material	PS Lacqrene 7240	PP H 7040
b_{1_l} (m^3/kg)	1.0064E-03	1.2600E-03
b_{2_l} (m^3/kg^oC)	6.2748E-07	1.2400E-07
b_{3_l} (Pa)	1.3957E08	1.0400E08
b_{4_l} $(^oC^{-1})$	4.0564E-03	9.1300E-03
b_{1_s} (m^3/kg)	1.0049E-03	1.6000E-03
b_{2_s} (m^3/kg^oC)	2.3766E-07	5.8300E-07
b_{3_s} (Pa)	1.9856E08	1.6000E08
b_{4_s} $(^oC^{-1})$	2.1512E-03	5.1300E-03
b_5 (^oC)	3.6407E02	4.2810E02
b_6 $(^oC/Pa)$	3.0068E-07	9.2000E-08
b_7 (m^3/kg)	0.0000E00	9.2500E-05
b_8 $(^oC^{-1})$	0.0000E00	1.6380E-01
b_9 (Pa^{-1})	0.0000E00	1.7200E-08

Table 4.6: *Specific volume Tait model constants for PS and PP from Atofina.*

Material	PS Lacqrene 7240	PP H 7040
Reference temperature (^oC)	245	220
c_p (J/kg^oC)	1.800E-01	1.630E-01
k (W/m^oC)	2.220E03	3.550E03

Table 4.7: *Summary of heat model constants for PS and PP from Atofina.*

Computations were performed for two different pressures and flow rates for the polystyrene (conditions PS1, PS2 and PS5 in table 4.4) and for the standard condition for the polypropylene (condition PP1 in table 4.4).

Experimental and numerical short-shots

Figure 4.17 illustrates the flow front progression of the polymer inside the cavity at different time steps, for the polystyrene part. On the left, we show the experimental results (short shots), and on the right the computed ones. We notice that globally, there is a good agreement. Furthermore, **REM3D** predicts well weld lines formation and the last zones in the cavity that are filled.
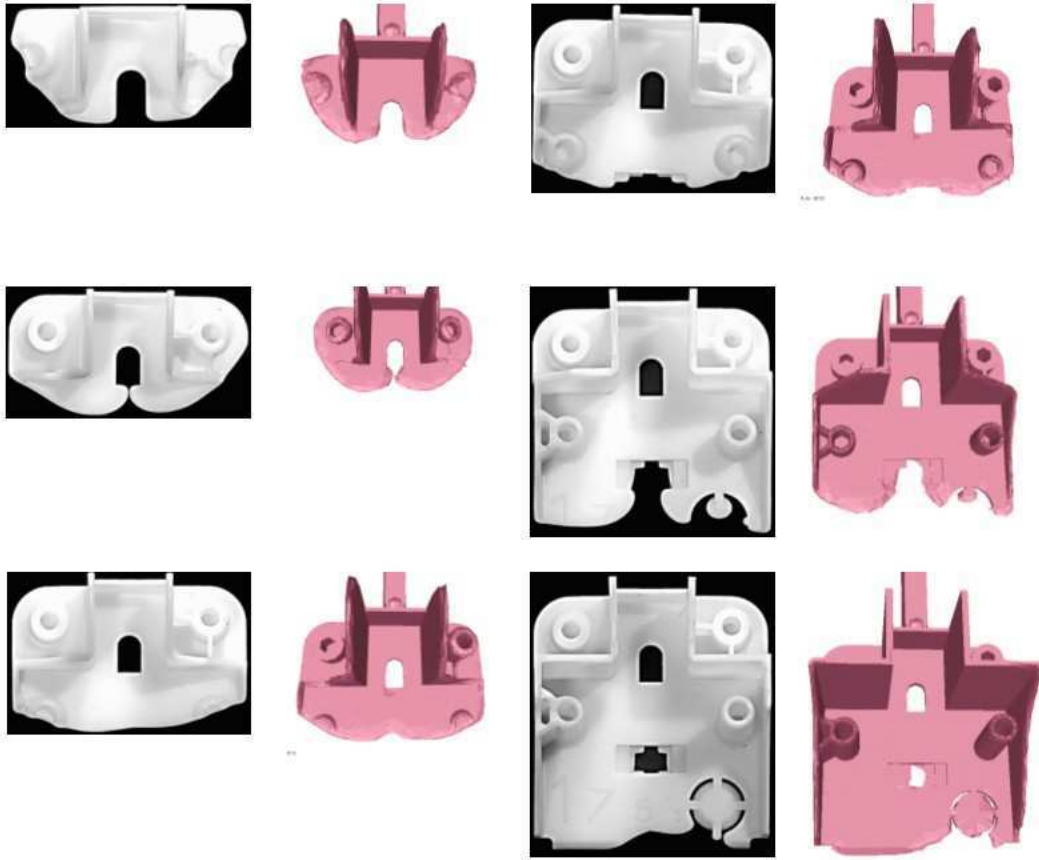
Figure 4.17: *Comparison between numerical and experimental short-shots.*

Pressure traces and sensitivity to the molding conditions

In this section, we only test the influence of the most influent processing parameters, i.e. packing pressure and injection rate. On figure 4.18 we observe that the pressure peak is well captured as well as the pressure decrease during the first instant of packing holding time. We also notice that the plateau pressure is less than the imposed one, in agreement with experiments. The final pressure decrease is also well captured. For a lower packing pressure (23 MPa) the agreement is less fair. On figure 4.19 we see that the influence of injection rate is well captured in what concerns: value and position of the pressure peak, pressure decrease at the initiation of packing stage and low sensibility of the pressure during the remaining part of packing stage.

In the case of the polypropylene, one simulation has been performed at the standard condition. We notice that the pressure increases during filling, it reaches a plateau during post-filling and decreases once the gate is frozen. However, the agreement is also less fair (figure 4.19), but qualitatively numerical results show the good tendency.

This difference between experimental and numerical data can be explained: solidification and the behavior of the solid state is still a very simple model. In fact, below the transition temperature, the

viscosity is supposed constant $(\eta = \eta(T_t))$ solving the same flow equations than in the liquid state. Since the pressure is measured at the part surface (and thus in the solidified layer), it is difficult to analyse the attained values. Nevertheless, we observe a good tendency.
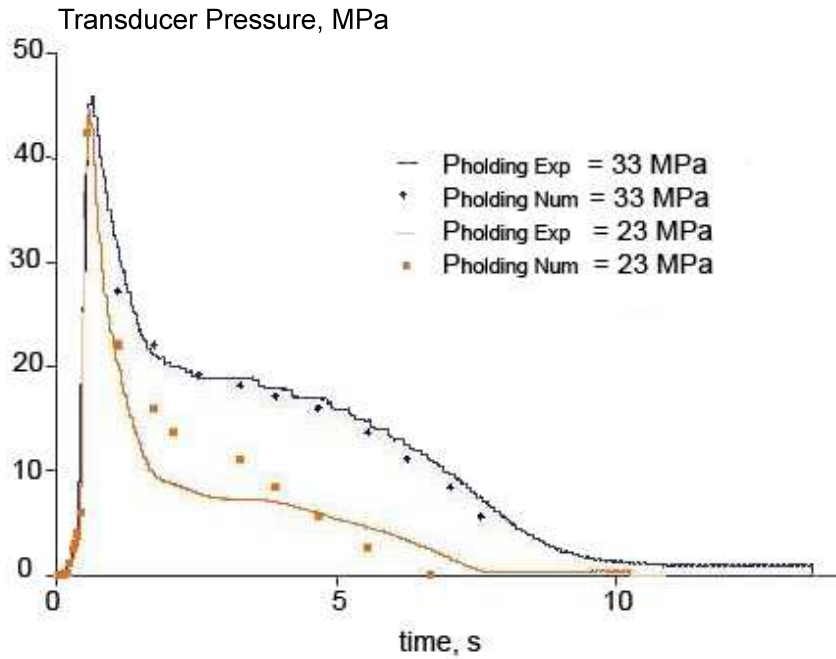
Figure 4.18: *Evolution of the pressure for the polystyrene part: influence of the packing pressure. Comparison between numerical and experimental results, the continuous lines are the numerical ones, the points are the experimental data.*
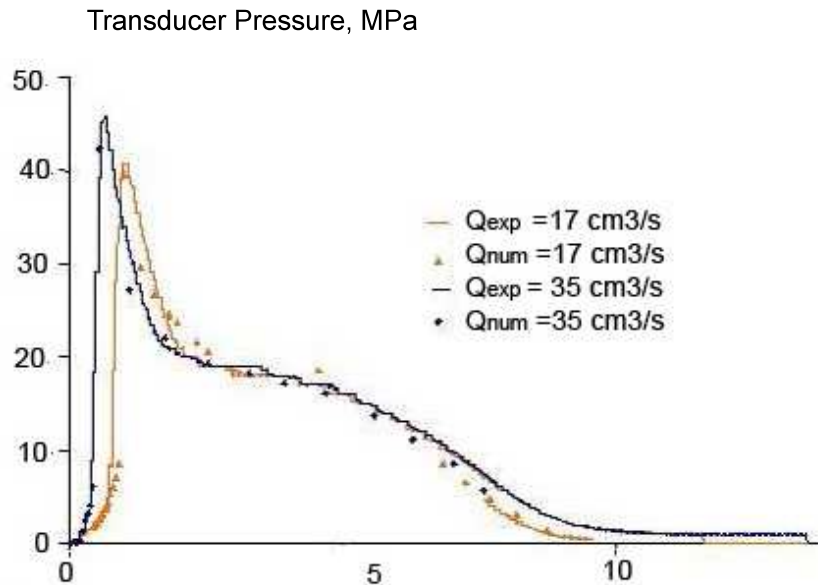
Figure 4.19: *Evolution of the pressure for the polystyrene part: influence of the flow rate. Comparison between numerical and experimental results, the continuous lines are the numerical ones, the points are the experimental data.*
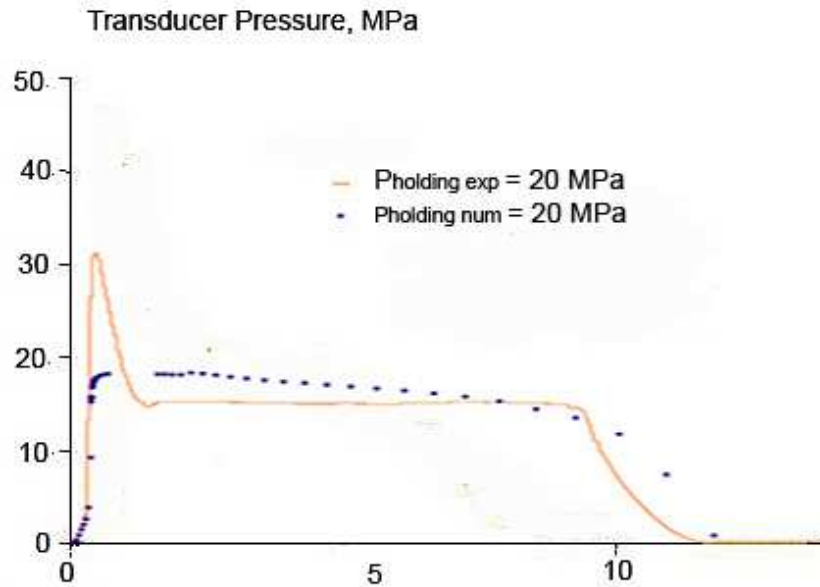
Figure 4.20: *Evolution of the pressure for the polypropylene part, standard condition. Comparison between numerical and experimental results, the continuous lines are the numerical ones, the points are the experimental data.*

From comparison with experiments, we notice that pressure "numerical" measurements present the same tendency than experimental ones. Furthermore, the sensitivity to material parameters is confirmed by **REM3D**.

4.4 Application in injection molding of a 3D complex geometry

In the preceding section, compressibility has only a weak influence on the part weight, not obvious on the pressure trace during packing. This is due to the fact that the cavity is, more or less, of uniform thickness. Now, we consider a more volumic piece (a biomedical implant) with very important thickness variations and we test the influence of compressibility and viscoelasticity. We consider the filling and post-filling stages with a constant flow rate during the filling stage, a commutation towards a packing pressure for the holding stage and then cooling inside the mold. The material used was a polyethylene (close to Stamylan's LDPE grade). Geometry's and material parameters are detailed in figure 4.21.

Material properties

Viscous (CarreauYasuda-WLF)

m, a	0.66687 , 2
τ^* [MPa]	0.0180
D_1 [MPas]	8.169e-3
D_2 [℃]	120
D_3 [℃/MPa]	0
A_1	20.4
A_2 [℃]	101.6

Viscoelastic

θ_b [s]	2.5e-3 1.14e-2 5.16e-2 2.35e-1 1.07e-1 4.84
θ_s [s]	1.25e-3 5.70e-3 2.58e-2 1.18e-1 0.535e-1 2.42
G_0 [MPa]	0.145 0.0984 0.0377 7.48e-3 1.4e-3 1.52e-4

Thermal

c_p [kJ/kgK]	2.3
k [W/mK]	0.22

PVT

b_{1l} [cm^3/g]	1.0064
b_{2l} [cm^3/gK]	0.00062748
b_{3l} [MPa]	139.57
b_{4l} [℃$^{-1}$]	0.0040564
b_{1s} [cm^3/g]	1.0049
b_{2s} [cm^3/gK]	0.00023766
b_{3s} [MPa]	198.56
b_{4s} [℃$^{-1}$]	0.0021512
b_5 [℃]	90.92
b_6 [℃/MPa]	0.30068
b_7 [cm^3/g]	0
b_8 [℃$^{-1}$]	0
b_9 [MPa^{-1}]	0

section cut

pressure numerical transducer

symmetry plane

gate

Process parameters

	1) Compressible	2) Incompressible	3) Viscoelastic
Flow rate [mm^3/s]	7000	7000	3750
Holding pressure [MPa]	30	30	30
Holding time [s]	9	9	9
Cooling time [s]	11	11	11
Mold temperature [℃]	50	50	50
Injection temperature [℃]	220	220	220
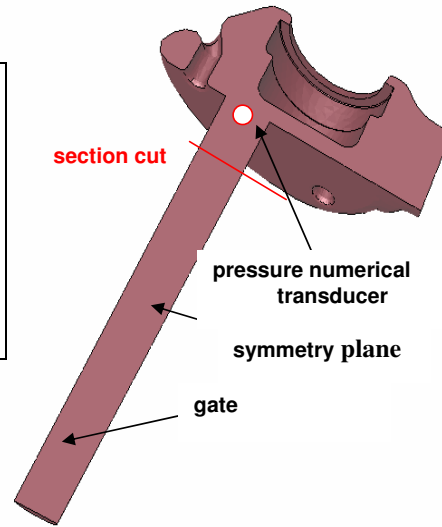
Figure 4.21: *Geometry of the biomedical implant, material and process parameters.*

Three computations were performed in a mesh with 23354 nodes and 126427 elements: one using a viscous incompressible material behavior, one considering a viscous compressible behavior, and finally one taking into account viscoelasticity. Computation times of the whole injection molding cycle were:

- in the viscous compressible case, 1 day and 19 hours in 8 processors;

- in the viscoelastic compressible case, 1 day and 16 hours in 8 processors.

Each processor is a Pentium IV 2.8Ghz and 1Gb RAM, linked to the other processors by a Myrinet network. We underline the fact that, given the number of elements, the viscoelastic computation could not be performed with only one processor. These computational times require further analysis and explanation. In fact, **REM3D**'s parallelization has been done progressively, through a global Master-Slave strategy and local SPMD modules. This means that purely sequential developments still exist, being one of them the mechanical resolution for a non-linear system of the non-newtonian viscous type. The main consequence is that we spend almost the same computing (in average) 7 to 10 Newton-Raphson iterations to converge to the correct velocity-pressure value in the viscous case,

as we spend in performing one velocity-pressure followed by a several-mode extra-stress computation in the viscoelastic case. This justify the computational of the same order attained.

In the following, results obtained concerning

- evolution of the <u>filling</u> rate

- evolution of the <u>pressure</u> inside the cavity

- compensation of <u>shrinkage</u> and amount (<u>mass</u>) of material entering the cavity

- birefringence and <u>internal stresses</u> evolution

- orientation and stretch frozen in the part at the moment of ejection

are shown and analyzed.

4.4.1   <u>Filling and evolution of the filling rate</u>

In this case, we compare simulations performed for both compressible and incompressible behavior consideration (cases 1 and 2 in figure 4.21). In the incompressible case, we supposed that the density is constant and computed at the atmospheric pressure and injection temperature ($\rho = \rho(p_{atm}, T_{inj})$). Figure 4.22 shows the evolution of the material in the cavity, as well as the evolution of the flow rate at the inlet. We notice that during the filling stage, no difference is observed in the filling rate's evolution.
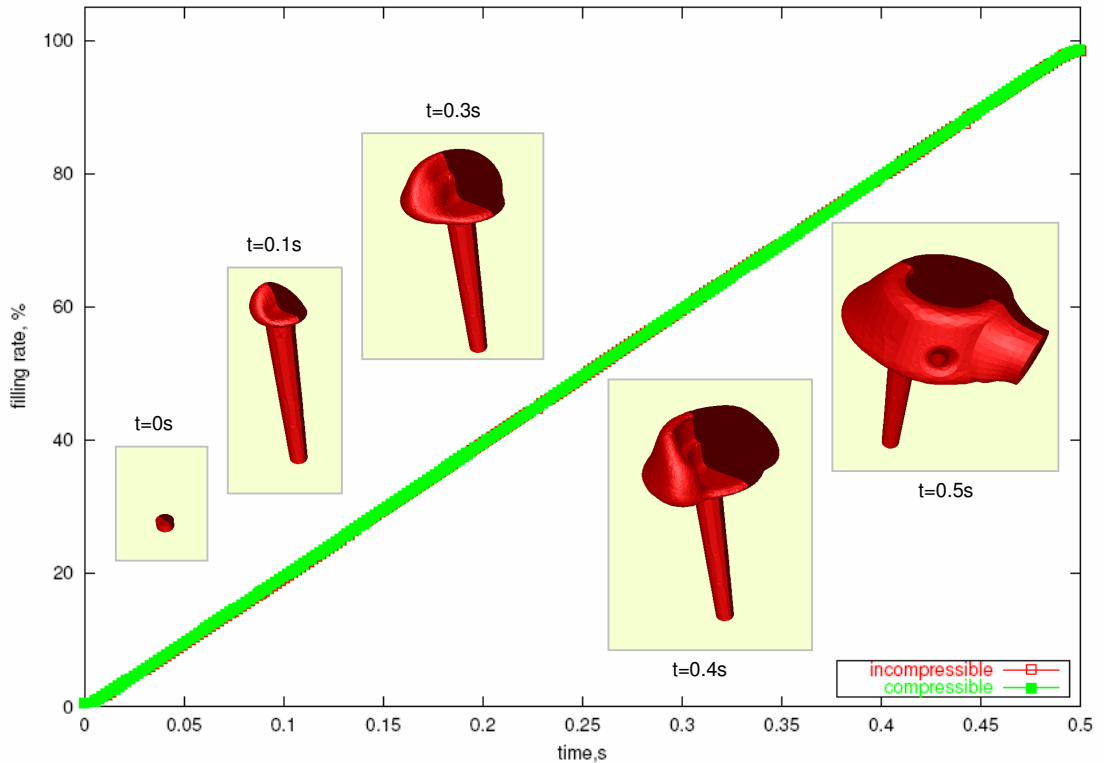
Figure 4.22: *Filling and flow rate function of time.*

4.4.2 Pressure trace

Figure 4.24 shows the pressure trace, numerically measured in one point of the part (transducer position indicated in figure 4.21) for both compressible and incompressible cases. We observe that there is a substantial difference, mainly during cooling.
In the incompressible case, the abrupt increase at the end of filling, followed the same decrease at the end of packing indicates that there is no transient period for the pressure to attain the packing value. Furthermore, it becomes automatically homogeneous in the part.

4.4.3 Mass and shrinkage rate

This difference in pressure is reflected in the mass of material entered in the cavity, that remains constant once the cavity is filled in the incompressible case, and continues to increase until ejection in the compressible case. Furthermore, we observe that during the post-filling stage the material flows from the regions with higher temperature towards colder ones, to compensate eventual shrinkage (figure 4.25).
The shrinkage rate evolution is a measure of the capability of the material to shrink. If we look at its distribution in the part at the end of the cooling stage (figure 4.26(d)), we notice that colder regions are potentially less likely to shrink a since its density is already close to the ambient temperature one. Furthermore, we notice that even though mass entering the cavity may compensate shrinkage, the shrinkage rate distribution follows the temperature field (figure 4.27).

4.4.4 Internal stresses distribution

Computations were also performed using a viscoelastic compressible model (material properties detailed in figure 4.21). Influence of material viscoelasticity is not observed generally in the pressure profile, which remains globally the same than in the viscous compressible case [Pantani et al., 2004]. However, during the filling stage, when the pressure is still rather small, the effects of the extra-stress may be observed in the pressure trace.

Nevertheless, we can see its influence in the internal stress distribution. Figure 4.28 illustrates the internal stress evolution at the end of filling (on the right) and its comparison with the pressure (on the left). The stress component represented in the figure is the first normal stress, σ_1. We notice different distributions between both values, even if the maximum and minimum values attained rest at the same order of magnitude.

These difference can be explained by the fact that due to viscoelastic behavior consideration, the first principal stress difference is not zero. In figure 4.29 we show the first principal stress field on the part throughout the process ($N_1 = \sigma_1 - \sigma_2$). This description is completed by plots of N_1 at three different instants (end of filling, end of packing and end of cooling) for a given section of the part (detailed in figure 4.30). Furthermore, we notice that at the end of the cooling phase, stresses are frozen-in near the wall.

When we compare these results with the ones from the literature described in Chapter 3, we conclude that they follow a good pattern:

- during filling, molecules located centered molecules are less oriented than the ones closer to the wall, due to the low shear rate, giving rise to lower flow-induces stresses and lower birefringence;

- at the end of filling, the stresses tend to relax, since velocity reduces drastically;

- during packing, flow-induced stresses still exist, either frozen or due to material's motion and increase of the relaxation times;

- at the end of cooling, stresses are frozen-in in the part in regions near the wall.

More accurate results could be obtained using a finer mesh, especially near the surface. Furthermore, we believe that quantitative results could be compared to experimental works if a model of the solid state closer to the real material behavior had been considered.

4.4.5   Orientation and stretch distributions

Furthermore, an orientation distribution is established during the filling stage. Figure 4.31 shows this distribution for the last mode chosen. Due to its high orientation relaxation time, these orientations did not relax in the processus duration and are present at the ejection moment. A similar analysis can be done for the stretch evolution (figure 4.32).

Through the injection molding simulation of a complex three-dimensional part we tested the feasibility of the developments. Firstly, in what concerns computational efficiency, we remark that computational times remain reasonable, even for a viscoelastic computation (with a eight-mode fluid). Secondly, evolution of the pressure is in agreement with the previous examples, and is at least qualitatively correct. We have also shown that the mass entering the cavity will compensate shrinkage, qualitatively evaluated through the shrinkage rate field. Finally, distribution of orientation and frozen-in distributions was given at each step of the process.
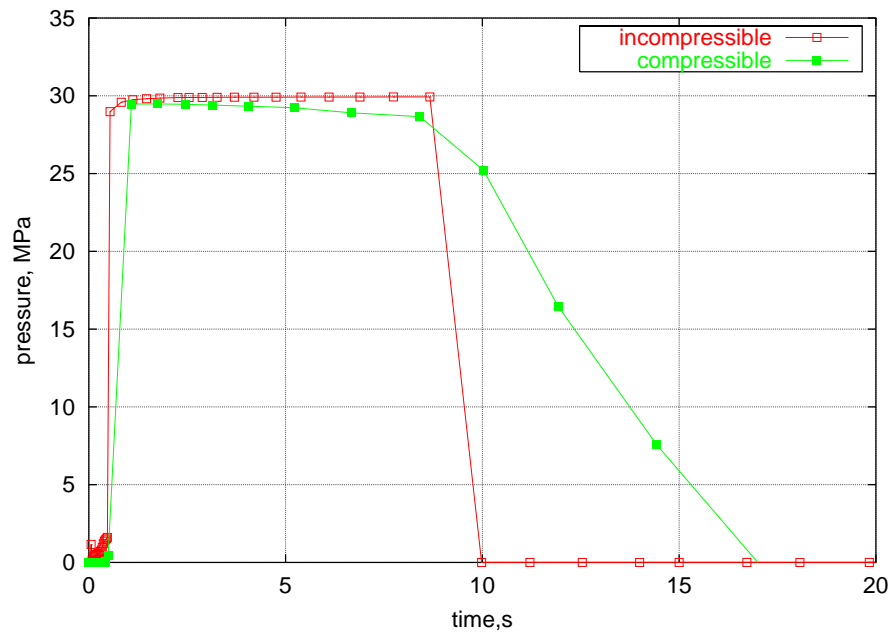
Figure 4.23: *Evolution of pressure in the cavity as function of time.*
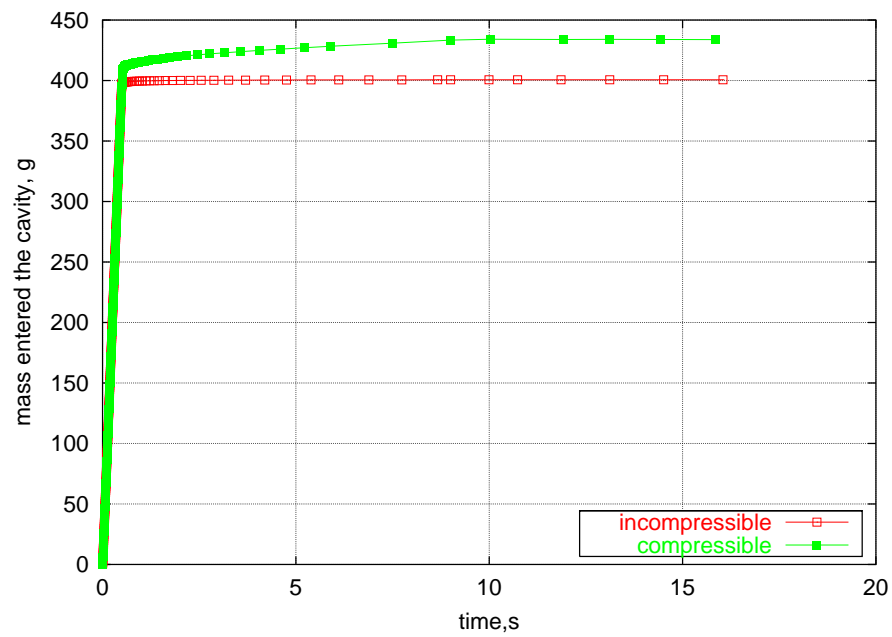
Figure 4.24: *Evolution of mass in the cavity as function of time.*
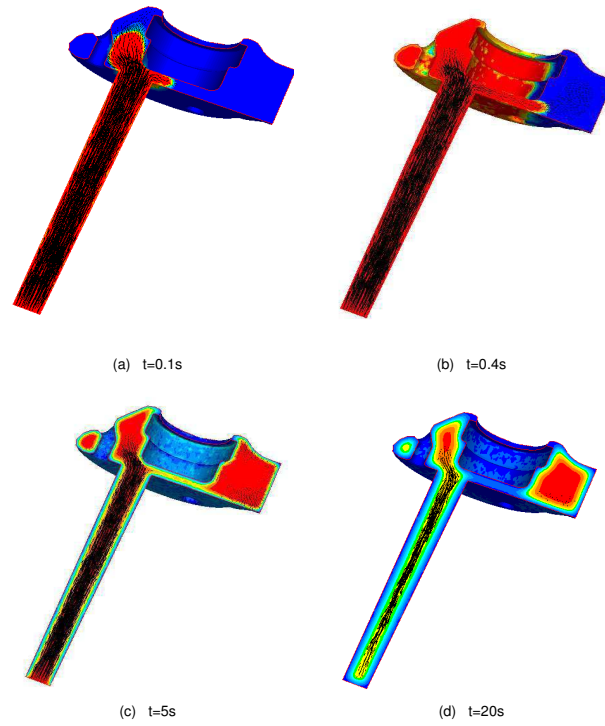
Figure 4.25: *Velocity in the part during filling and post-filling. During post-filling, the material moves from warmer to colder regions to compensate shrinkage.*
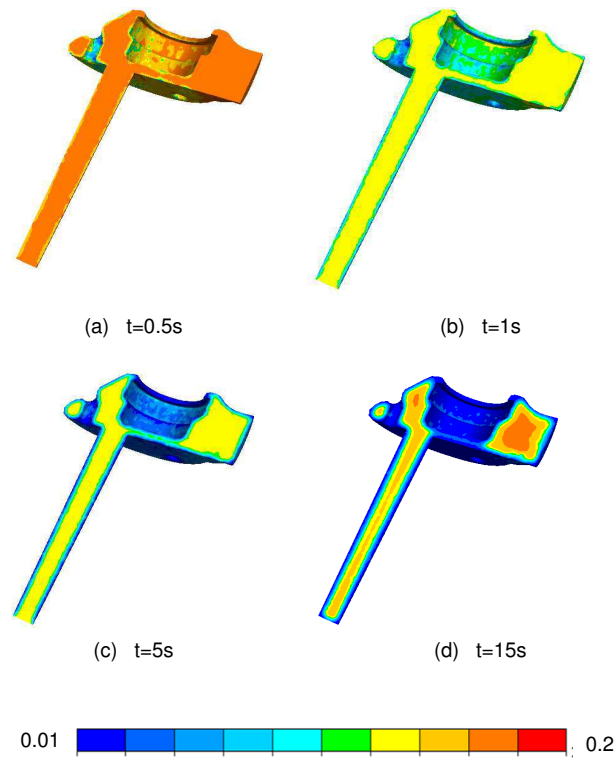
Figure 4.26: *Shrinkage rate distribution in the part during the whole process; it varies from 0.01 up to 0.2 of the part's mass, locally.*
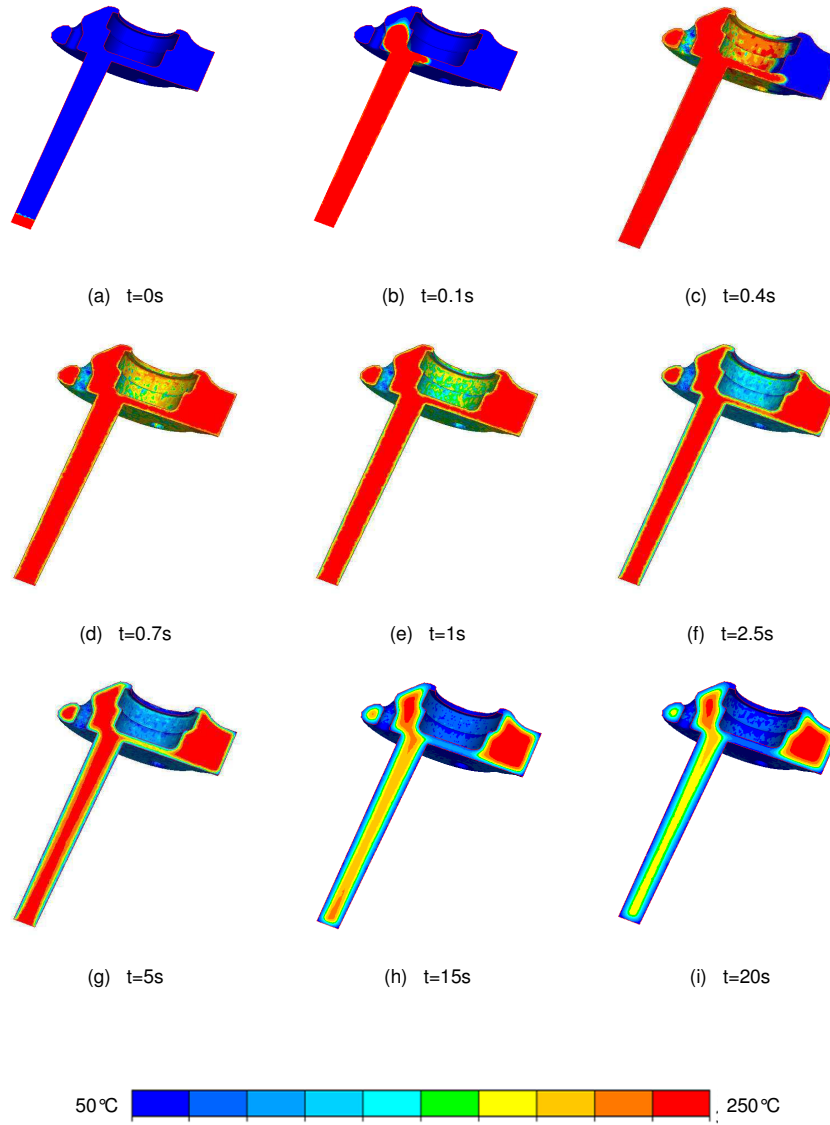
Figure 4.27: *Temperature distribution during filling, packing and cooling.*
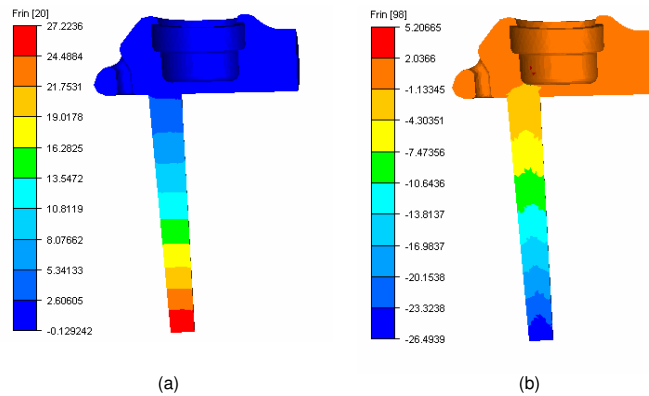
Figure 4.28: *Pressure (on the left) and first principal stress σ_1 (on the right) at the end of the filling stage (units MPa).*
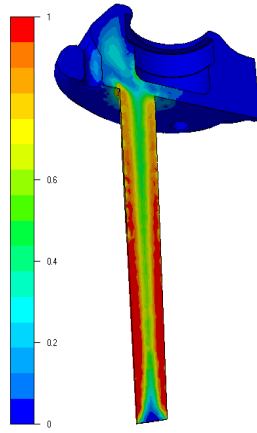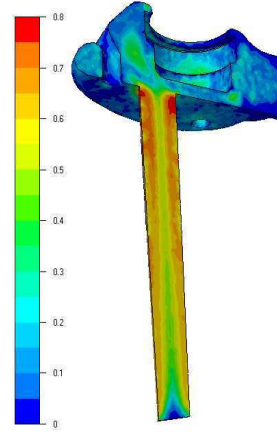
(a)   t=0.6s, filling

(b)   t=1s, end filling
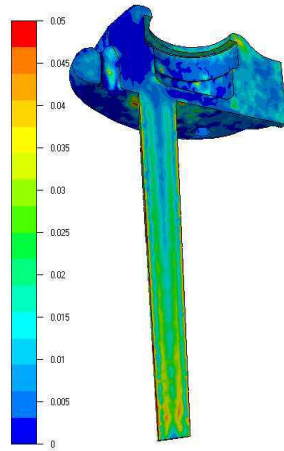
(c)   t=2.8s, packing
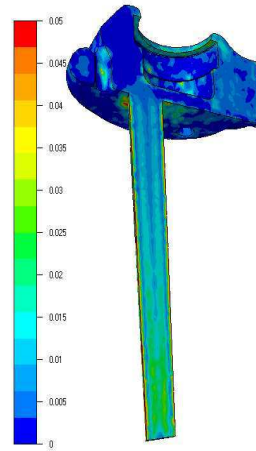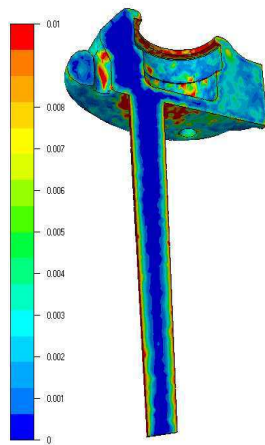
(d)   t=4.8s, cooling

(e)   t=8.8s, cooling
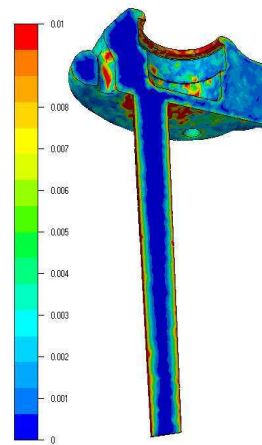
(f)   t=20s end cooling

Figure 4.29: *First principal stress difference distribution in the part, $N_1 = \sigma 1 - \sigma 2$.*
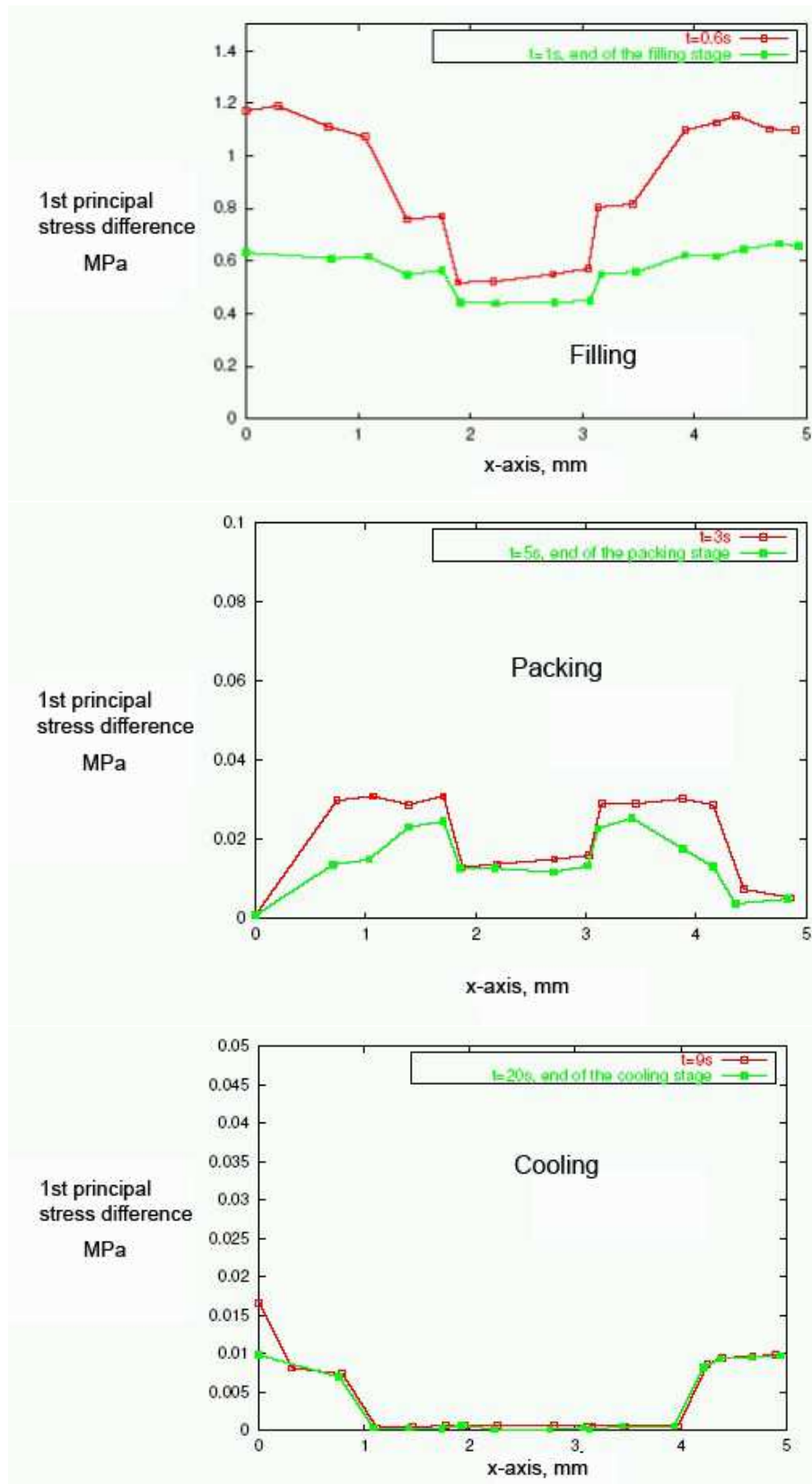
Figure 4.30: *First principal stress difference in a section of the part, (a) at the end of the filling stage, (b) at the end of the packing stage, (c) at the end of the cooling state.*

last mode

(a) equivalent orientation t=0.5s

(b) equivalent orientation t=1s

(c) equivalent orientation t=3s

(d) equivalent orientation t=5s

(e) equivalent orientation t=9s

(f) equivalent orientation t=15s
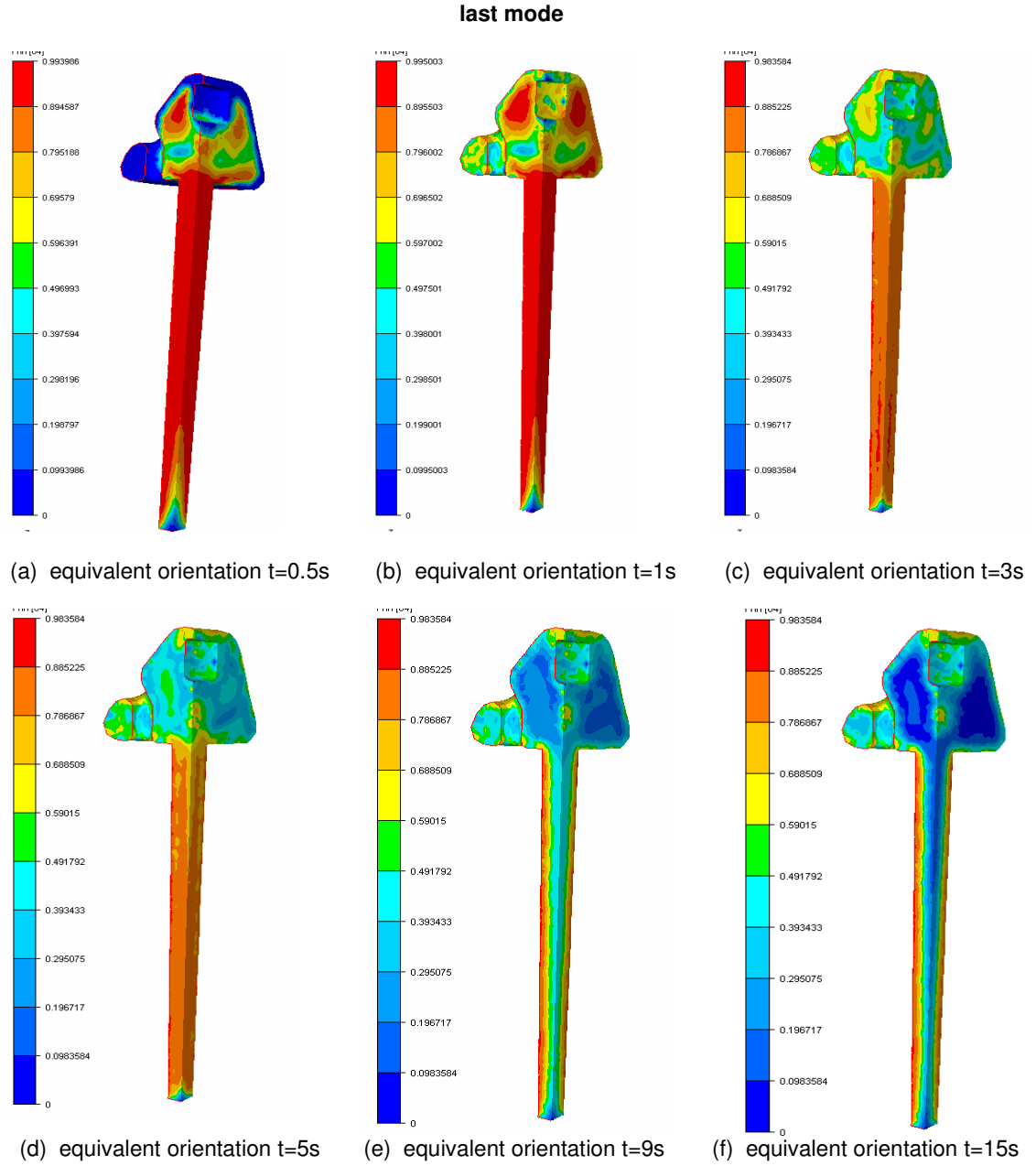
Figure 4.31: *Equivalent orientation and orientation tensor distribution for the last mode. For t=15s, we have an example of the frozen-in orientation.*

last mode

(a) equivalent stretch t=0.5s   (b) equivalent stretch t=1s   (c) equivalent stretch t=3s

(d) equivalent stretch t=5s   (e) equivalent stretch t=9s   (f) equivalent stretch t=15s
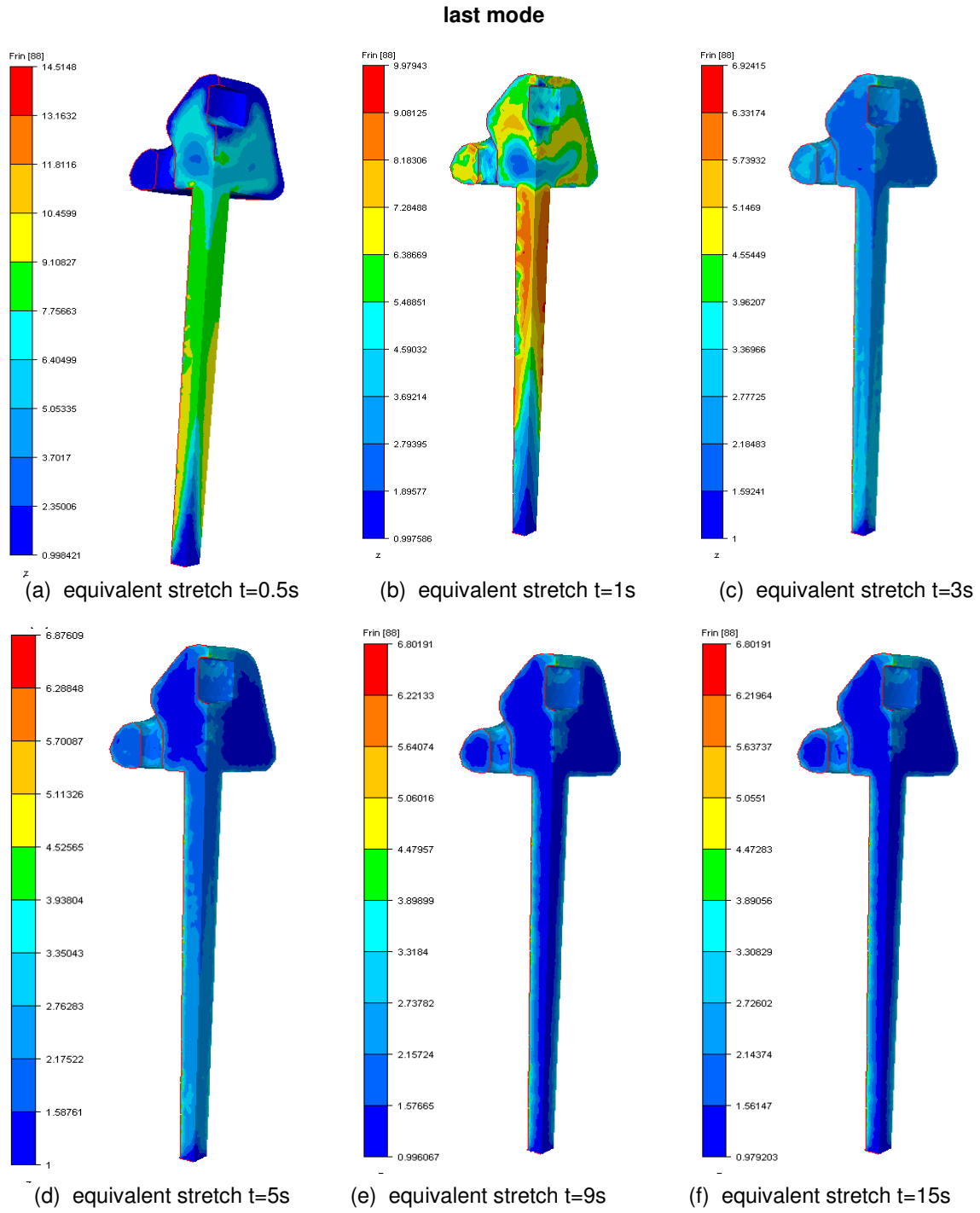
Figure 4.32: *Stretch distribution for the last mode; values of the frozen-in stretch reach locally 6.8.*

4.5   Conclusion

This chapter presented applications of the implemented compressible and viscoelastic models in injection molding situations. The use of these models involves:

- large number of material parameters

- large number of unknowns (velocity, pressure, free-surface, temperature, orientation, stretch,...)

Nevertheless, its feasibility in injection molding applications has been shown. Firstly, comparison with literature examples consolidate the validation of the numerical methods implemented both for compressibility and viscoelasticity. Secondly, experiments were performed in the injection molding of a complex part. They allowed a comparison between experimental and numerical results and, furthermore, they measured the sensitivity of experiments and computations to the process parameters (mainly material, flow rate and packing pressure). Finally viscoelastic compressible computation on a complex three dimensional part allowed to test the computational efficiency of the complete model in a concrete injection molding situation. In this case, we have shown that frozen-in stresses and orientation present logical patterns taking into account the fact that it is a 3D part.

Chapter 5

Conclusion and perspectives

5.1   Synthesis and conclusion

This work concerns simulation of viscoelastic compressible flows and applications in injection molding. Conclusions on the work developed can be done exploiting the different aspects (viscoelasticity, compressibility and process simulation) both from the physical and numerical points of view.

Compressibility

Compressibility has been integrated in **REM3D** by considering a density evolution for the material. Physically, it can be considered function of the pressure p and of the internal energy e, $\rho = \rho(p, e)$. Depending on the material chosen, the internal energy's dependence can be converted in a function of temperature, a chemical reaction or a solidification rate, for example. In the particular case of a thermoplastic material, the density was considered function of the pressure and temperature through the Tait law, $\rho = \rho(p, T)$. This dependence is generally represented in the literature as the material's PVT diagram, and the behavior remains weakly compressible.

Conservation equations from continuum mechanics were considered for a viscous or viscoelastic compressible material domain. Compressibility has a direct influence in the conservation of mass equation. Since the density is function of pressure and temperature, conservation of mass was written in terms of velocity, pressure and temperature, eliminating the direct contribution of the density, and giving rise to the notion of isothermal compressibility and dilatation, that are material dependent coefficients.

Using a splitting scheme, mass and momentum conservation were solved separately from energy conservation. Thus, we were led to a system with velocity and pressure as unknowns (for a given temperature). In the newtonian case, it is generally referred as the Stokes compressible problem.

Numerically, the Stokes compressible problem was solved using the Mixed Finite Element method. The computational domain was discretised using tetrahedral elements, and a continuous approximation for velocity and pressure was considered, with a bubble enrichment for velocity. We have shown that this interpolation respects the stability conditions of the problem, even in the incompressible limit. The linear system arising from the problem is non-symmetrical and two numerical solutions have been considered: semi-implicit, and completely implicit with variable change. Results in a simple mass conservation benchmark showed that both solutions are acceptable, but the first one conserves better the mass and was kept in the subsequent work. Dependence of the isothermal compressibility coefficient on the pressure is common in polymer engineering (even if weak) and was taken into account through a fixed-point scheme.

Influence of the temperature in the compressible flow equations and volume variation in the energy conservation equation was also taken into account. In analogy with gases, we can obviously deduce that compression of the material induces an increase on the temperature. Compressibility's influence was thus introduced in the temperature equation through a dilatation/contraction term, being the energy problem solved through the classical Space-Time Discontinuous Galerkin method.

Finally, we considered the existence of several materials, each following an appropriate physical behavior. The computational domain was composed from several subdomains, one (or several) being compressible and viscoelastic. Each subdomain is represented by a characteristic function, that is 1 in a point that belongs to the subdomain, and 0 elsewhere. This function is determined through a STDG method through the respective advection equation. Extension of the compressible solver (in velocity, pressure and temperature) was done from one subdomain to the whole computational domain using these characteristic functions. Applications in three-dimensional fluid shrinkage and expansion illustrated the validity and the feasibility of our approach.

Viscoelasticity

Since polymers are viscoelastic materials, the importance of considering a viscoelastic material has been demonstrated, especially in injection molding situations and in literature examples.

Physically, it means that an extra component has been added to the stress tensor. This extra-stress is considered function of microscopic properties of the material, such as molecular orientation and chain stretch. A molecular model from the literature has been implemented, the Pom-Pom model.

Conservation equations were modified to take into account for the extra-stress tensor. Numerically, elasticity was introduced as a perturbation in the velocity-pressure problem, and was approximated piecewise constant per element. Thus, at each time step velocity and pressure are computed supposing that the extra-stress tensor is known. The presence of a solvent viscosity guarantees the ellipticity of the problem, but it can be chosen very small since a stabilization scheme of the D.E.V.S.S. type has been adopted. The extra-stress tensor is computed from orientation and stretch. These last are obtained solving evolution equations, of the hyperbolic type. The method adopted was the STDG (used also for free surface and temperature determination).

Applications in incompressible and compressible viscoelastic flows were presented, showing the feasibility of the developments, even in strong flows. Free surface introduction complemented the range of applications field. Nevertheless, results remain rather qualitative, needing deeper study to perform quantitative comparisons.

Finally, a temperature equation for viscoelastic compressible models was derived, for a Pom-Pom type law. Using a thermodynamical formalism we have demonstrated that it respects also the second principle of thermodynamics. Furthermore, it allows separation of entropy stored energy and elastic stored energy.

Injection molding applications

At the beginning of this work, **REM3D** was a software devoted to injection mold filling. Today, it covers all the main stages of the injection molding process, from filling to part ejection. The first main result of this PhD thesis is thus the extension of **REM3D** from filling to post-filling, even if solidification and behavior of the polymer at the solid state are taken into account considering a very simple evolution. Determination of thermodynamical variables such as pressure or temperature distribution throughout the injection cycle became possible with our approach.

Introduction of an evolution law for the density allowed compensation of the material's shrinkage by an additional mass entering the cavity. However, process conditions (namely packing pressure and holding time) don't allow generally a complete compensation, and post-computation of the shrinkage rate was relevant to the prediction of the potential shrinkage distribution in the part.

Anisotropy in the internal stresses remaining in the part were also taken into account through the viscoelastic behavior introduced. Orientation distribution will affect the part's final mechanical, optical or dimensional properties and induce warpage once the part ejected. Even if several improvements can be made, values computed are qualitatively in agreement with the literature.

In this work, comparison with the literature and experiments was performed, mainly to validate the post-filling stage, showing a good agreement. And **REM3D** remains up to this date and to our knowledge, the only software that considers a 3D viscoelastic compressible behavior in all the stages of the injection molding process simulation.

5.2   Perspectives and improvements

At the current stage of development, improvements in the physical models and numerical methods developed can be proposed, as well as large perspectives of future developments. Like previously, they can be divided in the compressible, viscoelastic and injection molding areas.

For compressible fluids applications...

In what concerns compressibility, between all the possible perspectives we outline the improvement or even development of new numerical methods that may take into account:

- pressure strongly dependent isothermal compressibility coefficients strongly dependent on pressure

- high-speed flows (higher Mach numbers)

- strong thermal compressibility

We have shown that methods developed can be applied to polymer foam expansion simulation. Actually foam expansion remains an active area of research. But for high gas volumic rates, the isothermal compressibility coefficient depends on the pressure and may attain high values when compared with polymers used in injection molding. Validity of the numerical methods implemented for low isothermal compressibility coefficients need to be verified.

Most complex materials shrink or dilate during its processing. Implementation of state laws for these materials are interesting and open horizons to other applications rather than injection molding (for example, in thermoset applications).

Shrinkage is today performed in the mold at constant volume if there is no free surface capable of adjust the volume variation. Once the part ejected, it will change dramatically to equilibrium by shrinking. One way of controlling this shrinkage is to induce porosity formation in the part during its processing. Studying local compressibility effects may help to the control of this porosity.

For viscoelastic fluids applications..

In this work, viscoelasticity has been introduced supposing that the elastic contribution of the stress tensor is several orders of magnitude inferior to the pressure, as it is generally assumed for injection molding flows (even it may not be true for some parts of injection molded pieces), representing a small perturbation in the flow. The model chosen was a simple form of the Pom-Pom model, decoupling molecular orientation and chain stretch effects.

The first physical improvement may be the introduction of a stronger coupling between both variables. Furthermore, more recent models can be easily integrated to take into account phenomena like CCR (Convective Constraint Release) or shear modification of the relaxation times.

Numerically, deeper studies need to be done to estimate the importance of the numerical parameters introduced. For example, the sensitivity of the results obtained to the stabilisation viscosity or the shear rates attained need to be clearly examined.

Finally, thermoviscoelasticity has been introduced but the effects of elasticity in the temperature evolution need a deeper study and are an important area of research. Furthermore, thermal-compressible-viscoelasticity and coupled effects remain an interesting and not developed subject both from the physical and numerical point of view.

In the injection molding domain...

In what concerns process simulation, this work allowed computation of the whole injection molding cycle. However, the material behavior assumed in the solidified layers, as well as the liquid-solid transition remains quite simple: it behaves like a liquid with constant rheological parameters. The first perspective of this work concerns modelisation and implementation of adequate numerical methods to treat the liquid-solid transition and the behavior of the solid state.

Our research group does its first steps in this field, as a natural extension of this work. For example, a crystallization kinetics model was introduced in **REM3D** to better understand the liquid solid transition and influence of process parameters such as shear rate, orientation or temperature in the solidification of semi-crystalline polymers. Figure 5.1 show the evolution of the crystallinity rate during the injection molding of the biomedical implant perviously described.

| (a) | (b) | (c) | (d) |
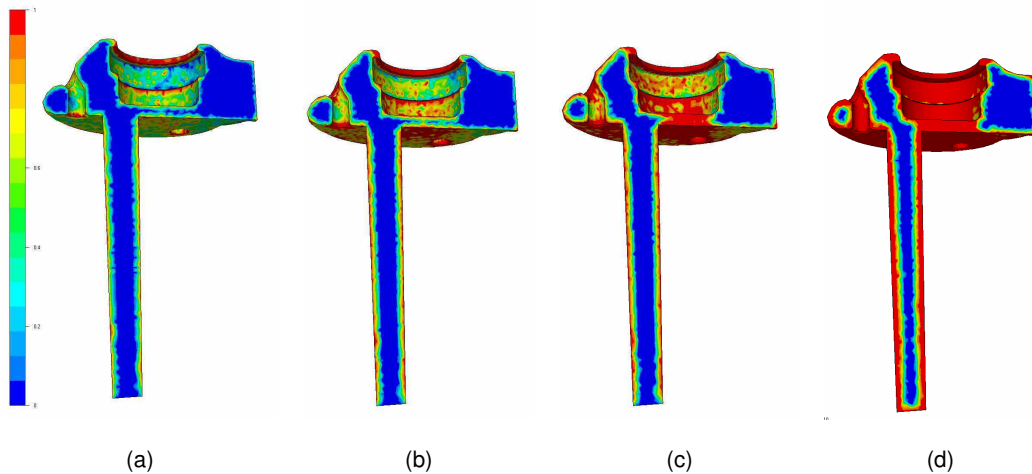
Figure 5.1: *Evolution of the crystallinity rate during injection molding of a biomedical implant [Smirnova* et al*, 2004].*

Behavior of the solid phase can be introduced using a displacement-based formulation instead of a velocity-pressure one, that may lead to numerical problems such as bad matrix conditioning when both solid and liquid phases coexist. In this case, a multiphase formulation can be exploited, and we obtain a typical fluid-structure interaction problem; first steps in the domain are currently in work (figure 5.3). Furthermore, an accurate rheological behavior of the solid layers will give us correct values for the residual stresses and part deformations.

In this context, it will be important to take into account for the mechanical properties affected by the anisotropy of the material. On one hand, molecular orientation that has frozen is of great importance; on the other hand, development of numerical methods to treat orientation evolution has allowed its application in injection molding of more complex materials such as fiber-reinforced polymers [Redjeb, 2003]. Furthermore, simulation of injection molding of oriented materials (like LCD's or multicharged) remains an unexplored area of research.
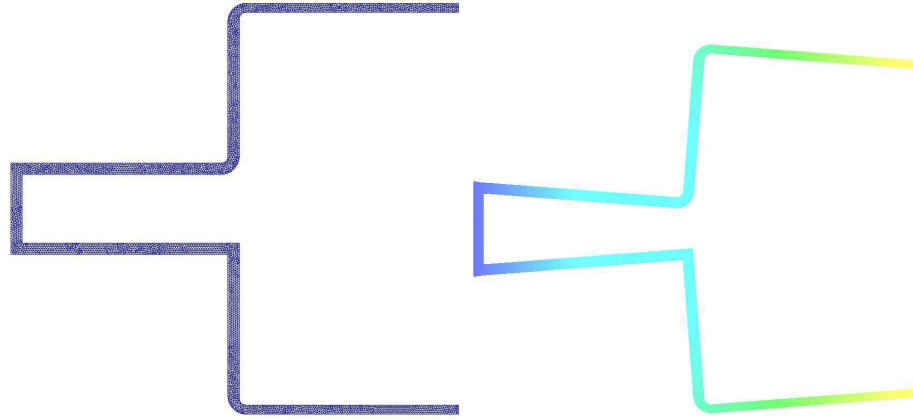
Figure 5.2: *Deformation post-ejection: on the left, initial state; on the right equilibrium; courtesy of Rodolphe Lanrivain.*

Finally, the detection of surface imperfections in molded parts represents an important industrial problem, since it is generally a criteria for part acceptation. One of the most common defects is the presence of flow marks that are often assumed to be cause by free surface instabilities during mold filling. Unstable behavior has been observed with **REM3D** but further investigation both numerical as experimental needs to be done.

*This work allowed the extension of **REM3D** from the filling to the post-filling phase of the injection molding process, supposing that the material is viscoelastic and compressible during the whole process, with a simplified behavior of the solid solidified layers. Improvements need to be done at this level to reach accurate levels of computed residual stresses and deformation. Nevertheless, perspectives of this work concern applications beyond the scope of injection molding, since numerical toolboxes developed to treat compressible viscoelastic flows can be improved to a wider range of applications in polymer engineering.*

(a)   (b)
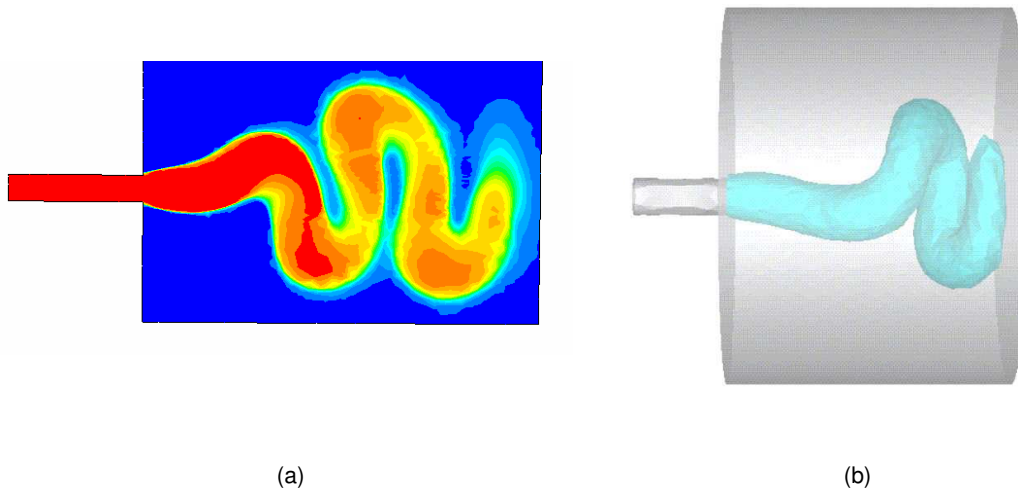
Figure 5.3: *Unstable behavior of the free surface in mold fillig (a) in 2D and (b) in 3D.*

Appendix

A. Numerical resolution of transport equations in **REM3D**

B. Thermodynamics of viscoelastic compressible media

C. Mathematical considerations on Stokes compressible flows

Appendix A

Numerical resolution of transport equations in REM3D

In this appendix we focus on the numerical resolution of convection equations of the scalar, vectorial and tensorial type, since we were often faced with throughout this work.

Numerical resolution through the STDG method

Let us consider the convection of a scalar, vectorial or tensorial field a in a space domain Ω, and during a time period $[0, \Theta]$ (where Θ is the total length time) :

$$\begin{cases} \dfrac{\partial a}{\partial t} + \mathbf{v}_c \cdot \nabla a + \varphi(a) = C \\ a(x, 0) = a_0(x) \qquad\qquad \forall x \in \partial\Omega_m^- \\ a(x, t) = a_b(x, t) \end{cases} \tag{A.1}$$

where $\mathbf{v}_c$ represents a velocity field defined in the whole space-time domain, $\varphi(a)$ is an operator depending on the nature of a (scalar, vectorial or tensorial), C is a source term, and $\partial\Omega_m^-$ is the inlet boundary of the domain:

$$\partial\Omega_m^- = \{x \in \partial\Omega_m : \mathbf{v}_c \cdot \mathbf{n} < 0\} \tag{A.2}$$

For example, considering $\varphi = 0$ and $C = 0$, we typically obtain a transport equation. The gradient operator and the velocity components can be extended in the fourth dimension by:

$$\tilde{\mathbf{v}} = \begin{pmatrix} \mathbf{v} \\ 1 \end{pmatrix} \quad \text{and} \quad \tilde{\nabla} = \begin{pmatrix} \nabla \\ \frac{\partial}{\partial t} \end{pmatrix} \tag{A.3}$$

Then, equation A.1 takes the form:

$$\tilde{\mathbf{v}} \cdot \tilde{\nabla} a + \varphi(a) = C \tag{A.4}$$

Let us consider that our time interval $[0, \Theta]$ is structured as follows: $0 = t_0 < t_1 < ... < t_{N_t}$. We define the time element I by $I =]t^n, t^{n+1}[$, such that

$$[0, \Theta] = \bigcup_n I \tag{A.5}$$

We introduce the notation:

$-\tilde{\Omega} = \Omega \times [0, \Theta]$ is the space-time domain

$-\mathcal{T}_h(\tilde{\Omega}) =$ is the space-time mesh, with $\bar{\bar{\Omega}} = \bigcup_{\tilde{K} \subset \mathcal{T}_h(\tilde{\Omega})} \tilde{K}$

$-\tilde{K} = K \times I$ is the space-time element , $\tilde{K} \subset \mathcal{T}_h(\tilde{\Omega})$

$-\tilde{F} = F \subset \partial\tilde{K}$ is the a face of $\tilde{K}$ (A.6)

$-\mathcal{F}(\mathcal{T}_h(\tilde{\Omega})) = \{F \subset \partial\tilde{K}; \forall\tilde{K} \subset \mathcal{T}_h(\tilde{\Omega})$ are all the faces of the mesh $\mathcal{T}_h(\tilde{\Omega})$

$-\mathcal{K}(\tilde{F}) = \{\tilde{K} \subset \mathcal{T}_h(\tilde{\Omega}); \tilde{F} \subset \partial\tilde{K}\}$ are all the elements sharing the same face $\tilde{F}$

$-\mathbf{n}_{\tilde{K}}^{\tilde{F}}$ is the outward unit normal to face $\tilde{F}$ in element

To simplify our method, we choose a space time mesh which is structured in time: each elementary slab is taken as the Cartesian product of a simplex K and a time interval I. We underline that this choice involves the orthogonality between the time normal and the space normal.

Let us introduce the discrete space as :

$$\mathcal{P}^{s,q}(\tilde{\Omega}) = \{f \in L^2(\tilde{\Omega}) : f_{\tilde{K}} \in P^s(K) \times P^q(I), \forall\tilde{K} \in \mathcal{T}_h(\tilde{\Omega})\} \tag{A.7}$$

The extended velocity field, $\tilde{\mathbf{v}}$ is supposed continuous in $\tilde{\Omega}$. Let us now choose a_h approximating a and piecewise continuous on each elementary slab $\tilde{K}$, $a_h \in \mathcal{P}^{s,q}$. Therefore, the discretised weak form of the equation A.4 is written:

$$\int_{\tilde{\Omega}} \phi(\tilde{\mathbf{v}} \cdot \tilde{\nabla} a_h + \varphi(a_h) - C) = \sum_{\tilde{K}} \left(-\int_{\tilde{K}} a_h \tilde{\nabla} \cdot (\phi\tilde{\mathbf{v}}) + \int_{\tilde{K}} \phi\varphi(a_h) - \int_{\tilde{K}} \phi C \right) = 0 \tag{A.8}$$

where $\phi : \tilde{\Omega} \to \mathbb{R}$ is the test function, such that $\phi \in \mathcal{C}_c^1()$. Applying the Green formula, we obtain to the convective term:

$$\int_{\tilde{\Omega}} \phi(\tilde{\mathbf{v}} \cdot \tilde{\nabla} a_h) = -\sum_{\tilde{K}} \left(\int_{\partial\tilde{K}} a_h \phi\tilde{\mathbf{v}} \cdot \mathbf{n}_{\tilde{K}} - \int_{\tilde{K}} \tilde{\nabla} a_h \cdot \tilde{\mathbf{v}}\phi \right) \tag{A.9}$$

Let us define the space-time jump operator $[.]_{\tilde{K}}^{\tilde{F}}$ as:

$$[f]_{\tilde{K}}^{\tilde{F}}(x) = \sum_{\tilde{K}' \in \mathcal{K}(\tilde{F})} f_{\tilde{K}'}(x) \mathbf{n}_{\tilde{K}'}^{\tilde{F}}, \mathbf{n}_{\tilde{K}}^{\tilde{F}} \tag{A.10}$$

where $\tilde{K}'$ is an arbitrary element of $\mathcal{K}(\tilde{F})$. Using this definition, we can write:

$$\int_{\tilde{\Omega}} \phi(\tilde{\mathbf{v}} \cdot \tilde{\nabla} a_h) = -\sum_{\tilde{F} \in \mathcal{F}} \int_{\tilde{F}} [a]_{\tilde{K}(\tilde{F})}^{\tilde{F}} \phi\mathbf{v} \cdot \mathbf{n}_{\tilde{K}(\tilde{F})}^{\tilde{F}} + \int_{\tilde{K}} \tilde{\nabla} a_h \cdot \tilde{\mathbf{v}}\phi \tag{A.11}$$

being $\tilde{K}(\tilde{F})$ is an arbitrary element of $\mathcal{K}(\tilde{F})$. We choose $a_h \in \mathcal{P}^{0,q}$: on each slab a_h is constant $(P0)$ in space and of q degree (Pq) in time. One space basis is:

$$\mathcal{B}^{0,q} = \{1_{\tilde{K}}(x,t)(t-t_n)^p\}_{\tilde{K} \in \mathcal{T}_h(\tilde{\Omega}); p=1,\ldots,q} \tag{A.12}$$

where

$$1_{\tilde{K}}(x,t) = \begin{cases} 1 & \text{if } (x,t) \in \tilde{K} \\ 0 & \text{otherwise} \end{cases} \quad \forall(x,t) \in \tilde{\Omega} \tag{A.13}$$

We can thus write, on each element, for a_h and the test function ϕ (also chosen in the same approximation space):

$$a_h(x,t)_{\tilde{K}} = \sum_{p=0}^{q} a_{\tilde{K}}^p (t - t_n)^p \qquad \phi_h(x,t) = 1_{\tilde{K}}(x,t)(t - t_n)^r \tag{A.14}$$

Finally, the local matrices computed on each element are:

- **temporal convection term**

  First of all, we have

$$
\begin{aligned}
\int_{\tilde{K}} \tilde{\nabla} a_h \cdot \tilde{\mathbf{v}} \phi &= \int_{K \times I} (t - t_n)^r \frac{\partial}{\partial t} \sum_{p=0}^{q} a_{\tilde{K}}^p (t - t_n)^p \\
&= |K| \sum_{p=0}^{q} a_{\tilde{K}}^p \int_I p(t - t_n)^{r+p-1} \\
&= |K| \sum_{p=0}^{q} a_{\tilde{K}}^p \frac{p}{p+r} |I|^{p+r}
\end{aligned} \tag{A.15}
$$

- **spatial convection term**

  We consider the decomposition of the material flux in its negative and positive parts:

$$\tilde{\mathbf{v}} \cdot \mathbf{n}_{\tilde{K}}^{\tilde{F}} = (\tilde{\mathbf{v}} \cdot \mathbf{n}_{\tilde{K}}^{\tilde{F}})^- + (\tilde{\mathbf{v}} \cdot \mathbf{n}_{\tilde{K}}^{\tilde{F}})^+ \tag{A.16}$$

  meaning that $(\tilde{\mathbf{v}} \cdot \mathbf{n}_{\tilde{K}(\tilde{F})}^{\tilde{F}})^-$ if $(\tilde{\mathbf{v}} \cdot \mathbf{n}_{\tilde{K}(\tilde{F})}^{\tilde{F}}) < 0$. Only two slabs sharing the same face, $\mathcal{K}(\tilde{F}) = \{\tilde{K}, \tilde{K}'\}$ and:

$$(\tilde{\mathbf{v}} \cdot \mathbf{n}_{\tilde{K}'}^{\tilde{F}})^+ = -(\tilde{\mathbf{v}} \cdot \mathbf{n}_{\tilde{K}}^{\tilde{F}})^- \qquad \forall x \in \tilde{F} \tag{A.17}$$

  Taking into account this relationship, the spatial convective term can be computed as:

$$\int_{\tilde{F}} [a]_{\tilde{K}(\tilde{F})}^{\tilde{F}} \phi \mathbf{v} \cdot \mathbf{n}_{\tilde{K}(\tilde{F})}^{\tilde{F}} = \int_{\tilde{F}} [a]_{\tilde{K}}^{\tilde{F}} \phi (\mathbf{v} \cdot \mathbf{n}_{\tilde{K}})^- \tag{A.18}$$

  Secondly, each structured in time space-time slab $\tilde{K}$ has $d + 3$ boundary faces (d being the space dimension). We may consider two kinds of faces, normal to the time direction, and normal to space directions:

  - two temporal faces, $\tilde{F}^-$ and $\tilde{F}^+$ (for example, the temporal neighbor of $\tilde{K}$ through $\tilde{F}^-$ is $K \times I^-$ where I^- is the previous time step of I), and we remark that the measure of each face is $|K|$;
  - $d + 1$ spatial faces, $\tilde{F}_x$ (each face is the product of one face F of ∂K with I: $F = K \times I$)

  In each face, the following scalar product is defined:

$$
\begin{aligned}
\tilde{\mathbf{v}} \cdot \mathbf{n}^{\tilde{F}_x} &= \begin{pmatrix} \mathbf{v} \\ 1 \end{pmatrix} \cdot \begin{pmatrix} \mathbf{n}_x \\ 0 \end{pmatrix} = \mathbf{v} \cdot \mathbf{n}_x \\
\tilde{\mathbf{v}} \cdot \mathbf{n}^{\tilde{F}^-} &= \begin{pmatrix} \mathbf{v} \\ 1 \end{pmatrix} \cdot \begin{pmatrix} 0 \\ -1 \end{pmatrix} = -1 \qquad \text{and} \qquad \tilde{\mathbf{v}} \cdot \mathbf{n}^{\tilde{F}^+} = \begin{pmatrix} \mathbf{v} \\ 1 \end{pmatrix} \cdot \begin{pmatrix} 0 \\ 1 \end{pmatrix} = 1
\end{aligned} \tag{A.19}
$$

Hence, the contribution of all the faces is given by:

$$
\begin{aligned}
\int_{\tilde{F}^-} [a]_{\tilde{K}}^{\tilde{F}^-} \phi(\mathbf{v} \cdot \mathbf{n}_{\tilde{K}}^{\tilde{F}^-})^- \;
&= \int_K (a_{\tilde{K}}^0 - \sum_{p=0}^q a_{\tilde{K}^-}^p |I^-|^p)(t_n - t_n)^r(-1) \\
&= |K|(\sum_{p=0}^q a_{\tilde{K}^-}^p |I^-|^p - a_{\tilde{K}}^0)\delta_{0r} \\
\int_{\tilde{F}^+} [a]_{\tilde{K}}^{\tilde{F}^+} \phi(\mathbf{v} \cdot \mathbf{n}_{\tilde{K}}^{\tilde{F}^+})^- \;
&= 0 \\
\int_{\tilde{F}_x} [a]_{\tilde{K}}^{\tilde{F}_x} \phi(\mathbf{v} \cdot \mathbf{n}_{\tilde{K}}^{\tilde{F}_x})^- \;
&= \int_{F \times I} \sum_{p=0}^q (a_{\tilde{K}}^p - a_{\tilde{K}(t_i^F{}_x)}^p)(t - t_n)^{p+r}(\mathbf{v}_c \cdot \mathbf{n}_K^F)^- \\
&= \sum_{p=0}^q (a_{\tilde{K}}^p - a_{\tilde{K}(t_i^F{}_x)}^p)\frac{|I|^{r+p+1}}{p+r+1}\int_F (\mathbf{v}_c \cdot \mathbf{n}_K^F)^-
\end{aligned}
\tag{A.20}
$$

where δ_{0r} is 1 if $r = 0$ and 0 otherwise. The sum of all contributions gives:

$$
\begin{aligned}
\int_{\tilde{F}} [a]_{\tilde{K}}^{\tilde{F}} \phi(\mathbf{v} \cdot \mathbf{n}_{\tilde{K}})^- \;
&= |K|(\sum_{p=0}^q a_{\tilde{K}^-}^p |I^-|^p - a_{\tilde{K}}^0)\delta_{0r} \\
&\quad + \sum_{p=0}^q (a_{\tilde{K}}^p - a_{\tilde{K}(\tilde{F}_x)}^p)\frac{|I|^{r+p+1}}{p+r+1}\int_F (\mathbf{v}_c \cdot \mathbf{n}_K^F)^-
\end{aligned}
\tag{A.21}
$$

- **reaction term**

Let us suppose that the operator φ is linear in a_h. In this case we have simply:

$$
\int_{\tilde{K}} \phi\varphi(a_h) \; = \int_{K \times I} \sum_{p=0}^q \varphi \cdot a_{\tilde{K}}^p (t - t_n)^{p+r} \; = |K| \sum_{p=0}^q \varphi \cdot a_{\tilde{K}}^p \frac{|I|^{p+r+1}}{p+r+1}
\tag{A.22}
$$

- **source term**

We have simply:

$$
\int_{\tilde{K}} \phi C_h \; = |K| C_K \sum_{p=0}^r \frac{|I|^{r+1}}{r+1}
\tag{A.23}
$$

Appendix B

Thermodynamics of viscoelastic compressible media

Basic notions from thermodynamics are necessary to obtain an equation on temperature from the balance of internal energy. Even if we are focusing on *viscoelastic compressible* materials, purely viscous and purely elastic cases are derived as a comparison to the coupled case.

Thermodynamics gives a rational procedure to obtain the state of equilibrium of a system through its principles of conservation and dissipation. To describe the behavior of the material it is necessary to quantify:

- how can the material *store* energy (choice of variables from which the free energy depends and the choice of the expression of this free energy);

- how can the material *dissipate* energy (definition of a potential or a pseudo-potential of energy).

The starting point of thermodynamics is the *Gibbs equation* for a material in equilibrium. The equilibrium Gibbs equation will be extended to non-equilibrium situations. Then internal variables will be introduced to describe relaxation phenomena. Combination of the resulting Gibbs equation with the balance of internal energy gives the balance of entropy. A first result is that a viscous fluid can only dissipate energy, a elastic solid can only store or release energy and a viscoelastic fluid can both store or release energy. Finally the temperature equation will be derived from the balance of entropy.

First law of thermodynamics and conservation of energy

The principle of the conservation of energy in a fluid flow is an application of the first law of thermodynamics to a flowing fluid. It can be expressed in the form: the rate of increase of total energy equals the rate of heat addition minus the rate at which work is done by the fluid element, or

$$\frac{dE}{dt} = \frac{dQ}{dt} - \frac{dW}{dt} \tag{B.1}$$

Let e be the internal energy per unit mass due to microscopic motion, and $\frac{\mathbf{v}^2}{2}$ the kinetic energy per unit mass due to macroscopic motion. Using the Reynolds transport theorem, the material derivative of the total energy becomes:

$$\frac{dE}{dt} = \frac{d}{dt}\int_{\Omega} \rho(e + \frac{\mathbf{v}^2}{2}) + \frac{d}{dt}\int_{\partial\Omega} \rho(e + \frac{\mathbf{v}^2}{2})\mathbf{v}\cdot\mathbf{n} \tag{B.2}$$

The first term is the rate of accumulation of E within the domain, and the second is the rate of transport of E out of the domain by the fluid flowing across its boundaries. On the other hand, heat is transferred because of temperature differences between adjacent locations in the fluid. For most fluids, the rate of heat flow per unit area across a surface in the fluid, ϕ, is proportional to the temperature gradient according to Fourier's law:

$$\phi = -k\nabla T \tag{B.3}$$

where $k \geq 0$ represents thermal conductivity of the molten polymer. The net rate of heat addition to the fluid is thus the integral of the heat flux over the whole surface:

$$\frac{dQ}{dt} = -\frac{d}{dt}\int_{\partial\Omega} \phi\cdot\mathbf{n} \tag{B.4}$$

Now we consider the rate at which work is done in the environment by the fluid in the domain. The rate at which the fluid does work is the sum of the rate of work by body forces and rate of work done by surface forces:

$$\frac{dW}{dt} = \frac{d}{dt}\int_{\Omega} \rho\mathbf{f}\mathbf{v} + \frac{d}{dt}\int_{\partial\Omega} \sigma\mathbf{n}\cdot\mathbf{v} \tag{B.5}$$

Using the Reynolds transport theorem, Gauss theorem and re-writing the work done by the surface stress, we obtain, in the differential form:

$$\rho\frac{de}{dt} = -\nabla\cdot\phi + \sigma : \varepsilon(\mathbf{v}) \quad \forall(\mathbf{x},t) \in \Omega(t)\times[0,\Theta] \tag{B.6}$$

Without any energy creation term, the first principle of thermodynamics is written as:

$$\rho\frac{de}{dt} = -\nabla\cdot\phi + \sigma : \varepsilon(\boldsymbol{v})$$

where e is the internal energy, ϕ is the heat flux, σ is the Cauchy stress tensor, and $\varepsilon(\boldsymbol{v})$ the rate of deformation tensor.

Second law of thermodynamics and mechanical dissipation

For an homogeneous system, the *entropy* per unit mass s is function of the *internal energy* per unit mass e and the deformation of the material (dependence represented by a set of mechanical state variables, such as the density, the Finger tensor, ...). The total energy that can be extracted from this system is usually referred as *free energy* and it measures not the energy content in this system (*internal energy*) but its "useful energy". One distinguishes often the *Helmholtz free energy f* as:

$$f = e - Ts \tag{B.7}$$

and the *Gibbs free energy g* as:

$$g = e - Ts - \mathbf{Z} : \frac{d\mathbf{z}}{dt} \tag{B.8}$$

where $\mathbf{z}$ are the mechanical state variables (the density, the Finger tensor or other internal variables) and $\mathbf{Z}$ are often referred as the conjugate forces. The independent state variables are the temperature T and the n state variables z_i.

For non-homogeneous systems, the principle of local and instantaneous equilibrium is assumed to hold. The assumption is that, although the system is not in equilibrium, it consists of small volume elements for which the local entropy is the same function as in real equilibrium. This means that the relations above remain valid.

The change of energy of a system can be described through the *Gibbs equation*:

$$\rho \frac{de}{dt} = \rho T \frac{ds}{dt} + \sum_{i=1}^{n} Z_i \frac{dz_i}{dt} = T \frac{ds}{dt} + \mathbf{Z} : \frac{d\mathbf{z}}{dt} \tag{B.9}$$

The entropy and the conjugate forces are given by the equations of state:
Combination of the Gibbs equation with the expression for the Helmholtz free energy (equation B.7) gives an expression for the change of free energy per unit mass:

$$\frac{df}{dt} = \frac{de}{dt} - s \frac{dT}{dt} - T \frac{ds}{dt} = -s \frac{dT}{dt} + \frac{1}{\rho} \mathbf{Z} : \frac{d\mathbf{z}}{dt} \tag{B.10}$$

and combination of the balance of internal energy (equation B.6) and the Gibbs equation gives the balance of entropy:

$$\rho T \frac{ds}{dt} = -\nabla \cdot \phi + \sigma : \varepsilon(\mathbf{v}) - \mathbf{Z} : \frac{d\mathbf{z}}{dt} \tag{B.11}$$

or in the local balance form

$$\rho \frac{ds}{dt} = -\nabla \cdot \mathbf{J}_s + \Pi_s \quad \text{with} \quad \mathbf{J}_s = \frac{\phi}{T} \quad \text{and} \quad T\Pi_s = -\frac{\phi}{T} \nabla T + \sigma : \varepsilon(\mathbf{v}) - \mathbf{Z} : \frac{d\mathbf{z}}{dt} \tag{B.12}$$

where $\mathbf{J}_s$ is the entropy flux and Π_s the entropy production.

The second law of thermodynamics (inequality of Clausius-Duhem) states that the entropy production must be non-negative, for all ∇T, for all $\varepsilon(\boldsymbol{v})$:

$$\rho \frac{ds}{dt} + \nabla \cdot (\frac{\phi}{T}) \geq 0 \quad \forall \nabla T, \forall \varepsilon(\boldsymbol{v})$$

or

$$-\frac{\phi \nabla T}{T} + \sigma : \varepsilon(\boldsymbol{v}) \geq 0 - \mathbf{Z} : \frac{dz}{dt} \geq 0 \quad \forall \nabla T, \forall \varepsilon(\boldsymbol{v})$$

Since it has to be valid for all ∇T (namely for $\nabla T = 0$), we assume that the mechanical entropy production has to be non-negative:

$$\sigma : \varepsilon(\mathbf{v}) - \mathbf{Z} : \frac{dz}{dt} \geq 0 \, \forall \nabla T \tag{B.13}$$

To be able to verify this conditions, the *equations of state* for the entropy and conjugate forces must be given:

- if we imagine an elastic dilatation thermal transformation, then the second principle is verified if

$$s = -(\frac{\partial f}{\partial T})_z \tag{B.14}$$

- for an elastic isothermal transformation, using the same reasoning, we obtain

$$Z_i = \rho(\frac{\partial f}{\partial z_i})_{T,z_i'} \tag{B.15}$$

where $()_x$ means a quantity at constant x. $()_{zi}$ is used if all mechanical state variables are constant and $()_{z_i'}$ if all state variables are constant except the ith variable. In the following, we will simplify this notation, not writing the index. Using the state equations, we establish for the variation of entropy:

$$\rho T \frac{ds}{dt} = \rho T \frac{\partial s}{\partial T} \frac{dT}{dt} + \rho T \frac{\partial s}{\partial \mathbf{Z}} : \frac{d\mathbf{Z}}{dt} = \rho T \frac{\partial s}{\partial T} \frac{dT}{dt} + \rho T \frac{\partial^2 f}{\partial T \partial \mathbf{Z}} : \frac{d\mathbf{Z}}{dt} = \rho T \frac{\partial s}{\partial T} \frac{dT}{dt} - T \frac{\partial \mathbf{Z}}{\partial T} : \frac{d\mathbf{z}}{dt} \tag{B.16}$$

which means that the variation of energy is, using the Gibbs equation :

$$\rho \frac{de}{dt} = \rho T \frac{\partial s}{\partial T} \frac{dT}{dt} + \mathbf{Z} : \frac{d\mathbf{z}}{dt} - T \frac{\partial \mathbf{Z}}{\partial T} : \frac{d\mathbf{z}}{dt} \tag{B.17}$$

Heat equations

In this section, we derive the heat equation for viscous, elastic and viscoelastic materials, using the definitions above. The procedure followed is:

- definition of the internal variables (the temperature and the mechanical state variables), (T, z_i);

- definition of the mechanical entropy production $T\Pi_s = \sigma : \varepsilon(\mathbf{v}) - \mathbf{Z} : \frac{d\mathbf{z}}{dt}$;

- determination of the conjugate forces Z_i, by considering the extreme case $T\Pi_s = 0$;

- verification of the second principle of thermodynamics;

- from the Gibbs equation, and the variation of entropy we obtain the variation of internal energy $\rho T \frac{\partial s}{\partial T} \frac{dT}{dt} + \mathbf{Z} : \frac{d\mathbf{Z}}{dt} - T \frac{\partial \mathbf{Z}}{\partial T} : \frac{d\mathbf{z}}{dt}$;

- using the conservation of energy equation (equation B.6) we derive the heat equation.

Viscous fluids

We have seen that the Cauchy stress tensor is defined for a viscous compressible fluid as (Chapter 2):

$$\sigma = -p\mathbf{I} + 2\eta[\varepsilon(\mathbf{v}) - \frac{1}{3}\eta\,\mathrm{tr}(\varepsilon(\mathbf{v}))\mathbf{I}] = -p\mathbf{I} + \tau_s \tag{B.18}$$

When all the forces are removed, the fluid relaxes to an hydrostatic stress state. In this case, the state variables are the temperature and the density, being the density the only mechanical, and its conjugate force is $Z_\rho = \rho\frac{\partial f}{\partial \rho}$. The Gibbs equation then becomes

$$\rho\frac{de}{dt} = \rho T\frac{ds}{dt} + Z_\rho\frac{d\rho}{dt} \tag{B.19}$$

and the equations of state

$$s = -\frac{\partial f}{\partial T} \quad \text{and} \quad \rho Z_\rho = \rho\frac{\partial f}{\partial \rho} \tag{B.20}$$

Thus, the viscous entropy production is simply:

$$T\Pi_s = -\frac{\phi}{T}\nabla T + \sigma : \varepsilon(\mathbf{v}) - Z_\rho\frac{d\rho}{dt} = -\frac{\phi}{T}\nabla T + \tau_s : \varepsilon(\mathbf{v}) + \frac{p}{\rho}\frac{d\rho}{dt} - Z_\rho\frac{d\rho}{dt} \tag{B.21}$$

Since the mechanical dissipation has to be non-negative, $\forall\varepsilon(\mathbf{v}), \forall\nabla T$ we get the expression of the conjugate force:

$$Z_\rho = \frac{p}{\rho} \tag{B.22}$$

and the entropy production is:

$$T\Pi_s = -\frac{\phi}{T}\nabla T + \sigma : \varepsilon(\mathbf{v}) - Z_\rho\frac{d\rho}{dt} = -\frac{\phi}{T}\nabla T + \tau_s : \varepsilon(\mathbf{v}) + \frac{p}{\rho}\frac{d\rho}{dt} - Z_\rho\frac{d\rho}{dt} \tag{B.23}$$

The mechanical dissipation is given by $\tau_s : \varepsilon(\mathbf{v})$ and is always positive (or zero, if the $\eta = 0$). It is useful now to introduce the following definitions for the thermodynamic coefficients of viscous fluids

$$c_p = T(\frac{\partial s}{\partial T})_p \qquad c_v = T(\frac{\partial s}{\partial T})_\rho$$

$$\chi_T = -\frac{1}{\rho}(\frac{\partial \rho}{\partial T})_p \quad \chi_p = \frac{1}{\rho}(\frac{\partial \rho}{\partial p})_T \tag{B.24}$$

where c_p is the heat capacity at constant pressure, c_v the heat capacity at constant specific volume, χ_T the thermal expansion coefficient and χ_p the isothermal compressibility.

The change of internal energy is given by equation B.17:

$$\rho\frac{de}{dt} = \rho(\frac{\partial s}{\partial T})_p\frac{dT}{dt} + \frac{p}{\rho}\frac{d\rho}{dt} + T\frac{1}{\rho^2}\frac{\partial\rho}{\partial T}\frac{d\rho}{dt} = \rho c_p\frac{dT}{dt} - p\nabla\cdot\mathbf{v} - T\chi_T\frac{dp}{dt} \tag{B.25}$$

Substitution of this expression in the energy balance (equation B.6) with the viscous entropy production gives the *temperature equation*:

$$\rho c_p\frac{dT}{dt} - p\nabla\cdot\mathbf{v} - T\chi_T\frac{dp}{dt} = -\nabla\cdot\phi + \tau_s : \varepsilon(\mathbf{v}) - p\nabla\cdot\mathbf{v} \tag{B.26}$$

or

$$\rho c_p\frac{dT}{dt} - T\chi_T\frac{dp}{dt} = -\nabla\cdot\phi + \tau_s : \varepsilon(\mathbf{v}) \tag{B.27}$$

where $\tau_s : \varepsilon(\mathbf{v})$ is the mechanical dissipation.

> *The temperature equation for a viscous compressible fluid is*
>
> $$\rho c_p \frac{dT}{dt} - T\chi_T \frac{dp}{dt} = -\nabla \cdot \phi + \tau_s : \varepsilon(\boldsymbol{v})$$

Elastic materials

The stress state of an isotropic elastic material may be described through the Finger tensor $\mathbf{B}$:

$$\sigma = -p\mathbf{I} + G(\mathbf{B} - \mathbf{I}) = -p\mathbf{I} + \tau_e \tag{B.28}$$

where G is the elastic modulus of the material. The deformation of an elastic material is completely reversible. When all external forces are removed, the elastic material returns to the original state. The Finger tensor follows an evolution equation of the type:

$$\frac{d\mathbf{B}}{dt} = \nabla \mathbf{v} \cdot \mathbf{B} + \mathbf{B} \cdot \nabla \mathbf{v}^T \tag{B.29}$$

The state variables are the temperature and the Finger tensor, being this last one the only mechanical state variable. The Gibbs equation then becomes

$$\frac{de}{dt} = T\frac{ds}{dt} + \mathbf{Z}_B : \frac{d\mathbf{B}}{dt} \tag{B.30}$$

and the equations of state

$$s = -\frac{\partial f}{\partial T} \qquad \text{and} \qquad \mathbf{Z}_B = \rho \frac{\partial f}{\partial \mathbf{B}} \tag{B.31}$$

The entropy production is:

$$
\begin{aligned}
T\Pi_s \ &= -\frac{\phi}{T} \cdot \nabla T + \sigma : \varepsilon(\mathbf{v}) - \mathbf{Z}_B : \frac{d\mathbf{B}}{dt} \\
&= -\frac{\phi}{T} \cdot \nabla T + \sigma : \varepsilon(\mathbf{v}) - \mathbf{Z}_B : (\nabla \mathbf{v} \cdot \mathbf{B} + \mathbf{B} \cdot \nabla \mathbf{v}^T) \\
&= -\frac{\phi}{T} \cdot \nabla T + (\sigma - 2\mathbf{Z_B}\mathbf{B}) : \varepsilon(\mathbf{v})
\end{aligned}
\tag{B.32}
$$

For an ideal elastic material it is assumed that no energy is dissipated due to mechanical work. Because the mechanical entropy production has to vanish for any $\varepsilon(\mathbf{v})$, the last equation gives a relation between the stress and the conjugate variable (or the elastic free energy):

$$\sigma = 2\mathbf{Z}_B\mathbf{B} \tag{B.33}$$

If the material is incompressible, ($\rho =$constant, det $\mathbf{B}=1$), we may write:

$$\mathbf{Z}_B = \frac{1}{2}\mathbf{B}^{-1}\tau_e = \frac{1}{2}G(I - \mathbf{B}^{-1}) \tag{B.34}$$

It is useful to introduce the following definitions for the heat capacities

$$c_\sigma = T\left(\frac{\partial s}{\partial T}\right)_\sigma \quad c_\mathbf{B} = T\left(\frac{\partial s}{\partial T}\right)_\mathbf{B} \tag{B.35}$$

where c_σ is the heat capacity at constant stress σ and $c_{\mathbf{B}}$ the heat capacity at constant Finger tensor $\mathbf{B}$. The change of internal energy can be written as:

$$\rho \frac{de}{dt} = \rho (\frac{\partial s}{\partial T})_{\mathbf{B}} \frac{dT}{dt} + \mathbf{Z}_B : \frac{d\mathbf{B}}{dt} - T \frac{\partial \mathbf{Z}_B}{\partial T} : \frac{d\mathbf{B}}{dt} = \rho \frac{c_B}{T} \frac{dT}{dt} + \mathbf{Z}_B : \frac{d\mathbf{B}}{dt} - T \frac{\partial \mathbf{Z}_B}{\partial T} : \frac{d\mathbf{B}}{dt} \tag{B.36}$$

Substitution in the energy balance gives the temperature equation:

$$\rho c_B \frac{dT}{dt} + \mathbf{Z}_B : \frac{d\mathbf{B}}{dt} - T \frac{\partial \mathbf{Z}_B}{\partial T} \frac{d\mathbf{B}}{dt} = -\nabla \cdot \phi + \sigma : \varepsilon(\mathbf{v}) \tag{B.37}$$

or

$$\rho c_B \frac{dT}{dt} - T \frac{\partial \mathbf{Z}_B}{\partial T} \frac{d\mathbf{B}}{dt} = -\nabla \cdot \phi + \sigma : \varepsilon(\mathbf{v}) - \mathbf{Z}_B : \frac{d\mathbf{B}}{dt} \tag{B.38}$$

Since there is no mechanical dissipation ($\sigma : \varepsilon(\mathbf{v}) - \mathbf{Z}_B : \frac{d\mathbf{B}}{dt} = 0$), we obtain:

$$\rho c_B \frac{dT}{dt} - T \frac{\partial \mathbf{Z}_B}{\partial T} \frac{d\mathbf{B}}{dt} = -\nabla \cdot \phi \tag{B.39}$$

We distinguish two cases:

- the elastic modulus G is dependent on the temperature, $G = G(T)$. This means that the conjugate force is also function of the temperature, $\mathbf{Z} = \mathbf{Z}(t)$, and

$$\frac{\partial \mathbf{Z}}{\partial T} = \frac{1}{2} \frac{\partial G}{\partial T} (I - \mathbf{B}^{-1})$$
$$\text{and} \tag{B.40}$$
$$T \frac{\partial \mathbf{Z}}{\partial T} : \frac{d\mathbf{Z}}{dt} = \frac{1}{2} \frac{\partial G}{\partial T} (I - \mathbf{B}^{-1}) : (\nabla \mathbf{v} \mathbf{B} + \mathbf{B} \nabla \mathbf{v}^T) = \frac{1}{G} \frac{\partial G}{\partial T} (\tau_e : \varepsilon(\mathbf{v}))$$

  In the particular case $G(T) = \frac{T}{T_{ref}} G_{ref}$, the fluid is called *entropy elastic* [Wapperom, 1996]. The internal energy is only function of the temperature and the reversible part of the free energy is stored as entropy. For an elastic modulus scaled linearly with temperature, all the work of the work of the elastic material is stored as entropy, which is attended with a (reversible) temperature rise;

- the elastic modulus G is not dependent on the temperature. This means that:

$$\frac{\partial \mathbf{Z}}{\partial T} = 0 \tag{B.41}$$

  The reversible part of the energy is all stored as internal energy and the material is called *energy elastic* [Wapperom, 1996].

Generally, the temperature equation for an incompressible thermal dependent elastic material is written:

$$\rho c_B \frac{dT}{dt} - T \frac{1}{G} \frac{\partial G}{\partial T} [\tau_e : \varepsilon(\boldsymbol{v})] = -\nabla \cdot \phi$$

Viscoelastic materials

Viscoelastic fluids show both viscous and elastic behavior when they are deformed. When all external forces are removed, the fluid relaxes to a hydrostatic stress state. In contrast with the elastic material, the hydrostatic stress state is not the initial stress state, since the viscous part of the deformation is irreversible. In our case, we assume that the stress tensor has an hydrostatic (pressure) contribution, a newtonian (solvent) contribution and the polymer chains contributions, determined by the deformation history of a fluid particle:

$$\sigma = -p\mathbf{I} + 2\eta[\varepsilon(\mathbf{v}) - \frac{1}{3}\mathrm{tr}(\varepsilon(\mathbf{v}))\mathbf{I}] + \sum_{i=1}^{m} \tau_i = -p\mathbf{I} + \tau_s + \tau_e \tag{B.42}$$

where m is the number of modes and τ_e the extra-stress tensor. Most of the viscoelastic models can be derived using the conformation tensor: $\mathbf{c}$. It describes the elastic deformation of a viscoelastic fluid, the deformation relative to the stress state that would be obtained after relaxation from the current state. The conformation tensor has to be positive definite to guarantee well-posedeness of the system of equations. For multi-mode models it is customary to assume that different modes do not couple. For all well-known differential models, the viscoelastic extra-stress can be found from the conformation tensor with the help of a simple algebraic relation. Let us suppose that this relation is simply:

$$\tau_i = G_i(\mathbf{c}_i - \mathbf{I}) \tag{B.43}$$

where β is a material parameter. Let us also suppose that we have one only mode, and thus one conformation tensor. It is supposed to satisfy a differential equation of the form

$$\frac{d\mathbf{c}}{dt} - \nabla\mathbf{v} \cdot \mathbf{c} - \mathbf{c} \cdot \nabla\mathbf{v}^T = -\frac{1}{\theta}(\mathbf{c} - \mathbf{I}) \tag{B.44}$$

For an isotropic viscoelastic material, the mechanical state variables are the density and the conformation tensors. For a 1-mode fluid, the Gibbs equation becomes:

$$\rho\frac{de}{dt} = \rho T\frac{ds}{dt} + \frac{p}{\rho}\frac{d\rho}{dt} + \mathbf{Z_c} : \frac{d\mathbf{c}}{dt} \tag{B.45}$$

and the equations of state for the conjugate variables

$$s = -\frac{\partial f}{\partial T} \quad p = -\rho^2\frac{\partial f}{\partial \rho} \quad \mathbf{Z_c} = \rho\frac{\partial f}{\partial \mathbf{c}} \tag{B.46}$$

The entropy production for a viscoelastic material becomes:

$$\begin{aligned} T\Pi_s &= -\frac{\phi}{T} \cdot \nabla T + \sigma : \varepsilon(\mathbf{v}) - \mathbf{Z_c} : \frac{d\mathbf{c}}{dt} - Z_\rho\frac{d\rho}{dt} \\ &= -\frac{\phi}{T} \cdot \nabla T + \tau_s : \varepsilon(\mathbf{v}) + \tau_e : \varepsilon(\mathbf{v}) - \mathbf{Z_c} : \frac{d\mathbf{c}}{dt} \\ &= -\frac{\phi}{T} \cdot \nabla T + \tau_s : \varepsilon(\mathbf{v}) + \tau_e : \varepsilon(\mathbf{v}) - \mathrm{tr}((2\mathbf{Z_c} \cdot \varepsilon(\mathbf{v}))) + \frac{1}{\theta}\mathrm{tr}(\mathbf{Z_c} \cdot [\mathbf{c} - \mathbf{I}]) \end{aligned} \tag{B.47}$$

Considering high elasticity extreme state, and that is local equilibrium, there is also no mechanical dissipation, as well as no relaxation ($\theta \to \infty$). We obtain a zero mechanical dissipation from equation B.47, $\forall\nabla T, \forall\varepsilon(\mathbf{v})$, if:

$$\tau_e = 2\mathbf{Z_c}\mathbf{c} \tag{B.48}$$

giving the expression of the conjugate variable

$$\mathbf{Z_c} = \frac{1}{2}(\mathbf{I} - \mathbf{c}^{-1}) \tag{B.49}$$

To verify if the second thermodynamical principle is respected, we need to checkout that:

$$\frac{1}{\theta}\text{tr}(\mathbf{Z_c} \cdot [\mathbf{c} - \mathbf{I}]) \geq 0 \tag{B.50}$$

In fact,

$$
\begin{aligned}
\frac{1}{\theta}\text{tr}(\mathbf{Z_c} \cdot [\mathbf{c} - \mathbf{I}]) &= \frac{G}{2\theta}\text{tr}([\mathbf{I} - \mathbf{c}^{-1}] \cdot [\mathbf{c} - \mathbf{I}]) \\
&= \frac{G}{2\theta}\text{tr}(\mathbf{c} - 2\mathbf{I} - \mathbf{c}^{-1}) \\
&= \frac{G}{2\theta}\text{tr}(\mathbf{c}) - 6 - \text{tr}(\mathbf{c}^{-1})
\end{aligned}
\tag{B.51}
$$

The trace of the conformation tensor can be obtained by adding all the eigenvalues α_i of the tensor. Thus we can rewrite the last expression as:

$$
\begin{aligned}
\frac{1}{\theta}\text{tr}(\mathbf{Z_c} \cdot [\mathbf{c} - \mathbf{I}]) &= \frac{G}{2\theta}\sum_{i=1}^{d}(\alpha_i + \frac{1}{\alpha_i} - 6) \\
&= \frac{G}{2\theta}\sum_{i=1}^{d}(\alpha_i + \frac{1}{\alpha_i} - 6) \\
&= \frac{G}{2\theta}\sum_{i=1}^{d}\frac{1}{\alpha_i}(\alpha_i^2 - 6\alpha_i + 1) \\
&= \frac{G}{2\theta}\sum_{i=1}^{d}\frac{1}{\alpha_i}(\alpha_i + 5.8)(\alpha_i + 0.7)
\end{aligned}
\tag{B.52}
$$

Since the conformation tensor is positive definite and $\text{tr}(\mathbf{c}) > 0$, all its eigenvalues are positive and the mechanical dissipation also.

It will be useful to introduce the following definitions for the thermodynamic coefficients of viscoelastic fluids

$$
c_{p,\tau_e} = T(\frac{\partial s}{\partial T})_{p,\tau_e} \quad c_{p,\mathbf{c}} = T(\frac{\partial s}{\partial T})_{p,\mathbf{c}}
$$

$$
\chi_T = -\frac{1}{\rho}(\frac{\partial \rho}{\partial T})_{p,\mathbf{c}} \quad \chi_p = \frac{1}{\rho}(\frac{\partial \rho}{\partial p})_{T,\mathbf{c}}
\tag{B.53}
$$

where c_{p,τ_e} is the heat capacity at constant pressure and elastic stress τ_e, $c_{p,\mathbf{c}}$ the heat capacity at constant pressure and conformation tensor, χ_T the thermal expansion coefficient and χ_p the isothermal compressibility.

We may now obtain the temperature equation with the internal energy variation (that is an nothing more than the additive contribution of the viscous and elastic cases):

$$
\rho\frac{de}{dt} = \rho c_p\frac{dT}{dt} - p\nabla\cdot\mathbf{v} - T\chi_T\frac{dp}{dt} + \mathbf{Z_c} : \frac{d\mathbf{c}}{dt} - T\frac{\partial\mathbf{Z_c}}{\partial T} : \frac{d\mathbf{c}}{dt}
\tag{B.54}
$$

The temperature equation is obtained as previously

$$
\rho c_p\frac{dT}{dt} - p\nabla\cdot\mathbf{v} - T\chi_T\frac{dp}{dt} + \mathbf{Z_c} : \frac{d\mathbf{c}}{dt} - T\frac{\partial\mathbf{Z_c}}{\partial T}\frac{d\mathbf{c}}{dt} = -\nabla\cdot\phi + \sigma : \varepsilon(\mathbf{v})
\tag{B.55}
$$

or

$$
\rho c_p\frac{dT}{dt} - T\chi_T\frac{dp}{dt} - T\frac{\partial\mathbf{Z_c}}{\partial T}\frac{d\mathbf{c}}{dt} = -\nabla\cdot\phi + \sigma : \varepsilon(\mathbf{v}) - \mathbf{Z_c} : \frac{d\mathbf{c}}{dt}
\tag{B.56}
$$

and even

$$\rho c_p \frac{dT}{dt} - T\chi_T \frac{dp}{dt} - T\frac{1}{G}\frac{\partial G}{\partial T}(\tau_e : \varepsilon(\mathbf{v})) = -\nabla\cdot\phi + \tau_s : \varepsilon(\mathbf{v}) + \frac{G}{2\theta}(\text{tr}(\mathbf{c}) - 3d - \text{tr}(\mathbf{c}^{-1})) \tag{B.57}$$

Like in the elastic case, we can distinguish two cases:

- the elastic modulus G is linearly dependent on the temperature, $G = G(T)$, and the fluid is called *entropy elastic*. The reversible part of the internal energy is stored as entropy;

- the elastic modulus G is not dependent on the temperature, and the material is *energy elastic*.

In both cases, we add to the mechanical viscous dissipation $(\tau_s : \varepsilon(\mathbf{v}))$, and the material's dissipation during its relaxation back to equilibrium: $(\frac{G}{2\theta}[\text{tr}(\mathbf{c}) - 3d - \text{tr}(\mathbf{c}^{-1})])$.

The temperature equation for a viscoelastic compressible material, with a simple constitutive law of the type $\tau_e = G(\mathbf{c} - \mathbf{I})$, may be written:

$$\rho c_p \frac{dT}{dt} - T\chi_T \frac{dp}{dt} - T\frac{1}{G}\frac{\partial G}{\partial T}(\tau_e : \varepsilon(\boldsymbol{v})) = -\nabla\cdot\phi + \tau_s : \varepsilon(\boldsymbol{v}) + \frac{G}{2\theta}(tr(\mathbf{c}) - 3d - tr(\mathbf{c}^{-1}))$$

Appendix C

Mathematical considerations on Stokes compressible flows

Generalities

We consider the steady-state compressible Stokes problem: *find $\boldsymbol{v} \in \mathcal{C}^2(\Omega)$ and the pressure $p \in \mathcal{C}^1(\Omega)$ such that, $\forall t \in]0, \Theta[$, $\forall x \in \Omega(t)$,*

$$\begin{cases} \nabla \cdot [2\eta(\varepsilon(\mathbf{v}) - \frac{1}{3}\nabla.\mathbf{v}I)] - \nabla p = 0 \\ \nabla \cdot \mathbf{v} + \chi_p \mathbf{v} \cdot \nabla p = g \end{cases} \tag{C.1}$$

Let us associate with the forms a, b, and d, operators $A : \mathcal{V} \to \mathcal{V}'$, $B : \mathcal{V} \to \mathcal{P}'$, $B' : \mathcal{P} \to \mathcal{V}'$, and $D : \mathcal{Q} \to \mathcal{P}'$, defined by

$$\begin{cases} \langle A\mathbf{v}, \mathbf{w} \rangle = a(\mathbf{v}, \mathbf{w}), & \forall \mathbf{v}, \mathbf{w} \in \mathcal{V} \\ \langle B\mathbf{w}, q \rangle = b(\mathbf{w}, q), & \forall \mathbf{w} \in \mathcal{V}, \forall q \in \mathcal{Q} \\ \langle B'q, \mathbf{w} \rangle = b(\mathbf{w}, q), & \forall \mathbf{w} \in \mathcal{V}, \forall q \in \mathcal{Q} \\ \langle Dp, q \rangle = d(p, q), & \forall p \in \mathcal{P}, \forall q \in \mathcal{Q} \end{cases} \tag{C.2}$$

Existence of solution to the compressible/incompressible case

As previously, we consider the operators $A_h : \mathcal{V}_h \to \mathcal{V}'_h$, $B_h : \mathcal{V}_h \to \mathcal{P}'_h$, $B'_h : \mathcal{P}_h \to \mathcal{V}'_h$, and $D_h : \mathcal{Q}_h \to \mathcal{P}'_h$, defined by

$$\begin{cases} \langle A_h\mathbf{v}_h, \mathbf{w}_h \rangle = a(\mathbf{v}_h, \mathbf{w}_h), & \forall \mathbf{v}_h, \mathbf{w}_h \in \mathcal{V}_h \\ \langle B_h\mathbf{w}_h, q_h \rangle = b(\mathbf{w}_h, q_h), & \forall \mathbf{w}_h \in \mathcal{V}_h, \forall q_h \in \mathcal{Q}_h \\ \langle B'_h q_h, \mathbf{w}_h \rangle = b(\mathbf{w}_h, q_h), & \forall \mathbf{w}_h \in \mathcal{V}_h, \forall q_h \in \mathcal{Q}_h \\ \langle D_h p_h, q_h \rangle = d(p_h, q_h), & \forall p_h \in \mathcal{P}_h, \forall q_h \in \mathcal{Q}_h \end{cases} \tag{C.3}$$

In terms of these operators, we can re-write

$$\begin{cases} A_h\mathbf{v}_h + B'_h p_h = \mathbf{f}_h \\ B_h\mathbf{v}_h + D_h p_h = g_h \end{cases} \tag{C.4}$$

[Kellog and Liu, 1996] showed that the compressible Stokes problem needs to respect the same conditions than the incompressible one to guarantee unicity of the solution. The next lemma and theorem show the existence and unicity of solutions, and refer to Chapter 2, pages 18-19.

LEMMA 1. *If 2.24, 2.25 and 2.26 are satisfied and if $\gamma \leq \frac{1}{2}\alpha\beta^2\|a\|^{-2}$, then the problem 2.30 has at most one solution.*

PROOF. From 2.24 the map $A_h : \mathcal{V}_h \to \mathcal{V}_h'$ is invertible, and $\|A_h^{-1}\| \leq \alpha^{-1}$, $\alpha^{-1} \leq \|A_h\|$. Thus, we eliminate $\mathbf{v}_h$, and write

$$D_h p_h + B_h A_h^{-1} B_h' p_h = g_h + B_h A_h^{-1} \mathbf{f}_h = \tilde{g}_h \tag{C.5}$$

To our problem to have a unique solution, it is sufficient to solve C.5 for any linear functional $\tilde{g}_h \in \mathcal{P}_h'$. Equation C.5 is also an identity in $\mathcal{P}_h'$; applying this identity to $q_h \in \mathcal{P}_h$, one obtains

$$\tilde{d}(p_h, q_h) = d(p_h, q_h) + b(A_h^{-1} B_h' p_h, q_h) = \langle \tilde{g}_h, q_h \rangle, \quad \forall q_h \in \mathcal{P}_h \tag{C.6}$$

From its definition, $\tilde{d}_h$ is a bounded bilinear form on $\mathcal{Q}_h \times \mathcal{P}_h$. We want now to estimate $\tilde{d}(p_h, q_h)$ from below. Let $\mathbf{u}_h = A_h^{-1} B_h' p_h$, so $A_h \mathbf{u}_h = B_h' p_h$. Then

$$a(\mathbf{u}_h, \mathbf{w}_h) = b(A_h^{-1} B_h' p_h, p_h), \quad \forall \mathbf{w}_h \in \mathcal{V}_h \tag{C.7}$$

Setting $\mathbf{w}_h = \mathbf{u}_h$

$$a(\mathbf{u}_h, \mathbf{u}_h) = b(\mathbf{u}_h, p_h) = b(\mathbf{u}_h, p_h), \quad \forall \mathbf{w}_h \in \mathcal{V}_h \tag{C.8}$$

Using 2.24, 2.26, we have

$$\tilde{d}(p_h, q_h) \geq -\gamma\|p_h\|_{\mathcal{P}}^2 + \alpha\|A_h^{-1} B_h' p_h\|_{\mathcal{V}}^2, \quad \forall p_h \in \mathcal{Q}_h \tag{C.9}$$

Since A_h is a bounded operator, $\|A_h^{-1}\mathbf{m}\|_{\mathcal{V}} \geq \|A_h\|^{-1}\|\mathbf{m}\|_{\mathcal{V}_h'} \geq \|a\|^{-1}\|\mathbf{m}\|_{\mathcal{V}_h'}$. Hence

$$\tilde{d}(p_h, q_h) \geq -\gamma\|p_h\|_{\mathcal{P}}^2 + \alpha\|a\|^{-2}\|B_h' p_h\|_{\mathcal{V}_h'}^2, \quad \forall p_h \in \mathcal{Q}_h \tag{C.10}$$

From the inf-sup condition, 2.25, in its discrete form

$$\|B_h' p_h\|_{\mathcal{V}_h'} = \sup_{\mathbf{w} \in \mathcal{V}_h} \frac{\langle B_h' p_h, \mathbf{w}_h \rangle}{\|\mathbf{v}\|_{\mathcal{V}}} \geq \beta\|p_h\|_{\mathcal{P}}, \quad \forall p_h \in \mathcal{Q}_h \tag{C.11}$$

Hence

$$\tilde{d}(p_h, q_h) \geq (\alpha\|a\|^{-1}\|\beta^2 - \gamma)\|p_h\|_{\mathcal{P}}^2, \quad \forall p_h \in \mathcal{Q}_h \tag{C.12}$$

Therefore, if γ satisfies the required condition,

$$\tilde{d}(p_h, q_h) \geq \tilde{\gamma}\|p_h\|_{\mathcal{P}}^2, \quad \forall p_h \in \mathcal{Q}_h \tag{C.13}$$

where $\tilde{\gamma} = \frac{1}{2}\alpha\beta^2\|a\|^{-1}$. Consequently, there is at most one solution.

Being this condition satisfied, we guarantee unicity of the solution in pressure. As we have seen, the Brezzi-Babuska theorem establishes existence and unicity of the solution for the mixed variational

form of the continuous problem, existence and unicity of the solution for the discrete formulation and and stability result to choose the spaces $\mathcal{V}_h$ and $\mathcal{Q}_h$. For a newtonian fluid, and if Brezzi-Babuska conditions are verified in the continuous and discrete cases, there is a constant C, such that

$$\|\mathbf{v} - \mathbf{v}_h\|_{\mathcal{V}} + \|p - p_h\|_{\mathcal{P}} \leq C[\|\mathbf{v} - \mathbf{w}_h\|_{\mathcal{V}} + \|p - q_h\|_{\mathcal{Q}}] \tag{C.14}$$

THEOREM 1. *If 2.24, 2.25 and 2.26 are satisfied and if $\gamma \leq \frac{1}{2}\alpha\beta^2\|a\|^{-2}$, then the approximate solution $(\boldsymbol{v}_h, p_h)$ satisfies*

$$\|\mathbf{v} - \mathbf{v}_h\|_{\mathcal{V}} + \|p - p_h\|_{\mathcal{P}} \leq C[\|\mathbf{v} - \mathbf{w}_h\|_{\mathcal{V}} + \|p - q_h\|_{\mathcal{Q}}] \tag{C.15}$$

where the infimum is taken over all $\mathbf{V}_h \in \mathcal{V}_h$ and $q_h \in \mathcal{Q}_h$.

PROOF. One has, $\forall \bar{\mathbf{w}}_h \in \mathcal{V}_h, \forall \bar{q}_h \in \mathcal{Q}_h$

$$\begin{cases} a(\mathbf{v} - \mathbf{v}_h, \bar{\mathbf{w}}_h) + b(\bar{\mathbf{w}}_h, p - p_h) = 0 \\ b(\mathbf{v} - \mathbf{v}_h, \bar{q}_h) + d(p - p_h, \bar{q}_h) = 0 \end{cases} \tag{C.16}$$

Therefore, $\forall \bar{\mathbf{w}}_h \in \mathcal{V}_h, \forall \bar{q}_h \in \mathcal{Q}_h$

$$\begin{cases} a(\mathbf{v}_h - \mathbf{w}_h, \bar{\mathbf{w}}_h) + b(\bar{\mathbf{w}}_h, p_h - q_h) = a(\mathbf{v} - \mathbf{w}_h, \bar{\mathbf{w}}_h) + b(\bar{\mathbf{w}}_h, p - q_h) \\ b(\mathbf{v}_h - \mathbf{w}_h, \bar{q}_h) + d(p_h - q_h, \bar{q}_h) = b(\mathbf{v} - \mathbf{w}_h, \bar{q}_h) + d(p - q_h, \bar{q}_h) \end{cases} \tag{C.17}$$

Let $\mathbf{F}_h \in \mathcal{V}'_h$ be the linear functional on $\mathcal{V}_h$ defined by

$$a(\mathbf{v} - \mathbf{w}_h, \bar{\mathbf{w}}_h) + b(\bar{\mathbf{w}}_h, p - q_h) = \langle \mathbf{F}_h, \bar{\mathbf{w}}_h \rangle \tag{C.18}$$

Since

$$\|\langle \mathbf{F}_h, \bar{\mathbf{w}}_h \rangle\| \leq C_1[\|\mathbf{v} - \mathbf{w}_h\|_{\mathcal{V}} + \|p - q_h\|_{\mathcal{P}}]\|\bar{\mathbf{w}}_h\|_{\mathcal{V}} \tag{C.19}$$

where $C1 = \max\{\|a\|, \|b\|\}$, we have

$$\|\mathbf{F}_h\|_{\mathcal{V}'_h} \leq C_2[\|\mathbf{v} - \mathbf{w}_h\|_{\mathcal{V}} + \|p - q_h\|_{\mathcal{P}}] \tag{C.20}$$

Similarly, Let $G_h \in \mathcal{P}'_h$ be the linear functional on $\mathcal{P}_h$ defined by

$$\|\langle G_h, \bar{q}_h \rangle\| = d(p - q_h, \bar{q}_h) + b(\mathbf{v} - \mathbf{w}_h, \bar{q}_h) \tag{C.21}$$

Since

$$\|\langle G_h, \bar{q}_h \rangle\| \leq C_2[\|\mathbf{v} - \mathbf{w}_h\|_{\mathcal{V}} + \|p - q_h\|_{\mathcal{Q}}]\|\bar{q}_h\|_{\mathcal{P}} \tag{C.22}$$

where $C_2 = \max\{\|b\|, \|d\|\}$, we have

$$\|G_h\|_{\mathcal{P}'_h} \leq C_2[\|\mathbf{v} - \mathbf{w}_h\|_{\mathcal{V}} + \|p - q_h\|_{\mathcal{Q}}] \tag{C.23}$$

The system C.17 may be written

$$
\begin{cases}
A_h(\mathbf{v}_h - \mathbf{w}_h) + B_h'(p_h - q_h) = \mathbf{F}_h \\
B_h(\mathbf{v}_h - \mathbf{w}_h) + D_h(p_h - q_h) = G_h
\end{cases}
\tag{C.24}
$$

Therefore

$$
D_h(p_h - q_h) + B_h A_h^{-1} B_h'(p_h - q_h) = G_h + B_h A_h^{-1} \mathbf{F}_h
\tag{C.25}
$$

Hence

$$
\tilde{d}_h(p_h - q_h, p_h - q_h) = \langle G_h, p_h - q_h \rangle + \langle B_h A_h^{-1} \mathbf{F}_h, p_h - q_h \rangle
\tag{C.26}
$$

where the bilinear form is defined in C.6. Using **LEMMA 1** to estimate $\tilde{c}_h(p_h - q_h, p_h - q_h)$, we obtain

$$
\|p_h - q_h\|_{\mathcal{P}}^2 \leq C_3[\|G_h\|_{\mathcal{P}'}\|p_h - q_h\|_{\mathcal{P}} + \|B_h A_h^{-1} \mathbf{F}_h\|_{\mathcal{P}_h'}\|p_h - q_h\|_{\mathcal{P}}]
\tag{C.27}
$$

where $C_3 = 2\|a\|\alpha^{-1}\beta^{-2}$. Applying the above bounds, we obtain

$$
\|p_h - q_h\|_{\mathcal{P}} \leq C_4[\|\mathbf{v} - \mathbf{w}_h\|_{\mathcal{V}} + \|p - q_h\|_{\mathcal{Q}}]
\tag{C.28}
$$

where $C_4 = C_2 C_3 + C_1 C_3 \|b\|\alpha^{-1}$. Writing $p - p_h = p + q_h - q_h - p_h$ and using the triangle inequality, we obtain the estimate for $p - p_h$ (error in p) in C.14, with $C = 1 + C_4$. To bound the error in $\mathbf{v}$, we set $\bar{\mathbf{v}} = \mathbf{v}_h - \mathbf{w}_h$ in C.16, obtaining

$$
a(\mathbf{v}_h - \mathbf{w}_h, \mathbf{v}_h - \mathbf{w}_h) = -b(\mathbf{v}_h - \mathbf{w}_h, p_h - q_h) + \langle \mathbf{F}_h, \mathbf{v}_h - \mathbf{w}_h \rangle
\tag{C.29}
$$

Using the coercivity of a bound to the left side from below, we obtain

$$
\|\mathbf{v}_h - \mathbf{w}_h\|_{\mathcal{V}} \leq \alpha^{-1}[\|p_h - q_h\|_{\mathcal{P}} + \|\mathbf{F}_h\|_{\mathcal{V}_h'}]
\tag{C.30}
$$

Using C.25 and the bound for $\mathbf{F}_h$, we get

$$
\|\mathbf{v}_h - \mathbf{w}_h\|_{\mathcal{V}} \leq C_5[\|\mathbf{v} - \mathbf{w}_h\|_{\mathcal{V}} + \|p - q_h\|_{\mathcal{Q}}]
\tag{C.31}
$$

where $C_5 = \alpha^{-1}(C_1 + C_4)$. Writing $\mathbf{v} - \mathbf{v}_h = \mathbf{v} - \mathbf{w}_h + \mathbf{w}_h - \mathbf{v}_h$ and using the triangle inequality, we obtain the estimate for $\mathbf{v} - \mathbf{v}_h$ contained in C.14, with $C = 1 + C_5$. We therefore obtain C.14 with $C = 1 + \max\{C_4, C_5\}$.

Notation

- **General and operators**

a	scalar
$\mathbf{a}$	vector
$\mathbf{a}$	tensor
$\mathbf{a}^T$	transposed vector/tensor
∇a	gradient
$\nabla \cdot a$	divergence
$\nabla^2 a$	laplacian
$\dfrac{da}{dt}$	material derivative
$\dfrac{\partial a}{\partial t}$	temporal derivative
a^t	value of a at time t
a_x	value of a at spatial coordinate x
δ_{0q}	Kronecker index
$\bar{a}$	average value on an element K
$\tilde{a}$	space-time operator
$\displaystyle\int_a$	integral over the domain of a
$\displaystyle\sum_a$	sum on all elements a

- **Temporal and spatial notations**

t	time variable
t_n	instant n
t_{n+1}	instant $n+1$
$I_n = [t_n, t_{n+1}]$	time element
$|I_n| = \Delta t = (t_{n+1} - t_n)$	time element length
$[0, \Theta]$	temporal computational domain, Θ is the processus duration
x	spatial coordinates
Ω	spatial computational domain
$\partial\Omega$	spatial boundary of the computational domain
Ω_i	subdomain i
Ω_h	discretized spatial computational domain
$\mathcal{T}_h(\Omega)$	spatial finite element mesh, $\Omega_h = \bigcup_{K \in \mathcal{T}_h(\Omega)} K$
K	mesh spatial element, $K \in \mathcal{T}_h(\Omega)$
K^f	subelement, $K^f \subset K$
$|K|$	volume of element K
$\mathcal{F}(\mathcal{T}_h(\Omega))$	all the faces of the mesh $\mathcal{T}_h(\Omega)$, $F \subset \partial K, \forall K \in \mathcal{T}_h(\Omega)$
F	mesh face of K, $F \subset K$
$|F|$	surface of face F
$\mathcal{K}(F)$	all the elements sharing the same face F, $KK \in \mathcal{T}_h(\Omega), F \subset K$
$\mathbf{n}_K^F$	outward unit normal to face F in element K
$[a]_{\tilde{K}}^{\tilde{F}}$	space-time jump operator
$\alpha_{\tilde{K}}^{\tilde{F}}$	weight

- **Variables and material properties**

$\mathbf{x}$	point coordinates
$\mathbf{v}$	velocity vector
p	pressure
T	temperature
$\mathbf{s}$	average molecular orientation tensor
λ	chain stretch
σ	Cauchy stress tensor
$\varepsilon(\mathbf{v})$	rate of deformation tensor
ρ	density kg/m^3
χ_p	isothermal compressibility coefficient Pa^{-1}
χ_T	dilatation coefficient K^{-1}
η	dynamical viscosity Pas
κ	volumic viscosity Pas
λ	second Lame coefficient
μ	first Lame coefficient
G	relaxation or elastic modulus Pa
θ_b	orientation relaxation time s
θ_s	stretch relaxation time s
ν	viscoelastic parameter $\nu = 1/q$, where q is the number of molecular arms
c_p	specific heat at constant pressure $J/(KgK)$
c_v	specific heat at constant volume $J/(KgK)$
k	conductivity $W/(mK)$
$\dot{w}$	mechanical dissipation $J/(m^3 s)$

- **Functional spaces**

$L^2(\Omega)$	Lebesgue space
$H^1(\Omega)$	Hilbert space
$\mathcal{V}$	velocity
$\mathcal{P}$	pressure
$\mathcal{Q}$	test function pressure
$\overline{\mathcal{P}}$	element average pressure
$\mathcal{S}$	orientation/extra-stress
$\mathcal{L}$	stretch
$\mathcal{P}_h^{s,q}$	Approximation space, order s in space and q in time

Bibliography

[Agassant et al., 1986] Agassant, J.-F., Avenas, P., Sergent, J.-P., Vergnes, B., and Vincent, M. (1986). *La mise en forme des matières plastiques.* Lavoisier, Paris, 3rd edition.

[Ammar, 2001] Ammar, A. (2001). *Modélisation numérique de la cristallisation induite par l'écoulement d'un thermoplastique.* PhD thesis, École Normale Supérieure de Cachan.

[Arnold et al., 1984] Arnold, D., Brezzi, F., and Fortin, M. (1984). A stable finite element for Stokes equations. *Calcolo*, 21:337–344.

[Baaijens, 1991] Baaijens, F. (1991). Residual stresses in injection molded products. *Rheologica Acta*, 30(3):284–299.

[Baaijens, 1998] Baaijens, F. (1998). Mixed finite element method for viscoelastic flow analysis: a review. *Journal of Non-Newtonian Fluid Mechanics*, 79:361–386.

[Baaijens et al., 1998] Baaijens, F., Selen, S., Baaijens, H., and Peters, G. (1998). Viscoelastic flow past a confined cylinder of a low density polyethylene. *Journal of Non-Newtonian Fluid Mechanics*, 68:173–203.

[Batkam et al., 2003] Batkam, S., Bruchon, J., and Coupez, T. (2003). A space-time discontinuous Galerkin method for convection and diffusion in injection moulding. *International Journal of Forming Processes*, Accepted.

[Beraudo et al., 1998] Beraudo, C., Fortin, A., Coupez, T., Demay, Y., Vergnes, B., and Agassant, J. (1998). A finite element method for computing the flow of multi-mode viscoelastic fluids: Comparison with experiments. *Journal of Non-Newtonian Fluid Mechanics*, 75:1–23.

[Beris and Edwards, 1994] Beris, A. and Edwards, B. (1994). *Thermodynamic of flowing systems.* Oxford, New York.

[Bigot and Coupez, 2000] Bigot, E. and Coupez, T. (2000). Capture of 3d moving free surfaces and material interfaces by mesh deformation. *ECCOMAS 2000*, Barcelona, 11-14 September 2000.

[Bikard et al., 2004] Bikard, J., Bruchon, J., Coupez, T., and Silva, L. (2004). Polyurethane foam expansion macro-modelling. *International Journal for Numerical Methods in Fluids*, Submitted.

[Blackwell et al., 2000] Blackwell, R., McLeish, T., and Harlen, O. (2000). Molecular drag-strain coupling in branched polymer melts. *Journal of Rheology*, 44:121–136.

[Bogaerds et al., 1999] Bogaerds, A., Verbeeten, W., Peters, G., and Baiijens, F. (1999). 3d viscoelastic analysis of a polymer solution in a complex flow. *Computer Methods in Applied Mechanics and Engineering*, 180:413–430.

[Bourrigaud et al., 2003] Bourrigaud, S., Marin, G., and Poitou, A. (2003). Shear modification of long-chain branched polymers: A theoretical approach using the pom-pom model. *Macromolecules*, 36:1388–1394.

[Brezzi and Fortin, 1991] Brezzi, F. and Fortin, M. (1991). *Mixed and hybrid finite element methods.* Springer-Verlag, Berlin.

[Bristeau et al., 1990] Bristeau, M., Glowinski, R., Dutto, L., Periaux, J., and Roge, G. (1990). Compressible viscous flow calculations using compatible finite element approximations. *International Journal for Numerical Methods in Fluids*, 11:719–749.

[Broyer et al., 1974] Broyer, E., Guttfinger, C., and Tadmor, Z. (1974). Flow-analysis network (fan) method for solving flow problems in polymer processing. *Polymer Engineering and Science*, 14:660.

[Bruchon and Coupez, 2003] Bruchon, J. and Coupez, T. (2003). The foam structure prediction by the 3d calculation of the bubble growth in a molten polymer. *Journal of Non-Newtonian Fluid Mechanics*, Submitted.

[Brujan, 2001] Brujan, E. (2001). The equation of bubble dynamics in a compressible linear viscoelastic liquid. *Fluid Dynamics Research*, 298:287–294.

[Chang, 1994] Chang, M. (1994). On the study of surface defects in the injection moulding of rubber-modified thermoplastics. *ANTEC94*, pages 360–367.

[Chiang et al., 1991] Chiang, H., Hieber, C., and Wang, K. (1991). A unified simulation of filling and post-filling stages in injection molding. part 1: formulation. *Polymer Engineering and Science*, 31(2):116–140.

[Chinesta et al., 2000] Chinesta, F., Poitou, A., and Torres, R. (2000). A semi-lagrangian strategy to predict the fiber orientation in the steady flows of reinforced thermoplastics. *Computer Methods in Applied Mechanics and Engineering*, 189:233–247.

[Clemeur et al., 2002] Clemeur, N., Rutgers, R., and Debbaut, B. (2002). On the evaluation of some differential formulations for the 'pom-pom' constitutive model. *Rheologica Acta*, 14(1):25–32.

[Cormenzana et al., 2001] Cormenzana, J., Ledda, A., Laso, M., and Debbaut, B. (2001). Calculation of free surface flows using CONNFESSIT. *Journal of Rheology*, 45(1):237–258.

[Coupez, 1996] Coupez, T. (1996). Stable-stabilized finite element for 3d forming calculation. *CEMEF, ENSMP, internal report.*

[Crochet and Keunings, 1982] Crochet, M. and Keunings, R. (1982). Finite element analysis of die swell of a highly elastic fluid. *Journal of Non-Newtonian Fluid Mechanics*, 10:339–356.

[Cruickshank and Munson, 1981] Cruickshank, J. and Munson, B. (1981). Viscous buckling of plane and axisymetric jets. *Journal of Fluid Mechanics*, 13:221–239.

[Davis, 1983] Davis, G. D. (1983). Natural convection of air in a square cavity: a benchmark numerical solution. *International Journal for Numerical Methods in Fluids*, 3:249–264.

[Dee and Walsh, 1988] Dee, G. and Walsh, D. (1988). Equations of state for polymer liquids. *Macromolecules*, 21:815–817.

[des Cloizeaux, 1989] des Cloizeaux, J. (1989). Relaxation of entangled polymers in melt. *Macromolecules*, 23(17):3992–4006.

[Dietz et al., 1978] Dietz, W., White, J., and Clark, E. (1978). Orientation development and relaxation in injection molding of amorphous polymers. *Polymer Engineering and Science*, 18:273.

[Digonnet and Coupez, 2003] Digonnet, H. and Coupez, T. (2003). Object-oriented programming for "fast-and-easy" development of parallel applications in forming processes simulation. In K.J.Bathe, editor, *Second MIT Conference on Computational Fluid and Solid Mechanics*, pages 1922–1924. Massachussets Institute of Technology, Elsevier.

[Doi and Edwards, 1986] Doi, M. and Edwards, S. (1986). *The theory of polymer dynamics*. Oxford University Press, Oxford.

[Dressler et al., 1999] Dressler, M., Edwards, B., and Ottinger, H. (1999). Macroscopic thermodynamics of flowing polymeric liquids. *Rheologica Acta*, 38:117–136.

[Flaman, 1990] Flaman, A. (1990). *Built-up and relaxation of molecular orientation in injection molding*. PhD thesis, Technische Universiteit Eindhoven.

[Flory et al., 1964] Flory, P., Orwoll, R., and Vrij, A. (1964). Statistical thermodynamics of chain molecule liquids. i: the equation of state for paraffin hydrocarbons. *Journal of American Chemical Society*, 86:3507–3514.

[Fulchiron, 2002] Fulchiron, R. (2002). Comportement des matériaux sous-pression. *École thématique CNRS, Injection des polymères*.

[Gennes, 1970] Gennes, P. D. (1970). Reptation of a polymer chain in the presence of fixed obstacles. *Journal of Chemical Physics*, 55:572–579.

[Graham et al., 2001] Graham, R., McLeish, T., and Harlen, O. (2001). Using the pom-pom equations to analyze polymer melts in exponential shear. *Journal of Rheology*, 45(1):27–52.

[Greener and Pearson, 1983] Greener, J. and Pearson, G. (1983). Orientation residual stresses and birefringence in injection molding. *Journal of Rheology*, 27:115.

[Guenette and Fortin, 1995] Guenette, R. and Fortin, M. (1995). A new finite element method for computing viscoelastic flows. *Journal of Non-Newtonian Fluid Mechanics*, 60:275–290.

[Hammer, 2001] Hammer, C. (2001). Calcul des contraintes et deformations residuelles lors de la mise en oeuvre de verre ophtalmique en polymère thermodurcissable. *Ecole Nationale Superieure des Mines de Paris*.

[Harlow and Amsden, 1971] Harlow, F. and Amsden, A. (1971). A numerical fluid dynamics calculation method for all flow speeds. *Journal of Computational Physics*, 8:197–213.

[Harry and Parrot, 1970] Harry, D. and Parrot, R. (1970). Numerical simulation of injection mold filling. *Polymer Engineering and Science*, 10:209–.

[Hauke and Hughes, 1994] Hauke, G. and Hughes, T. (1994). A unified approach to compressible and incompressible flows. *Computer Methods in Applied Mechanics and Engineering*, 113:389–395.

[Hieber and Shen, 1980] Hieber, C. and Shen, S. (1980). A finite element/finite difference method of the injection mold-filling process. *Journal of Non-Newtonian Fluid Mechanics*, 7:1–32.

[Hoff, 1995] Hoff, D. (1995). Global solutions of the navier-stokes equations for multidimensional compressible flow with discontinuous initial data. *Journal of Differential Equations*, 120(1):215–254.

[Illinca and Hetu, 2001] Illinca, F. and Hetu, J.-F. (2001). Three dimensional filling and post-filling of polymer injection molding. *International Polymer Processing*, 16:291–301.

[Inkson et al., 1999] Inkson, N., McLeish, T., Harlen, O., and Groves, D. (1999). Predicting low density polyethylene melt rheology in elongational and shear flows with 'pom-pom' constitutive equations. *Journal of Rheology*, 43:873–869.

[Isayev, 1983] Isayev, A. (1983). Orientation development in the injection molding of amorphous polymers. *Polymer Engineering and Science*, 23:271.

[Isayev, 1987] Isayev, A. (1987). *Injection and Compression Molding Fundamentals*. Marcel Dekker, New York.

[Isayev and Hieber, 1980] Isayev, A. and Hieber, C. (1980). Towards viscoelastic modelling of the injection molding of polymers. *Rheologica Acta*, 19:168–182.

[Issa et al., 1986] Issa, R., Gosman, A., and Watkins, A. (1986). The computation of compressible and incompressible free recirculating flows by a non-iterative implicit scheme. *Journal of Computational Physics*, 62:66–82.

[Janeschitz, 1977] Janeschitz, H. (1977). Injection molding of plastics: some ideas about the relationship between mold filling and birefringence data. *Rheologica Acta*, 16:327.

[Kamal et al., 1986] Kamal, M., Chiu, E., Lafleur, P., and Ryan, M. (1986). Computer simulation of injection mold filling for viscoelastic melts with fountain flow. *Polymer Engineering and Science*, 26:190–196.

[Kamal and Kenig, 1972] Kamal, M. and Kenig, S. (1972). The injection molding of thermoplastics. *Polymer Engineering and Science*, 12:294–308.

[Kanel, 1968] Kanel, Y. (1968). A model system for the one-dimensional motion of a gas. *Differencial'nya Uravenenija*, 4:721–734.

[Kellog and Liu, 1996] Kellog, R. and Liu, B. (1996). A finite element method for the compressible navier-stokes equations. *SIAM Journal of Numerical Analysis*, 33:780–788.

[Kellog and Liu, 1997] Kellog, R. and Liu, B. (1997). A penalized finite element method for a compressible stokes systems. *SIAM Journal of Numerical Analysis*, 34:1093–1105.

[Keshtiban et al., 2004] Keshtiban, I., Belbidlia, F., and Webster, M. (2004). Numerical simulation of compressible viscoelastic liquids. *Journal for Non-Newtonian Fluid Mechanics*, 122:131–146.

[Keunings, 1986] Keunings, R. (1986). An algorithm for the simulation of transient viscoelastic flows with free surfaces. *Journal of Computational Physics*, 62:199–220.

[Keunings and Bousfield, 1987] Keunings, R. and Bousfield, D. (1987). Analysis of surface tension driven levelling in horizontal viscoelastic films. *Journal of Non-Newtonian Fluid Mechanics*, 22:219–233.

[Khazikov and Shelukh, 1977] Khazikov, A. and Shelukh, V. (1977). Unique global solution with respect to time of initial-boundary value problems for one-dimensional equations of a viscous gas. *Journal of Applied Mathematics in Mechanics*, 41:273–282.

[Khazikov and Weigant, 1995] Khazikov, A. and Weigant, V. (1995). On the existence of global solutions of two-dimensional navier-stokes equations of a compressible viscous fluids. *Journal of Siberian Mathematics*, 36:1108–1141.

[Kim et al., 1999] Kim, I., Park, S., Chung, J., and Kwon, T. (1999). Numerical modeling of injection/compression molded center-gated disk. *Polymer Engineering and Science*, 39:1930–1942.

[Kuo and Kamal, 1976] Kuo, Y. and Kamal, M. (1976). The fluid mechanics and heat transfer of injection mold filling of thermoplastics materials. *A.I.C.H.E. Journal*, 22:661–669.

[Kuo and Kamal, 1977] Kuo, Y. and Kamal, M. (1977). Flow of thermoplastics in the filling and packing stages of injection molding. In *International Conference on Polymer Processing*, pages 329–348. Cambridge, Massachussets.

[Kwon, 1996] Kwon, Y. (1996). On hadamard stability for compressible viscoelastic constitutive equation. *Journal of Non-Newtonian Fluid Mechanics*, 65:151–163.

[Lee et al., 2001] Lee, K., Mackley, M., MacLeish, T., Nicholson, T., and Harlen, O. (2001). Experimental observation and numerical simulation of transient "stress fangs" within flowing molten polyethylene. *Journal of Rheology*, 45(6):1261–1277.

[Lefebvre, 1993] Lefebvre, L. (1993). *Numerical simulation of the flow of polyurethane foams.* PhD thesis, Louvain-la-Neuve.

[Leonov, 1976] Leonov, A. (1976). Non-equilibrium thermodynamics and rheology of compressible viscoelastic media. *Rheologica Acta*, 15:85–98.

[Lions, 1993] Lions, P. (1993). Existence globale de solutions pour les equations de navier-stokes compressibles isentropiques. *Comptes-Rendus de l'Académie des Sciences*, 316:1335–1340.

[Lord, 1979] Lord, H. (1979). Flow of polymers with pressure dependent viscosity. *Polymer Engineering and Science*, 19:469–473.

[Mahishi, 1998] Mahishi, M. (1998). Material characterization for thin wall molding simulation. In *ANTEC1998*, pages 547–551.

[Maillot, 1993] Maillot, I. (1993). *Simulation du remplissage/compactage pour la mise en forme des thermoplastiques par injection. Applications industrielles.* PhD thesis, Université Joseph Fourier, Grenoble.

[Marchal and Crochet, 1987] Marchal, J. and Crochet, M. (1987). A new mixed finite element for calculating viscoelastic flow. *Journal of Non-Newtonian Fluid Mechanics*, 26:77–114.

[Marrucci, 1983] Marrucci, G. (1983). Testing of a constitutive equation for entangled networks by elongational and shear data of polymer melts. *Rheologica Acta*, 12:269.

[Marrucci, 1985] Marrucci, G. (1985). Relaxation by reptation and tube enlargement: a model for polydisperse polymers. *Journal of Polymer Science: Polymer Physics*, 23:159–177.

[Matsumura and Nishida, 1979] Matsumura, A. and Nishida, T. (1979). The initial value problem for the equations of motion of compressible viscous and heat conductive fluids. *Proceedings of the Japan Academy*, 55:337–342.

[Matusu-Necasova et al., 1999] Matusu-Necasova, S., Sequeira, A., and Videman, J. (1999). Existence of classical solutions for compressible viscoelastic fluids of Oldroyd type past an obstacle. *Mathematical Methods in Applied Sciences*, 22:449–460.

[Mavridis et al., 1988] Mavridis, H., Hrymak, A., and Vlachopoulos, J. (1988). Finite element simulation of fountain flow in injection molding. *Polymer Engineering and Science*, 26:449.

[McLeish and Larson, 1998] McLeish, T. and Larson, R. (1998). Molecular constitutive equations for a class of branched polymers: the Pom-Pom polymer. *Journal of Rheology*, 42:81–110.

[Nigro et al., 1997] Nigro, N., Storti, M., and Idelsohn, S. (1997). A general algorithm for compressible and incompressible flow. stability analysis and explicit time integration. *International Journal of Numerical Methods for Heat and Fluid Flow*, 7(2/3):141–168.

[Nonaka and Nakayama, 1996] Nonaka, N. and Nakayama, T. (1996). A unified method for the numerical analysis of compressible and incompressible viscous flows. *Computational Mechanics*, 19:369–376.

[Ottinger, 2001] Ottinger, H. (2001). Thermodynamic admissibility of the pompon model for branched polymers. *Rheologica Acta*, 40(4):317–321.

[Pantani et al., 2004] Pantani, R., Sorrentino, A., Speranza, V., and Titomanlio, G. (2004). Molecular orientation in injection molding: experiments and analysis. *Rheologica Acta*, 43:109–118.

[Peters and Baaijens, 1997] Peters, G. and Baaijens, F. (1997). Modelling of non-isothermal viscoelastic flows. *Journal of Non-Newtonian Fluid Mechanics*, 168:205–224.

[Pichelin and Coupez, 1998] Pichelin, E. and Coupez, T. (1998). Finite element solution of the 3d mold filling problem for viscous incompressible fluid. *Computer Methods in Applied Mechanics and Engineering*, 163:359–371.

[Pontes, 2002] Pontes, A. (2002). *Shrinkage and ejection forces in injection molded products*. PhD thesis, Universidade do Minho.

[Rajagopalam et al., 1990] Rajagopalam, D., Armstrong, R., and Brown, R. (1990). Finite element method for steady calculation of viscoelastic flow using constitutive equations with a newtonian viscosity. *Journal of Non-Newtonian Fluid Mechanics*, 36:159–192.

[Redjeb, 2003] Redjeb, A. (2003). Simulation numérique de l'orientation de fibre en injection de thermoplastiques renforcés. *Rapport d'avancement, CEMEF*.

[Rodgers, 1993] Rodgers, P. (1993). PVT relationships for polymeric liquids: a review of equations of state and their characteristic parameters for 56 polymers. *Journal of Applied Polymer Science*, 48:1061–1080.

[Ryan and Chung, 1980] Ryan, M. and Chung, T. (1980). Conforming mapping analysis of injection mold filling. *Polymer Engineering and Science*, 20:642.

[Saez, 2003] Saez, E. (2003). *Étude numérique du remplissage 3D en fonderie*. PhD thesis, École Nationale Supérieure des Mines de Paris.

[Shyu et al., 2003] Shyu, G., Isayev, A., and Lee, H. (2003). Numerical simulation of flow induced birefringence in injection molded disk. *Korea-Australia Rheology Journal*, 15:159–166.

[Simha and Somcynski, 1969] Simha, R. and Somcynski, T. (1969). On the statistical thermodynamics of spherical and chain molecule fluids. *Macromolecules*, 2:342–350.

[Simo, 1987] Simo, J. (1987). On a fully three dimensional finite strain viscoelastic damage model: formulation and computational aspects. *Computer Methods in Applied Mechanics and Engineering*, 60:153–173.

[Sirakov, 2000] Sirakov, I. (2000). *Etude par éléments finis des écoulements viscoélastiques des polymères fondus dans des géometries complexes. Résultats numériques et expérimentaux*. PhD thesis, École des Mines de Saint-Etienne.

[Smirnova et al., 2004] Smirnova, J., Silva, L., Monasse, B., Chenot, J., and Haudin, J. (2004). Structure development in injection molding. A 3d simulation with a differential formulation of the kinetics equations. *International Polymer Processing*, Submitted.

[Sun et al., 1996] Sun, J., Phan-Thien, N., and Tanner, R. (1996). An adaptive viscoelastic stress splitting scheme and its applications: Avss/si and avss/supg. *Journal of Non-Newtonian Fluid Mechanics*, 65:75–91.

[Szadi et al., 1995] Szadi, M., Salmon, T., Liu, A., Bornside, D., and Armstrong, R. (1995). New mixed finite element method for viscoelastic flows governed by differential constitutive equations. *Journal of Non-Newtonian Fluid Mechanics*, 59:215–243.

[Tadmor, 1974] Tadmor (1974). Molecular orientation in injection molding. *Journal of Applied Polymer Science*, 18:1753.

[Takeshima and Funakoshi, 2001] Takeshima, M. and Funakoshi, N. (2001). Molecular orientation distribution in polycarbonate disks. *Journal of Applied Polymer Science*, 32:3457–3468.

[Tanner, 1970] Tanner, R. (1970). A theory of die swell. *Journal of Polymer Science*, 8:2067–2078.

[Titomanlio et al., 1980] Titomanlio, G., D.Acierno, and Mantia, F. L. (1980). Modelling of the filling and packing step in the injection molding of thermoplastic materials. *Ing.Chim.It.*, 16:110.

[Valette, 2003] Valette, R. (2003). The matching of numerical simulation involving time dependent compressible viscoelastic flow with precise polyethylene processing data. *AERC Conference, Portugal*.

[Verbeeten et al., 2002] Verbeeten, W., Peters, G., and Baaijens, F. (2002). Viscoelastic analysis of complex polymer melt flows using the extended pompom model. *Journal of Non-Newtonian Fluid Mechanics*, 108:301–326.

[Wakashima and Saitoh, 2004] Wakashima, S. and Saitoh, T. (2004). Benchmark solutions for natural convection in a cubic cavity using the high-order space time method. *International Journal of Heat and Mass Transfer*, 47:853–864.

[Wales, 1976] Wales, J. (1976). *The application of flow birefringence to rheological studies of polymer melts*. PhD thesis, Delft University.

[Wang et al., 1986] Wang, K., Hieber, C., and Wang, K. (1986). Dynamic simulation and graphics for the injection molding of three dimensional thin parts. *Journal of Polymer Engineering*, 7:21–45.

[Wapperom, 1996] Wapperom, P. (1996). *Non-isothermal flows of viscoelastic fluids*. PhD thesis, Delft University.

[Wapperon and Hulsen, 1998] Wapperon, P. and Hulsen, M. (1998). Thermodynamics of viscoelastic fluids: the temperature equation. *Journal of Rheology*, 42(5):999–1019.

[Westover, 1992] Westover, R. (1992). Measuring polymer melt viscosities at high pressures: The hydrostatic pressure rheometer. *Advances in Polymer Technology*, 11(2):147–151.

[Williams and Lord, 1975] Williams, G. and Lord, H. (1975). Mold filling studies for the injection molding of thermoplastic materials. *Polymer Engineering and Science*, 15:553–268.

[Yabe and Wang, 1991] Yabe, T. and Wang, P. (1991). Unified numerical procedure for compressible and incompressible flows. *Journal of the Physical Society of Japan*, 60:2105–2108.

[Zienkiewicz and Wu, 1992] Zienkiewicz, O. and Wu, J. (1992). A general explicit or semi-explicit algorithm for compressible and incompressible flows. *International Journal for Numerical Methods in Engineering*, 35:475–479.

Abstract

This work concerns simulation of viscoelastic compressible flows and applications in injection molding. Compressibility has been integrated in REM3D by considering a density evolution for the material, function of the pressure and temperature through the Tait law. Conservation of mass is written in terms of velocity, pressure and temperature, using the isothermal compressibility and dilatation material parameters. We are led to the Stokes compressible problem, which is solved using the Mixed Finite Element method. The linear system arising from the problem is non-linear and non-symmetrical. Thermal coupling is also taken into account, being the energy problem solved through the Space-Time Discontinuous Galerkin method. Extension of the compressible Stokes problem to a multi-domain configuration is given through the characteristic functions, computed by advection equations.

Viscoelasticity is introduced using the Pom-Pom model. The extra-stress is considered function of microscopic properties of the material, such as molecular orientation and chain stretch. Elasticity is a perturbation in the mechanical problem. The presence of a solvent viscosity guarantees the ellipticity of the problem, and a stabilization scheme of the DEVSS type is adopted. Orientation and stretch are obtained solving evolution equations, of the hyperbolic type, through the Space-Time Discontinuous Galerkin method. Finally, a temperature equation for viscoelastic compressible models is derived.

In what concerns injection molding applications, REM3D covers now all the main stages of the injection molding process, from filling to part ejection. Solidification and behavior of the polymer at the solid state are taken into account considering a very simple evolution. Compensation of the material's shrinkage is done using the material's compressible character. Anisotropy in the internal stresses remaining in the part affects its final mechanical, optical or dimensional properties and induce warpage once the part ejected. Comparison with the literature and experiments is performed, mainly to validate the post-filling stage, showing a good agreement.

Keywords: **injection molding**, **mixed and space-time finite element method**, **compressibility**, **viscoelasticity**, **moving free surfaces**.

Résumé

Ce travail concerne la simulation d'écoulements viscoélastiques compressibles appliquée à l'injection de polymères. La compressibilité est intégrée dans Rem3D en supposant que la densité du matériau suit une loi d'évolution du type loi de Tait. La conservation de la masse est écrite comme une équation en vitesse, pression et température, à travers des coefficients de compressibilité isotherme et de dilatation isobare. Le système obtenu est désigné "Stokes compressible" et sa résolution numérique est faite par la méthode des éléments finis mixtes. Le système obtenu est non-lineaire et non-symétrique. Le couplage thermique et l'extension à des problèmes avec surface libre sont aussi considérés.

Le modèle viscoélastique choisi est le modèle Pom-Pom, issu de la dynamique moléculaire. L'extra-contrainte est fonction des propriétés microscopiques du matériau, comme l'orientation moléculaire et son étirement. L'élasticité est vue comme une perturbation dans le problème mécanique, et une méthode de stabilisation du type DEVSS est utilisée. L'orientation et l'étirement sont déterminés par la résolution de deux équations d'évolution via une méthode espace-temps Galerkin discontinu. Finalement, la thermoviscoélasticité est abordée brièvement.

Dans le contexte de l'injection de polymères, REM3D couvre aujourd'hui toutes les phases du procédé. Néanmoins, la solidification et la transition liquide-solide sont approximées par un comportement du type liquide de très haute viscosité. L'introduction de la compressibilité permet de compenser le retrait du matériau par un apport supplémentaire de matière. D'un autre côté, la prise en compte d'un comportement viscoélastique détecte d'éventuelles anisotropies des propriétés de la pièce injectée. Les diverses comparaisons des résultats obtenus avec la littérature et l'expérience montre une bonne concordance, validant les modèles implémentés.

Mots clefs: **injection**, **éléments-finis mixtes et espace-temps**, **compressibilité**, **viscoelasticité**, **surface libres**.